Development of a fast Monte Carlo code for dose calculation in treatment planning and feasibility study of high contrast portal imaging.

Keivan Jabbari

Department of Physics

McGill University
Montreal
December 2008

A thesis submitted to the faculty of graduate studies and research in partial fulfillment of the requirements of the degree of Doctor of Philosophy

ABSTRACT

A fast and accurate treatment planning system is essential for radiation therapy and Monte Carlo (MC) techniques produce the most accurate results for dose calculation in treatment planning. In this work, we developed a fast Monte Carlo code based on pre-calculated data (PMC, Pre-calculated Monte Carlo) for applications in radiation therapy treatment planning. The PMC code takes advantage of large available memory in current computer hardware for extensive generation of pre-calculated data. Primary tracks of electrons are generated in the middle of homogeneous materials (water, air, bone, lung) and with energies between 0.2 and 18 MeV using the EGSnrc code. Secondary electrons are not transported but their position, energy, charge and direction are saved and used as a primary particle. Based on medium type and incident electron energy, a track is selected from the pre-calculated set. The performance of the method is tested in various homogeneous and heterogeneous configurations and the results were generally within 2% compared to EGSnrc but with a 40-60 times speed improvement.

The limitations of various techniques for the improvement of speed and accuracy of particle transport have been evaluated. We studied the obstacles for further increased speed ups in voxel based geometries by including ray-tracing and particle fluence information in the pre-generated track information. The latter method leads to speed-increases of about a factor of 500 over EGSnrc for voxel-based geometries. In both approaches, no physical calculation is carried out during the runtime phase after the pre-generated data has been stored even in the presence of heterogeneities. The pre-calculated data is generated for each particular material and this improves the performance of the pre-calculated Monte Carlo code both in terms of accuracy and speed.

The PMC is also extended for proton transport in radiation therapy. The pre-calculated data is based on tracks of 10000 primary protons using general purpose MCNPX code. The proton energy range was 20, 40, …100, 110, …200 MeV with ECUT=200 keV. Protons produce many different secondary particles such as neutrons, deuterons, tritons, alphas, secondary protons, etc and they are handled in three categories: 1-Secondary protons: treated like a primary protons and transported using a track picked up from pre-calculated tracks; 2- Neutrons: The energy of the neutron are deposited far from the initial

point and neglected. 3- All other secondaries: Since other secondaries have a very short range their energy is deposited locally. In comparison of the code with MCNPX as the reference the difference is generally between 2-4% and it runs 100 times faster than MCNPX.

Pre-calculated Monte Carlo codes are accurate, fast and physics-independent and therefore applicable to different radiation types including heavy-charged particles.

In another project, we worked on Monte Carlo feasibility study to use orthogonal bremsstrahlung beams for imaging in radiation therapy. The basic characteristics of orthogonal bremsstrahlung beams are studied and the feasibility of improved contrast imaging in linear accelerator with such a beam is evaluated. In the context of this work orthogonal bremsstrahlung beams represent the component of the bremsstrahlung distribution perpendicular to the electron beam impinging on an accelerator target. In this set up the bending magnet of the linac is turned off and the primary electron beam directly hits a target from the side and the orthogonal beam in downward direction is used for imaging purposes. Monte Carlo modeling (BEAM code) is used to design the shape of different targets and to obtain the energy spectrum and the relative intensity of the orthogonal beams. After optimizing the shape of the target, two different target and a collimator was designed and built. The CLINAC 18 in Montreal General Hospital was used for the experiments. The simple lucite objects one of which with 1 cm steps was placed in the way of the orthogonal beams to verify the contrast. The simulations showed that in the orthogonal direction 80 % of the CSDA range is enough to stop all of the scattered electrons. The intensity of the orthogonal beam for high-z targets is larger compared to low Z targets i.e., by a factor 20 for W/Be. The energy spectrum of the photon spectrum for low-z targets energy is lower (330 KeV for Al and 170 keV for Be) compare to higher z targets (900 KeV for Pb). In the experimental setup as well as Monte Carlo simulation it was illustrated that the contrast of the images created with the orthogonal beam is better than that of the forward beam.

ABRÉGÉ

Un plan de traitement rapide et précis est essentiel en radiothérapie et les techniques par Monte-Carlo produisent les résultats les plus précis pour le calcul de dose. Dans la présente recherche, nous avons développé un script de Monte-Carlo rapide basé sur des données pré-calculée (PMC, Monte Carlo pré-calculé) pour des applications en radiothérapie. Le code informatique PMC prend l'avantage d'une grande quantité de mémoire actuellement installée de nos jours sur les ordinateurs afin de générer des données pré-calculées. Les traces primaires des électrons sont générées au centre de matériaux homogènes (eau, air, os, poumons) avec des énergies entre 0.2 et 18 MeV en utilisant le code EGSnrc. Les électrons secondaires ne sont pas transportés, mais leurs positions, énergies, charges et directions sont sauvegardées et utilisées comme particules primaires. D'après le type de matériel et d'énergie de l'électron, le tracé est sélectionné et utilisé comme particule primaire. La performance de cette méthode est testée dans plusieurs types de configurations homogènes et non- homogènes. Les résultats, lorsque comparés à ceux de EGSnrc, sont à l'intérieur d'une marge de 2% tandis que la rapidité de calcul est de 40 à 60 fois supérieure.

Les limitations de certaines techniques pour l'amélioration de la rapidité et de la précision du transport des particules à été auparavant évaluées. Nous avons étudié les divers obstacles qui entravent l'augmentation de la rapidité dans le cadre de géométries basées sur des voxels en incluant dans les données de traces pré-générés les informations sur le tracé de faisceau ainsi que la fluence des particules. Cette dernière méthode mène à une diminution du temps de calculs d'un facteur de 500 comparé a EGSnrc dans le cadre de géométries basées sur des voxels. Dans les deux approches, aucun calcul de nature physique n'a été effectué durant la phase d'exécution après que les données pré-générées eussent été enregistrées, même en présence d'inhomogénéités. Les données pré-calculées sont générées pour chaque type de matériel et cette approche améliore les performances du code PMC en termes de précision et de rapidité.

Le code PMC est aussi étendu pour le transport de protons en radiothérapie. Les données pre-calculées utilisant le code informatique MCNPX sont basées sur le tracé des 1000 premiers protons. L'énergie des protons va de 20, 40, …, 100, 110, à 220 MeV avec

ECUT = 200 keV. Les protons produisent plusieurs particules secondaires telles que les neutrons, deutérons, tritons, alphas, protons secondaires, etc ; elles sont gérées dans trois catégories. 1- Protons secondaires : sont considérés comme des protons secondaires et transportés en utilisant un tracé tiré des tracés pré calculés. 2- Neutrons : l'énergie des neutrons est déposée loin du point initial et est négligée. 3- Toutes les autres particules secondaires : puisque les autres particules secondaires ont un parcourt minime, leur énergie est déposée localement. En comparaison avec le code informatique MCNPX, la différence est généralement entre 2 et 4 % et tourne 100 fois plus rapidement que MCNPX.

Les codes informatiques pré calculés de Monte-Carlo sont précis, rapide et indépendant de la physique et par conséquent applicables à plusieurs type de faisceaux tels que les particules à haute charge.

Dans un autre projet, nous avons étudié la capacité du code Monte-Carlo à utiliser des faisceaux orthogonaux de bremsstrahlung dans le cadre d'imagerie en radiothérapie. Les caractéristiques de base des faisceaux orthogonaux de bremsstrahlung sont étudiées et la possibilité d'améliorer le contraste dans les systèmes d'imagerie installés dans les accélérateurs linéaires est évaluée. Dans le contexte de cette recherche, les faisceaux orthogonaux de bremsstrahlung représentent la composante de la distribution de Bremsstrahlung perpendiculaire au faisceau d'électron incident à la cible de l'accélérateur linéaire. Dans cette configuration, l'aimant de déviation du Linac est désactivé et le faisceau d'électron primaire frappe la cible de coté et le faisceau orthogonal dirigé vers la bas est utilisé à des fins d'imagerie. La méthode par Monte-Carlo (code BEAM) est utilisée pour concevoir la forme de différentes cibles et pour obtenir le spectre énergétique et l'intensité relative du faisceau orthogonal. Après avoir optimisé la forme de la cible, deux cibles différentes et un collimateur ont été conçus et construits. Le LINAC 18 à l'Hôpital Général de Montréal a été utilisé pour nos travaux. Des objets en lucite ont été placés dans le champ du faisceau orthogonal afin de vérifier le contraste. La simulation a démontré que dans la direction orthogonale 80 % du parcourt CSDA est assez pour arrêter tous les électrons dispersés. L'intensité du faisceau pour les cibles à haut nombre atomique est plus grande comparée à celle des cibles ayant un faible nombre atomique, par exemple un facteur de 20 pour W/Be. L'énergie spectrale du spectre photonique pour les cibles à faible numéro Z est plus faible (330 keV pour Al et 170 keV pour Be) comparée a celle des cibles

ayant un haut nombre atomique (900 keV for Pb). L'expérience ainsi que la simulation Monte-Carlo ont démontré que le contraste des images crées avec le faisceau orthogonal est meilleur que celui des images crées avec le faisceau de transmission.

Acknowledgements

In the name of God, the Merciful and Compassionate

First and foremost, I would like to thank my supervisor, Dr. Jan Seuntjens, for his encouragement, patience and support throughout this thesis. I appreciate his kindness, care and concerns regarding student's life and family.

I would like to thank Dr. Ervin Podgorsak for his support and helpful advices throughout the experimental portion of this project. I also joined his radiation therapy and dosimetry classes and learned from a great instructor how to teach various techniques of Medical Physics.

I am grateful to Dr. Paul Keall at Stanford University for useful discussions while revisiting the SMC (Super position Monte Carlo) approach and for sharing his experience in fast Monte Carlo with me.

I like to thank Dr. Wamied Abdel-Rahman for many interesting discussions. He was always ready to help students in solving problems of all kinds and for maintaining the blade cluster.

I like to tank Emily Heath for setting up the EGSnrc code for me so I could modify the source on my own. I would also like to thank Dr. Christoph Furstoss for constructive discussions on application of MCNPX. Their help saved me lots of time.

I would like to thank Arman Sarfehnia for great contribution in experiments of target designing for LINAC and continuing the project. I also thank him for reading and editing of this thesis. Many thanks to John Thebaut for translating the abstract.

I would like to thank all students and staff in the McGill Medical Physics Unit for interesting discussions, sharing of their viewpoints, and their smiles.

I would like to thank my parents for their love and lifetime support. Without their help, I would not have made it so far.

Finally, I would like to thank my wife, Marzieh, who gave me her loving support, patience, taking care of the kids, Maryam and Amin, and her understanding throughout this long work.

Table of contents

Chapter 1

Introduction

1.1 Radiation therapy

Radiation therapy is the use of high-energy particles or rays to damage cancer cells and prevent them from growing. This treatment modality can be used alone or in conjunction with surgery, chemotherapy or hormonal therapy to treat cancer. The source of radiation could be x-rays, gamma rays, electrons, neutrons, protons, etc. Although some normal cells may be affected by radiation, most of them can recover from the effects of radiation and function properly. The goal of radiation therapy is to damage as many cancer cells as possible, while limiting harm to nearby healthy tissue and irradiate minimal dose in critical organs.[1]

Radiation therapy can be delivered either externally or internally. External beam radiation therapy is the more common form of radiation therapy. The radiation used in external radiation therapy can come from a variety of sources, including x-rays, electron beams or gamma rays. A linear accelerator (linac) produces high-energy radiation beams that are directed at the tumor. One can rotate the linac gantry to aim the beams at different angles. External radiation therapy is usually given five days a week for one to eight weeks, depending on the disease. The daily treatment usually takes only a few minutes. The total dose of radiation and the exact number of treatment fractions depend on the size, location, and the type of cancer, as well as the patient's overall health and other types of treatments he or she may be receiving.

In the case of internal radiation therapy, also called brachytherapy, the radiation source is implanted in the body in or near the cancer tumor. The source is sealed in a small holder called an implant. The implant may be thin wires, plastic tubes, capsules, or seeds. The implant is placed for a few hours, a few days, or it may be left in place. The

doctor will decide the amount of time that the implant will be in place. If it is to be left in the body, the implant will lose its intensity of radioactivity in a short time. Internal radiation therapy allows the physician to deliver a higher total dose of radiation in a shorter period of time than can be achieved with external treatment.

The delivery of radiation as a therapeutic modality demands strict attention to the training and experience of all associated personnel, the accuracy and robustness of the equipments used, as well as the general safety of the patients and personnel throughout the delivery.

1.2 Role of physics in radiation therapy

The foundation of radiation oncology is based on the interactions between matter and energy. Beginning with the discovery of x-rays in 1895 by Wilhelm Roentgen, the role of the physicist has been critical in understanding how radiation interacts with matter. Radioactivity was discovered by Henri Becquerel in 1896 and the separation of radium was achieved for the first time by Marie and Pierre Curie in 1898 when it became known that certain materials emitted radiation. The biological effects of radiation have been studied by many scientists and radiation has been a part of medicine for the good part of the past century. The medical application of x-rays and radioactivity has given rise to the discipline of Medical Physics. Medical physics applies physics to the needs of medicine, and has been instrumental in the development of the medical fields of radiology, radiation oncology, and nuclear medicine. Modern Radiation Therapy is delivered using very sophisticated state-of-the-art equipments, computers and treatment planning systems and algorithms, developed by physicists and engineers, to selectively pinpoint and treat target volumes while minimizing radiation dose to normal tissues[3]. Some of these modern treatment techniques include Intensity Modulated Radiation Therapy (IMRT), Image Guided Radiation Therapy (IGRT), Intensity Modulated Proton Therapy (IMPT), etc.

1.3 Steps of radiation therapy

Before radiation therapy can begin, a radiation oncologist must prescribe the dose of radiation that is needed, taking into consideration the general health of the patient and the

type and stage of the cancer. Various steps of radiation therapy including diagnostic sections defined by J Van Dyk [3] are illustrated in Figure 1.1.

Treatment Simulation: After imaging and diagnostic, the first step in the radiation therapy process is simulation. During simulation, the radiation therapist uses an x-ray imaging machine (Simulator) or alternatively a computer tomography simulator (CT-Simulator) to pinpoint the location of the tumor.

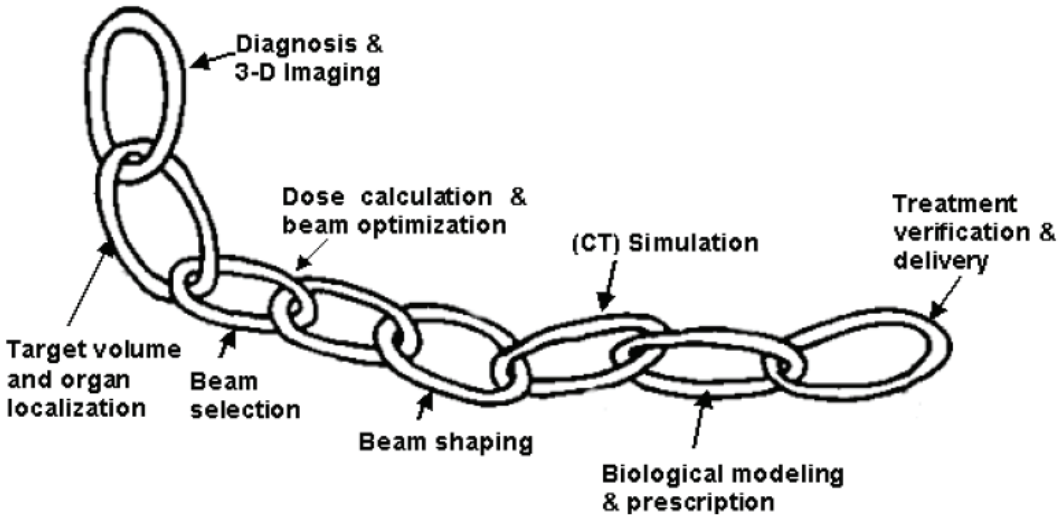

Figure 1.1 Steps of entire radiation treatment process. (Figure from Ref.[3])

The simulator has the same geometry and can perform the same movements with the treatment machine (LINAC), but uses low energy, diagnostic X-rays, instead of high-energy treatment rays.

In general, CT-Simulators are softwares that use the patient's digital data, mainly coming from computed tomography scanner, instead of the real patient to perform the simulation process. In the case of external radiotherapy, the radiation therapist places markings on the patient's skin to align the body to the machine for treatment. Sometimes, if the treatment is complex the therapist may ask the patient to keep these markings on.

*Treatment Planning***:** In the treatment planning stage, using all available information, including those obtained from the simulation, the final plan will determine the technique, type of therapy, size and a number of x-ray beams, frequency and duration of treatments, how much radiation is given through each beam (dose) and dose limiting

structures. The treatment planning team includes the radiation oncologist, dosimetrist and physicist. As treatment plans have become more sophisticated, the ability of Radiation Oncology facilities to cure tumors without harming the patients has improved. Typical plans display both the tumor(s) and sensitive normal tissues in 3-dimensional space and seek to include the entire tumor and as little of the normal tissues within the radiation field. Such plans are said to conform to the tumor and are often referred to as 'conformal irradiation'.

Treatment verification: Radiation treatment accuracy is divided into dosimetric accuracy and geometric accuracy. Both of these have to be verified with special techniques. The dosimetric accuracy deals with radiation beam calibration and dose calculations. The geometric accuracy covers issues related to patient positioning and immobilization that have a strong effect on how well we can accurately cover a specified anatomical volume with a desired radiation dose. Errors in patient positioning and beam placement can be quantified by various equipments. Electronic portal imaging devices (EPID) attached to the treatment machines are able to study and verify the accuracy and reproducibility of the treatment execution[2] and document the delivered radiation dose.

Dose delivery: For most cancers, external radiation therapy is given four or five days a week for a total of five to seven weeks. Taking two or three days off per week helps normal cells to recover. Research has shown that delivering many smaller radiation dose fractions is more advantageous than the delivery of a few large dose fractions[3]: The treatment is just as effective while the damage to healthy tissues is reduced. Radiation is usually given once daily, but sometimes the treatment is divided into two or more fractions with reduced daily dose. This is called fractionated radiation therapy.

In the case of internal radiation therapy, the patient might stay at the hospital for a few days (only for temperorary). The radioactive material may be placed in small tubes that are implanted into the cancerous tumor or a body cavity, or swallowed or injected into the bloodstream. Once an implant is removed, there is no radioactivity in the body. The amount of radiation in a permanent implant goes down to a safe level before the patient leaves the hospital.

1.4 Dose calculation methods for treatment planning

There are several methods for dose calculation in radiation therapy such as pencil beam algorithm[8-10], superposition-convolution algorithm[11-14] and Monte Carlo techniques. In pencil beam algorithm an electron beam is modeled as a collection of forward-directed "pencils" after collimation device of accelerator. The electron pencil beams at subsequent planes are redistributed in a Gaussian distribution due scatter in the medium and air.

In superposition-convolution algorithm the 'total energy released per unit mass' is convolved with 'energy deposition kernels'[11] generated in homogeneous media of different densities to obtain the dose distribution.

The Monte Carlo (MC) method is a statistical simulation method based on random sampling.[4-6] For radiation transport problems, this technique simulates the tracks of individual particles by sampling appropriate quantities from the probability distributions governing the individual physical processes using machine-generated random numbers (the details of MC method is discussed in Chapter 2).

The physical description of the electron transport in heterogeneous media is more complicated than photons because of the strong scattering effects. The analytical pencil beam algorithms in electron transport may produce a large error, up to 20 %, near the small high density heterogeneities.[15,17] The problem with superposition method is that the track of the electrons are assumed to be straight lines and the tracks are simply scaled by density[18]. This limitation produces a large error in high energies and there are also methods to overcome the density interface problem of superposition method and improve the accuracy of the results.

1.5 Monte Carlo treatment planning

MC technique is the most accurate method for radiotherapy treatment planning dose calculation, which is capable, in principle, of accurately computing the dose under almost all circumstances.[19-24] Extensive efforts have been made to improve the MC dose calculation algorithms used in treatment planning systems to accurately reproduce all beam geometries and beam modification devices and to account for the effects of heterogeneities in the full 3-dimensional (3D) patient geometry. Monte Carlo methods

use detailed phase-space information for the particles in the beam (including the energy, charge, angular, and spatial distributions).

The 'general purpose' MC codes such as EGSnrc,[25] MCNPX,[26] and GEANT4[27] are relatively slow. Therefore in recent years, many groups have developed fast MC codes particularly for dose calculation in radiation therapy.[28-33] The increase in simulation efficiency compared to traditional general purpose MC packages is achieved in these codes via the use of suitable variance reduction techniques and a much faster simulation of electron transport. These codes and various techniques for fast MC are reviewed in Chapter 2.

1.6 Objectives of the project and outline of the thesis

The main objective of this PhD project is to develop a fast Monte Carlo code, suitable for electron dose calculation in treatment planning. The hypotheses of the thesis are:

1.The speed limit of current fast MC codes are 10-50 times faster than the reference code (a general propose MC code e.g. EGSnrc) and using new dose calculation methods it is feasible to reach a higher speed factor, on the order of 500 times faster than the reference code.

2. The fast MC code based on Pre-calculated data has capability of transport of various particles (such as electrons and protons) with the same transport algorithm.

Another motivation to develop an in-house fast MC code is a greater flexibility of a code and the ease of use for future research and further developments in contrast to an imported fast MC code which is often nothing more than a black box for most users. This greater flexibility proved advantageous as shown in the extension of the code to proton transport.

Our approach for development of a fast MC code was based on using pre-calculated data. The code is hence named Pre-calculated Monte Carlo (PMC). This approach has several advantages. The most important advantage is that the calculation of various parameters and physical equations is handled by a reliable general purpose code. Therefore, in terms of the physics, the code is very simple and runs faster than a general

purpose code since most of the information for particle transport is available in pre-calculated data. Overview of fast MC codes and the accuracy and limitations of each technique is discussed in Chapter 2.

The project is developed in three main sections. First, a standard fast MC for electrons was developed from scratch based on the pre-calculated data. This required modification of the source code of the general purpose code (EGSnrc for electrons) to generate pre-calculated data as well as various benchmarks. The development of the main code (PMC) and the results are presented in Chapter 3.

In the second part of the project, several techniques were studied to further improve the speed of the code. Most of these techniques are adopted from the past fast MC papers while a few novel techniques were also used. Limitation and consideration of each technique is discussed in Chapter 4. Following several techniques of MC speed enhancements, we were left to conclude that the major limitation in speeding up the fast MC is "ray tracing" which is referred to as an "un-avoidable task" in the literature[33]. After a major amount of work and testing of many mathematical and physical tricks, one novel approach was developed in which the code does not do the ray tracing calculation. In this approach, the ray tracing information is included in pre-calculated data. This approach is discussed in Chapter 5. The related paper of fast MC code for electron transport including limitation and consideration of various speed-up techniques has been accepted for publication in Medical Physics journal.

In the next step of this project, the PMC code was developed for proton transport. The motivation for the development of the code for protons was the growing interest in the use of this treatment modality. The pre-calculated data for proton transport were generated with general purpose code MCNPX. The PMC code is developed for proton transport in relatively a short time and the accurate results of the code illustrated the flexibly of the PMC code. The development of the PMC code for proton transport is discussed in Chapter 6.

Although the main focus of the this PhD project is the development of a fast MC code, in the first year of this PhD, a Monte Carlo project in conjunction with experimental results was carried out in "high contrast portal imaging using orthogonal bremsstrahlung beams". The hypotheses of this project are then:

1.Using new targets and modification of standard setup in clinical LINAC (linear accelerator) it is possible to reduce the average energy of them photon beam.

2. With reduced energy of the linac beam the resulting portal images have better contrast compare to the conventional portal images.

The project was based on a novel method for production of high contrast images in LINACs using new targets. The final results were backed up by experimental results and followed up by Arman Sarfehnia[34] as a master project. The whole project had two published papers[34,35] as an outcome. The discussion of this project and the results is presented in Chapter 7.

References

1. F. M. Khan, *The Physics of Radiation Therapy* (Lippincott, Williams & Wilkins,Philadelphia, PA, 2003).
2. F. M. Khan, *Treatment Planning in Radiation Oncology* (Lippincott, Williams & Wilkins, Philadelphia, PA, 2003).
3. J. Van Dyk, *The Modern Technology of Radiation Oncology* (Medical Physics Publishing, Madison, WI, 1999).
4. D. W. Rogers, "Fifty years of Monte Carlo simulations for medical physics," Phys. Med. Biol. **51**, R287-301 (2006).
5. I. Chetty *et al*., "Guidance report on clinical implementation of the Monte Carlo method in external beam radiation therapy treatment planning: Report of the AAPM Task Group No. 105," Med. Phys. **34**, 4818–4853 (2007).
6. F. Verhaegen and J. Seuntjens, "Monte Carlo modelling of external radiotherapy photon beams," Phys. Med. Biol. **48**, R107–R164 (2003).
7. H. Attix, Introduction to radiological physics and radiation dosimetry (Whily & Son, New York, NY, 1986).

8. K. R. Hogstrom, "Evaluation of electron pencil beam dose calculation," Med. Phys. **12**(4), 554 (1985).

9. A. S. Shiu and K. R. Hogstrom, "Pencil-beam redefinition algorithm for electron dosedistributions," Med. Phys. **18**, 7–18 (1991).

10. J. Cygler, J. J. Battista, J. W. Scrimger, E. Mah, and J. Antolak, "Electron dose distributions in experimental phantoms: a comparison with 2D pencil beam calculations," Phys. Med. Biol. **32**, 1073–1086 (1987).

11. T. R. Mackie, J. W. Scrimger, and J. J. Battista, "A convolution method of calculating dose for 15-MV x rays," Med. Phys. **12**, 188–196 (1985).

12. A. L. Boyer and E. C. Mok, "A photon beam distribution model employing convolution calculation," Med. Phys. **12**, 169–177 (1985).

13. R. Mohan, C. Chui, and L. Lidofsky, "Differential pencil beam dose computation model for photons," Med. Phys. **13,** 64–73 (1986).

14. G. X. Ding, J. E. Cygler, G. G. Zhang, and M. K. Yu, "Evaluation of a commercial three dimensional electron beam treatment planning system," Med. Phys. **26,** 2571–2580 (1999).

15. K. R. Shortt, C. K. Ross, A. F. Bielajew, and D. W. O. Rogers, "Electron beam dose distribution near standard inhomogeneities," Med. Phys. **31**, 235–249 (1986).

16. G. X. Ding, J. E. Cygler, C. W. Yu, N. I. Kalach, and G. Daskalov, "A comparison of electron beam dose calculation accuracy between treatment planning systems using either a pencil beam or a Monte Carlo algorithm," Int. J. Radiat. Oncol. Biol. Phys. **63,** 622–633(2005).

17. E. Mah, J. Antolak, J. W. Scrimger, and J. J. Battista, "Experimental evaluation of 2D and 3D electron pencil beam algorithm," Phys. Med. Biol. **34**, 1179–1194 (1989).

18. T. Knoos, A Ahnesjo, P. Nilsson, and L. Weber, "Limitation of pencil beam approach to photon dose calculation in lung tissue," Phys. Med. Biol. **40**, 1411–1420 (1995).

19. A. F. Bielajew, D. W. Rogers, J. Cygler, and J. J. Battista, "A comparison of electron pencil beam and Monte Carlo calculation methods," in: The Use of Computers in Radiation Therapy, edited by A.D. Bruinvis (Elsevier, Amestrdam, 1987).

[20] C.-M. Ma, E. Mok, A. Kapur, T. Pawlicki, D. Findley, S. Brain, K. Forster, and A. L. Boyer, "Clinical implementation of a Monte Carlo treatment planning system," Med. Phys. **26**, 2133–2143 (1999).

[21] C. M. Ma, J. S. Li, T. Pawlicki, S. B. Jiang, J. Deng, M. C. Lee, T. Koumrian, M. Luxton, and S. Brain, "A Monte Carlo dose calculation tool for radiotherapy treatment planning," Phys. Med. Biol. **47,** 1671–1689 (2002).

[22] G. X. Ding, D. M. Duggan, C. W. Coffey, P. Shokrani, and J. E. Cygler, "First macro Monte Carlo based commercial dose calculation module for electron beam treatment planning--new issues for clinical consideration," Phys. Med. Biol. 51**,** 2781-2799 (2006).

[23] J. E. Cygler, G.M. Daskalov, G.H. Chan, and G.X. Ding, "Evaluation of the first commercial Monte Carlo dose calculation engine for electron beam treatment planning," Med. Phys. 31**,** 142-153 (2004).

[24] J. S. Li, T. Pawlicki, J. Deng, S. B. Jiang, E. Mok, and C. M. Ma, "Validation of a Monte Carlo dose calculation tool for radiotherapy treatment planning," Phys. Med. Biol. 45**,** 2969-2985 (2000).

[25] I. Kawrakow and D. W. O. Rogers, "The EGSnrc code system: Monte Carlo simulation of electron and photon transport," NRC, Report PIRS–701, 2000.

[26] J. F. Briesmeister, "MCNP-A general Monte Carlo N-particle transport code, Version 4C," Report LA-13709-M, Los Alamos National Laboratory, NM, 2000.

[27] S. Agostinelli *et al*., "GEANT4—A simulation toolkit," Nucl. Instrum. Methods Phys. Res. A 506, 250–303 (2003).

[28] H. Neuenschwander and E. J. Born, "A Macro Monte Carlo method for electron beam dose calculations," Phys. Med. Biol. **37**, 107–125 (1992).

[29] H. Neuenschwander, T. R. Mackie, and P. J. Reckwerdt, "MMC— A high-performance Monte Carlo code for electron beam treatment planning," Phys. Med. Biol. **40**, 543–574 (1995).

[30] P. J. Keall and P. W. Hoban, "Super-Monte Carlo: a 3D electron beam dose calculation algorithm," Med. Phys. **23**, 2023–2034 (1996).

[31] P. J. Keall and P. W. Hoban, "Superposition dose calculation incorporating Monte Carlo generated electron track kernels," Med. Phys. **23**, 479–485 (1996).

32. I. Kawrakow, M. Fippel, and K. Friedrich, "3D Electron Dose Calculation using a Voxel based Monte Carlo Algorithm," Med. Phys **23**, 445–457 (1996).

33. I. Kawrakow, "VMC++, electron and photon Monte Carlo calculations optimized for Radiation Treatment Planning," *Advanced Monte Carlo for Radiation Physics, Particle Transport Simulation and Applications: Proceedings of the Monte Carlo 2000 Meeting Lisbon*, edited by A. Kling, F. Barao, M. Nakagawa, L. Távora, and P. Vaz (Springer, Berlin, 2001), pp. 229–236.

34. A. Sarfehnia, K. Jabbari, J. P. Seuntjens, and E. B. Podgorsak, "Experimental verification of beam quality in high-contrast imaging with orthogonal bremsstrahlung photon beams," Med. Phys. **34**, 2896–2906 (2007).

35. K. Jabbari, A. Sarfehnia, E. B. Podgorsak, and J. P. Seuntjens, "Monte Carlo feasibility study of using orthogonal bremsstrahlung beams for improved radiation therapy imaging," Phys. Med. Biol. **52**, 1171–1184 (2006).

Chapter 2

Review of fast Monte Carlo techniques

2.1 Monte Carlo technique

Monte Carlo (MC) methods are stochastic techniques which are based on the use of random numbers and probability statistics to investigate problems.[1-4] Thus MC methods are a collection of different methods that perform the same process: This process involves performing many simulations using random numbers and probability distributions to get an approximation of the answer to the problem. The defining characteristic of the MC methods is its use of random numbers throughout the simulation process. One of the most important usages of MC methods is in the evaluation of difficult integrals. This is especially true of multi-dimensional integrals which have few methods for computation and thus are suited to getting an approximation due to their complexity. It is in these situations that MC approximations become a valuable tool to use, as they may be able to give a reasonable approximation in a shorter time in comparison to other formal techniques.[5-7]

An example of a MC technique is illustrated in Fig. 2.1. In this example, the area s_2

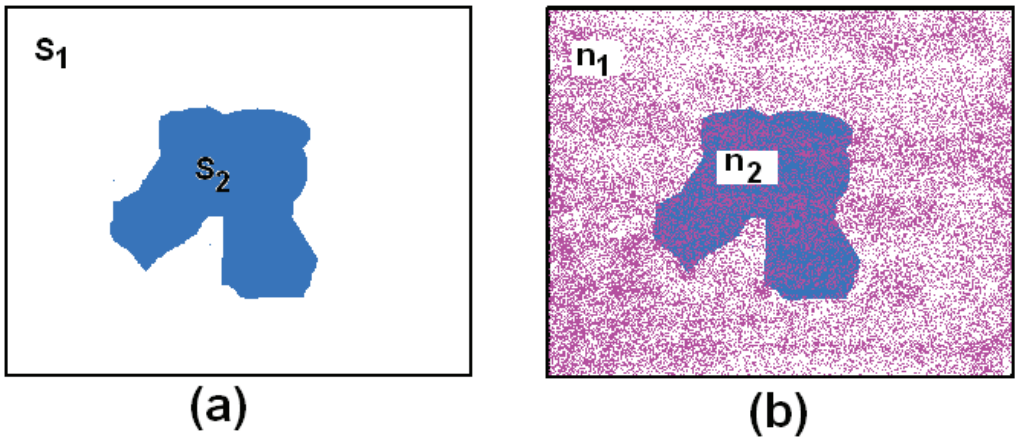

Figure 2.1 An example of Monte Carlo technique for area calculation of an irregular shape.

with irregular shape is to be calculated. First, we place the area s_2 inside a regular (rectangular) shape s_1, the area of which is known. Subsequently, we cover the s_2 with many (n_1) randomly distributed dots and we count the number of dots that hit the s_2. The ratio of the two numbers is proportional to ratio of the surfaces:

$$\frac{n_1}{n_2} = \frac{s_1}{s_2} \rightarrow s_2 = s_1 \frac{n_2}{n_1} \qquad 2.1$$

There are two requirements to have an acceptable answer:

1- The number of the points has to be large so that the ratio of the numbers approaches the ratio of the areas.

2- The points have to be distributed randomly to avoid a systematic error.

The obligation of having a large number of points (or simulations for other types of the problems) makes the Monte Carlo method generally a slow technique.

2.2 Monte Carlo in radiation therapy

Monte Carlo techniques have been used in various branches of radiation therapy[8,9], from simulation of radiation therapy equipments and sources to dose calculation in various geometries[10-18]. For simulation of the photon and electron particles one has to apply physics of the transport for modeling which requires the knowledge of interactions of the particle, cross section of each interaction and stopping powers for a wide range of energy. When an electron traverses matter, it will interact with the electrons and the nuclei of the medium and begins to lose energy as it penetrates the medium.

The interaction can be generally categorized as collisions between the electron and either the atomic electrons or the nucleus. [19] The collisions are described as *soft* and *hard* collisions. In *soft* collisions, the electron passes an atom at a relatively large distance, and the Coulomb force field affects the whole atom with an excitation or ionization. In this kind of collision, a small amount of energy can be transferred to the medium. The Coulomb interaction of the electron with an external nuclear field produces bremsstrahlung radiation.

The *hard* collision is the interaction of the particle with a single bound electron. The electron loses energy mainly through Coulomb interactions with orbital electrons. This often leads to the ionization of the atoms in matter, in which knock-on electrons (or δ-rays) are produced.

An electron in reality undergoes very large number of elastic and inelastic interactions and it is not possible to simulate each electron collision explicitly. Therefore in MC calculations, inelastic collisions are grouped into a discrete process and continuous energy loss (condensed history simulation, Fig. 2.2)[8]. In a discrete process (hard collisions) secondary particles are produced with an energy above a user defined threshold. The energy of the electrons is supposed to be deposited in the surrounding medium continuously between the hard collisions (between *A* and *B* in Fig. 2.2). The elastic collisions are described by changes of the direction of the movement after each electron step.

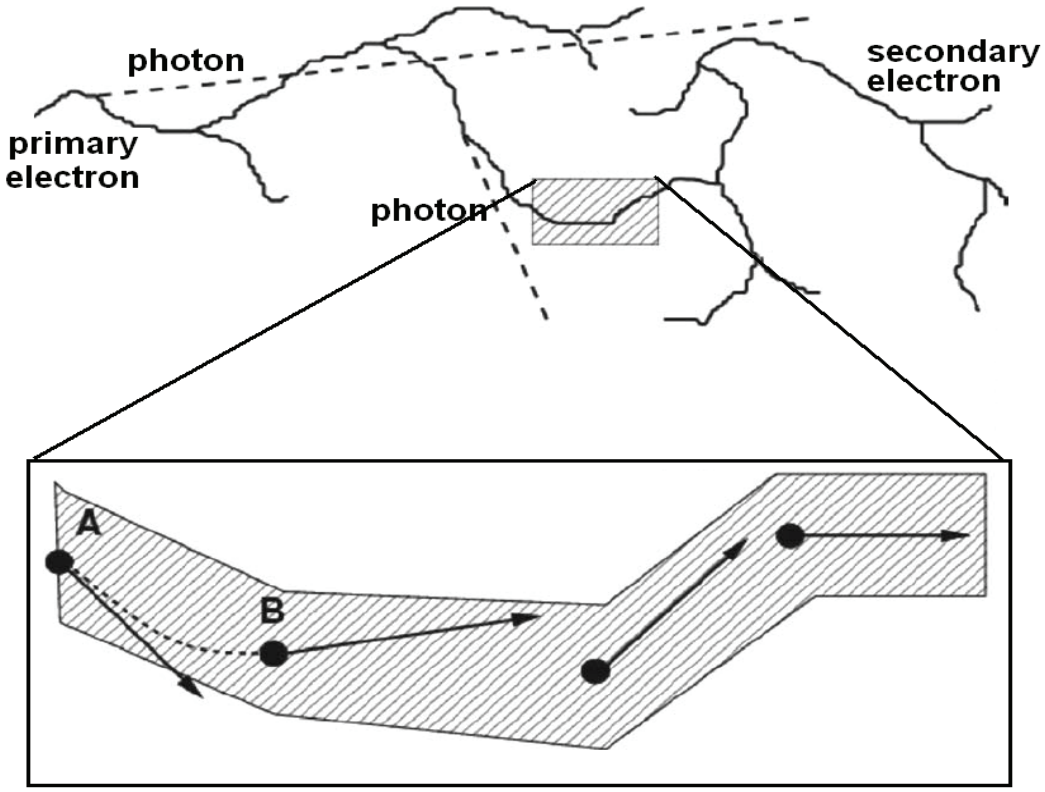

Fig 2.2 Illustration of the condensed history algorithm. The track of the electron (above) includes many secondary electrons and photons (dashed line in upper panel). The electron track in the shaded box is simulated with a condensed history algorithm. The initial and final position of the electron in one step are A and B which includes the scattering of the electron in the medium. However, condensed history implementation does not provide information on how the particle goes from *A* to *B*. The curved dashed line connecting *A* and *B* is a more realistic representation of the trajectory than a straight line from *A* to *B*. (Figure modified from Ref. [8]).

The particles in MC calculations are transported until they reach a user defined energy cut-off (e.g. 0.01 MeV for photons and 0.6 MeV for electrons). Through a large number of simulations (histories) the quantity of interest can be calculated, e.g. deposited energy in each voxel, or the energy spectrum. Because of the statistical nature of MC calculations, each calculated parameter is subject to a statistical uncertainty and one can reduce the uncertainty with a larger number of histories or many variance reduction techniques. [20-23] Variance reduction techniques reduce the time for particle simulations and improve the speed of the code. These techniques (few of which are discussed in following sections) are important elements of any MC code and may be different for various application and geometries.

A general purpose MC code should consider all aspects of the electron and photon transport and it should be able to produce accurate results in a heterogeneous phantom. Several general purpose MC codes have been developed for radiation transport calculation which are used in medicine such as EGS4[24], EGSnrc[25], MCNP[26], GEANT[27]. The MC codes for simulation of linear accelerators and dose calculation in the patient are BEAMnrc[28] and DOSXYZnrc[29] which are based on EGS4/EGSnrc.

EGSnrc/BEAMnrc/DOSXYZnrc is one of the most widely used packages in radiation therapy.[9] EGSnrc is a version of the program Electron Gamma Shower 4 (EGS4) and has been applied to all areas of radiation protection, dosimetry and medical physics, and has been extensively validated.[30-37] BEAMnrc is used to simulate many types of radiotherapy sources and clinical accelerators.[38-40] The BEAMnrc can produce a phase-space output of the beam (including energy, charge, position and direction) at any specified plain in geometry. DOSXYZnrc is designed for dose calculations in 3D rectilinear voxel geometry. Voxel dimensions in each direction and material of each voxel can be assigned by the user. The phase-space data calculated by BEAMnrc can be used as an input file for DOSXYZnrc. DOSXYZnrc produces a data file that contains geometry specification such as the number of the voxels in all three directions and their boundaries as well as the related dose values and statistical uncertainties. All three codes (EGSnrc/BEAMnrc/DOSXYZnrc) can run under UNIX or Windows operating systems.

Significant improvements in BEAMnrc/DOSXYZnrc have been reported in recent literature. [41,42] A variance reduction technique, the directional bremsstrahlung splitting[42]

technique is used in BEAMnrc and improves the speed of the simulations by a factor of 25. The simulation of linear accelerator with BEAMnrc is combined with DOSXYZnrc in which the CT data set can be used as an input file and simulation of each particular patient can be handled. The main advantage of this process is to eliminate the need to store intermediate phase-space files. This also decreases the total time needed for simulation of the equipment and dose calculation in phantom.

2.3 The need for Fast Monte Carlo code

The general-purpose MC codes transport the particles in a wide range of energies and materials with the best available transport algorithms and cross-sections. The general-purpose codes have been designed for all application types and have not been optimized for clinical situations. Hence, despite clever variance reduction techniques, they are relatively slow for dose calculations in treatment planning systems.[43] Consequently in the past decade, several fast MC codes have been developed to improve the efficiency and decrease the calculation time such as Macro Monte Carlo,[44,45] Superposition Monte Carlo,[46,47] Voxel based Monte Carlo (VMC,VMC++),[48-51] Dose Planning Method (DPM),[52] and MCDOSE.[53]

Although with the speed of recent computer hardware and using parallel processing techniques, it has become possible to run a general purpose code in a reasonable amount of time, fast MC techniques are still essential for applications such as 4-dimensional MC (Monte Carlo including time-dependent components) and inverse planning[54-57]. All of the mentioned fast MC codes benchmark their results to the EGS4 or the EGSnrc code and the gain of speed has been 10-50 times faster for electron transport. Most of the fast MC codes have been improved from their original versions over the past few years; they have also been compared with benchmark experiments and produce mostly accurate results.[58-67] MMC, SMC and VMC++ have reached speed up factors of 20, 30 and 50 times faster than EGS4, respectively, and their dose distributions are typically within 3-4%, 2% and 1% of EGS4 results respectively. The details of different approaches for fast MC are discussed in following sections.

2.4 Macro Monte Carlo

2.4.1 Sphere by sphere transport of the electron

Macro Monte Carlo (MMC) is one of the very first fast MC codes which was developed in 1992.[44] At that time, the pencil beam algorithm were the most successful methods to calculate the electron beam dose in radiation therapy.[68,69] However large differences between pencil beam calculations and experiments were reported.[70-72] MC methods were also very slow with available computers and MMC code was developed to apply the MC techniques in a more efficient way.

MMC code transports the MMC in sphere-by-sphere macroscopic steps as is illustrated in Fig. 2.3. The characteristics of electron after each sphere are determined from the pre-calculated database. The resulting parameters of the electron after each step are sampled from a pre-calculated probability distribution.

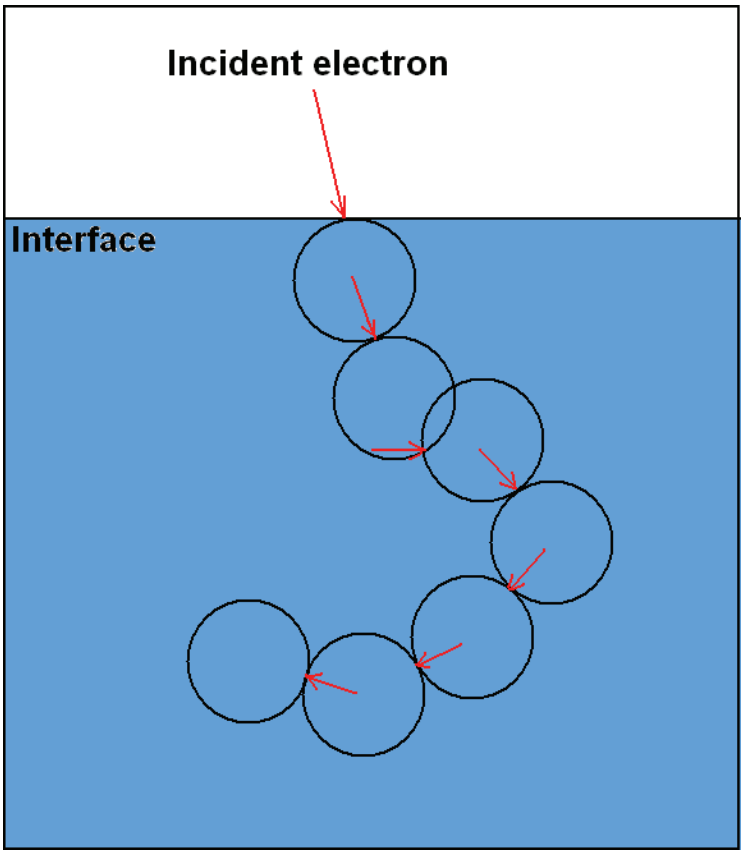

Figure 2.3 Electron transport in MMC. The direction of electron after each spherical step is indicated by arrows and is determined using per-calculated data.

2.4.2 Generation of probability functions

Pre-calculated data are generated by EGS4 in which an electron is incident vertically on the surface of the macroscopic sphere. The geometry of the incident electron and the sphere is illustrated in Fig. 2.4. The initial parameters for generation of pre-calculated data are radius of the sphere, density and material of the sphere and incident energy of electron.

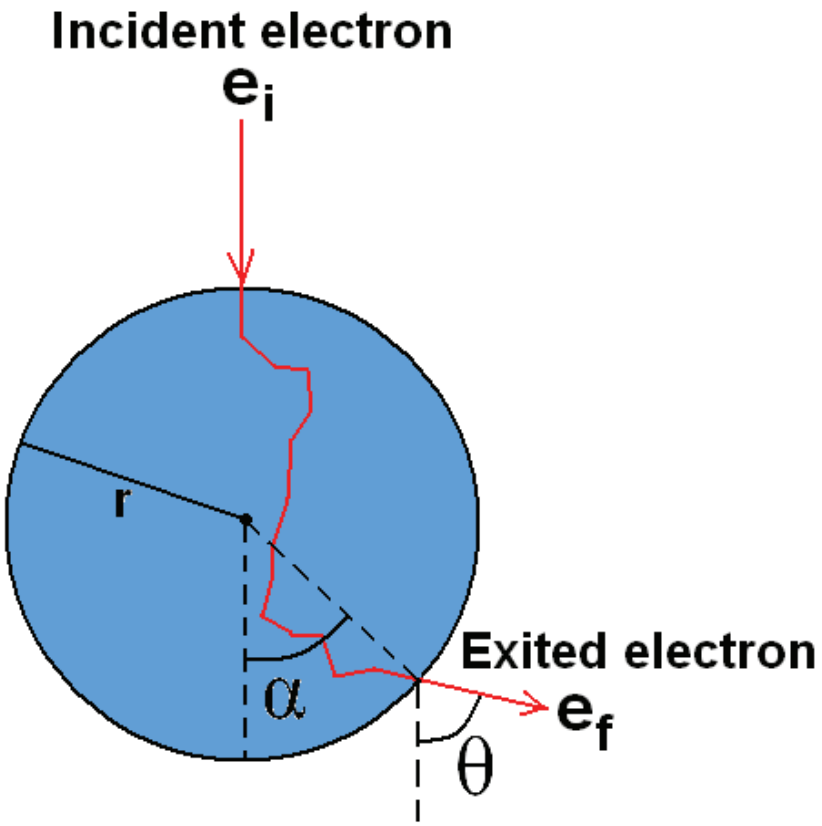

Figure 2.4 Geometry of incident electron and various parameters which is used for the database for MMC.

The radius of the sphere has a constant value of r =0.2 cm. Keeping the radius constant certainly produces some artifacts near inhomogeneities which will be discussed later. In this method, the sphere is like a black box from which several secondary particles as well as primary electrons come out. The electron with highest energy is considered the primary electron. For various material and energies, the following parameters are stored in database:

1-The distribution of scattering angle (θ in Fig. 2.4) and the angle of exited primary electron (α). The α angle technically determines the exited position of the primary electrons since the radius is known. The possible range of the angles split up into 18 bins. In the stored set, probability of emergence in each angular beam and the mean angles (θ,α) are saved as a discrete cumulative density function.

2- Energy distribution of exited primary electron (e_f in Fig. 2.4). The possible range of e_f (which is from 0 to the energy of the primary electron) is divided in 20 bins and the probability of each bin is saved in a discrete cumulative energy function.

3- Probability of absorption of the primary electron in the sphere. This probability is calculated by dividing the number of exited primary electrons by total the number of incident primary electron.

4- Probability that 'transferred energy' (e_i-e_f) is deposited in sphere or transferred to secondary electron or secondary photons.

5-A few other parameters that are required for complete transport of the particle are also saved. These include the range of the exited secondary electrons with Continuous Slowing Down Approximation (CSDA range). The secondary electrons in MMC are not transported explicitly and the energy is deposited according to CSDA approximation.

The pre-calculated data is generated for different materials such as lung (ρ=0.3 g/cm^3), water (ρ=1g/cm^3), Lucite (ρ=1.19g/cm^3), solid bone phantom material (ρ=1.84 g/cm^3) and aluminum (ρ=2.7g/cm^3). The energy cut-offs were set to 190 keV for electrons and 100 keV for photons. For each material the simulations were done using an energy range of 0.2-20 MeV (0.2, 0.4, 0.6, 0.8, 1, 1.5, 2, 3, …, 19 , 20 MeV). To have a statistical uncertainty of 1 % for primary electron parameters in MMC, 30000 electrons are simulated for each sphere (with various energy and materials).

2.4.3 Comparison of MMC results with EGS4

An interesting illustration of the results for distribution of exited primary electron on the surface of the sphere for various energies is illustrated in Fig. 2.5. The length of the vectors are proportional to the number of the electrons and the results are illustrated for

three sets of the incident parameters: water-8 MeV, water-1.5MeV and bone-1.5 MeV. At high energies, the electrons emerge in the forward direction with a small scattering angle. Because of the larger scattering power of the bone, the emerged electrons are widely scattered in the orthogonal direction.

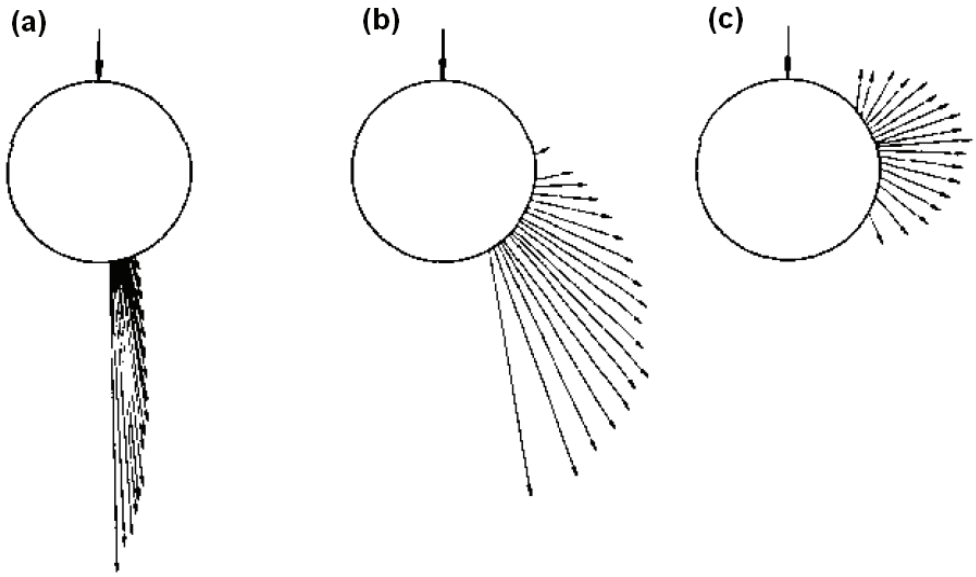

Figure 2.5 Spatial distributions of exited primary electrons on the surface of the sphere. (a) water sphere , incident energy (e_i) =8 MeV , (b) water sphere e_i=1.5 MeV, (c) bone sphere e_i=1.5 MeV(Figures from Ref. [40]).

The results of MMC are compared to EGS4 with the same cut-off parameters. Fig. 2.6(a) illustrates the depth dose distribution for monoenergetic electron beams of various energies incident normal to the surface of a water phantom. The data are collected on the central axis for a 20 cm×20 cm field and the differences between MMC and EGS4 are 2-4 %.

Figure 2.6(b) illustrates an example of MMC results in heterogeneous medium in which a slab of bone and lung is embedded in a water phantom. The energy of the incident electron is 20 MeV and there are relatively large discrepancies of up to 8 % near interfaces. The MMC code is implemented in many clinical cases such as the head phantom, and the errors compare to EGS4 are in the range of 2-7 %.

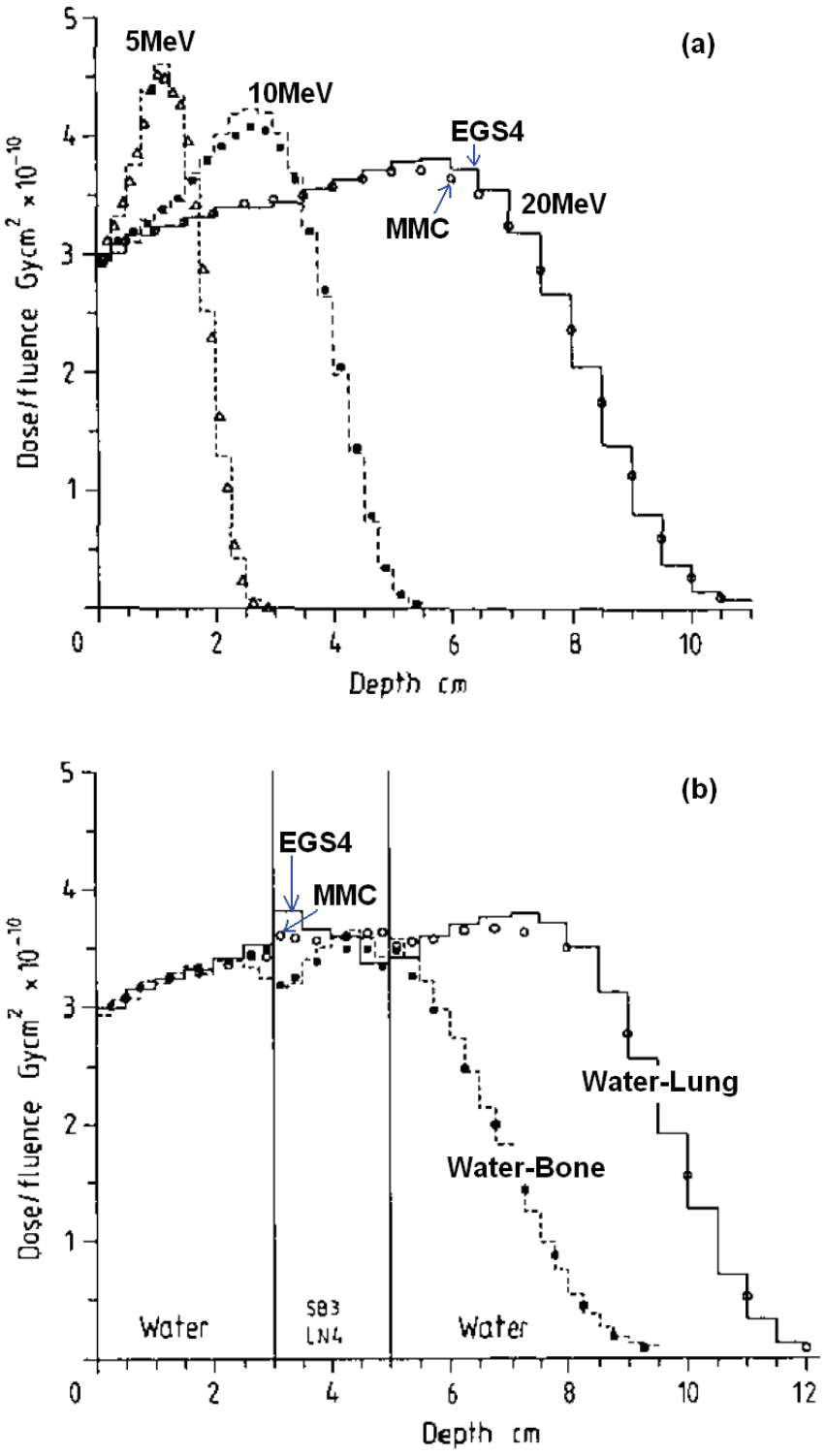

Figure 2.6 (a)Depth dose of central axis for various energies in water phantom in comparison with EGS4. The field size of the electrons beams are 20×20 cm^2. (b) Central axis depth dose of 20 MeV electrons in water with a lung and bone slab (Figures modified from Ref. [40]).

2.4.4 Discussion of MMC results

MMC generally has a large discrepancy in the build up region of the dose distribution and near the interfaces of different materials. The errors are mainly due to several approximations for the transport of primary and secondary electrons. An approximation that produces large errors in the build up region is due to the transport of the electrons in a straight path between the entrance and the exit point as is illustrated in Fig. 2.7. In MMC, the path of the electrons is lost in pre-calculated spheres, although the real path of the electrons is a random path. This assumption particularly produced large errors for regions with large dose gradients such as the build up region. It is possible to reduce the size of the spheres in pre-calculated data, however, the total size of the pre-calculated data will increase as a result.

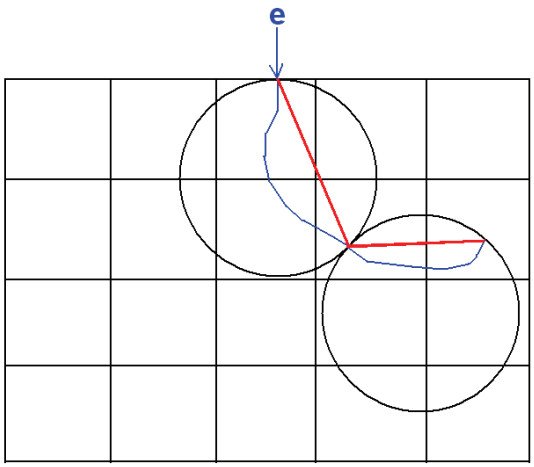

Figure 2.7 Transport of the electron in MMC in a voxel based phantom. The energy of the electron is deposited in a straight line from the entrance to the exit point of the sphere.

Other approximations that produce large errors are: 1) Constant radius of the sphere. An extension of the pre-calculated data for various size spheres increases the size of the pre-calculated data; however, it improves the accuracy of the results as will be discussed later. 2) Transport of the secondary electrons with CSDA approximation. 3) Approximation of the angular distribution of exited electrons in bin angles.

Above approximations in MMC were imposed by a limited available computer RAM at that time. The size of the pre-stored data in MMC for each material is around 100 kb which is also suitable for parallel processing. The speed factor of MMC with respect to EGS4 is

4-10 for various geometries. MMC is commercially available for linear accelerator and the performance of the clinical implementation has been evaluated in the literature.[61,73]

2.4.5 Further developments in MMC

As mentioned above, the early version of MMC produced large artifacts in the build up region and near the interfaces of different materials. In a follow up development[45], the original version of MMC is significantly modified in order to increase the speed, and address the relatively large errors of the code. The constant size of the sphere was recognized as the major reason for poor performance of the code near interfaces. The authors implemented a newly developed adaptive step size algorithm in which the size of the spheres depends on the distance of the electron from the interface. There are other features in the new version of the MMC which improved the results of the code and will be discussed in this section.

Adaptive step size algorithm: The original MMC database contained a single sphere size of r=0.2 cm. To develop an adaptive step size algorithm, the database has to be expanded to include data for different sphere sizes. In the new version, five different sphere sizes are used in the generation of pre-calculated data (0.05, 0.1, 0.15, 0.2, and 0.3 cm). The size of the spheres had to be smaller than 3 mm since the larger size of the sphere produces large artifacts in the dose build up region. The resulting MMC database requires 200 kb of memory.

Pre-process of the absorber volume: To use various sphere sizes, at each step, the distance of the electron from the closest boundary should be calculated. This calculation in-the-fly is time consuming and an algorithm is developed that allows the determination of the sphere sizes and mean density in each voxel of the CT phantom by pre-processing of the whole CT volume prior to MMC simulation. For this purpose, first the CT volume is converted to a density volume with user defined resolution (0.1 -0.2 cm) through the application of CT to density conversion factors.

In the second step, the resulting density volume is scanned for heterogeneities. A sphere size is assigned to each voxel of the volume which corresponds to maximum radius of the sphere that can be placed in the center of the voxel without reaching into the other materials. This process results in small sphere sizes near interfaces of different material,

and large spheres to the point at large distance to the interfaces. The interface is defined between the voxels in which the ratio of densities are larger than 1.5. An example of pre-processed head phantom is illustrated in Fig. 2.8. The importance of this technique is that a similar idea can also be used for fast transport of the particles in other MC codes.

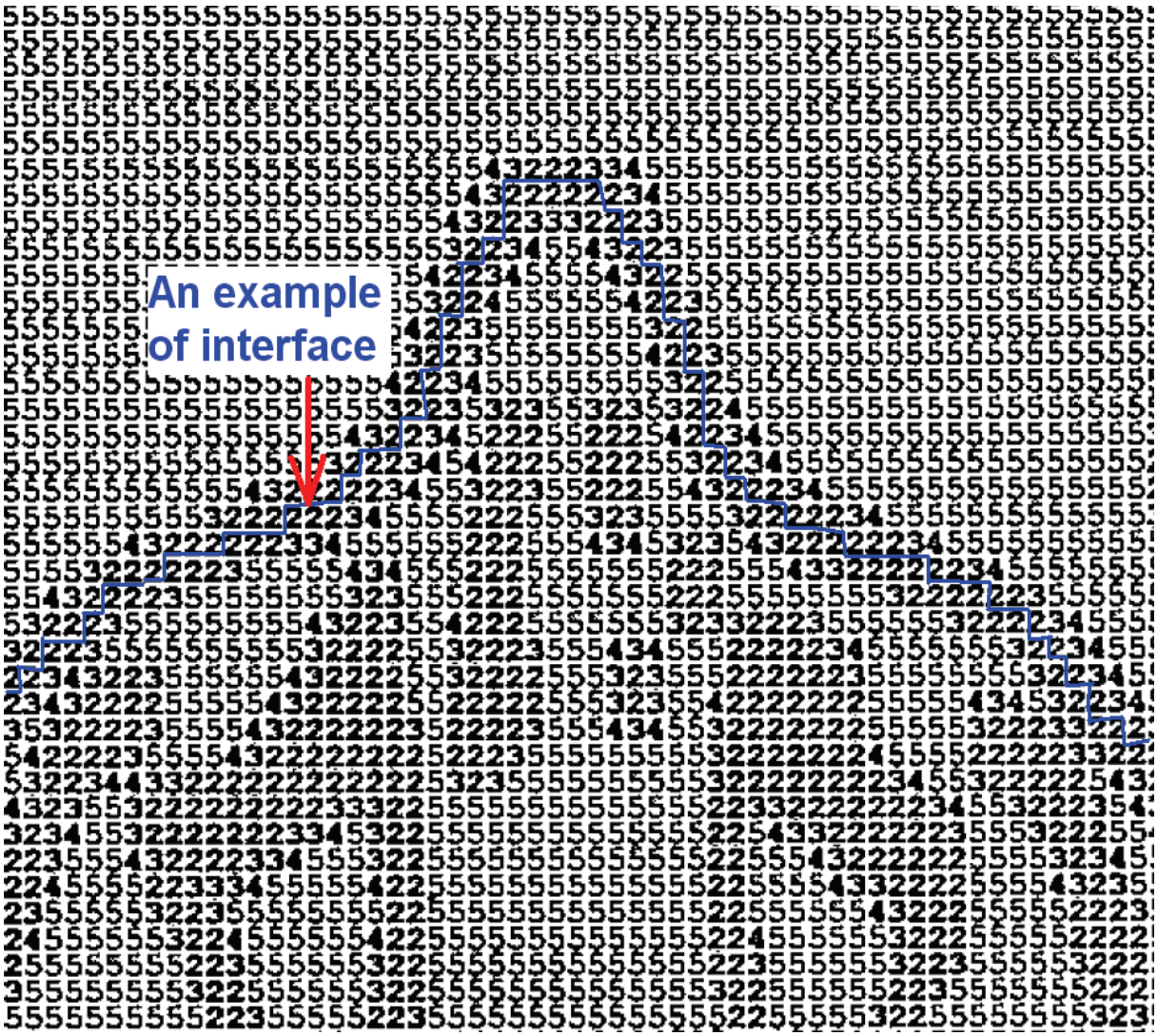

Figure 2.8 A pre-processed CT slice of the head. The resolution of the voxels are 2 mm in each direction. The numbers illustrates the sphere size that can be used for that voxel without crossing the interfaces. The number 2 is the related to the smallest spheres size, 2mm (Figure modified from Ref. [21]).

Transport algorithm: An illustration of an adaptive step size algorithm is shown in Fig. 2.9. Using the pre-processed volume, the step size of the electron in each voxel is already available. The center of the sphere is placed at the distance of one radius of the maximum allowed sphere size in the current position of the electron. The direction of the motion is determined from the direction of exited electron from the previous sphere.

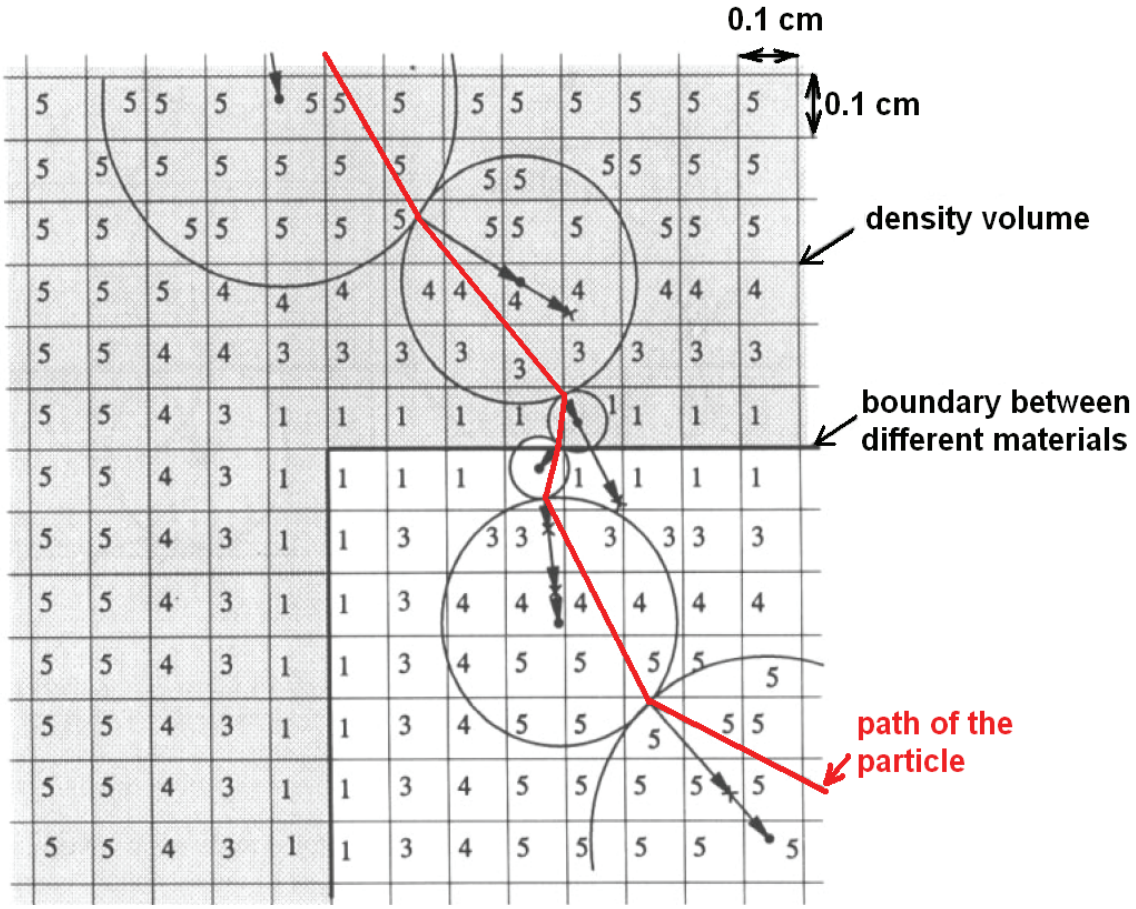

Figure 2.9 Transport of the electron using adaptive step size algorithm. The arrows illustrate the direction of exited primary electron and the straight line illustrates the path of the electron. The position of the spheres is determined by number of the voxel (representing the size of the sphere) and direction of the emerged primary electron from the surface of the previous sphere (Figure modified from Ref. [41]).

The energy of the primary electron is deposited along a straight line from the point the electrons enter the sphere to the exit point as illustrated in Fig. 2.9. The ray tracing is performed by the Siddon ray tracing algorithm[74] through the voxels of the dose volume. This algorithm is discussed in Section 3.5.

Other developments: Another important development of the MMC is the increasing the resolution n of the angular bins. In the original version of the MMC, the angle of emerged primary electron is approximated in 18 bins as illustrated in Fig. 2.10. For example, all of the electrons that come out with angles between 10-20 degrees are approximated to 15 degrees. In the new version of MMC, the data is stored for 100 bins which produces a more accurate sampling of angular distribution of the primary electron around the surface of the sphere and improves the accuracy of the results.

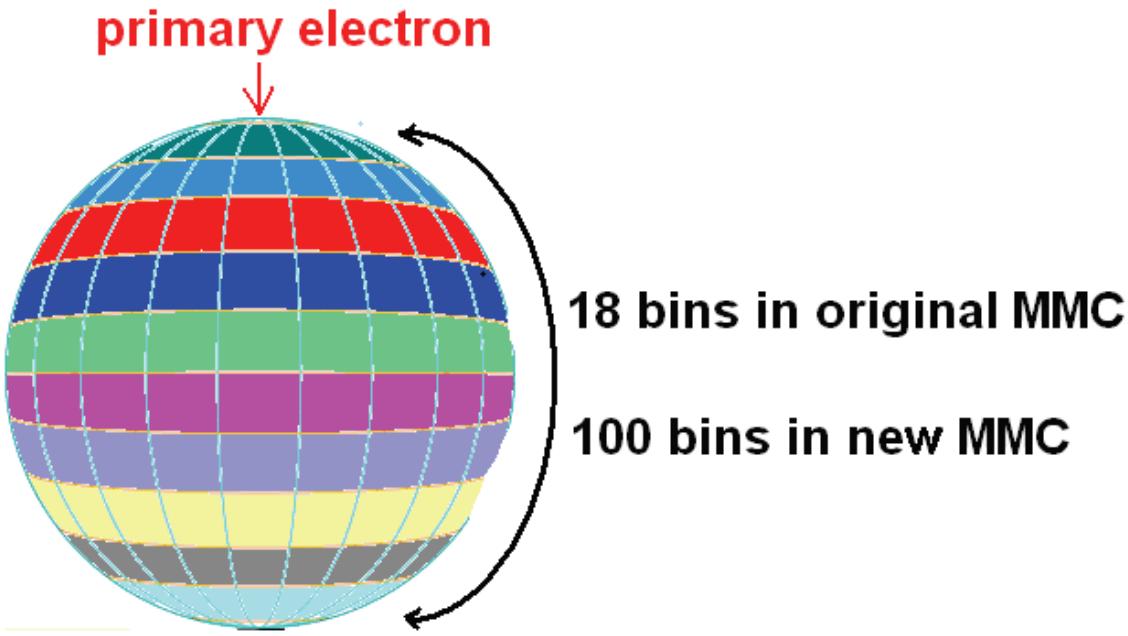

Figure 2.10 The angular range of the exited primary electron in original MMC is 18 bins and it is increased to 100 bins in new version of MMC to improve the accuracy.

The results of MMC are improved in the new version for homogeneous and heterogeneous phantoms. An example for a heterogeneous phantom is illustrated in Fig. 2.11. The discrepancy between EGS4 and MMC reaches 4 % (this is in contrast to the original MMC version in which the discrepancies of up to 8 % were observed).

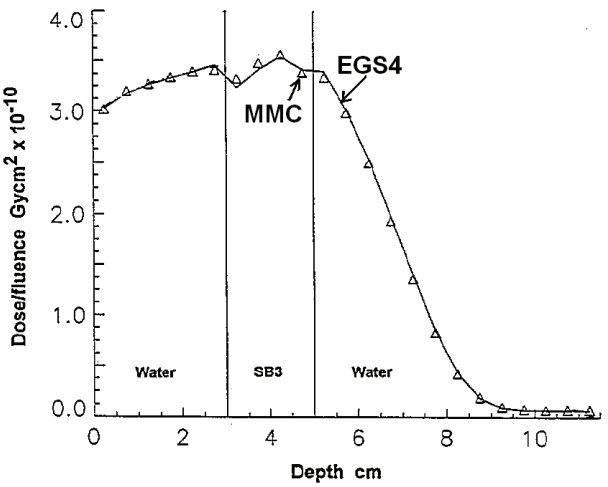

Figure 2.11 Comparison of central axis depth dose between EGS4 and MMC for 20 MeV electron beam, and 20×20 cm^2 field size (Ref.[41]).

2.5 Superposition Monte Carlo

2.5.1 Implementation of pre-calculated tracks

The Superposition Monte Carlo (SMC) for electron transport is based on a simple and accurate technique in which the code transports each electron explicitly through a microscopic "pre-calculated" track.[46,47] The general purpose code, EGS4, is used for generation of per-calculated data. Using EGS4, electrons are transported in a large water phantom to avoid the track cut-off. The maximum allowable step size of the particle (SMAX) [24] was set to 0.05. The default setup configuration of EGS4 assigns a large step to the electron in such a medium since the electron is far from the boundaries of the phantom; however, with decreasing maximum allowable step size, the code transports the electron in smaller steps.

In each step, various parameters such as position (x, y, z), deposited energy and kinetic energy of the electron are saved in a file. The tracks of secondary electrons are also saved with a different flag. The track of 3000 electrons with energy of 6 MeV and 15 MeV were simulated and saved in this way. The total energy cut-off for electron transport is ECUT=0.611 MeV which means that the secondary electrons with kinetic energies above 100 keV are transported while those with energies below that are deposited locally. In the final step for generation of pre-calculated data, the stored data is post-processed. At each

step, the position of the electron is converted to spherical coordinates such as step length, azimuthal angles and polar angles (r, θ, φ).

In SMC the electron tracks are generated in water (ρ=1 g/cm^3). To transport the electrons in water-like materials (similar composition but different density), each step is multiplied by the inverse of the density.[75] However, for other materials with different composition and atomic number, various parameters of the electron track in water have to be modified such as change in scattering, stopping power ratios and collision energy loss and bremsstrahlung production. These modifications are discussed in detail in the related paper.[47]

2.5.2 Electron transport in SMC

The tracks of electrons with energies of 6 or 15 MeV are picked up from pre-calculated data and transported step by step in the voxel based phantom. If the material of the voxel is not water, modification and scaling is done in each step. An example of an electron track for water and the same track modified for aluminum is illustrated in Fig. 2.12. The track of the electron in aluminum is shorter because of larger stopping power.[76] The aluminum track also has larger lateral deflection due to larger scattering power of the aluminum.

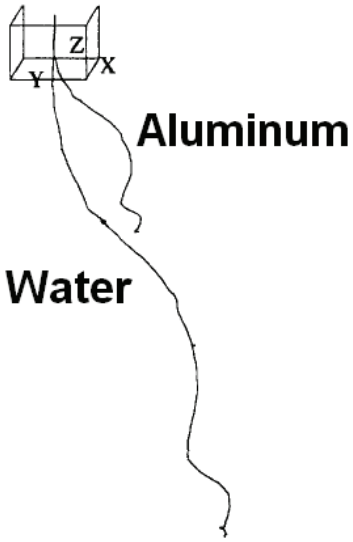

Figure 2.12 A track of the electron in water and the same track modified for aluminum. Secondary electrons are not shown. (Figure from Ref.[23]).

For boundary crossing and ray tracing, in each step, if the step goes beyond the boundary of the voxel, the deposited energy is decremented by the ratio of the path length in the original voxel divided by the total length of the step. The energy deposition of bremsstrahlung photons generated by electrons in water is ignored since the contribution of these photons to the dose for tissue equivalent materials are negligible.[77] In the track of the primary electron, if a secondary electron is generated, the position of the primary is saved on the stack and the secondary electron is transported using the pre-generated track.

2.5.3 Results and discussion of the SMC

Comparison of the SMC and EGS4 results as a reference generally shows good agreement. An example of SMC results in water-bone phantom is illustrated in Fig. 2.13. The results are generally in agreement to within 2-3 % and the maximum difference between EGS4 and SMC is 5 %. Differences of the same magnitude are observed in other homogeneous and heterogeneous cases.

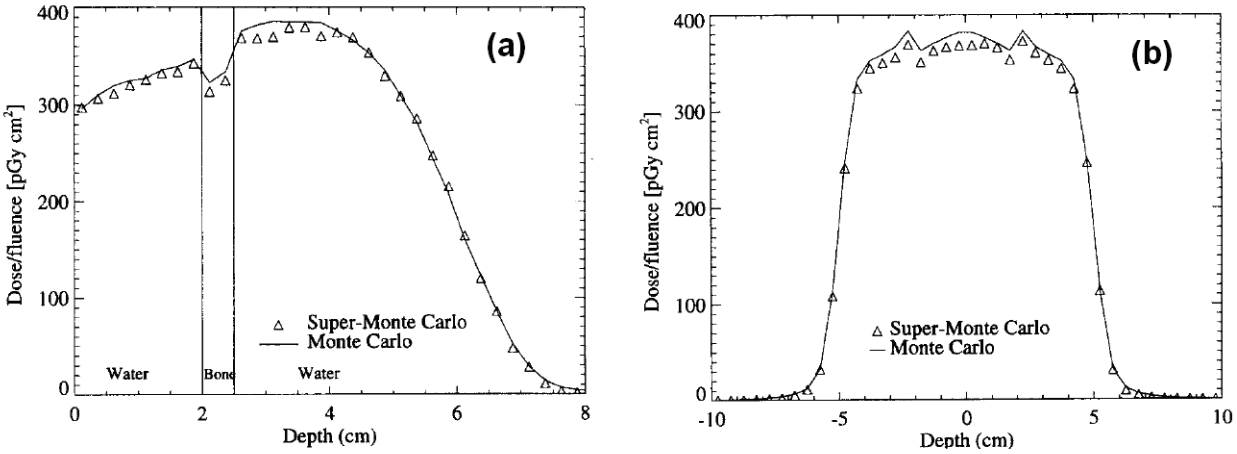

Figure 2.13 The depth dose curve of central axis (a) and the dose profile curves of the water-bone phantom(b) for SMC and EGS4. The energy of electrons is 15 MeV and the field size is 10×10 cm^2.

For the same geometry and energy cut-off, SMC runs 20 times faster than EGS4 to reach the same uncertainty. The size of the pre-calculated data for 15 MeV electrons were 15 Mb. Although the algorithm has the capability of transporting electrons with various energies, the pre-calculated electron tracks are done only for 6 and 15 MeV and no further development has been made towards including various electron energies and

implementation of the code using a real phase-space data (including the energy, charge, angular, and spatial distributions). Many optimizations for improvement of SMC were possible in transport parameters such as the number of the electron tracks, energy cut offs and pre-processing of electron track to join very small steps. Finally, further development of SMC was required for its potential clinical application[47].

2.6 Voxel based Monte Carlo

2.6.1 Introduction to VMC/VMC++

Voxel based MC (VMC) was developed by Kawrakow *et al.* in 1996[48] which applies some approximations and simplifications into the electron transport algorithm. One of the main approximations of VMC is a simplified treatment of multiple scattering compared to EGS4. The VMC code is very fast and produces good results and it has been improved from its original version[78]. The code is originally developed for electron transport and then extended to photons transport (XVMC) [49]. In XVMX, the transport of the photon is speed up using several variance reduction techniques. VMC simulation of the electron/photon transport is among the fastest MC codes[8].

The VMC and XVMC have been re-developed in C++ and along with other improvements in modeling of the physical processes and variance reduction techniques, have been introduced as VMC++ code.[50,51] The history repetition is also implemented in VMC and VMC++ (known as STOPS) technique which is discussed in the following sections.

2.6.2 Transport modeling in VMC

VMC uses some approximations and modifications applicable in a typical radiation therapy problem in which the energy range is 1-30 MeV and the density of material is in the range of 1-3 g/cm^3. The transport of the electron is approximated with simplified multiple scattering algorithm with respect to general purpose MC codes. With new simplified multiple scattering model the code takes 'smaller number of steps' with respect to EGS4 transport (the detail of calculation and formulations are discussed in Ref [24]).

In VMC there are also approximations in the production of secondary electrons, production of bremsstrahlung photons and continuous energy loss of electrons. In some of

these approximations, the behavior of various parameters such as stopping power are formulated considering the specific situation in radiation therapy (e.g. , energy range 0.2-30 MeV and water like materials). These formulations are used instead of the exact values and they are more efficient than table lookup which is used in a general purpose MC code.

Reducing the number of histories with track repetition: First we assume that there are two sources of tracks with similar energy and direction. The two sources are far enough from each other that none of the tracks intersects with tracks from the other source as illustrated in Fig. 2.14. Because the two beams, s_1 and s_2 do not interfere with each other, they have the same statistical uncertainty. Instead of generating new histories for s_2, the source s_1 can be reused.

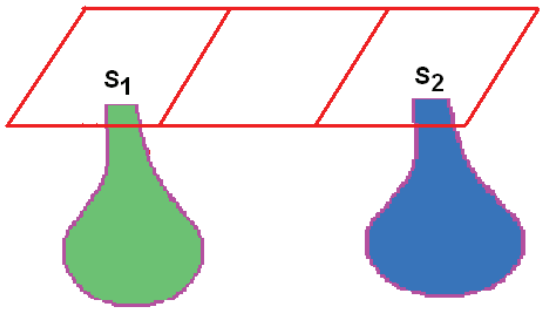

Figure 2.14 Two identical source of radiation that are far from each other without any interfere.

In this way, significantly computing time can be saved since parameters such as path length to discrete interactions, energies from secondary particle and scattering angles was calculated only once. Therefore, once the electron history is generated, it can be used at various positions on the surface of the phantom or patient. The only condition is that they have to be removed from each other, e.g. for 15 MeV electrons the points have to be more than 2 cm away from each other.[48]

Track repetition is subject to change in a heterogeneous phantom. For this purpose, the track of the electron is initially produced in water. The characteristics of the electron track such as deposited energy, path length, scattering angle and electron energy are saved on the fly. The path length and scattering angles are then adjusted according to the material and the density of the medium. The difference between the track repetition in SMC and VMC is that in SMC the entire track is already available in pre-calculated data

while in VMC the track is generated on the fly and it is repeated for various positions. Each of these techniques has their own advantages which are discussed later.

2.6.3 Results of VMC

The calculations using the original version of VMC were done with 0.2 MeV energy cut-off for electron and 0.01 MeV cut off for photons. The results were compared with EGS4 that served as reference. As an example of track repetition, for a 10×10 cm^2 field and 1 million histories, 50000 electrons are generated and repeated 20 times in 20 different locations. Figure 2.15.a illustrates the results of VMC for monoenergetic electrons in comparison with EGS4.

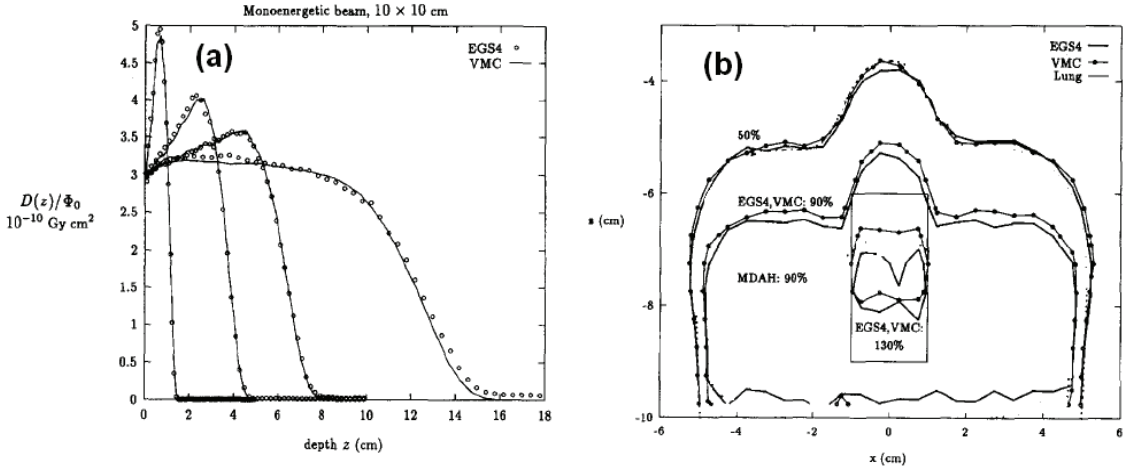

Figure 2.15 (a) Depth dose calculation of VMC for 2, 9, 30 MeV electron beams with EGS4 code. The uncertainties in calculations are less than 1 %. (b) Comparison of isodose lines of VMC and EGS4 in water phantom with a lung slab , density = 0.26 g/cm^3. (Figures from Ref[48])

In discussion of the results for monoenergetic electrons, about the big discrepancies it is mentioned that [48]: "When performing dose calculation for beams used in radiation therapy, these deviations will be removed in homogeneous phantoms due to the fact that different energy spectra are required for VMC and EGS4 in order to describe measured dose distribution."

VMC code performs well in various heterogeneous cases such as water-lung and water-air phantoms as illustrated in Fig. 2.15(b). There is generally a good agreement

between the two codes and deviations are due to approximations in cross sections and multiple scattering method. The computational speed is increased by a factor of 35 with respect to EGS4. In the first paper of VMC[48], the linear accelerator is modeled in a very simple manner and good agreement between VMC results and measurements of dose distribution for a 16 MeV electron beam is found. Since no pre-calculated data is needed for the VMC dose calculation, the amount of the needed memory is very small and depends on the resolution of the 3D phantom, e.g. for a 128×128×50 matrix representing a CT phantom , 16Mb of RAM is required. In the follow up papers VMC has been improved and licenced to a number of manufactuturs.[35]

2.6.4 VMC++ and STOPS

VMC++ was developed by Kawrakow in 2000 with the C++ programming language using an object oriented design.[50] The code includes all VMC/XVMC variance reduction techniques but incorporates several improvements in the modeling of the underlying physical processes:

1- Use of the exact multiple elastic scattering theory employed in EGSnrc.[51]

2- Use of STOPS technique instead of history repetition.

3- Refinements in the simulation of various scattering processes such as corrections for Compton scattering.

VMC++ is used as the dose calculation tool for the first commercial electron MC algorithm from Nucletron and is being incorporated into the Masterplan (Nucletron) and Eclipse (Varian) treatment planning systems for photon beam dose calculations.[79]

Simultaneous Transport Of Particle Sets (STOPS): Track repetition in VMC introduces systematic uncertainties and limits the applicability of the algorithm to low z materials discussed in the previous section. VMC++ uses a new technique for the track repetition that removes the systematic uncertainties. In STOPS technique, a group of the particles are transported at the ‘same time’ from various positions. The particles have the same energy but different position and direction. The interaction type of the particle is sampled separately based on the interaction probabilities of each medium. For all particles in each group several material independent parameters are sampled once such as interpolation indices, azimuthal scattering angles and distances to discrete interactions.

An example of VMC++ in comparison with EGSnrc is illustrated in Fig. 2.16. 20 MeV electrons inside a lead medium with a 10×10 cm^2 field size have been simulated. As one sees there is an excellent agreement between the results of the code with errors up to 1 %.

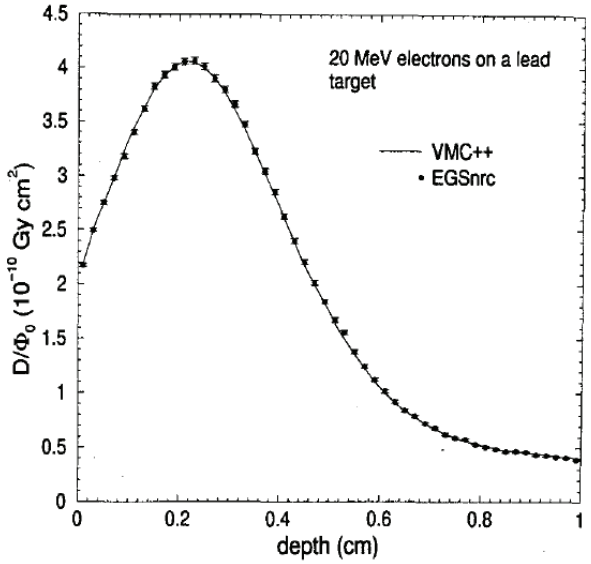

Figure 2.16 Comparison of VMC++ code with EGSnrc general purpose code for 20 MeV electrons. The material is lead and field size is 10×10 cm^2 (Figure from Ref [27]).

In discussion of STOPS technique there is a very important hint about track repetition and its effect on statistical uncertainties which is discussed here.

The efficiency of the Monte code is defined as

$$\varepsilon = \frac{1}{\sigma^2 T}, \qquad (2.3)$$

in which T is the computing time and σ is the statistical uncertainty. Each particle group in STOPS can have various number of particles; however, after a certain number of repetitions, the tracks of the particles are correlated and efficiency is not improved.

An example of the effect of track repetition on efficiency, denoted by Kawrakow[27], is illustrated in Fig. 2.17. The figure shows the relative efficiency of VMC++ code for 20 MeV electrons and 10×10 cm^2 field size in a phantom of 4 randomly distributed materials

(lung, carbon, water, aluminum). The size of the voxels is 5 mm in each direction and the efficiency is plotted versus number of repetitions.

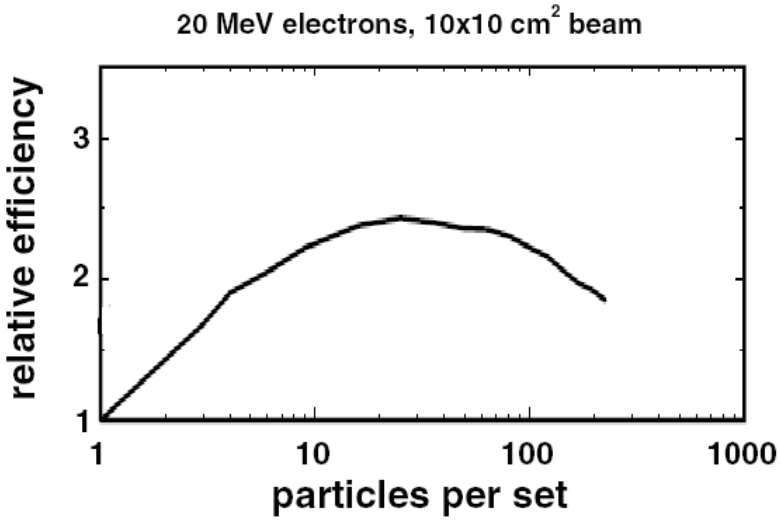

Figure 2.17 The relative efficiency of VMC++ code as a function of the number of track repetition (particle per set). (Figure from Ref. [27])

As one sees the change of the efficiency versus number of repetitions is initially increased, reaches a maximum and then decreases for large number of repetitions. The initial rise is because of the time that is saved by STOPS (up to 20-30 repetitions) and then the efficiency decreases since the uncertainty reaches a limit and the time still increases in Eq. 2.3.

VMC++ is benchmarked with various clinical situations and it is also evaluated and implemented in photon-electron transport by other groups.[65,79-87] The results of the code agrees with EGSnrc in the sub-percent level, while the code itself runs 50 times faster than EGS4 for electron transport.

2.7 Other fast MC codes

In the past decade, many fast MC codes have been developed for application in medical physics.[88-92] Considering the detailed discussion of MMC, SMC and VMC, fast MC codes take two general approaches to accelerate dose calculations. In one approach, the transport parameters and algorithms of the particles are formulated in an efficient form considering the specific conditions that one encounters in clinical situations. These specific conditions

include a relatively smaller energy range, i.e., <30 MeV, and low-Z materials with densities of up to 3 g/cm^3. This general feature is employed in "from scratch" MC codes such as the VMC[48], Dose Planning Method (DPM) [52], and MCDOSE[53]code suites. DPM[93-100] and MCDOSE[100-103] are integrated into the treatment planning systems and they are currently being used for a variety of electron-photon beam treatment planning studies.

In another approach fast MC codes use pre-generated data for particle transport. An important advantage of developing a fast MC code using pre-generated data is that the physics can be handled accurately by a general purpose code and after generation of the pre-calculated tracks, one technically only needs simple methods to apply the tracks to the problem of interest. In this way various particles can be simulated with the same transport algorithm. The dramatic evolution in computer speed and large available memory has enabled several groups to develop their own fast MC codes based on pre-calculated data for application in radiation therapy.[104-107] Most of the codes used the EGS4/EGSnrc code for generation of pre-calculated data and they need a relatively large amount of memory to load the data.

References

1. M. Goitein and J. Busse, "Immobilization error: Some theoretical considerations," Radiology **117**, 407–412 (1975).
2. A. Ito, in *Monte Carlo Transport of Electrons and Photons*, edited by W. R. Nelson, T. M. Jenkins, A. Rindi, A. E. Nahum, and D. W. O. Rogers (Plenum, New York, 1988), pp. 573–598.
3. A. E. Nahum, in *Monte Carlo Transport of Electrons and Photons*, edited by W. R. Nelson, T. M. Jenkins, A. Rindi, A. E. Nahum, and D. W. O. Rogers (Plenum, New York, 1988), pp. 3–20.
4. M. J. Berger, in *Methods in Computational Physics*, edited by S. Fernbach, B. Alder, and M. Rothenberg (Academic, New York, 1963), Vol. 1.
5. D. W. Rogers and A. F. Bielajew, "Monte Carlo techniques of electron and photon transport for radiation dosimetry," *The Dosimetry of Ionization Radiation*, Chapter 5, Vol III (1990).

6. P. Andreo, "Monte Carlo techniques in medical radiation physics," Phys. Med. Biol. **36**, 861–920 (1991).
7. D. E. Raeside "Monte Carlo principles and applications," Phys. Med. Biol. **21**, 181–197 (1976).
8. I. Chetty *et al*., "Guidance report on clinical implementation of the Monte Carlo method in external beam radiation therapy treatment planning: Report of the AAPM Task Group No. 105," Med. Phys. **34**, 4818–4853 (2007).
9. F. Verhaegen and J. Seuntjens, "Monte Carlo modelling of external radiotherapy photon beams," Phys. Med. Biol. **48**, R107–R164 (2003).
10. M. Berger and S. Seltzer, "ETRAN Monte Carlo code system for electron and photon transport through extended media," Radiation Shielding Information Center (RSIC) Report CCC-107, Oak Ridge National Laboratory, Oak Ridge, TN, 1973.
11. C. M. Ma and S. B. Jiang, "Monte Carlo modelling of electron beams from medical accelerators," Phys. Med. Biol. **44**, R157–R189 (1999).
12. R. Doucet, M. Olivares, F. DeBlois, E. B. Podgorsak, I. Kawrakow, and J. Seuntjens, "Comparison of measured and Monte Carlo calculated dose distributions in inhomogeneous phantoms in clinical electron beams," Phys. Med. Biol. **48**, 2339–2354 (2003).
13. L. Wang, C. S. Chui, and M. Lovelock, "A patient-specific Monte Carlo dose-calculation method for photon beams," Med. Phys. **25**, 867–878 (1998).
14. M. Pacilio, D. Aragno, R. Rauco, S. D'Onofrio, M. C. Pressello, L. Bianciardi and E.Santini, "Monte Carlo dose calculations using MCNP4C and EGSnrc/BEAMnrc codes to study the energy dependence of the radiochromic film response to beta-emitting sources," Phys. Med. Biol. **52**, 3931–3948 (2007).
15. M. Berger and S. Seltzer, "ETRAN Monte Carlo code system for electron and photon transport through extended media," Radiation Shielding Information Center (RSIC) Report CCC-107, Oak Ridge National Laboratory, Oak Ridge, TN, 1973.
16. D. Sheikh-Bagheri and D. W. O. Rogers, "Sensitivity of megavoltage photon beam Monte Carlo simulations to electron beam and other parameters," Med. Phys. **29**, 379–390 (2002).

17. G. X. Ding, "Energy spectra, angular spread, fluence profiles and dose distributions of 6 and 18 MV photon beams: Results of Monte Carlo simulations for a Varian 2100EX accelerator," Phys. Med. Biol. **47**, 1025–1046 (2002).

18. N. Tyagi, J. M. Moran, D. W. Litzenberg, A. F. Bielajew, B. A. Fraass, and I. J. Chetty, "Experimental verification of a Monte Carlo-based MLC simulation model for IMRT dose calculation," Med. Phys. **34**, 651–663 (2007).

19. E. B. Podgorsak, *Radiation Physics for Medical Physicists* (Springer, 2005).

20. I. J. Chetty, "Monte Carlo treatment planning: The influence of 'variance reduction' techniques (ECUT, PCUT, ESTEP) on the accuracy and speed of dose calculations," Med. Phys. **32**, 2018 (abstract) (2005).

21. D. W. O. Rogers, B. A. Faddegon, G. X. Ding, C. M. Ma, J. We, and T. R. Mackie, "BEAM: A Monte Carlo code to simulate radiotherapy treatment units," Med. Phys. **22**, 503–524 (1995).

22. I. Kawrakow, D. W. O. Rogers, and B. R. B. Walters, "Large efficiency improvements in BEAMnrc using directional bremsstrahlung splitting," Med. Phys. **31**, 2883–2898 (2004).

23. D. W. O. Rogers and A. F. Bielajew, in *Monte Carlo Transport of Electrons and Photons*, edited by W. R. Nelson, T. M. Jenkins, A. Rindi, A. E. Nahum, and D. W. O. Rogers (Plenum, New York, 1988), pp. 407–419.

24. W. R. Nelson, H. Hirayama, and D. W. O. Rogers, "The EGS4 Code System," SLAC Report No. SLAC-265, 1985.

25. I. Kawrakow and D. W. O. Rogers, "The EGSnrc code system: Monte Carlo simulation of electron and photon transport," NRC, Report PIRS–701, 2000.

26. J. F. Briesmeister, "MCNP-A general Monte Carlo N-particle transport code, Version 4C," Report LA-13709-M, Los Alamos National Laboratory, NM, 2000.

27. S. Agostinelli *et al*., "GEANT4—A simulation toolkit," Nucl. Instrum. Methods Phys. Res. A 506, 250–303 (2003).

28. D. W. O. Rogers, B. Walters, and I. Kawrakow, "BEAMnrc Users Manual," NRC Report PIRS 509(a)revH, 2004.

29. B. R. B. Walters, I. Kawrakow, and D. W. O. Rogers, DOSXYZnrc Users Manual, NRC Report PIRS 794 (rev B), 2005.

30. L. L. Wang and D. W. Rogers, "Calculation of the replacement correction factors for ion chambers in megavoltage beams by Monte Carlo simulation," Med. Phys. **35**, 1747–1755 (2008).

31. C. P. Joshi, J. Darko, P. B. Vidyasagar, and L. J Schreiner, "Investigation of an efficient source design for Cobalt-60-based tomotherapy using EGSnrc Monte Carlo simulations," Phys. Med. Biol. **53**, 575–592 (2008).

32. D. J. La Russa, M. McEwen, and D. W. Rogers, "An experimental and computational investigation of the standard temperature-pressure correction factor for ion chambers in kilovoltage x rays." Med. Phys. **34**, 4690–4699 (2007).

33. W. C. Toye, K. R. Das, S. P. Todd, M. B. Kenny, R. D. Franich, and P. N. Johnston, "An experimental MOSFET approach to characterize (192)Ir HDR source anisotropy," Phys. Med. Biol. **52**, 5329–5339 (2007).

34. A. Fogliata, E. Vanetti, D. Albers, C. Brink, A. Clivio, T. Knöös, G. Nicolini, and L. Cozzi, "On the dosimetric behaviour of photon dose calculation algorithms in the presence of simple geometric heterogeneities: comparison with Monte Carlo calculations," Phys. Med. Biol. **52**, 1363–1385 (2007).

35. L. Strigari, E. Menghi, M. D'Andrea, and M. Benassi, "Monte Carlo dose voxel kernel calculations of beta-emitting and Auger-emitting radionuclides for internal dosimetry: A comparison between EGSnrcMP and EGS4," Med. Phys. **33**, 3383–3389 (2006).

36. W. Abdel-Rahman, J. P. Seuntjens, F. Verhaegen, and E. B. Podgorsak, "Radiation induced currents in parallel plate ionization chambers: measurement and Monte Carlo simulation for megavoltage photon and electron beams," Med. Phys. **33**, 3094–3104 (2006).

37. F. Verhaegen, "Evaluation of the EGSnrc Monte Carlo code for interface dosimetry near high-Z media exposed to kilovolt and 60Co photons," Phys. Med. Biol. **47**, 1691–1705 (2002).

38. A. Fogliata, E. Vanetti, D. Albers, C. Brink, A. Clivio, T. Knöös, G. Nicolini, and L. Cozzi, "On the dosimetric behaviour of photon dose calculation algorithms in the presence of simple geometric heterogeneities: comparison with Monte Carlo calculations," Phys. Med. Biol. **52**, 1363–1385 (2007).

39. L. E. Court, L. Jahnke, D. Chin, J. Song, R. Cormack, P. Zygmanski, R. B. Tishler, and L. Chin, "Dynamic IMRT treatments of sinus region tumors: comparison of Monte Carlo calculations with treatment planning system calculations and ion chamber measurements," Technol. Cancer Res. Treat. **5**, 489–95 (2006).

40. S. H. Cho, O. N. Vassiliev, S. Lee, H. H. Liu, G. S. Ibbott, and R. Mohan," Reference photon dosimetry data and reference phase space data for the 6 MV photon beam from varian clinac 2100 series linear accelerators," Med. Phys. **32**, 137–148 (2005).

41. I. Kawrakow and B. Walters, "Efficient photon beam dose calculations using DOSXYZnrc with BEAMnrc," Med. Phys. **33**, 3046–3056 (2006).

42. I. Kawrakow, D. W. O. Rogers, and B. R. B. Walters, "Large efficiency improvements in BEAMnrc using directional bremsstrahlung splitting," Med. Phys. **31**, 2883–2898 (2004).

43. C.-M. Ma, E. Mok, A. Kapur, T. Pawlicki, D. Findley, S. Brain, K. Forster, and A. L. Boyer, "Clinical implementation of a Monte Carlo treatment planning system," Med. Phys. **26**, 2133–2143 (1999).

44. H. Neuenschwander and E. J. Born, "A Macro Monte Carlo method for electron beam dose calculations," Phys. Med. Biol. **37**, 107–125 (1992).

45. H. Neuenschwander, T. R. Mackie, and P. J. Reckwerdt, "MMC— A high-performance Monte Carlo code for electron beam treatment planning," Phys. Med. Biol. **40**, 543–574 (1995).

46. P. J. Keall and P. W. Hoban, "Super-Monte Carlo: a 3D electron beam dose calculation algorithm," Med. Phys. **23**, 2023–2034 (1996).

47. P. J. Keall and P. W. Hoban, "Superposition dose calculation incorporating Monte Carlo generated electron track kernels," Med. Phys. **23**, 479–485 (1996).

48. I. Kawrakow, M. Fippel, and K. Friedrich, "3D Electron Dose Calculation using a Voxel based Monte Carlo Algorithm," Med. Phys. **23**, 445–457 (1996).

49. I. Kawrakow and M. Fippel, "Investigation of variance reduction techniques for Monte Carlo photon dose calculation using XVMC," Phys. Med. Biol. **45**, 2163–2184 (2000).

50. I. Kawrakow and M. Fippel, "VMC++, a MC algorithm optimized for electron and photon beam dose calculations for RTP," in *Proceedings of the 22nd Annual*

International Conference of the IEEE (Engineering in Medicine and Biology Society, Piscataway, NJ, 2000).

51. I. Kawrakow, "VMC++, electron and photon Monte Carlo calculations optimized for Radiation Treatment Planning," *Advanced Monte Carlo for Radiation Physics, Particle Transport Simulation and Applications: Proceedings of the Monte Carlo 2000 Meeting Lisbon*, edited by A. Kling, F. Barao, M. Nakagawa, L. Távora, and P. Vaz (Springer, Berlin, 2001), pp. 229–236.

52. J. Sempau, S. J. Wilderman, and A. F. Bielajew, "DPM, a fast, accurate Monte Carlo code optimized for photon and electron radiotherapy treatment planning dose calculations," Phys. Med. Biol. **45**, 2263–2291 (2000).

53. C. Ma, J. S. Li, T. Pawlicki, S. B. Jiang, J. Deng, M. C. Lee, T. Koumrian, M. Luxton, and S. Brain, "MCDOSE - A Monte Carlo dose calculation tool for radiation therapy treatment planning," Phys. Med. Biol. **47**, 1671–1689 (2002).

54. M. Rosu, J. M. Balter, I. J. Chetty, M. L. Kessler, D. L. Mc Shan, P. Balter, and R. K. Ten Haken, "How extensive of a 4D dataset is needed to estimate cumulative dose distribution plan evaluation metrics in conformal lung therapy?," Med. Phys. **34**, 233–245 (2007).

55. P. J. Keall, J. V. Siebers, S. Joshi, and R. Mohan, "Monte Carlo as a four-dimensional radiotherapy treatment-planning tool to account for respiratory motion," Phys. Med. Biol. **49**, 3639–3648 (2004).

56. R. Jeraj and P. Keall, "The effect of statistical uncertainty on inverse treatment planning based on Monte Carlo dose calculation," Phys. Med. Biol. **45**, 3601–3613 (2002).

57. R. Jeraj and P. J. Keall, "Monte Carlo-based inverse treatment planning," Phys. Med. Biol. **44**, 1885–1896 (1999).

58. I. J. Chetty, P. M. Charland, N. Tyagi, D. L. Mc Shan, B. A. Fraass, and A. F. Bielajew, "Photon beam relative dose validation of the DPM Monte Carlo code in lung-equivalent media," Med. Phys. **30**, 563–573 (2003).

59. I. J. Chetty, J. M. Moran, T. S. Nurushev, D. L. McShan, B. A. Fraass, S. J. Wilderman, and A. F. Bielajew, "Experimental validation of the DPM Monte Carlo

code using minimally scattered electron beams in heterogeneous media," Phys. Med. Biol. **47**, 1837–1851 (2002).

60. M. Fippel, I. Kawrakow, and K. Friedrich, "Electron beam dose calculations with the VMC algorithm and the verification data of the NCI working group," Phys. Med. Biol. **42**, 501–520 (1997).

61. R. A. Popple, R. Weinberg, J. A. Antolak, S. J. Ye, P. N. Pareek, J. Duan, S. Shen, and I. Brezovich, "A Comprehensive evaluation of a commercial macro Monte Carlo electron dose calculation implementation using a standard verification data set," Med. Phys. **33**, 1540–1551 (2006).

62. G. X. Ding, D. M. Duggan, C. W. Coffey, P. Shokrani, and J. E. Cygler, "First macro Monte Carlo based commercial dose calculation module for electron beam treatment planning--new issues for clinical consideration," Phys. Med. Biol. **51**, 2781–2799 (2006).

63. J. Gardner, J. Siebers, and I. Kawrakow, "Dose calculation validation of VMC++ for photon beams," Med. Phys. **34**, 1809–1818 (2007).

64. F. Hasenbalg, M. K. Fix, E. J. Born, R. Mini, and I. Kawrakow, "VMC++ versus BEAMnrc: A comparison of simulated linear accelerator heads for photon beams," Med. Phys. **35**, 1521 (2008).

65. J. V. Siebers, I. Kawrakow, and V. Ramakrishnan, "Performance of a hybrid MC dose algorithm for IMRT optimization dose evaluation," Med. Phys. **34**, 2853 (2007).

66. I. Kawrakow, "Improved modeling of multiple scattering in the Voxel Monte Carlo model," Med. Phys. **24**, 505–517 (1997).

67. C. Ma, J. Li, J. Deng, and J. Fan, "Investigation of Fast Monte Carlo Dose Calculation for CyberKnife SRS/SRT Treatment Planning," Med. Phys. **34**, 2589–2590 (2007).

68. K. R. Hogstrom, "Evaluation of electron pencil beam dose calculation," Med. Phys. **12**(4), 554 (1985).

69. A. S. Shiu and K. R. Hogstrom, "Pencil-beam redefinition algorithm for electron dosedistributions," Med. Phys. **18**, 7–18 (1991).

70. J. Cygler, J. J. Battista, J. W. Scrimger, E. Mah, and J. Antolak, "Electron dose distributions in experimental phantoms: a comparison with 2D pencil beam calculations," Phys. Med. Biol. **32**, 1073–1086 (1987).

71. I. Lax, "Inhomogeneity corrections in electron beam dose planning. Limitations with the semi-infinite slab approximation," Phys. Med. Biol. **31**, 879-892 (1986).
72. C. Cris, E. Born, R. Mini, H. Neuenschwander, and W. Volken, "A scaling method for multiple source models," in Proceedings of the 13th ICCR, edited by T. Bortfeld and W. Schlegel (Springer-Verlag, Heidelberg, 2000), pp. 411–413.
73. P. Pemler, J. Besserer, U. Schneider, and H. Neuenschwander, "Evaluation of a commercial electron treatment planning system based on Monte Carlo techniques (eMC) ," Med. Phys. **16**, 313–329 (2006).
74. R. L. Siddon, "Prism representation: a 3D ray-tracing algorithm for radiotherapy applications," Phys. Med. Biol. **30**, 817–24 (1985).
75. J. E. O Connor, "The variation of scattered x-rays with density in an irradiated body," Phys. Med. Biol. **1**, 352-369 (1957).
76. International Commission on Radiological Protection. *Report of the Task Group on Reference Man,* Vol. 23 (Pergamon, New York, 1974).
77. S. N. Rustgi and J. E. Rodgers, "Analysis of the bremsstrahlung component in 6-18 MeV electron beams," Med. Phys. **14**, 884–888 (1987).
78. I. Kawrakow and A. F. Bielajew, "On the representation of electron multiple elastic-scattering distributions for Monte Carlo calculations," Nucl. Instrum. Methods Phys. Res. B 134, 325–336 (1998).
79. C. Scherf, J. Scherer, and L. Bogner, "Verification and application of the Voxel-based Monte Carlo (VMC++) electron dose module of oncentratrade mark MasterPlan," Strahlenther. Onkol. **183**, 81–88 (2007).
80. J. Gardner, J. Siebers, and I. Kawrakow, "Dose calculation validation of VMC++ for photon beams," Med. Phys. **34**, 1809–1818 (2007).
81. F. Hasenbalg, M. K. Fix, E. J. Born, R. Mini, and I. Kawrakow, "VMC++ versus BEAMnrc: a comparison of simulated linear accelerator heads for photon beams," Med. Phys. **35**, 1521–1531 (2008).
82. A. Fogliata, G. Nicolini, E. Vanetti, A. Clivio, P. Winkler, and L. Cozzi, "The impact of photon dose calculation algorithms on expected dose distributions in lungs under different respiratory phases," Phys. Med. Biol. **53**, 2375–2390 (2008).

83. T. Vatanen, E. Traneus, and T. Lahtinen, "Dosimetric verification of a Monte Carlo electron beam model for an add-on eMLC," Phys. Med. Biol. **53**, 391–404 (2008).

84. J. K. Gardner, J. V. Siebers, and I. Kawrakow, "Comparison of two methods to compute the absorbed dose to water for photon beams," Phys. Med. Biol. **52**, 439–447 (2007).

85. F. Hasenbalg, H. Neuenschwander, R. Mini, and E. J. Born, "Collapsed cone convolution and analytical anisotropic algorithm dose calculations compared to VMC++ Monte Carlo simulations in clinical cases," Phys. Med. Biol. **52**, 3679–3691 (2007).

86. P. E. Lindsay, I. El Naqa, A. J. Hope, M. Vicic, J. Cui, J. D. Bradley, and J. O. Deasy, "Retrospective monte carlo dose calculations with limited beam weight information," Med. Phys. **34**, 334–346 (2007).

87. C. Zakarian and J. O. Deasy, "Beamlet dose distribution compression and reconstruction using wavelets for intensity modulated treatment planning," Med. Phys. **31**, 368–375 (2004).

88. K. Eklund and A. Ahnesjö, "Fast modelling of spectra and stopping-power ratios using differentiated fluence pencil kernels," Phys. Med. Biol. **53**, 4231–4247 (2008).

89. M. Oliver, R. Staruch, A. Gladwish, J. Craig, J. Chen, and E. Wong, "Monte Carlo dose calculation of segmental IMRT delivery to a moving phantom using dynamic MLC and gating log files," Phys. Med. Biol. **53**, 187–196 (2008).

90. M. Fippel, "Fast Monte Carlo dose calculation for photon beams based on the VMC electron algorithm," Med. Phys. **26**, 1466–1475 (1999).

91. J. S. Li, B. Shanine, E. Fourkal, and C.-M. Ma, "A particle track-repeating algorithm for proton beam dose calculation," Phys. Med. Biol. **50**, 1001–1010 (2005).

92. V. A. Semenenko and R. D. Stewart, "Fast Monte Carlo simulation of DNA damage formed by electrons and light ions," Phys. Med. Biol. **51**, 1693–1706 (2005).

93. I. J. Chetty, P. M. Charland, N. Tyagi, D. L. McShan, B. A. Fraass, and A. F. Bielajew, "Photon beam relative dose validation of the DPM Monte Carlo code in lung-equivalent media," Med. Phys. **30**, 563–573 (2003).

94. I. J. Chetty, N. Tyagi, M. Rosu, P. M. Charland, D. L. McShan, R. K. Ten Haken, B. A. Fraass, and A. F. Bielajew, "Clinical implementation, validation and use of the

DPM Monte Carlo code for radiotherapy treatment planning," in Nuclear Mathematical and Computational Sciences: A Century in Review, A Century Anew, Gatlinburg, TN (American Nuclear Society, LaGrange Park, IL, 2003), Vol. 119, pp. 1–17.

95. N. Tyagi, A. Bose, and I. J. Chetty, "Implementation of the DPM Monte Carlo Code on a parallel architecture for treatment planning applications," Med. Phys. **31**, 2721–2725 (2004).

96. I. J. Chetty, P. M. Charland, N. Tyagi, D. L. McShan, B. Fraass, and A. F. Bielajew, "Experimental validation of the DPM Monte Carlo code for photon beam dose calculations in inhomogeneous media," Med. Phys. **29**, 1351 (abstract) (2002).

97. N. Tyagi, A. Bose, and I. J. Chetty, "Implementation of the DPM Monte Carlo code on a parallel architecture for treatment planning applications," Med. Phys. **31**, 2721–2725 (2004).

98. X. Weng, Y. Yan, H. Shu, J. Wang, S. B. Jiang, and L. Luo, "A vectorized Monte Carlo code for radiotherapy treatment planning dose calculation," Phys. Med. Biol. **48**, 111–120 (2003).

99. T. K. Lee and G. A. Sandisonm, "The energy-dependent electron loss model: backscattering and application to heterogeneous slab media," Phys. Med. Biol. **48**, 259–273 (2003).

100. M. Rosu, I. J. Chetty, D. S. Tatro, and R. K. Ten Haken, "The impact of breathing motion versus heterogeneity effects in lung cancer treatment planning," Med. Phys. **34**, 1462–1473 (2007).

101. C.-M. Ma, J. S. Li, T. Pawlicki, S. B. Jiang, and J. Deng, "MCDOSE—A Monte Carlo dose calculation tool for radiation therapy treatment planning," in Proceedings of the 13th ICCR, edited by T. Bortfeld and W.Schlegel (Springer-Verlag, Heidelberg, 2000), pp. 411–413.

102. M. Blomquist, J. Li, C. M. Ma, B. Zackrisson, and M. Karlsson, "Comparison between a conventional treatment energy and 50 MV photons for the treatment of lung tumors," Phys. Med. Biol. **47**, 889–897 (2002).

103. M. C. Lee, S. B. Jiang, and C. M. Ma, "Monte Carlo and experimental investigations of multileaf collimated electron beams for modulated electron radiation therapy," Med. Phys. **27**, 2708–2708 (2000).

[104.] R. Sheu, C. Chui, T. LoSasso, S. Lim, and A. Kirov, "Accurate and Efficient Monte Carlo Dose Calculation for Electron Beams," Med. Phys. **33**, 2067 (2006).

[105.] S. Stathakis, J. Li, and C. M. Ma, "Monte Carlo determination of radiation-induced cancer risks for prostate patients undergoing intensity- modulated radiation therapy," J. Appl. Clin. Med. Phys. **8**, 2685 (2007).

[106.] S. Flampouri, S. B. Jiang, G. C. Sharp, J. Wolfgang, A. A. Patel, and N. C. Choi , "Estimation of the delivered patient dose in lung IMRT treatment based on deformable registration of 4D-CT data and Monte Carlo simulations," Phys. Med. Biol. **51**, 2763–2779 (2006).

[107.] J. Yang, J. S. Li, L. Qin, W. Xiong, and C. M. Ma "Modelling of electron contamination in clinical photon beams for Monte Carlo dose calculation," Phys. Med. Biol. **49**, 2657–2673 (2004).

Chapter 3

Methods for Pre-Calculated Monte Carlo

3.1 Introduction

Development of a fast MC code based on pre-calculated data has the following advantages:

1- Use of the reliable general purpose code to calculate the physical parameters of the particle transport.[1-4] The general purpose codes are compared with benchmark experiments in a wide range of energies, materials and geometries [4-9] and the generated data could be used as a base for a fast MC code. General purpose codes are very flexible and many physical parameters for transport of the particle can be adjusted by the user. These codes can usually be modified straightforwardly to generate pre-calculated data.

2- The code is simple. Most of the physical parameters are calculated by a general purpose code, and the fast MC code is not a complicated algorithm in terms of the physics especially when pre-calculated data is generated for each material.

3- The code can be simply extended to various particles without a need for any modification or approximations in the transport parameters of each particle. In "from scratch" fast MC codes such as VMC[10], DPM[11] or MCDOSE[12], the physics of each new particle (such as protons) has to be handled properly including stopping powers, scattering power and other transport parameters .

As discussed in Chapter 2, there are different approaches for development of fast MC based on pre-calculated data. One approach is based on pre-calculated probability functions such as with MMC in which the code takes sphere by sphere steps and the characteristics of exited electrons are determined from the pre-calculated probability distribution[13]. The major limitation in this approach is that the electron cannot take large steps through large spheres since the sphere is considered as a black box and the track of the electron inside the sphere is lost and with a large step the build up region can

not be simulated properly. Another approach (Superposition MC) for fast MC is straight forward in which the code uses the exact track of the particles, pre-calculated by a general purpose MC code. In this method instead of probability functions, the details of each step is saved in pre-calculated data therefore the size of the pre-calculated data is relatively large.

Our approach for development of a fast MC code is also based on using the details of pre-calculated track of the particles in which the characteristics of the particle is saved in each step. We generically label our fast MC code PMC, Pre-calculated Monte Carlo, and discuss the implementation of a new method for pre-generation and handling of electron tracks which is efficient and produces accurate results. PMC takes advantage of large available memory resources in current computer hardware for use of pre-calculated data.

3.2 Fast Monte Carlo based on pre-calculated tracks

PMC uses pre-generated tracks by the EGSnrc general MC code for transport of the particle. The tracks include the path of primary particle for a wide range of initial energies and materials. The track does not need to be modified for each material using stopping power and scattering power ratios; hence, the transport algorithm in PMC is very simple and is capable of being applied to any particle. Secondary particles are not transported explicitly in the pre-calculated data; instead their characteristics are saved and they are transported in the same way as the primary particle. This technique reduces the size of the pre-calculated data.

3.3 Modification of EGSnrc

EGSnrc is the enhanced version of EGS4 and currently is one of most widely used general purpose codes.[16-18] The EGSnrc code is very well documented and it is available as a free package in the web site of National Research council of Canada (NRC).[19] The code performs the MC simulation of coupled electron-photon transport in energy range of 1 keV - 10 GeV. In recent development, the user can install the EGSnrc on both Windows and Unix machines. The code is developed in Mortran language. Mortran programs may be written without regard to column or card boundaries as it is the case in Fortran 77. Statements may begin anywhere on the input line and may end anywhere on the line and this feature permits free-form programming.

Since for generation of pre-calculated tracks some modification of EGSnrc is required, one needs to have access to the source code of EGSnrc. As it is discussed later the final goal of this preparation is that the code writes the characteristics of a primary particle and at the same time the secondary particles are not transported. This needs the change of many default parameters and routines of the code.

To prepare the EGSnrc for generation of pre-calculated data, we started with modification of Tutor 4. The tutorials in EGSnrc are written on the assumption that the reader is generally familiar with the contents of the EGSnrc reference manual. The `tutor4.mortran` has the added ability to use the auxiliary `SUBROUTINE WATCH` that provides detailed information about each particle interaction which occurs during the simulation. `SUBROUTINE WATCH` is a part of `nrcaux.mortran` which can be controlled by parameter `iwatch`. Parameter `iwatch` determines the format of the output of the `SUBROUTINE WATCH`. A typical output of `SUBROUTINE WATCH` for 20 MeV photons is illustrated in Fig. 3.1. For the purposes of this work, `iwatch`=2 is selected in which the output includes information on every single electron step. The user of `SUBROUTINE WATCH` should be aware that the size of the output explodes for large number of histories.

The tracking of the transport through the geometry in EGSnrc is performed by the user-written subroutines HOWFAR and HOWNEAR[20]. The subroutine HOWFAR calculates the distance, *d*, from the particle's position and in the particle's direction to the geometry-limiting surface. USTEP is the distance between the current position of the particle and the subsequent interaction position, calculated by EGSnrc. The intercept distance, *d*, is then compared with USTEP and if USTEP is greater than or equal to *d*, USTEP is shortened to *d*, and the new region number must be identified otherwise the particles just move the distant USTEP. This is the reason that in literature[5,10] it is mentioned that EGSnrc stops particles at the boundaries while this is not the case for most of the fast MC codes. Repeated boundary checking by HOWFAR can become very inefficient for charged particles when they are at a considerable distance to the nearest boundary, compared with the small steps they take, in which case subroutine HOWNEAR helps to avoid unnecessary calls to HOWFAR. The subroutine HOWNEAR calculates the minimum perpendicular distance, d_{min}, from the charged particle's position to the user-

defined surfaces. In this way the code does not have to calculate d in each step and USTEP is compared to d_{min}.

```
                                  NP   ENERGY  Q REGION    X       Y     Z      U      V      W   LATCH  WEIGHT

 INITIAL SHOWER VALUES            :    1   20.000  -1   2   0.000   0.000 0.000  0.000  0.000  1.000    0 1.000E+00
 bremsstrahlung  about to occur   :    1   19.656  -1   2   0.001   0.002 0.020 -0.046  0.089  0.995    0 1.000E+00
        Resulting electron        :    1   18.695  -1   2   0.001   0.002 0.020 -0.046  0.089  0.995    0 1.000E+00
        Resulting photon          :    2    0.962   0   2   0.001   0.002 0.020 -0.052  0.092  0.994    0 1.000E+00
 Discard -user request            :    2    0.962   0   3  -0.003   0.009 0.100 -0.052  0.092  0.994    0 1.000E+00
        Now on top of stack       :    1   18.695  -1   2   0.001   0.002 0.020 -0.046  0.089  0.995    0 1.000E+00
 bremsstrahlung  about to occur   :    1   18.196  -1   2   0.003   0.007 0.049  0.329  0.264  0.907    0 1.000E+00
        Resulting electron        :    1   18.120  -1   2   0.003   0.007 0.049  0.329  0.264  0.907    0 1.000E+00
TEST < E         Resulting photon :    2    0.076   0   2   0.003   0.007 0.049  0.330  0.268  0.905    0 1.000E+00
 Discard  AE,AP< E< ECUT          :    2    0.076   0   2   0.003   0.007 0.049  0.330  0.268  0.905    0 1.000E+00
        Now on top of stack       :    1   18.120  -1   2   0.003   0.007 0.049  0.329  0.264  0.907    0 1.000E+00
 Discard -user request            :    1   17.185  -1   3   0.009   0.026 0.100 -0.073  0.401  0.913    0 1.000E+00
 END OF HISTORY       1   ****************************************

 INITIAL SHOWER VALUES            :    1   20.000  -1   2   0.000   0.000 0.000  0.000  0.000  1.000    0 1.000E+00
 bremsstrahlung  about to occur   :    1   19.016  -1   2  -0.007  -0.001 0.058 -0.158 -0.188  0.969    0 1.000E+00
        Resulting electron        :    1   18.747  -1   2  -0.007  -0.001 0.058 -0.158 -0.188  0.969    0 1.000E+00
        Resulting photon          :    2    0.268   0   2  -0.007  -0.001 0.058 -0.012 -0.347  0.938    0 1.000E+00
 Discard -user request            :    2    0.268   0   3  -0.007  -0.017 0.100 -0.012 -0.347  0.938    0 1.000E+00
        Now on top of stack       :    1   18.747  -1   2  -0.007  -0.001 0.058 -0.158 -0.188  0.969    0 1.000E+00
 bremsstrahlung  about to occur   :    1   18.577  -1   2  -0.009  -0.004 0.067 -0.268 -0.271  0.925    0 1.000E+00
        Resulting electron        :    1   18.418  -1   2  -0.009  -0.004 0.067 -0.268 -0.271  0.925    0 1.000E+00
        Resulting photon          :    2    0.159   0   2  -0.009  -0.004 0.067 -0.293 -0.298  0.909    0 1.000E+00
 Discard -user request            :    2    0.159   0   3  -0.020  -0.015 0.100 -0.293 -0.298  0.909    0 1.000E+00
        Now on top of stack       :    1   18.418  -1   2  -0.009  -0.004 0.067 -0.268 -0.271  0.925    0 1.000E+00
 bremsstrahlung  about to occur   :    1   18.256  -1   2  -0.011  -0.007 0.076 -0.177 -0.310  0.934    0 1.000E+00
        Resulting electron        :    1   17.321  -1   2  -0.011  -0.007 0.076 -0.177 -0.310  0.934    0 1.000E+00
        Resulting photon          :    2    0.935   0   2  -0.011  -0.007 0.076 -0.175 -0.335  0.926    0 1.000E+00
 Discard -user request            :    2    0.935   0   3  -0.016  -0.016 0.100 -0.175 -0.335  0.926    0 1.000E+00
        Now on top of stack       :    1   17.321  -1   2  -0.011  -0.007 0.076 -0.177 -0.310  0.934    0 1.000E+00
 bremsstrahlung  about to occur   :    1   17.231  -1   2  -0.012  -0.009 0.081 -0.278 -0.252  0.927    0 1.000E+00
        Resulting electron        :    1   12.065  -1   2  -0.012  -0.009 0.081 -0.278 -0.252  0.927    0 1.000E+00
        Resulting photon          :    2    5.167   0   2  -0.012  -0.009 0.081 -0.261 -0.216  0.941    0 1.000E+00
 Discard -user request            :    2    5.167   0   3  -0.017  -0.013 0.100 -0.261 -0.216  0.941    0 1.000E+00
        Now on top of stack       :    1   12.065  -1   2  -0.012  -0.009 0.081 -0.278 -0.252  0.927    0 1.000E+00
 Discard -user request            :    1   11.720  -1   3  -0.018  -0.015 0.100 -0.311 -0.280  0.908    0 1.000E+00
 END OF HISTORY       2   ****************************************
```

Figure 3.1 A typical output of EGSnrc code using `SUBROUTINE WATCH` for 20 MeV photons. Parameters (u,v,w) represents the cosine direction of the motion and Q is the charge of the particle. The NP is the stack pointer (i.e., the particle currently being pointed to).

3.4 Generation of pre-calculated tracks

3.4.1 Geometry and material of homogeneous medium

The electrons are incident in the middle of large homogeneous phantom. The size of the media should be at least 80 cm in each direction[21], which is more than the maximum range in a typical clinical phantom or patient. The shape of the phantom could be a sphere with radius of 40 cm or a cube with half side of 40 cm. We chose a cube phantom in which the electrons are incident in the middle of the phantom at a depth of 40 cm. The electrons

in most of the materials do not reach the boundary of the phantom but if they do for a particular material such as air, the truncated track has to be handled properly as discussed later.

The materials which are used to fill up the phantom are all available in EGSnrc: water (1 g/cm^3) , bone (1.82 g/cm^3), lung (0.26 g/cm^3), air (1.205×10^{-3} g/cm^3). These are the materials that are used in a typical clinical treatment planning; however, if any other material is required, it can be added to the pre-calculated data as long as the composition of the material is known.

3.4.2 Energy range, energy cut-offs and number of the particles

The energy range of the electron beam was 0.2, 0.4, 0.6, 0.8, 1, 2, 3 … 17, 18 MeV. The upper limit and energy bins of this range are according to a typical range of the electrons used in radiation therapy. The lower limit comes from the fact that the electrons below that energy have a very short range.[10] The total energy cut-off parameter for electron transport was ECUT = 0.611 MeV. This means that all of the electrons are transported until their kinetic energy falls below 100 keV. At this point the energy of the electrons is deposited locally. The energy cut-off range in other fast MC codes for electrons is between 100-200 keV.[10-15]

For each energy, 5000 electrons are transported from the middle of a large homogeneous phantom. The number of particles is selected based on a consideration for the available size of the RAM. Larger number of electrons can be included in pre-calculated data if one desires. The reference coordinate of the system is put in the middle of the phantom and the initial direction of the particles are in +Z direction. The direction cosines of the particle in this case are (u,v,w) = (0,0,1).

3.4.3 Saving the transport parameters of electron

The main section of the code is designing and saving the appropriate matrixes that contains the information of electron sets. Each set contains tracks of 5000 electrons with the same initial energy. For each step of the primary electron, the following parameters are saved:

1- Position of the particle in Cartesian coordinate (x,y,z) in *cm* .

2- Energy of the particle at the beginning of the step, e, in MeV.

3- The deposited energy, *edep*, in MeV.

4- Characteristics of secondary particle (energy, direction, porition) if there is any.

These parameters for all 5000 particles are saved in 2 dimensional matrixes as illustrated in Fig. 3.2. Since electrons do not necessarily have the same number of steps, a separate matrix of indices are needed to point out the position of each track in the entire matrix. Although with use of a 3-dimensional matrix it is possible to avoid the indices (by having 5000 levels in the third dimension for each particle) while making the coding simpler, this is not efficient in terms of the total size of the file and as a result the size of the pre-calculated data will be larger (almost double in our test).

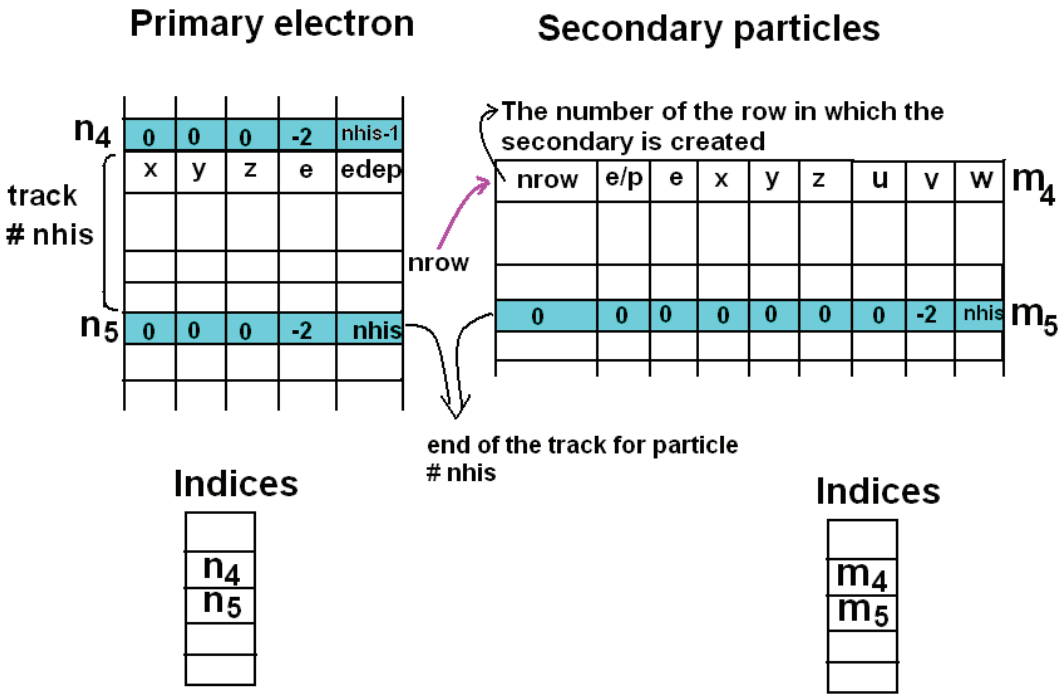

Figure 3.2 Description of the of the matrixes containing the track of the primary particles and characteristics of the secondary particles. Since all of the tracks are saved in 2-dimensional matrixs an extra 1-dimensional matrix is needed that contains the indices relates to each primary electron (5000 indices) as well as 5000 indices for secondary particles. For secondary particles the following parameters are saved : the related row in primary track in which the secondary is generated (nrow) , charge (e/p , -1 for electron and 0 for photons) , energy (*e*), position (*x*,*y*,z) and direction of motion (*u*,*v*,*w*).

It should be noted that although in some points of the particle transport for the primary particle we need the direction of the motion (*u*,*v*,*w*) and while this information is

available in the EGSnrc output as is illustrated in Fig. 3.1, this information is not included in pre-calculated data to reduce the size of the data. The direction of the motion can be calculated from two successive position of the particle. Assuming the position of the electron at the beginning and end of one step are (x_1,y_1,z_1) and (x_2,y_2,z_2) respectively, the direction cosine of the step can be calculated as :

$$d = \sqrt{(x_2 - x_1)^2 + (y_2 - y_1)^2 + (z_2 - z_1)^2} \tag{3.1}$$

$$u = \frac{x_2 - x_1}{d} \tag{3.2}$$

$$v = \frac{y_2 - y_1}{d} \tag{3.3}$$

$$w = \frac{z_2 - z_1}{d} \quad . \tag{3.4}$$

For the secondary particles, since just the initial characteristics are saved, the direction of the particles has to be included in the pre-calculated data. After saving the needed information, all of the secondary particles are terminated and not transported in the EGSnrc code. This makes generation process of pre-calculated data very fast (in order of few seconds for each energy).

3.4.4 Step size of the electron

An important parameter for generation of pre-calculated tracks and reusing of the tracks in various geometries is the electron step size. In our geometry in which the electron moves through a large homogeneous phantom, the boundary of phantom is far and EGSnrc, in the default set up, automatically transports the electron with large steps. The problem with this assumption is that once the track of the electron is saved, for transport in a clinical phantom (performed by PMC code) electrons might cross a boundary of another material in any step. Since the size of the steps cannot be reduced in the pre-calculated data (as it is calculated by EGSnrc just once) the electron will take a large step even close to inhomogeneities and this causes artifacts in the dose calculation.[25] The artifact arises from the fact that in each step, in reality, the electron does not move in a straight line. It is possible to ignore deflections due to multiple elastic scattering during the condensed

history step and to transport the electron on a straight line along the initial direction of motion. In order for this approach to be accurate, the condensed history steps must be sufficiently short so that the straight line approach does not represent an improper approximation. This issue is discussed in more details in Section 4.8.

In the first stage for generation of the pre-calculated tracks, to avoid possible artifacts, the track of the electron has to be transported in a short distance in every step. In the EGSnrc code, the XIMAX is one of the parameters that controls the condensed history step size, and limits the maximum value of the first Goudsmit and Saunderson moment per step. There is a complete description of XIMAX in EGSnrc manual and other literatures. [8,19,24] In our code, the maximum electron step length is controlled by setting XIMAX=0.05, which is equivalent to assuming that the electron is moving close to a boundary for each step. To have a numerical impression of the step size, the average length of the first step for 6 MeV electrons is 1.1 mm for XIMAX=0.05. The default value of XIMAX in EGSnrc code is 0.5. A 2D projection of the tracks of few 6 MeV electrons and position of the secondaries in water is illustrated in Fig. 3.3.

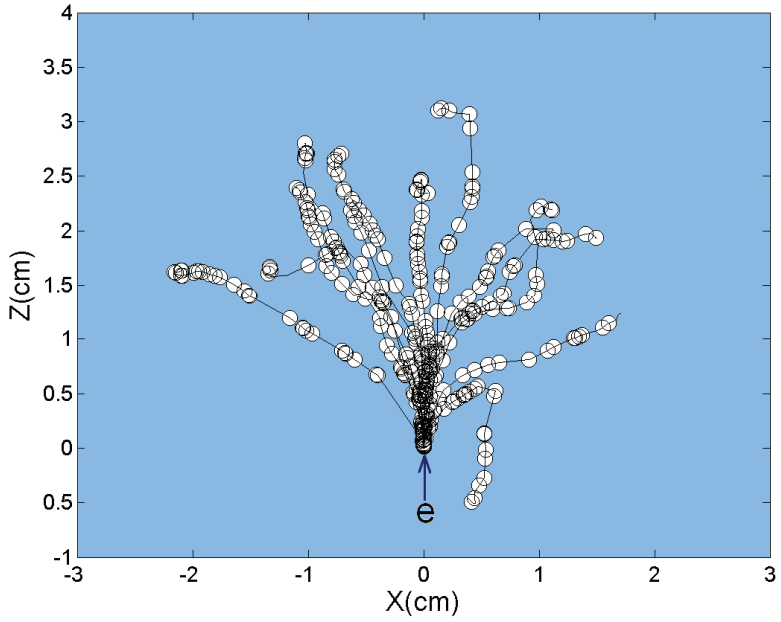

Figure 3.3 Track of 6 MeV electrons in the middle of a water phantom and position of the secondaries (o). The tracks are generated by the EGSnrc code and are saved as pre-calculated data to be used in PMC code.

3.5 Transport of electrons in PMC

3.5.1 Rotation and translation of the tracks

One of the basic mathematical transformations in the PMC code is the translation and rotation of the pre-calculated tracks. The general problem is illustrated in Fig. 3.4. The electron, e, from pre-calculated data is started at position $(x,y,z)=(0,0,0)$ with direction cosine $(u,v,w)=(0,0,1)$ and we want to translate and rotate the track to an arbitrary position and direction of $(x,y,z)=(x_0,y_0,z_0)$ and $(u,v,w)=(u,v,w)$.

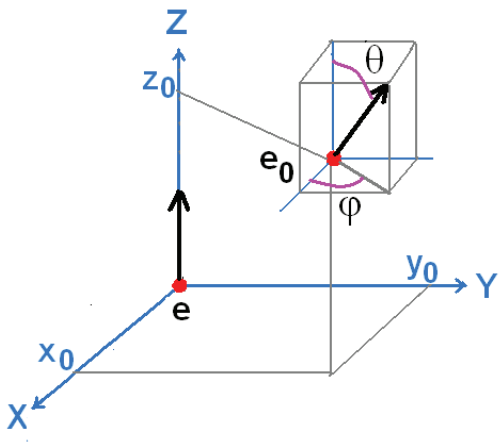

Figure 3.4 The position and direction of the electron in pre-calculated data(e) which should be translated to another incident electron (e_0) located in arbitrary position and direction,

The translation of the track is very simple; however, for rotation of the electron, we have to use Euler Angles and matrix of rotations. The Euler angles are useful to describe rotations or relative orientations of orthogonal coordinate systems. The definition of Euler angles is not unique and in the literature there are many different conventions. The convention employed here is one of the more common ones[25]. Using the Euler angles, a three-dimensional problem can be dissected into a sequence of two-dimensional rotations, whereby in each rotation, one axis remains invariant.

The rotation of an object about the x, y, and z-axes in a clockwise direction when looking towards the origin gives the rotation matrices listed below:

$$R_y(\beta)=\begin{bmatrix}\cos\beta & 0 & -\sin\beta\\ 0 & 1 & 0\\ \sin\beta & 0 & \cos\beta\end{bmatrix} \quad (3.5)$$

$$R_z(\gamma)=\begin{bmatrix}\cos\gamma & \sin\gamma & 0\\ -\sin\gamma & \cos\gamma & 0\\ 0 & 0 & 1\end{bmatrix} \quad (3.6)$$

In the first rotation, we rotate the electron track around Y axis (Fig. 3.5) through the angle θ counterclockwise ($\beta=-\theta$). The second rotation is also counterclockwise around z though the angle φ (γ=−φ).

The entire transformation of the track to the new position and direction is:

$$T=\begin{bmatrix}\cos\varphi & -\sin\varphi & 0\\ \sin\varphi & \cos\varphi & 0\\ 0 & 0 & 1\end{bmatrix}\times\begin{bmatrix}\cos\theta & 0 & \sin\theta\\ 0 & 1 & 0\\ -\sin\theta & 0 & \cos\theta\end{bmatrix}+\begin{bmatrix}x_0 & y_0 & x_0\end{bmatrix} \quad (3.7)$$

Finally the new track of the electron *i.e.* (x',y',z') versus the track of the electron in pre-calculated data (x,y,z) is calculated as:

$$x' = cos(\varphi)cos(\theta)x - sin(\varphi)y + cos(\varphi)sin(\theta)z + x_0 \quad (3.8)$$

$$y' = sin(\varphi)cos(\theta)x + cos(\varphi)\,y + sin(\varphi)sin(\theta)z + y_0 \quad (3.9)$$

$$z' = -sin(\varphi)\,x + cos(\theta)\,z + z_0 \quad (3.10)$$

This transformation applies to the first three columns in Fig. 3.2 and the energy and deposited energy remains unchanged.

3.5.2 Transport of electrons in PMC

As illustrated in Fig. 3.5, the PMC code transports electrons in the following steps: Using the energy of the electron and medium of the first voxel, the related set from pre-generated data is considered and one track is selected from the set. The selected track is

transported and rotated to the position and direction of the incident electron. Then the electron is transported step by step. If the next voxel is not the same (inhomogeneity) according to the energy of the particle at the boundary and material of the next voxel, a new track is picked up from the pre-calculated tracks of the appropriate material and energy. The new track is again translated and rotated to the direction of the current particle. At each step, if the entire step lies in the current voxel, the pre-calculated deposited energy is deposited in the voxel.

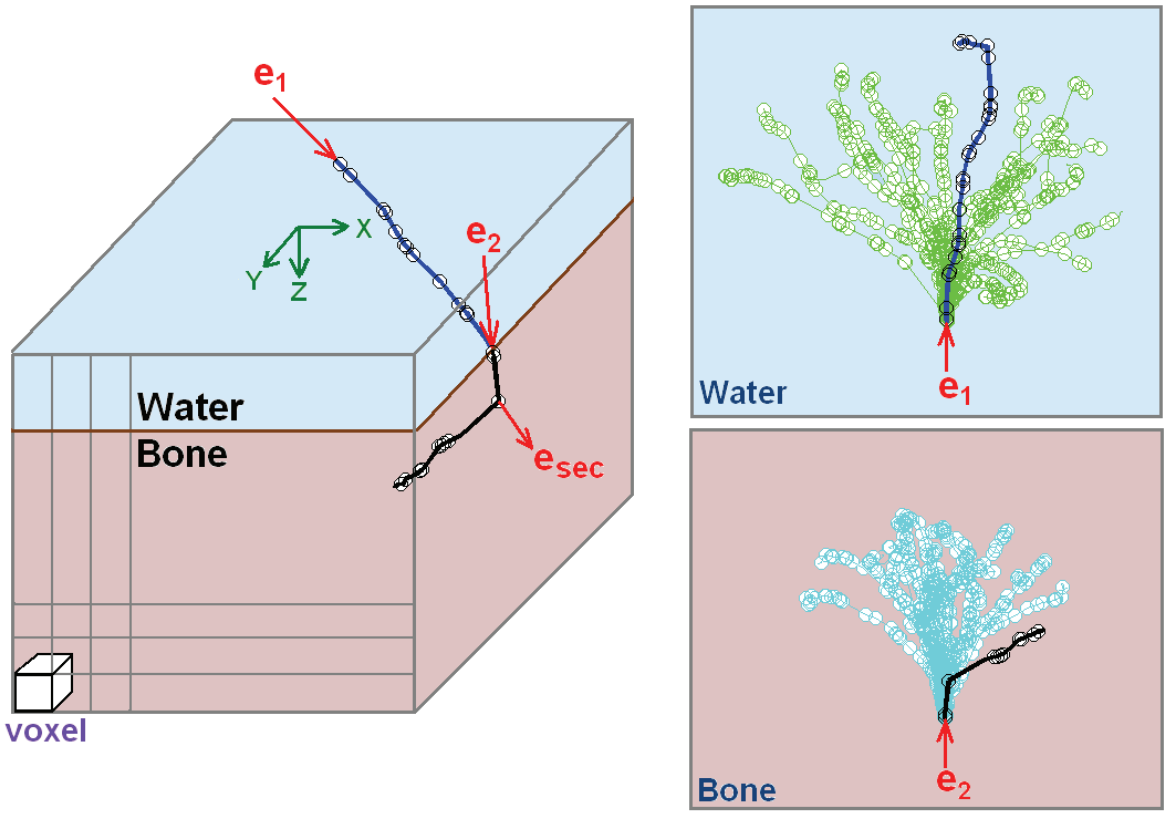

Figure 3.5 Transport of an electron in PMC. The electron starts with initial energy e_1. A track is selected from the related material (water) and rotated and translated to the position and direction of incident electron. Once the electron reaches a new material, a new track is picked up according to energy (e_2) and type of new material (Bone). The energy of secondaries (o) are deposited locally on-the-fly unless the energy (e_{sec}) is greater than ECUT. In this case after transport of the primary, the same process will apply for remaining secondary electrons.

At each step, PMC checks whether a secondary particle is generated using pre-calculated data for secondary particles. If the kinetic energy of secondary electrons is below the PMC cut off energy (100 keV), it is deposited locally on the fly. Otherwise its position, charge, energy and direction are saved on a stack. Once the track of the primary electron is finished, each secondary electron is transported in the same manner as the primary electron.

If the energy of an electron is 6.2 MeV, for example, a track from 6 MeV is picked up and linear scaling is performed to adjust for energy, deposited energy, and track length. For a similar material but with different density, the entire track length is scaled proportionally to the inverse of density. [10,14]

In a particular case, if one has a very large phantom and the track comes to the boundary of the media in the pre-calculated data (i.e., the particle is more than 40 cm away from the initial point) a new track from the same material with a new energy is picked up and the transport continues until the energy falls below ECUT.

Characteristics of all of the secondary particles including photons are saved in the pre-calculated data; however, photons are not transported in the current version of PMC as the goal of this work was to evaluate the speed limits for electron transport. The dose contribution of bremsstrahlung photons produced in tissue equivalent material in the clinical energy range of the electron is small and can be corrected for.[10,14] This assumption is also confirmed in comparison of our results of monoenergetic electrons because with the reference code EGSnrc, the bremsstrahlung photons are transported.

3.5.3 Ray tracing and boundary crossing

Ray tracing and boundary crossing is one of the simpler yet time-consuming tasks in MC calculation.[26-28] An example of the energy deposition in the case of boundary crossing is illustrated in Fig. 3.6. The particle is moving from point 1 to point 3 with a separation of r. The total deposited energy in this step, *edep*, and energy of the particle at points 1 and 3 are available in the pre-calculated data. The particle crosses the boundary of the voxel at point 2 separated by a distance of r_v from point. The energy of $edep \times r_v/r$ is deposited in the voxel and it is subtracted from the total energy of the particle. Assuming the electron is

moving in direction (u,v,w) with initial position (x_1,y_1,z_1), the position of the electron is calculated as:

$$x_2=x_1+u\times r_v \quad (3.11)$$

$$y_2=y_1+v\times r_v \quad (3.12)$$

$$z_2=z_1+w\times r_v \quad (3.13)$$

One can have a more accurate calculation of deposited energy in the voxel versus *edep*, *r* and r_v using stopping power of the material[28-31]; however, linear approximation produces accurate results and it is also used in other fast MC codes such as SMC or VMC.[10,14]

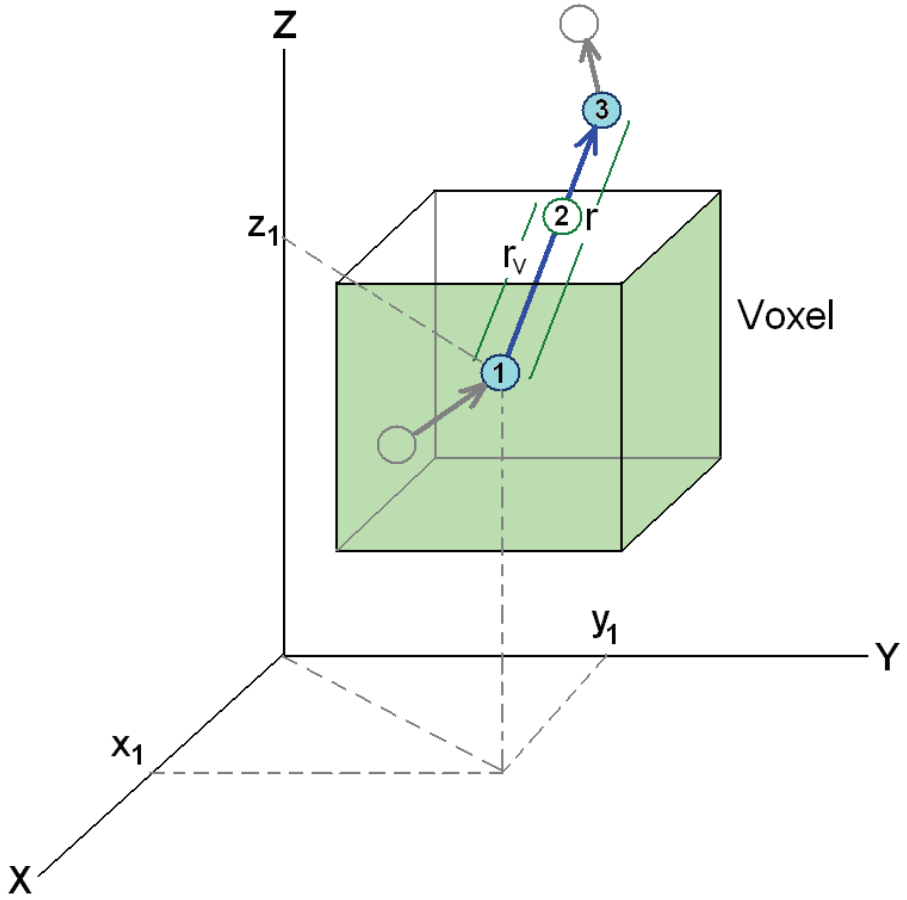

Figure 3.6 Energy deposition in a step length which expands over the boundary of a voxel. The particle is moving from point 1 to 3 in pre-calculated track with total energy deposition *edep*. The deposited energy in the current voxel is $edep\times r_v/r$. The particle is then moved to the boundary of the next voxel, point 2.

3.6 Evaluation of PMC

3.6.1 Statistical uncertainty and efficiency

Results of the MC calculation are subject to statistical uncertainty. In contrast to conventional deterministic dose algorithms, Monte Carlo statistical uncertainty is a new problem for treatment planning and plan evaluation. In a dose distribution calculated by the Monte Carlo method, the dose value in a scoring voxel always contains statistical uncertainty. The smaller the statistical uncertainty, the better the estimation of the Monte Carlo dose value to the expectation value.[32,35]

The usual way to calculate the uncertainty of a quantity during a MC calculation is to divide the simulation to N number of batches and to take the uncertainty estimate for the average of scored quantity, X, as:

$$s_{\overline{X}} = \sqrt{\frac{\sum_{i=1}^{N}\left(X_i - \overline{X}\right)^2}{N(N-1)}} \qquad (3.14)$$

There are some problems with this method: N is usually selected as 10 -20 and there is considerable fluctuation on the uncertainty since N is not very large in Eq.(1). Another problem is that this method ignores any correlation between the tracks of the particles.

In order to eliminate the problem with calculation of the uncertainty with batch method, an alternative approach called 'history by history method' is used. [31,36-38] In this method, the statistical uncertainty in the parameter of interest is calculated using the contribution of each primary history.

In our code the uncertainty in the calculated dose is determined using the history-by-history method where the uncertainty and efficiency of the code is calculated in the following steps:

1-The uncertainty for each voxel is calculated as:

$$\Delta D_j = \sqrt{\frac{1}{N-1}\left(\frac{\sum_{i=1}^{N} D_i^2}{N} - \left(\frac{\sum_{i=1}^{N} D_i}{N}\right)^2\right)} \quad , \qquad (3.15)$$

in which N is the number of histories and D_i is deposited dose due to each history and its secondaries.

2- At the end of the simulation an average uncertainty is calculated for the voxels with the dose more that 50 % of the maximum dose (D_{max}):

$$s^2 = \frac{1}{N_{50}} \sum_{D_j \geq D\max/2} \left(\frac{\Delta D_j}{D_j} \right)^2 . \qquad (3.16)$$

D_j is the average dose of the voxel per history at the end of the simulation, and N_{50} is the number of the voxels with dose greater that 50% maximum dose, D_{max}.

3- The efficiency is defined as:

$$\varepsilon = \frac{1}{s^2 T}, \qquad (3.17)$$

where T is the CPU time. This definition of the efficiency is reviewed by Rogers and Mohan[37] and an efficient way for calculation of D_i and D_i^2 for each history is discussed by Walters *et al.*[36] Using the above algorithm, the problems associated with the batch method are removed. In the alternative method, N is a large number (number of histories) and any possible track correlation is taken into account.

Track repetition in any MC code is subject to track correlation and reduction of efficiency up to a certain limit.[39] In a small field size, repetition of 5000 particles for 200 times produces a large statistical uncertainty than 1 million independent histories. The efficiency of the code starts to decrease after a certain number of repetitions that that depends on energy and field size. This is because the uncertainty approaches an lower limit while the time still increases in Eq. (3.17). The effect of the track repetition on statistical uncertainty is discussed in Section 4.5.

3.6.2 Reference code and programming language

The results obtained with the PMC code have been compared with DOSXYZnrc user code in its default settings which uses the EGS4/PRESTA-I boundary crossing algorithm[40]. The code requires one input file to be generated by the user, giving a complete description of the phantom and the source. The input file could also be an imported CT

based phantom.[41-47] Using the DOSXYZnrc GUI, it is very convenient for users to design and simulate various voxel based geometries and input files.

DOSXYZnrc after each run produces an `output.3ddose` file which contains the input information and the deposited dose for all the voxels of the phantom as well as the related uncertainties. The uncertainty in DOSXYZnrc is also calculated using a history by history technique. The code writes the results of the dose for a 3D phantom in a 1 dimensional sequence of numbers. For example, for a phantom containing 20×20×20 voxels, the output file contains 8000 numbers related to dose of each voxel, and 8000 numbers related to the uncertainty on the dose of each voxel (These numbers follow the header and other values related to geometry). An in-house series of MATLAB and Fortran codes is developed which reads the `output.3ddose` file, and extracts and plots various information such as Percentage Depth Dose (PDD) and isodose curves.

The voxel size is user-defined in PMC and is set at 0.3^3 cm^3 for all of the benchmarks in this work and the phantom dimensions varies between 20-100 cm. The PMC code is written in Fortran 90 and has also been tested in other programming languages and softwares such as MATLAB (The MathWorks, Inc., MA), C++ with MATLAB library and Fortran 77. The reason that the code was also tested in MATLAB was the great capability of MATLAB in image processing and other toolboxes which are used in various fields of medical physics.[48-52] Many different techniques are implemented to improve the efficiency of the code. The advantages and restrictions of each method are discussed in Chapter 4.

3.6.3 Test with water as inhomogeneity

A major challenge for all fast Monte Carlo codes is the transport of the particles near inhomogeneities and interfaces where most of the discrepancies occur. Two different kinds of errors can occur at the interface of two materials. The first type is the intrinsic errors due to particular approximations of each code in transport of the particle which remains the same in the homogenous case. For example, in MMC the angle of exited electron from each sphere is approximated in a number of bins which produces error in transport of the electron in a homogeneous phantom.

A second type of error is associated with the proper handling of the track in the new material as inhomogeneity. As mentioned before, most of the Fast MC codes do not stop the particles at the boundary of the voxel near heterogeneities (as is the case in EGSnrc), but they only interpolate and modify the track of the particle. To investigate the errors of the second type, we introduce a phantom with an inhomogeneity of the same material. In electron transport, when the particle reaches the inhomogeneity, the track is truncated and a new in-water track is picked up. If there were no artifacts introduced by track storage, pick-up and energy scaling procedures, the code should yield accurate dose distributions in the homogeneous medium. This test is also very useful in debugging the code in its early stages.

References

1. W. R. Nelson, H. Hirayama, and D. W. O. Rogers, "The EGS4 Code System," SLAC Report No. SLAC-265, 1985.
2. S. Agostinelli *et al*., "GEANT4—A simulation toolkit," Nucl. Instrum. Methods Phys. Res. A 506, 250–303 (2003).
3. I. Kawrakow and D. W. O. Rogers, "The EGSnrc code system: Monte Carlo simulation of electron and photon transport," NRC, Report PIRS–701, 2000.
4. J. F. Briesmeister, "MCNP-A general Monte Carlo N-particle transport code, Version 4C," Report LA-13709-M, Los Alamos National Laboratory, NM, 2000.
5. I. Chetty *et al*., "Guidance report on clinical implementation of the Monte Carlo method in external beam radiation therapy treatment planning: Report of the AAPM Task Group No. 105," Med. Phys. **34**, 4818–4853 (2007).
6. F. Verhaegen and J. Seuntjens, "Monte Carlo modelling of external radiotherapy photon beams," Phys. Med. Biol. **48**, R107–R164 (2003).
7. O. Chibani and X. A. Li, "Monte Carlo dose calculations in homogeneous media and at interfaces: A comparison between GEPTS, EGSnrc, MCNP, and measurements," Med. Phys. **29**, 835–847 (2002).
8. I. Kawrakow, "Accurate condensed history Monte Carlo simulation of electron transport. I. EGSnrc, the new EGS4 version," Med. Phys. **27**, 485–498 (2000).

9. E. Poon and F. Verhaegen, "Accuracy of the photon and electron physics in GEANT4 for radiotherapy applications," Med. Phys. **32**, 1696–1711 (2005).

10. I. Kawrakow, M. Fippel, and K. Friedrich, "3D Electron Dose Calculation using a Voxel based Monte Carlo Algorithm," Med. Phys. **23**, 445–457 (1996).

11. J. Sempau, S. J. Wilderman, and A. F. Bielajew, "DPM, a fast, accurate Monte Carlo code optimized for photon and electron radiotherapy treatment planning dose calculations," Phys. Med. Biol. **45**, 2263–2291 (2000).

12. C. Ma, J. S. Li, T. Pawlicki, S. B. Jiang, J. Deng, M. C. Lee, T. Koumrian, M. Luxton, and S. Brain, "MCDOSE - A Monte Carlo dose calculation tool for radiation therapy treatment planning," Phys. Med. Biol. **47**, 1671–1689 (2002).

13. H. Neuenschwander, T. R. Mackie, and P. J. Reckwerdt, "MMC— A high-performance Monte Carlo code for electron beam treatment planning," Phys. Med. Biol. **40**, 543–574 (1995).

14. P. J. Keall and P. W. Hoban, "Super-Monte Carlo: a 3D electron beam dose calculation algorithm," Med. Phys. **23**, 2023–2034 (1996).

15. P. J. Keall and P. W. Hoban, "Superposition dose calculation incorporating Monte Carlo generated electron track kernels," Med. Phys. **23**, 479–485 (1996).

16. J. Borg, I. Kawrakow, D. W. O. Rogers, and J. P. Seuntjens, ''Monte Carlo study of correction factors for Spencer–Attix cavity theory at photon energies at or above 100 keV,'' Med. Phys. **27**, 1804–1813 (2000).

17. F. Verhaegen, "Evaluation of the EGSnrc Monte Carlo code for interface dosimetry near high-Z media exposed to kilovolt and 60Co photons," Phys. Med. Biol. **47**, 1691–1705 (2002).

18. M. Fragoso, F. Verhaegen, and A. Nahum, "A comparison of Monte Carlo (EGSnrc, PENELOPE) and commercial treatment planning system (PLATO) calculations of the dose distribution delivered by low dose-rate 137Cs sources in intracavitary brachytherapy," Med. Phys. (abstract) **29**, 1350 (2002).

19. I. Kawrakow and D. W. O. Rogers, "The EGSnrc code system: Monte Carlo simulation of electron and photon transport," NRC, Report PIRS–701, 2000.

20. A. F. Bielajew, ‘‘HOWFAR and HOWNEAR: geometry modelling for Monte Carlo particle transport,’’ Technical Report PIRS-0341, National Research Council of Canada, Ottawa, 1995. (http://www.slac.stanford.edu/egs/docs/pdf/nrc-pirs0341.pdf.)
21. W. Huda, S. C. Bushong, and W. R. Hendee, “In x-ray computed tomography, technique factors should be selected appropriate to patient size,” Med. Phys. **28**, 1543 (2001).
22. E. Poon, J. P. Seuntjens, and F. Verhaegen, “Consistency test of the electron transport algorithm in the GEANT4 Monte Carlo code,” Phys. Med. Biol. **50**, 681–694 (2005).
23. I. Kawrakow and A. F. Bielajew, “On the condensed history technique for electron transport,” Nucl. Instrum. Methods Phys. Res. B 142, 253–280 (1998).
24. I. Kawrakow, “Accurate condensed history Monte Carlo simulation of electron transport. I. EGSnrc, the new EGS4 version,” Med. Phys. **27**, 485–498 (2000).
25. http://mathworld.wolfram.com/RotationMatrix.html
26. I. Kawrakow and B. R. B. Walters, “Technical note: Overprediction of dose with default PRESTA-I boundary crossing in DOSXYZnrc and BEAMnrc,” Med. Phys. **34**, 547–650 (2007).
27. R. L. Siddon, “Prism representation: a 3D ray-tracing algorithm for radiotherapy applications,” Phys. Med. Biol. **30**, 817–24 (1985).
28. B. R. B. Walters and I. Kawrakow ”A “HOWFARLESS” option to increase efficiency of homogeneous phantom calculations with DOSXYZnrc ,” Med. Phys. **34**, 3794-3807 (2007).
29. R. Mohan, C. Chui, and L. Lidofsky, “Energy and angular distributions of photons from medical linear accelerators,” Med. Phys. **12**, 592–597 (1985).
30. I. Kawrakow and B. R. B. Walters, “Efficient photon beam dose calculations using DOSXYZnrc with BEAMnrc,” Med. Phys. **33**, 3046–3056 (2006).
31. J. Baro, J. Sempau, J. M. Fernandez-Varea, and F. Salvat, “PENELOPE: an algorithm for Monte Carlo simulation of the penetration and energy loss of electrons and positrons in matter,” Nucl. Instrum. Methods Phys. Res. B 100, 31–46 (1995).
32. W. Feller, *An Introduction to Probability Theory and Its Applications*, 3rd ed.)Wiley, New York, 1967), Vol. I.

33. C.-M. Ma, B. A. Faddegon, D. W. O. Rogers, and T. R. Mackie, "Accurate characterization of Monte Carlo calculated electron beams for radiotherapy," Med. Phys. **24**, 401–416 (1997). 1

34. J. Sempau and A. F. Bielajew, "Towards the elimination of Monte Carlo statistical fluctuation from dose volume histograms for radiotherapy treatment planning," Phys. Med. Biol. **45**, 131–157 (2000).

35. P. J. Keall, J. V. Siebers, R. Jeraj, and R. Mohan, "The effect of dose calculation uncertainty on the evaluation of radiotherapy plans," Med. Phys. **27**, 478–484 (2000).

36. B. R. B. Walters, I. Kawrakow, and D. W. O. Rogers, "History by history statistical estimators in the BEAM code system," Med. Phys. **29**, 2745–2752 (2002).

37. D. W. O. Rogers and R. Mohan, "Questions for comparison of clinical Monte Carlo codes," *The Use of Computers in Radiotherapy, XIIIth Int'l Co*, e *nf., Heidelberg*dited by W. Schlegel and T. Bortfeld (Springer-Verlag, Heidelberg, 2000), pp. 120–122.

38. P. Andreo, "Monte Carlo techniques in medical radiation physics," Phys. Med. Biol. **36**, 861–920 (1991).

39. I. Kawrakow, "VMC++, electron and photon Monte Carlo calculations optimized for Radiation Treatment Planning," *Advanced Monte Carlo for Radiation Physics, Particle Transport Simulation and Applications: Proceedings of the Monte Carlo 2000 Meeting Lisbon*, edited by A. Kling, F. Barao, M. Nakagawa, L. Távora, and P. Vaz (Springer, Berlin, 2001), pp. 229–236.

40. B. R. B. Walters and D. W. O. Rogers, "DOSXYZnrc Users Manual," NRC Report PIRS 794 (rev B), 2004.

41. E. K. Osei, J. Darko, A. Mosseri, and J. Jezioranski, "EGSNRC Monte Carlo study of the effect of photon energy and field margin in phantoms simulating small lung lesions," Med. Phys. **30**, 2706–2714 (2003).

42. G. X. Ding, D. M. Duggan, and C. W. Coffey, "A theoretical approach for non-equilibrium radiation dosimetry." Phys. Med. Biol. **53**, 3493–3499 (2008).

43. J. C. Chow, M. K. Leung, M. K. Islam, B. D. Norrlinger, and D. A. Jaffray, "Evaluation of the effect of patient dose from cone beam computed tomography on prostate IMRT using Monte Carlo simulation," Med. Phys. **35**, 52–60 (2008).

44. F. Araki, " Monte Carlo study of a Cyberknife stereotactic radiosurgery system," Med. Phys. **33**,2955–2963 (2006).

45. S. H. Cho, O. N. Vassiliev, S. Lee, H. H. Liu, G. S. Ibbott, and R. Mohan, "Reference photon dosimetry data and reference phase space data for the 6 MV photon beam from varian clinac 2100 series linear accelerators," Med. Phys. **32**, 137–148 (2005).

46. F. Crop, N. Reynaert, G. Pittomvils, L. Paelinck, W. De Gersem, C. De Wagter, L. Vakaet, W. De Neve, and H. Thierens, "Monte Carlo modeling of the ModuLeaf miniature MLC for small field dosimetry and quality assurance of the clinical treatment planning system," Phys. Med. Biol. **52**, 3275–3290 (2007).

47. A. Fogliata, E. Vanetti, D. Albers, C. Brink, A. Clivio, T. Knöös, G. Nicolini, and L. Cozzi, "On the dosimetric behaviour of photon dose calculation algorithms in the presence of simple geometric heterogeneities: comparison with Monte Carlo calculations." Phys. Med. Biol. **52**, 1363–1385 (2007).

48. K. Jabbari and S. Pistorius, "A novel method for automatic detection of patient out-of-plane rotation by comparing a single portal image to a reference image," Med. Phys. **32**, 3678–3687 (2005).

49. M. Todorovic, M. Fischer, F. Cremers, E. Thom, and R. Schmidt, "Evaluation of GafChromic EBT prototype B for external beam dose verification," Med. Phys. **33**, 1321 (2006).

50. I. M. Gagné and D. M. Robinson, "The impact of tumor motion upon CT image integrity and target delineation" Med. Phys. **31**, 3378 (2004).

51. S. Lee, G. Fichtinger, and G. S. Chirikjian, "Numerical algorithms for spatial registration of line fiducials from cross-sectional images," Med. Phys. **29**, 1881 (2002).

52. J. Seco, G. C. Sharp, J. Turcotte, D. Gierga, T. Bortfeld, and H. Paganetti ,"Effects of organ motion on IMRT treatments with segments of few monitor units," Med. Phys. **34**, 923 (2007).

Chapter 4

Results and discussion of PMC code for electron transport.

4.1 Input for PMC and processing of the results

A 3D matrix of real numbers is allocated for the phantom and the elements of the matrix are related to density of each material. Two other matrices with identical sizes are allocated for deposited dose and related uncertainty for deposited dose in each voxel of the phantom. The size of the matrices are calculated according to the user's input for size of the phantom and voxel. The shape of the voxel should be rectangular and the size of the voxels in PMC code can vary in each direction. For each run in PMC, the energy of the electron and the energy cut-offs are determined by the user.

Process of pre-calculated data generation is done just once in which the output file of Tutor4/EGSnrc[1] is converted to a file used as an input for PMC code. The output of EGSnrc user code for the pre-calculated data is in the form of an ASCII file (the file often has a very large size). This file (exported from Unix machine to Windows) is converted to an unformatted file. Subsequently, using a Fortran code, the 2 dimensional matrixes containing tracks of the electrons are constructed in the format discussed in Chapter 3. The resulting file is readable by PMC which is loaded in the computer before simulation.

In PMC code, the output file contains two arrays of real numbers representing the dose and dose uncertainty. The arrays are real numbers with real or double precision upon the user's choice. The results of the PMC code are read and interpolated automatically by an in-house MATLAB code. As mentioned in Chapter 3, the results of the reference code (DOSXYZnrc[2]) are also converted to a MATLAB and file final comparison of dose and isodoses are done using MATLAB.

4.2 Results for homogeneous phantoms and different materials

PDD (percentage depth dose) calculations using the PMC code for monoenergetic electrons in water are illustrated in Fig. 4.1. The graph shows the PDD for 4, 9, 12 MeV electrons in comparison with EGSnrc (implemented in DOSXYZnrc) results. The PDDs are related to the dose at the central axis and the discrepancy is generally between 1-2 % of the PDD with maximum of 3%. The electrons are incident on a 4×4 cm^2 field normal to the surface and the size of the phantom is 70×70×56 cm^3. The size of the voxel is 0.3 cm in each direction and the uncertainty of the dose in each voxel is up to 1.5 %.

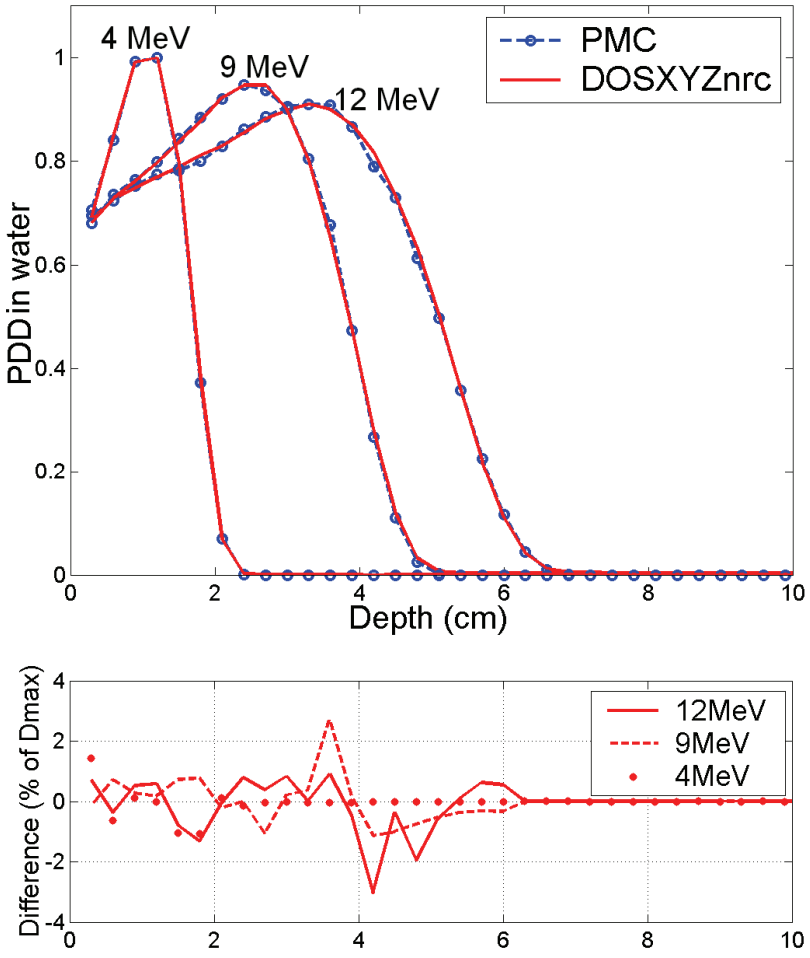

Figure 4.1 Relative PDD of 4, 9 and 12 MeV electrons incident perpendicular on a 4×4 cm^2 field in water. The differences are scaled with respect to the maximum dose for each energy.

The results of PMC for mono-energetic electrons in materials different from water are illustrated in Fig. 4.2. The figure illustrates the PDD of the central axis for homogeneous bone and lung phantom as well as the water. The field size is 4×4 cm^2 and the energy of the electron beam is 6 MeV and incidents normal to the surface. There is generally very good agreement between PMC and EGSnrc and the error is less than 1% for bone and less than 2% for lung and water. The statistical uncertainties of all calculations are in the order of 1.5 %. The same energy and materials also were simulated for broad beam (10×10 cm^2) and the same order of discrepancies and uncertainties were observed.

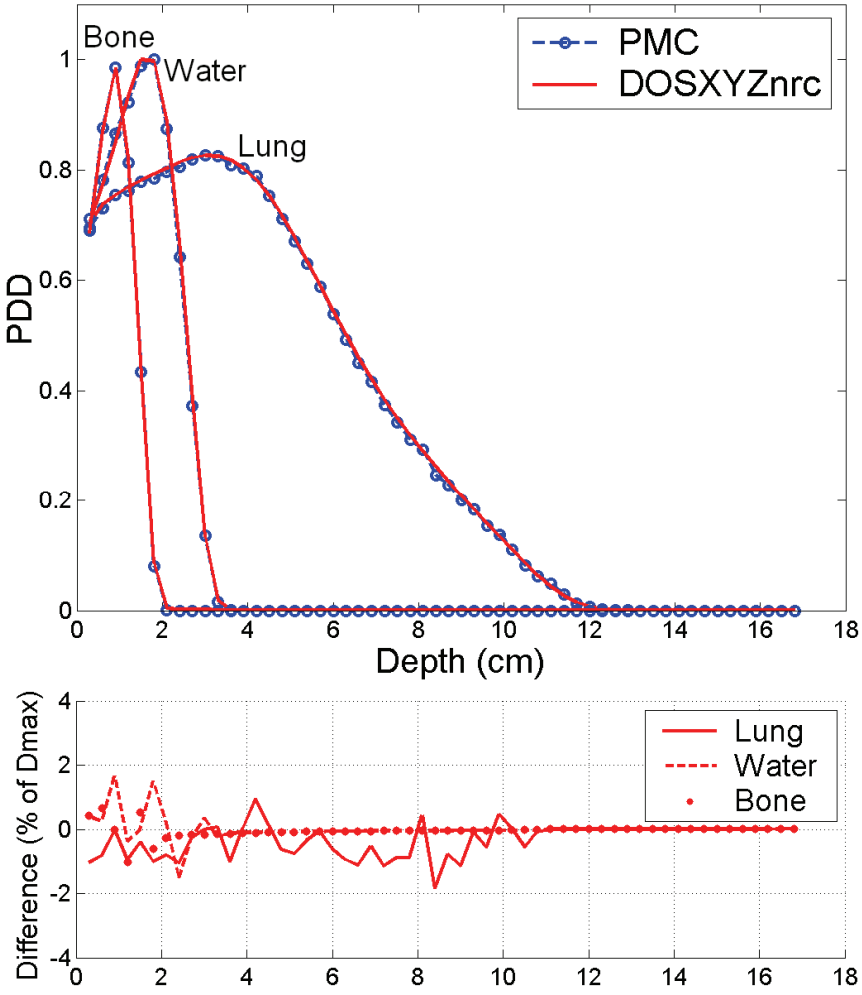

Figure 4.2 Results of relative PDD for various materials with 6 MeV incident electron along the central axis. The field size is 4×4 cm^2 and the results illustrate the PDD for central axis.

4.3 Comparisons of PMC and DOSXYZnrc in heterogeneous phantoms

The PMC code has been tested in various heterogeneous cases. One of the basic examples of heterogeneities is illustrated in Fig. 4.3. In this example the water phantom has a slab of lung at a depth of 1.8 cm and the energy of incident electrons are 6 MeV. The electron beam is incident perpendicular to the surface of the phantom with a 10×10 cm^2 field size. Isodose curves and PDD results are generally in excellent agreement. The discrepancy between PMC results and EGSnrc (implemented in DOSXYZnrc) for PDD can be up to 1%.

An example of 3D isodose surface of the PMC results is also illustrated in Fig. 4.3(a). As mentioned before, these isodose surfaces are generated using image processing toolbox of MATLAB. An important point in this example is that the tracks of all electrons are truncated in water-lung and lung-water interfaces and for each electron a new track from the new material is selected. As illustrated in Fig. 4.3.b the expansion of isodose curves because of a low density material (lung, ρ= 0.26 g/cm^3) is handled very accurately.

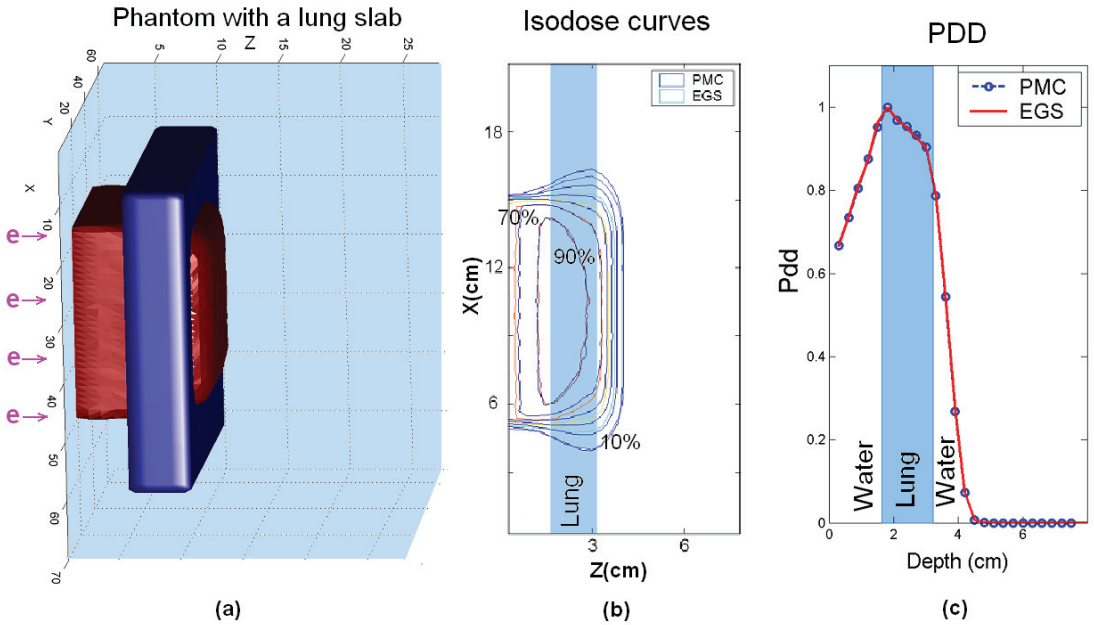

Figure 4.3 Results of PMC code for transport of 6MeV electrons from 10×10 cm^2 field size. (a): The 3D illustration of phantom in which a slab of lung is embedded. The 50% isodose surface of PMC is also illustrated. (b) and (c): Comparison of isodose curves and PDD of the central axis with EGS.

Figure 4.4 illustrates an example of a calculated central axis PDD and an isodose curve in a phantom with water, lung and bone with 6 MeV electrons incident on the surface of the water. This phantom contains both parallel and perpendicular interfaces with the incident beam as well as higher to lower density interface and vice-versa. The incident electron on the surface of the phantom is perpendicular and monoenergetic, however at the interfaces, a phase-space of electrons with various energies enters into the new material. The linear interpolation between the finite energy sets that we have in the pre-calculated data is done for almost all of the electrons in the interfaces and accuracy of the results show the adequacy of the selected energy bins (for example 1MeV step from 1-18MeV) as well as the linear interpolation scheme between them as discussed in Section 3.5.2. The comparison of isodose and PDDs are illustrated and the agreement is better than 1.6%. The isodose of the hot spots are handled very accurately in Fig. 4.4.a.

Another example of PDD and isodose curves for the same phantom but smaller field size is illustrated in Fig. 4.5. The field size of the electrons in this case is 4×4 cm^2. The same order of differences (up to 2 %) is observed for the small field size.

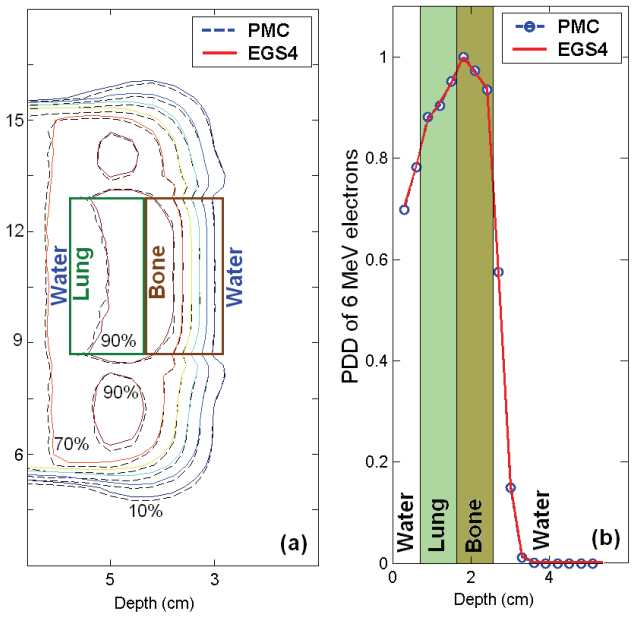

Figure 4.4 Isodose (a) curves and PDD of central axis (b) for 6 MeV electrons in heterogeneous phantom,10×10cm^2 field. The lung and bone slabs are placed in the middle of the electron field.

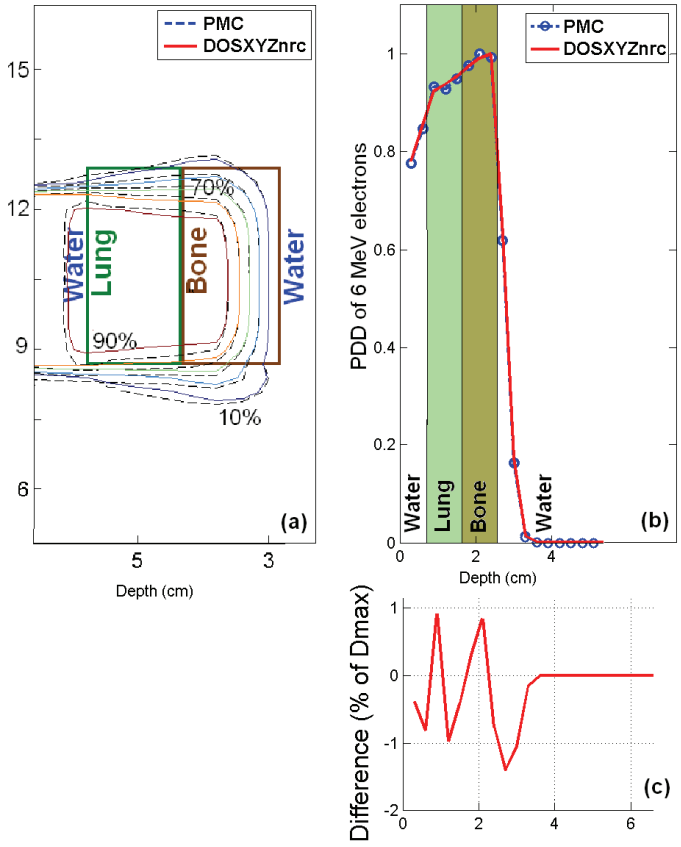

Figure 4.5 Water-Lung-bone phantom for small field size. The energy of electron beam is 6 MeV and the field size is 4×4cm^2. Figure (b) and (c) illustrate the PDD of the central axis and the differences.

4.4 Test with water as inhomogeneity

As discussed in Section 3.6.3, the purpose of this test is to illustrate the possible errors or limitations of the code in transport of the particle near heterogeneities. The phantom in this test is homogeneous; however, the code treats the transfer to the adjacent material as heterogeneity (e.g., a slab). The results of this setup should be identical to those of a homogeneous phantom.

In this section the tests were performed using a water phantom with the same material treated as an inhomogeneity located after the second voxel. The code truncates the track of the electrons once they reach the surface of the third voxel. Then according to the energy of the electron at that point, a new track is picked up from the pre-generated set in water. The result of this test is illustrated in Fig. 4.6. The PDDs are a comparison of PMC

with pre-generated tracks using two different step control parameter values, XIMAX=0.5 (EGSnrc default) and XIMAX=0.02. The energy of the electron beam is 12 MeV, the field size is 10×10 cm^2 and PDDs are related to central axis. The reference code for this test is DOSXYZnrc (EGSnrc) for simulation of a 'homogeneous ' water phantom with the same electron beam energy and setup as described above. The graph (Fig. 4.6) shows the improvement of the results for smaller pre-calculated step sizes as the average error for XIMAX=0.5 and 0.02 is 6.1% and 1% respectively. This discrepancy does not show up in a standard PDD of homogeneous water in which the track of electrons are not truncated. In homogeneous water for both XIMAX's the average errors are below 1%.

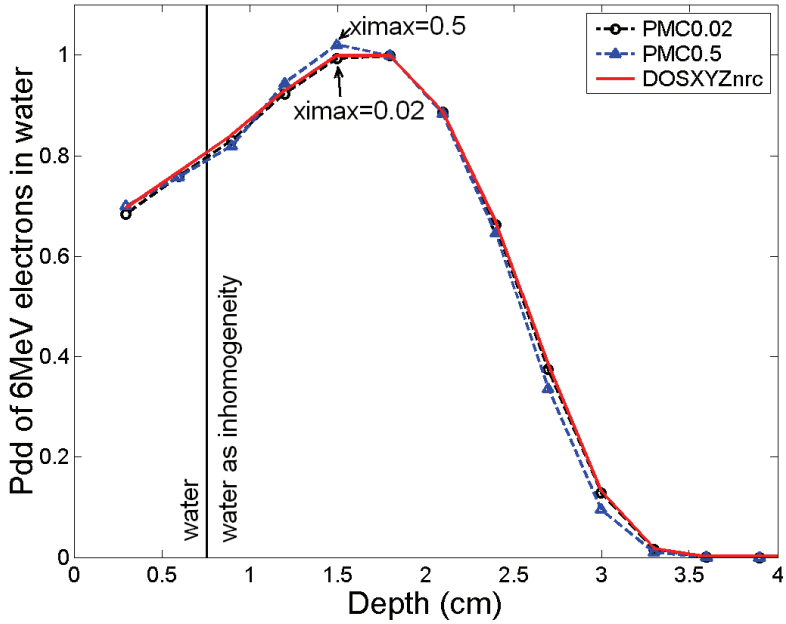

Figure 4.6 PDD of 6 MeV electrons in water phantom with inhomogeneity as water. The tracks of the electrons after the second voxel are replaced by new tracks in water. The results compares PDD of DOSXYZnrc and PMC with two different set of the pre-calculated data with XIMAX=0.5 (long steps) and 0.02 (very small steps).

4.5 Effect of track repetition on efficiency

The PMC code in the current version is based on the 5000 particle tracks for each energy and the track of the particles are repeated for various positions of the electron with the same energy. Repetition of tracks very close to each other causes a correlation of the tracks[3-5] and a reduction in the efficiency of the code and limits the uncertainty of code. In

this section the effect of track repetition on uncertainty for a small field size of 4×4 cm^2 and 6 MeV monoenergetic electron beam is illustrated.

Figure 4.7 shows the efficiency of the code versus the number of repetitions. The efficiency reaches a maximum value and then decreases after 400 repetitions. This is the point after which the statistical uncertainty approaches a lower limit (close to 1.3%) and with larger number of histories the time increases without any improvement in uncertainty. This limit is for mono-energetic electrons. The uncertainty will be improved for a typical phase-space source since the energy varies and for each energy (between the energy grids discussed in section 3.4.2) there are 5000 independent histories. If a lower uncertainty is desired, the pre-calculated data sets have to be extended to hold larger number of particles, e.g., 10000 particles instead of 5000 for each energy. The total number of particles for each energy is limited by the size of the available RAM on the computer.

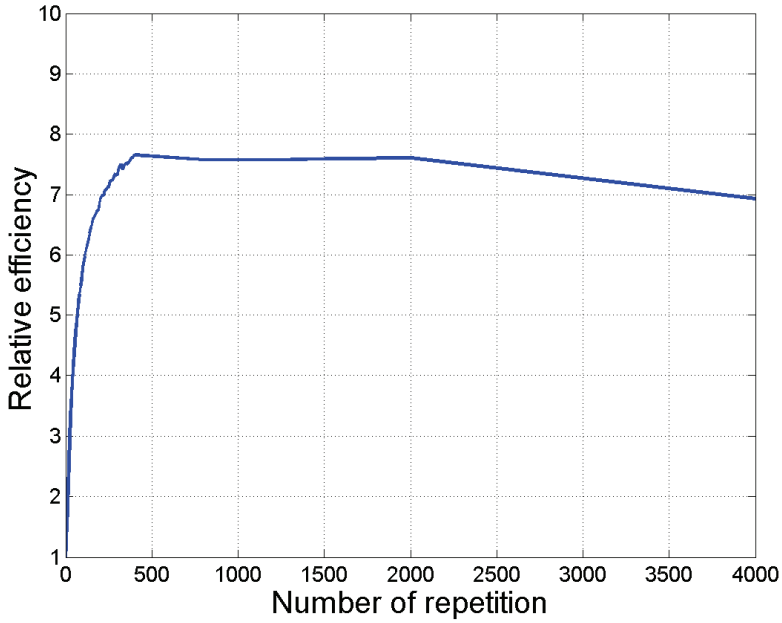

Figure 4.7 Relative efficiency of the PMC for 6 MeV electrons in 4×4 cm^2 field size.

4.6 Discussion of PMC results for electron transport

In the early version of fast Monte Carlo codes based on pre-calculated tracks such as SMC[6,7] the electron track was generated in water and then modified for other materials. This was because of restrictions on available computer RAM (in the order of 100 Mb) a decade ago. For accurate results, one has to also make a correction for lateral deflection of

the track in the new material, which again needs a table look up as well as some approximations. PMC avoids all of these calculations and approximations by picking up a new track for the material at the expense of larger pre-calculated data for each material but with the benefit of improved speed and accuracy. The track of the particle is saved in Cartesian coordinates (*x*,*y*,*z*) and modification for a change in density within the same material (*i.e.,* scaling of the entire track proportional to the density) is done in the same way as the other codes[5,6].

The size of the pre-calculated data for each material is in the order of 300-400 Mb which is reasonable for current day desktop computers with 4-8 Gb RAM. One can use more than 5000 particles for each set of pre-generated data as long as there is enough RAM. This improves the intrinsic uncertainty of the code. The PMC transports 10^6 particles in times on the order of 1 min which is about 40 times faster than EGSnrc producing the same uncertainty on the same computer. Since execution of the code consists of picking up tracks from a database for both primary and secondary particles, no random numbers are involved in code execution.

The accuracy of the results near the boundary of the heterogeneities illustrates the efficiency of the energy interpolation in this work. However, in case of large artifacts, one can use smaller energy bins, e.g., 0.5 MeV instead of 1 MeV for generation of pre-calculated data. There is also another approach for energy interpolation which is used in particle track-repeating method by Ma *et al*.[40] In this approach, for a particle of 5.6 MeV, a track with closest higher energy neighbor is picked up (*i.e*., 6 MeV) and, within this track, one moves down in energy until a step with an energy closest to 5.6 MeV is reached. That step is interpolated to reach the 5.6 MeV point and the rest of the track is picked up for transport of the particle.

4.7 Time profile of fast Monte Carlo code

The time profile of the PMC code representing the time that is spent in various sections of the MC code is illustrated in Fig. 4.8. Percentage of the total time is illustrated for three major tasks in PMC: picking up a track form pre-generated tracks (16%); rotation and translation of the track (26%); and ray tracing (56%). More than 50% of the total time is spent in voxel-by-voxel ray tracing. Therefore, even if no time was to be spent for

generation, rotation, translation of the track, the speed up factor would not go above about 100. A similar conclusion was made for VMC++ in which, using STOPS technique, 90 % of the time is spent on ray tracing, and the relative speed compared to EGSnrc is about 50.[3]

Another important point is the relatively large fraction of the time (16%) spent on picking up a track from large pre-calculated set of tracks. This is one of the reasons that a fast Monte Carlo code using pre-generated data such as PMC and SMC is not much faster than DPM and VMC/VMC++. In VMC, a track is generated with an efficient transport algorithm at a speed exceeding the time needed to pickup a track from a stored set such as is the case for PMC and SMC.

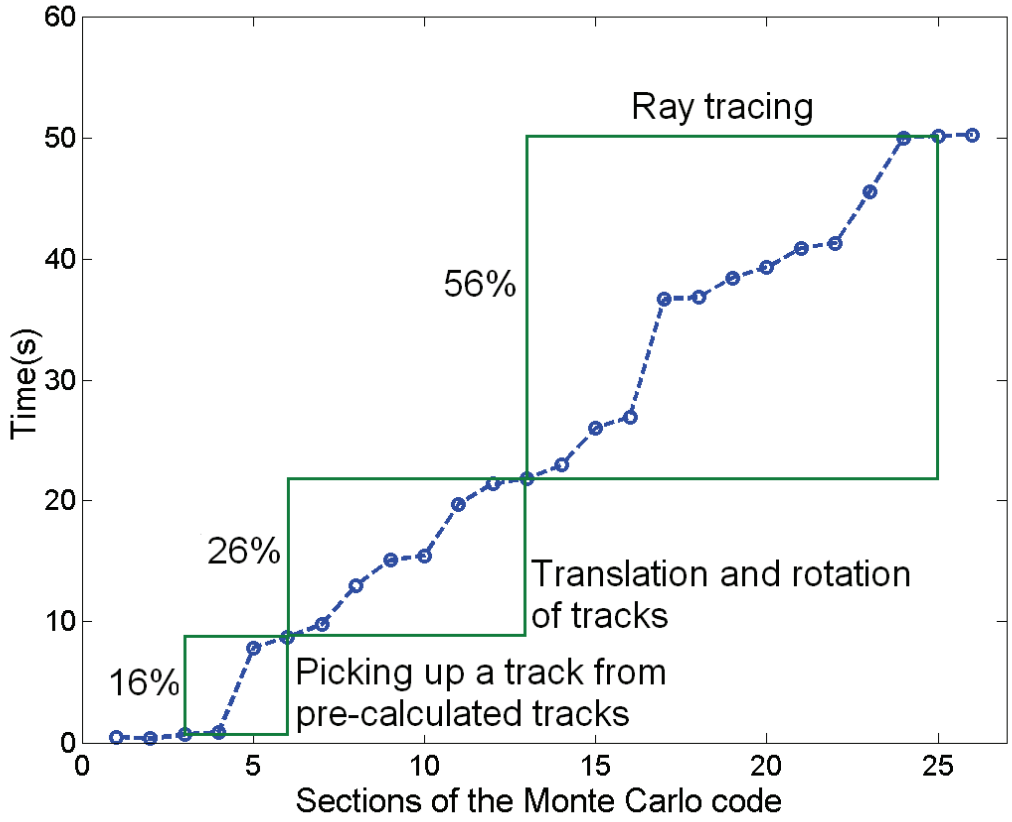

Figure 4.8 Time profile of fast Monte Carlo code for 1 million electrons. Percentage of total time that is consumed in each task is illustrated.

4.8 Importance of electron step size

One of the most important parameters which affects the result of any Monte Carlo code is the electron step size.[9,10] Choosing an optimal maximum step size is a necessary task in either a general propose[11-14] or a fast Monte Carlo[7] code. Long step sizes may produce artifacts near boundaries with heterogeneities, and very short step sizes are time consuming and inefficient. In EGSnrc, the condensed history step in a homogeneous medium is controlled by step control parameters such as ESTEPE, XIMAX, SMAX, etc. As it is mentioned in the EGSnrc manual[1] modifying XIMAX to control the condensed history step is the most appropriate method since the difference of elastic scattering in various media automatically is taken into account. The step size cannot be changed in the pre-calculated data because once the tracks are generated and saved by EGSnrc, the electron steps remain constant for all geometries, and as a result an optimization is needed for the choice of electron step sizes in EGSnrc.

To evaluate the effect of a change in XIMAX, the entire pre-calculated tracks were generated with four different XIMAX values: 0.5 (EGSnrc default), 0.1, 0.05 and 0.02. PMC was then run in our particular phantom with water as inhomogeneity as described in Section 3.6.3. The size of the voxel was 3 mm in each dimension as mentioned before. The average error as benchmarked against EGSnrc, running times, and size of the pre-calculated data for water are illustrated in Fig. 4.9.

The average error is calculated as an average over the voxels with more than 50% of the maximum dose in comparison with the dose calculated with EGSnrc. The time is calculated in μs per history on a 1.3 GHz Pentium for 1 million 6 MeV electrons in water. A large error is observed for XIMAX= 0.5 and while the error is smaller for 0.02, but the calculation time increases significantly. Although the size of the error is smaller for XIMAX=0.02, the size of the pre-calculated data is very large and this is not an optimized value. The choice of 0.05 or 0.1 for XIMAX is reasonable in terms of time and error and total size of the pre-calculated data. As one compares the time and size of the data in Fig. 4.9, there is an almost linear relationship between the size of the pre-calculated data and the CPU time.

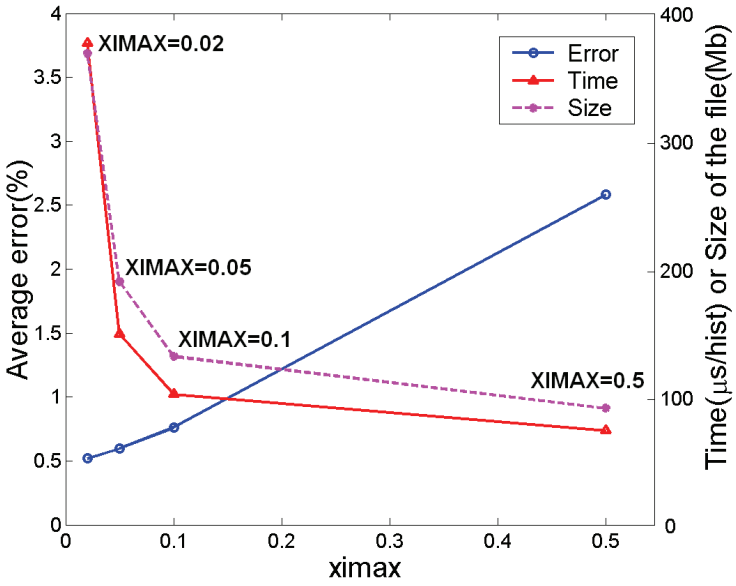

Figure 4.9 Time, size of the data and average error in PMC with various XIMAXs in pre-regenerated electron tracks. The average relative error is over the voxels with the dose of 50% more of maximum dose compared to EGS. The size of the file corresponds to the entire set of pre-calculated data for water.

Figure 4.9 illustrated the magnitude of errors as a function of step size. The reason for larger error associated with larger step size is related to electron transport algorithm in EGSnrc.[15] As mentioned before, a class-II condensed-history[16-18] implementation of Monte Carlo transport dictates that the electron track can be subdivided in straight line segments between hard collisions leading to either secondary electrons or bremsstrahlung.[9] Energy loss over the linear segments is through soft collisions. For accurate tracking, the electron steps should be sufficiently small near boundaries.

As illustrated in Fig. 4.10, the path of the electron is truncated as it reaches the inhomogeneity. In reality, the electron does not follow a straight line and the real position of the electron in the boundary of the voxel may be point C (Fig. 4.10). The initial and final points of the path (A and B) are accurate while the path of the electron in condensed history method is approximated as the dashed line. If the electron is moved from point A to B through a large single step, the crossing point is D_1 at which time a new track is picked up. However, if the electron moves through smaller steps from point A to B, the crossing point D_2 is closer to the real position of the electron C and gives more accurate characteristics of electron in terms of energy, position and direction. This explains the larger error for large steps sizes in Fig 4.9.

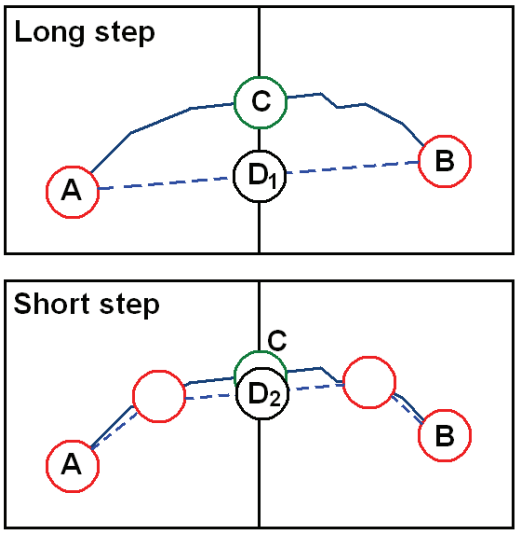

Figure 4.10 The real path (solid line) and simulated path of the electron with straight line approximation (dashed line). The real position of the electron in boundary is C and the simulated positions are D_1 and D_2 with taking large step and small step respectively.

In homogeneous phantoms, the electron can take a large step using random-hinge algorithm.[19-22] In this technique, the dose is deposited by approximating the curved path of the charged particle by two straight-line steps joined at the hinged point. The hinged step can be calculated using either the particle's known initial direction or its known final direction. Walters and Kawrakow[22] have recently applied this technique to DOSXYZnrc gaining 50-90 % efficiency. Random-hinge technique can be used to increase the efficiency of beam commissioning calculations in homogeneous phantoms.[23-25] However, this technique is not applicable to fast MC codes based on pre-calculated tracks since the electron step size is not calculated on the fly and it also cannot be adjusted in the pre-calculated data. A possible solution is to generate a set of pre-calculated data with a large step size (e.g. with XIMAX=0.5 or larger) as well and small step size and for the homogeneous case we use set of data with XIMAX=0.5. The size of the pre-calculated data in this case is not large since each electron track has much lower number of steps.

References

1. I. Kawrakow and D. W. O. Rogers, "The EGSnrc code system: Monte Carlo simulation of electron and photon transport," NRC, Report PIRS–701, 2000.
2. B. R. B. Walters and D. W. O. Rogers, "DOSXYZnrc Users Manual," NRC Report PIRS 794 (rev B), 2004.
3. I. Kawrakow, "VMC++, electron and photon Monte Carlo calculations optimized for Radiation Treatment Planning," *Advanced Monte Carlo for Radiation Physics, Particle Transport Simulation and Applications: Proceedings of the Monte Carlo 2000 Meeting Lisbon*, edited by A. Kling, F. Barao, M. Nakagawa, L. Távora, and P. Vaz (Springer, Berlin, 2001), pp. 229–236.
4. B. R. B. Walters, I. Kawrakow, and D. W. O. Rogers, "History by history statistical estimators in the BEAM code system," Med. Phys. **29**, 2745–2752 (2002).
5. I. Kawrakow, M. Fippel, and K. Friedrich, "3D Electron Dose Calculation using a Voxel based Monte Carlo Algorithm," Med. Phys **23**, 445–457 (1996).
6. P. J. Keall and P. W. Hoban, "Super-Monte Carlo: a 3D electron beam dose calculation algorithm," Med. Phys. **23**, 2023–2034 (1996).
7. P. J. Keall and P. W. Hoban, "Superposition dose calculation incorporating Monte Carlo generated electron track kernels," Med. Phys. **23**, 479–485 (1996).
8. Ma C-M *et al.* "MCSIM—a Monte Carlo dose calculation tool for radiation therapy," *Proc. 14th ICCR*, (Seoul,Korea, 2004), pp. 123–126.
9. I. Chetty et al., "Guidance report on clinical implementation of the Monte Carlo method in external beam radiation therapy treatment planning: Report of the AAPM Task Group No. 105," Med. Phys. **34**, 4818–4853 (2007).
10. F. Verhaegen and J. Seuntjens, "Monte Carlo modelling of external radiotherapy photon beams," Phys. Med. Biol. **48**, R107–R164 (2003).
11. E. Poon and F. Verhaegen, "Accuracy of the photon and electron physics in GEANT4 for radiotherapy applications," Med. Phys. **32**, 1696–1711 (2005).
12. E. Poon, J. P. Seuntjens, and F. Verhaegen, "Consistency test of the electron transport algorithm in the GEANT4 Monte Carlo code," Phys. Med. Biol. **50,** 681–694 (2005).

13. H. W. Lewis, "Multiple scattering in an infinite medium," Phys. Rev. **78**, 526–529 (1950).

14. S. Agostinelli *et al*., "GEANT4—A simulation toolkit," Nucl. Instrum. Methods Phys. Res. A 506, 250–303 (2003).

15. I. Kawrakow and B. R. B. Walters, "Efficient photon beam dose calculations using DOSXYZnrc with BEAMnrc," Med. Phys. **33**, 3046–3056 (2006).

16. I. Kawrakow and A. F. Bielajew, "On the condensed history technique for electron transport," Nucl. Instrum. Methods Phys. Res. B 142, 253–280 (1998).

17. E. W. Larsen, "A theoretical derivation of the condensed history algorithm," Ann. Nucl. Energy 19, 701–714 (1992).

18. I. Kawrakow, "Accurate condensed history Monte Carlo simulation of electron transport. II. Application to ion chamber response simulations," Med. Phys. **27**, 499–513 (2000).

19. J. Baro, J. Sempau, J. M. Fernandez-Varea, and F. Salvat, "PENELOPE: an algorithm for Monte Carlo simulation of the penetration and energy loss of electrons and positrons in matter," Nucl. Instrum. Methods Phys. Res. B 100, 31–46 (1995).

20. J. Sempau, S. J. Wilderman, and A. F. Bielajew, "DPM, a fast, accurate Monte Carlo code optimized for photon and electron radiotherapy treatment planning dose calculations," Phys. Med. Biol. **45**, 2263–2291 (2000).

21. I. J. Chetty, N. Tyagi, M. Rosu, P. M. Charland, D. L. McShan, R. K. Ten Haken, B. A. Fraass, and A. F. Bielajew, "Clinical implementation, validation and use of the DPM Monte Carlo code for radiotherapy treatment planning," in Nuclear Mathematical and Computational Sciences: A Century in Review, A Century Anew, Gatlinburg, TN (American Nuclear Society, LaGrange Park, IL, 2003), Vol. 119, pp. 1–17.

22. B. R. B. Walters and I. Kawrakow "A "HOWFARLESS" option to increase efficiency of homogeneous phantom calculations with DOSXYZnrc ," Med. Phys. **34**, 3794-3807 (2007).

23. B. Fraass, K. Doppke, M. Hunt, G. Kutcher, G. Starkschall, R. Stern, and J. Van Dyke, "American Association of Physicists in Medicine Radiation Therapy

Committee Task Group 53: Quality assurance for clinical radiotherapy treatment planning," Med. Phys. **25**, 1773–1829 (1998).

24. S. B. Jiang, J. Deng, J. Li, P. Pawlicki, A. Boyer, and C.-M. Ma, "Modeling and commissioning of clinical photon beams for Monte Carlo treatment planning," in Proceedings of the 13th ICCR, edited by T. Bortfeld and W. Schlegel (Springer-Verlag, Heidelberg, 2000), pp. 434–436.

25. J. Deng, S. B. Jiang, P. Pawlicki, J. Li, and C.-M. Ma, "Electron beam commissioning for Monte Carlo dose calculation," in Proceedings of the 13th ICCR, edited by T. Bortfeld and W. Schlegel (Springer-Verlag, Heidelberg, 2000), pp. 431–433.

Chapter 5

Speed up techniques for Fast Monte Carlo

5.1 Simultaneous Transport Of Particle Sets (STOPS)

In STOPS, used in VMC++ discussed in Section 2.6.4[1-3], several electrons of the same energy are transported at the same time for various positions far enough from each other. In this way, few parameters such as the azimuthal angle are sampled only once for all particles. STOPS can also be applied in the PMC code in a particular way. In the standard PMC code, the track of the particles for each particular energy is picked up one after another. For example, in the case of a 4 MeV mono-energetic electrons in a 10×10^2 field size, for the first history, one track (e.g. track # 1) is picked up, and for history number 5001 the same track is picked up again (since for each energy there are 5000 particles). A very important point to note is that if track #1 has a secondary particle with 3 MeV energy, each time that the track is used, a different track for a 3 MeV secondary electron is also picked up from the 3 MeV set up to 5000 times. This was the case for the standard PMC code and in the STOPS technique one primary electron track as well as the track of its secondary are picked up and this history is transported from 10 different positions in the field size.

Using the STOPS technique, a factor of 1.5 in efficiency was gained (*i.e.,* the code runs 60 times faster than EGSnrc on the same hardware). However, the STOPS technique has certain limitations: The field size should be large (e.g., more than 2 cm^2 for 15 MeV electrons);[12] Moreover, STOPS is also not applicable to large fields that do not have a uniform energy spectrum since the particle sets should have the same energy. An example of the field size for which the STOPS technique is not applicable is illustrated in Fig. 5.1. The field size is 8×10 cm^2 and for each section with 2×2 cm^2 surface, a different mono-energetic electron beam is applied. For this kind of energy distribution, for example if a 1 MeV electron track is used for the first section, it cannot be used again for any other point

on the surface. On the other hand, it is not possible to start few electrons with the same energy but different position for such a distribution, although the field size is large. Therefore any idea for transporting a "group" of the particles at the same time may present problems associated with possible non-uniformity of the source energy and angular distribution.

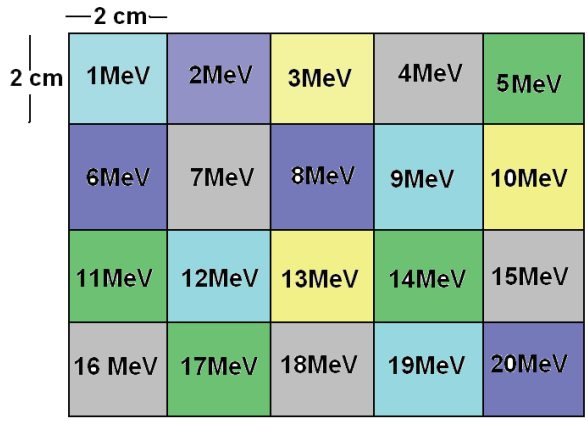

Figure 5.1 An example of an energy distribution in a large field size for which the STOPS technique is not applicable.

5.2 Modification of cut-offs and electron tracks

One way to improve the speed of a Monte Carlo code is to adjust various energy cut-offs within an acceptable range for which a major change in the results is not observed.[1] It's also possible to modify the track of the electrons considering various physical and geometrical conditions. Trying various modification of energy cut-offs and electron tracks, a gain of 110 – 120% in speed was obtained.

Energy cut-offs: The energy cut-off for transport of the electron is 100 keV and when the electron reaches this energy the transport is terminated and the energy of the electron is deposited locally. This energy could be 200 keV as it is used in other fast MC codes[3] which increases the speed of the code since the electron tracks are terminated earlier (compare to 100 keV). The range of the electron in this energy cut-off is very short and this approximation produces acceptable results.

Joining very short steps of electron tracks: This technique, proposed by P. Keall[4-5], needs process of the pre-calculated tracks before applying in the MC code based on pre-calculated tracks. Especially for low electron energies, the pre-calculated tracks of the

electron contain some steps with very short range compare to the boundary of the voxels (typically 1-2 mm). These tracks with a particular threshold are joined together and this reduces the number of electrons steps. An example of tracks and the steps of 6 MeV electrons in water are illustrated in Fig. 5.2. The steps of the electron are marked with (*) and the point at which the steps are very close to each other is marked with a circle.

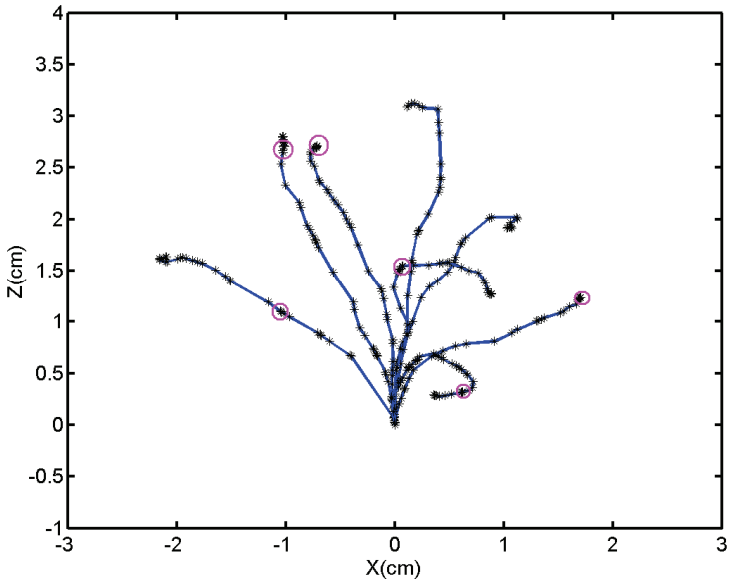

Figure 5.2 The track of the 6 MeV electrons in water. The position of the electron after each step is shown with (*) and the circles illustrates the points at which the steps are very close to each other.

Deposition of the energy of the electrons with very short range in the voxel. Through this approach, initial and last position of the electron are taken into account and the related voxel is calculated. If both points are in the same voxel, the entire energy of the electrons is deposited locally. A similar technique (called range-rejection) is used in other MC codes[6-9] in which the range of the electron is calculated by CSDA (continuous-slowing-down approximation) and if the calculated range is less than the distance of the electron with boundaries of the voxel, the energy is deposited locally.[10]

Mathematical model for electron path: Photons take large steps in water like materials and it is possible to use a mathematical trick to calculate boundary crossing in more efficient ways.[11] The technique is based on straight path of photons between each step. It might be possible to apply this technique to a part of the electron path with long step size particularly when they move in a large homogeneous phantoms. However, these techniques are not generally applicable for electrons as they move through small steps and

use non-straight paths. Since the electrons move through a 3 dimensional random path it is not possible to model the path of the electron with a well behaved function.

5.3 Various ray tracing techniques

After generation of electron tracks in a fast MC code either using simplified and efficient equations or using pre-calculated data, the codes have to go through tracking procedures, boundary crossing and energy deposition in each voxel. These steps still represent a major time consuming part in the recent versions of the fast MC codes such as DPM[12-14] and VMC++.[2] For example in VMC++ which is 50 times faster that EGSnrc, the code spends 90% of the CPU time in ray tracing and boundary crossing. This argument is confirmed in our first attempts (speed up techniques discussed in previous sections and discussion of time profile in section 4.7) in the development of a fast MC codes and the feasibility of avoiding ray tracing and boundary crossing are studied.

In this section we discuss various techniques through which the ray tracing section of the PMC code was attempted to be improved. The limitation of each technique that prevents it from general use is discussed in this section. These limitations lead us to the only general solution that resulted in a significant improvement in speed of the code. This solution is discussed in the next section (MC without ray tracing).

5.3.1 Enhanced STOPS technique.

In this idea, the position of the incident electrons with respect to boundary of the voxel is the same. As illustrated in Fig. 5.3, first we check the material of the first voxel (water) for the incident electron and then the electron is transported with the same geometry in a homogeneous water phantom. The entire information during the transport of the electron is saved. Such information includes deposited energy in each voxel, position of the electron in the boundary of the voxels (boundary crossing information) and direction of exited electron from each voxel and characteristics of the outgoing secondary particles from each voxel. Subsequently, this electron is transported in various position of the phantom surface in which the electrons have the same position with respect to the boundary of the voxel. In this kind of electron transport, as long as the medium is water no boundary crossing and ray tracing is needed since it is the same as the first electron in Fig. 5.3(a) When the electron reaches another material (bone in Fig. 5.3(b)) the position and

direction of the electron is available in the saved data. After this point, the electron is transported with the standard ray tracing calculation in the new medium.

The speed of the code in the first part of the transport (in water), for which no boundary crossing in needed, is extremely fast (in the order of 500 times faster than EGS); however, the speed improvement is lost when the electron reaches the first inhomogeneity since it goes through a voxel-by-voxel ray tracing calculation which is just 40 times faster than EGSnrc. This problem is more evident in a realistic clinical phantom in which there are many voxels with different material. We tried many mathematical methods to find a general solution to calculate and save the boundary crossing in heterogeneous medium. For example, we tried to find the boundary crossing information of the bone using boundary crossing information of the water; however, no general solutions were found. The limitations mentioned for the STOPS technique in higher level are applied in this method, e.g., the direction of the incident electrons, as well as the position of the electrons with respect to boundary of the voxel have to be the same.

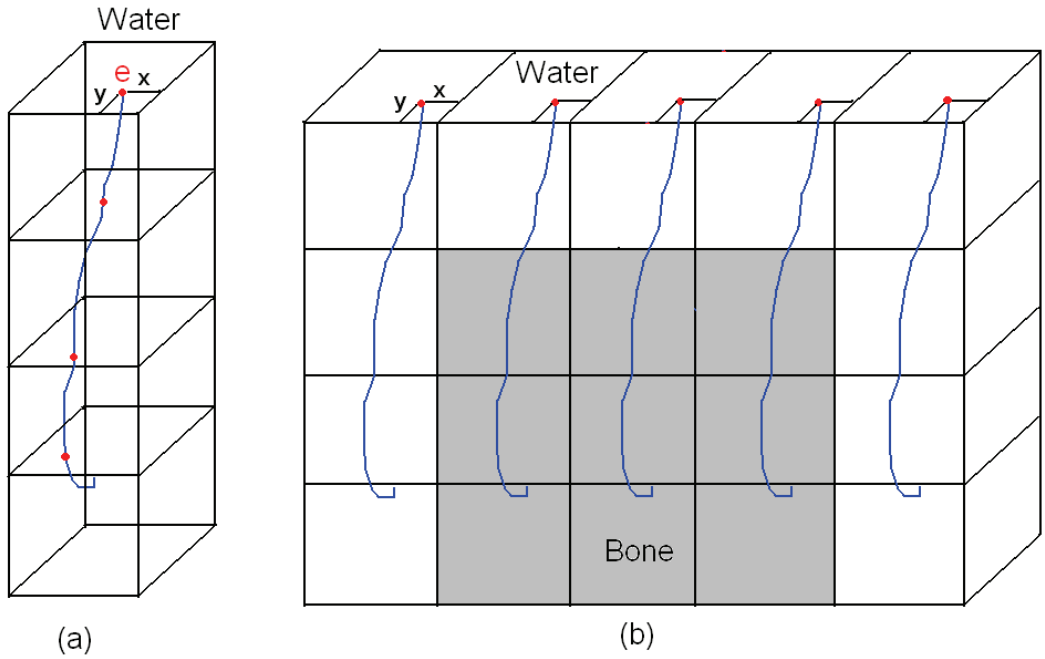

Figure 5.3 Enhanced STOPS technique. The material of the first voxel in the phantom is considered, water in (b), and in the first step the electron is transported in homogeneous phantom (a). The entire boundary crossing information such as position of the electron in each surface (dots in (a)) and energy deposition is saved. In the second step, the this track is applied for various position of the electron is the surface of the phantom. All the incident electrons have the same distance from boundary of the voxel (x,y).

5.3.2. Transport of a large group of particles

Few techniques similar to that described in the last section using the transport of a large group of particles at the same time have been tested. One of these is the transport of 5000 particles into the surface of one voxel and saving all characteristics of transport the including deposited energy, secondary particles and boundary crossing information for each voxel. This is then applied to various voxels far enough from each other that the tracks remain uncorrelated. The particle beam covers the surface of the voxel as is illustrated in Fig. 5.4. The size of the saved data in this case is very large. The speed of the code is in the order of 800 times faster than EGSnrc for homogeneous cases but the heterogeneities are still a problem as discussed in the last section (5.3.1). This technique can be used for homogeneous cases and commissioning process. However any idea for transporting a "group" of the particles at the same time may present problems associated with possible non-uniformity of energy in the phase-space and angular distribution.

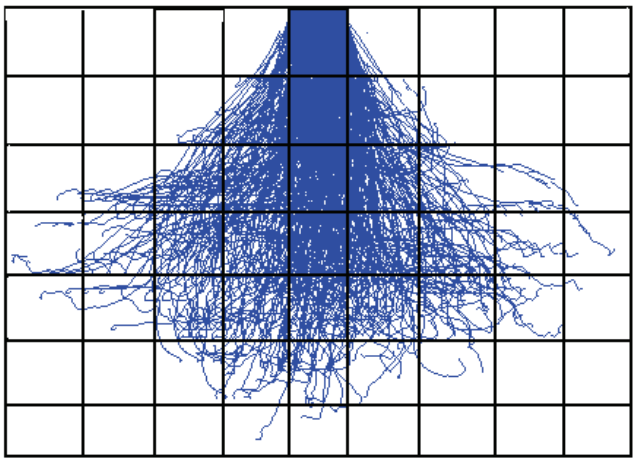

Figure 5.4 Transport of 5000 incident electron at the same time from the surface of one voxel.

5.3.3 Very small steps with no ray tracing

Although not developed completely, this idea is one through which ray tracing is avoided completely. The track of the electron is saved with very small steps in the pre-calculated data and in the transport of the particle, the energy is deposited at middle of each step. The steps should be small enough that a big error is not accrued near the boundary of

the voxels. In this method as well as the time which is saved for the boundary crossing, there are some mathematical methods to transport the particle in a very fast and efficient way using matrix operations. Although not developed further, an interesting test performed is illustrated in Fig. 5.5. In this test, we used the set of the pre-calculated data with very small step size XIMAX=0.02 while no boundary crossing is performed. The energy of the electron beam is 12 MeV and the field size is 10×10 cm^2. Although there is a large discrepancy at some points, the general follow-up of the PDD curve (with errors up to 5 %) is very interesting (while we are not doing any boundary crossing calculation and just deposition of the energies at the spot). With further optimization of the electron step size one may find better results.

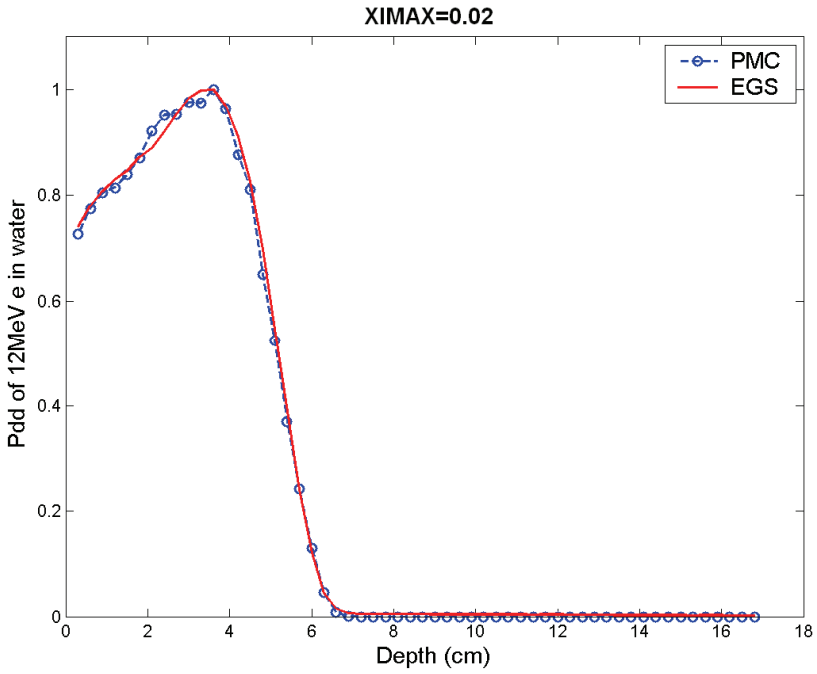

Figure 5.5 Transport of 12 MeV electrons without any boundary crossing non ray tracing and the deposited energy should be added to dose of each voxel in the middle of each step. The steps size of the electrons are very small (XIMAX=0.02). The results are compared to EGSnrc and the phantom in homogeneous water.

5.4 Fast Monte Carlo without ray tracing

5.4.1 Introduction

Our conclusion after trying many different speed up techniques as discussed in the last sections was that the major obstacle for speed increase in fast Monte Carlo codes has been

the ray tracing calculation. In this section we present a new method to perform Monte Carlo calculations in which boundary crossing and ray tracing are included in the pre-calculated data. In this method, the electron is transported in all possible cases that could enter the surface of a voxel for various energies, materials, directions, and position with respect to boundaries of the voxel. This was the only method which could be used generally for homogeneous and heterogeneous phantoms, avoiding the boundary crossing and ray tracing for transport of the electron.

5.4.2 Inclusion of ray tracing in pre-calculated data

As illustrated in Fig. 5.6 all the possible cases that an electron can enter the surface of a voxel is categorized and digitized with the following assumptions:

1- Position of the particle with respect to the boundary of the voxel (Fig. 5.6(b)): The surface of the voxel is divided to 3600 (60×60 in x and y directions) sub-pixels. The electrons incident in the middle point of the sub-pixels.

2- Direction of the electron: For each position of the electron in the middle of a sub-voxel, a set of electrons with various azimuthal and polar angles with 10° bins are transported as illustrated in Fig. 5.6(c). The 10° size of the angle bin was chosen after few trials and errors to check the size of the pre-calculated data and its compatibility with available ram.

3- Energy and material: Energy of the electrons and material of the voxels are other dimensions of the pre-calculated data. The energy and material range is the same as Section 3.4.2 and with energy of up to 6 MeV (0.2, 0.4, 0.6, 0.8, 1, 2, 3, 4, 5, 6MeV).

In the transport of the electron, the voxel is behaving as a black box and for each incident electron during the transport the following parameters are saved:

1- The voxel track of the electron. An array of integer numbers including the coordinates of the voxels that the electron is passed through is saved in pre-calculated data(as it is illustrated in Fig. 5.6(a) for a primary electron).

2- Deposited energy. Deposited energy of each primary electron 'and' its secondaries in each voxel are saved as a single real number '*edep*'. The deposited energy of the secondary electrons are added to the *edep* as long as they are in the initial voxel while if they reach the boundary of the voxel they are not transported any longer.

3- Characteristics of the primary electron at the boundary of each voxel. The energy, direction and position of the primary electrons at the surface of the voxel are saved. The position of the particle is saved with respect to the boundary of the voxel as discussed above. A voxel has six surfaces and the number of the surface from which the electron exits is also saved.

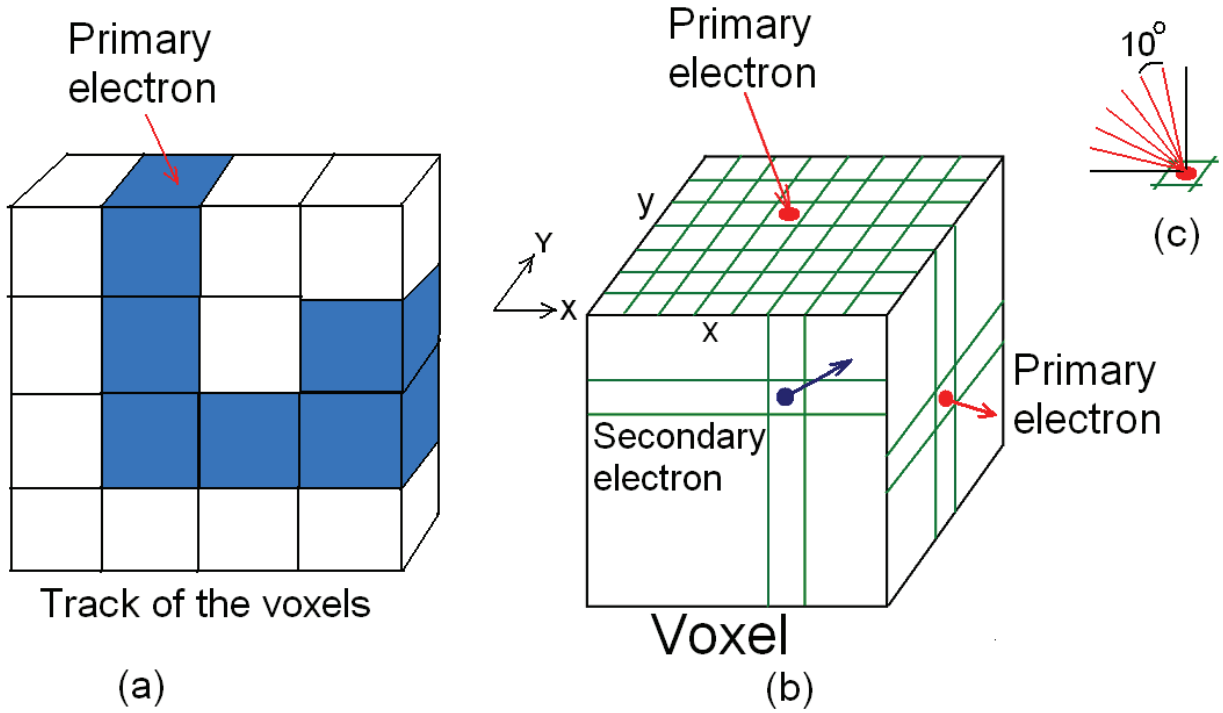

Figure 5.6 Geometry of the incident electron in PMC without ray tracing in which the ray tracing and boundary crossing information is included in the pre-calculated data The pre-calculated data includes the deposited energy and characteristics of the primary and secondary electrons at the exit points of the voxel surface.

4- Characteristics of the secondary electrons which get to the boundary of the voxel. If a secondary electron is generated in a voxel and it does not reach the boundary of the voxel, its energy is simply added to '*edep*' otherwise its characteristics at the surface of the voxel are saved in the same manner as for the primary electron.

5.4.3 Compression of the Pre-calculated data

As one can expect, the size of the pre-calculated data becomes very large; however, through an extensive amount of work and with several data compression techniques and mathematical symmetries, we were able to generate a reasonably sized file relative to memory of the current computers. Some of these techniques are discussed in this section.

Use of integer(2) or integer(1) instead of integer(4): Integer(1) ,(2) and (4) can hold numbers of 256, 2^{16} and 2^{32} as they are 1 byte , 2 bytes and 4 bytes respectively. Various parameters in pre-calculated data could be saved in an integer (1) or (2) considering the range of the variables. One of most important of these parameters is the position and direction of the primary particle with respect to boundary of the voxel. These parameters take more than 50 % of the pre-calculated data since they are saved for each voxel in the track of the electron. The position of the electron in the pre-calculated data are represented by two integer numbers (*nx*,*ny*) in Fig. 5.6(b) with range of 1-60. Therefore, these two numbers are saved in a matrix with integer(1). The track of the voxels includes the array of 3 numbers that considering the size of the voxel (e.g., 0.3 cm) and the range of the electrons (in the order of 10-20 cm) and integer(2) is adequate to handle the range of the voxel coordinates.

Since the pre-calculated data in this method contains several variables for incident electrons and we have approximation, digitization and data compression in many levels, the design of the code for this purpose, matrices and various indices were extremely complicated and time consuming. More than 4000 lines of code were written just for the generation of the pre-calculated data and the code is designed in a way that most of the tasks are done automatically.

5.4.4 Voxel by voxel transport of the electron

Although the code for generation of the pre-calculated data is very long and complicated, the main code in which the electron is transported in a user defined phantom is rather simple. The transport of the particle is illustrated in Fig. 5.7. According to energy, material, direction and position of the incident electron with respect to the boundary of the voxel, the related track as well as its boundary crossing information are picked up from the pre-calculated data. The transport of the electron in the same material is very simple and in

a voxel by voxel manner. The transport algorithm, after checking the material of the voxel, is just the deposition of the energy (*edep*) in each voxel without ray tracing. The parameter includes the deposited energy of the primary electron in the voxel, total energy of the secondary particles that does not reach the boundary of the voxel and part of the secondary electrons as they reach the boundary of the voxel. The code does not look up the boundary crossing information (such as position of the voxel between two voxels) as long as the electron moves in the same material.

When the electron reaches a new material one has its energy (e_2 in Fig. 5.7) and entry characteristics of the electron with respect to the boundary of the voxel from pre-calculated data. The new track of the voxels is picked up from the related material and the track is rotated and aligned to the position of the electron and the transport continues. The rotations are six simple and known rotations with 90° increments for the 6 surfaces of the voxel. As mentioned in the last section, the track of the voxels is an array of integer(2) numbers and rotation, translation and other matrix operations are performed faster than an array with real or integer(4) numbers. The same algorithm is applied for secondary electrons that have reached the surface of the voxel.

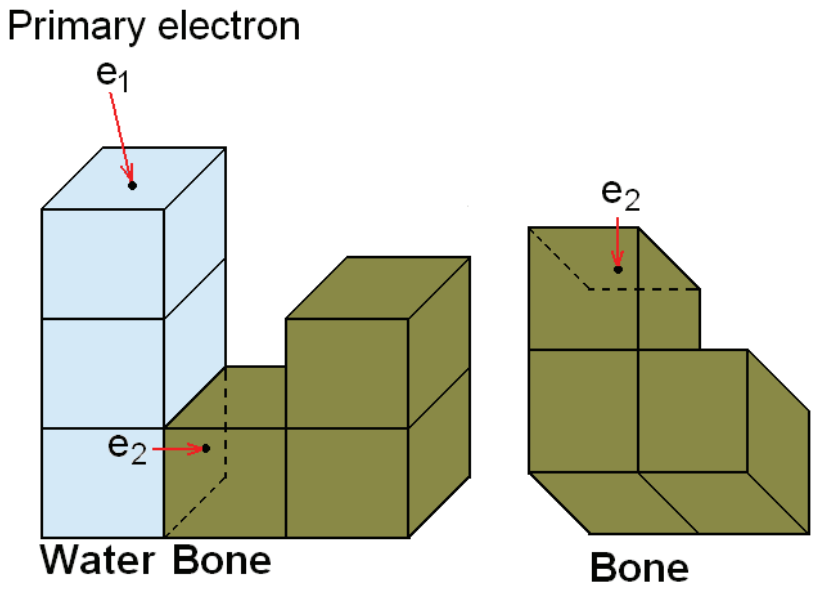

Figure 5.7 Transport of the electron without ray tracing. The code transports the electron in voxel by voxel manner for each material. If the electron reaches a new material a new track of the voxels is picked up from pre-calculated data from the related material (bone).

5.4.5 The results of the PMC code without ray tracing

The results of the PMC code without ray tracing are illustrated in Fig. 5.8 In this example, monoenergetic electrons are transported in water and water-bone phantom. In water-bone phantom, a slab of bone with 1.2 cm thickness is embedded in the water. The same geometry is simulated with EGS [15] and the results are used as a reference. The energy of the electron beam is 6 MeV and the field size is 10×10 cm^2.

In comparison with EGS the errors are in the order of 3-10 % for water and water-bone phantom respectively with 2 % uncertainty. The same order of error (up to 10 %) was observed in other combinations of inhomogeneities such as water-lung phantoms or water as an inhomogeneity test (this test is discussed in Section 3.6.3). However the code runs a million particles in 6 seconds in a Pentium M 1.3 GHz which is 560 times faster than EGS on the same computer for the same statistical uncertainty. The size of the pre-calculated data for water, bone and lung was 0.31, 0.207 and 1.02 Gb respectively. There are still limitations in this technique as is further discussed in the next section. The major sources of error and possible options for improvement of the results are also discussed in the next section.

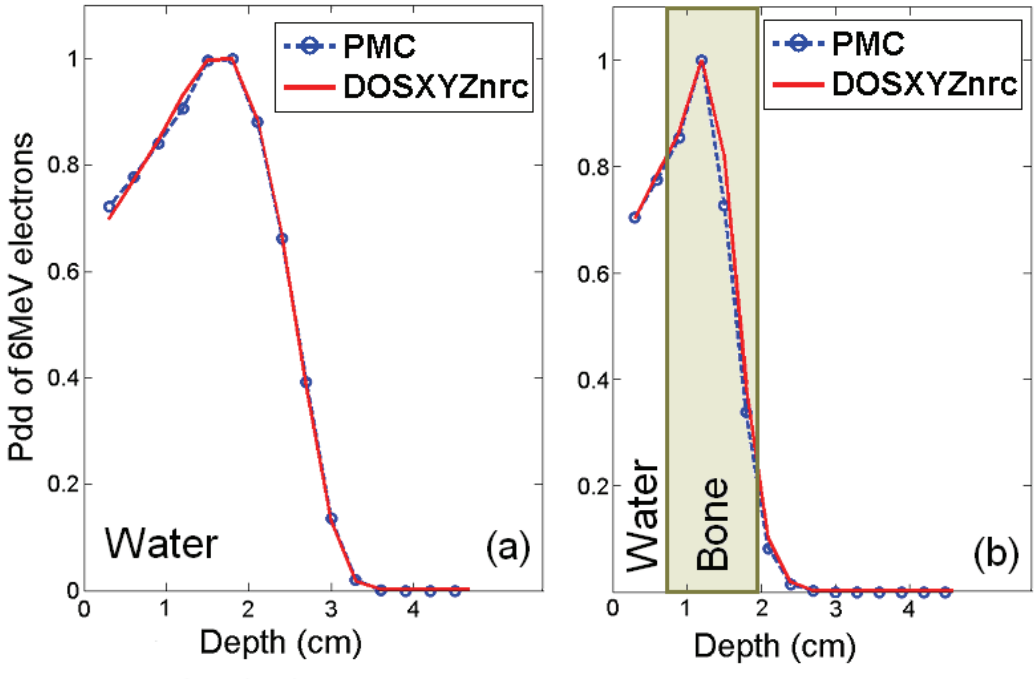

Figure 5.8 The PDD comparison of PMC without ray tracing with EGSnrc. The phantoms are consists of homogeneous water (a) and water with a bone slab (b).

5.4.6 Advantages and limitations of the Monte Carlo without ray tracing

Implementation of a calculation scheme that does not require boundary crossing and ray tracing was the only technique that could bring us to a new speed limit of 560 times faster than EGSnrc. The idea stems from the fact that for clinical applications, no dose deposition information below CT resolution is required. The following factors contribute to the significant speed increase:

a) No boundary crossing is performed in the transport of the particle and it is included in the pre-calculated data.

b) More than 70% of secondary particles with energy above cut-off energy are not transported and included in deposited energy of the voxel. These are the secondaries that do not reach the boundary of the voxel.

c) The track of the particles is represented by an array of integer numbers allowing for various operations such as track pick-up and rotation to be faster.

The method presented needs development in the following areas:

a) Data compression is needed to reduce the size of the pre-calculated data and improve all aspects of the code such as including higher energy electrons and decreasing the angle bin.

b) A correction for variable density of the same material is needed. This must be limited to modification of deposited energy and boundary crossing information or using a brute-force solution such as extending the pre-calculated set to various densities.

c) Resolution of the polar and azimuthal angle distributions should be better than 10°. We evaluated this requirement by improving the resolution to 2° for a discrete energy and obtaining consistent results in the heterogeneity calculation. This implies that the size of pre-calculated data needs to be increased by a factor of 25 (5^2) which underlines the need for a major improvement in data compression or available RAM.

d) Application of this method in deformed voxel used in 4-D MC[16] and IGRT (image guided radiation therapy) application is also a challenge since in the current approach the size of the voxel is fixed.[17-19] While extension of pre-calculated data for various deformed states of the voxel in this case is unreasonable, trilinear interpolation techniques have been used successfully to remap the dose from a deformed state to a reference state.[17]

The results of the code with smaller sub-pixels, 70×70 (4900 instead of 3600), were tested and no major improvement in accuracy was noticed.

5.5 Programming language considerations

There are relatively few references that compare efficiency of different languages for Monte Carlo calculations in radiation therapy.[20,21] Most of the current fast Monte Carlo codes have been developed in either Fortran which has a fast learning curve or C++ which is more difficult to learn although it is a more powerful language.[22]

Although PMC has originally been developed in Fortran 90, the entire code has been translated and run in many different high level (MATLAB (The MathWorks, Inc., MA)) and low-level languages to check their efficiency. The results are illustrated in table 1. The original MATLAB code was translated in an efficient way in which most of the loops are performed in matrix operations. In spite of the fact that MATLAB is a high level language and is slow especially in the loops as compared to Fortran90, the gain of a speed factor of 100 was surprising. The reason is that the nature of Monte Carlo calculations is based on repetitions of the same loop for large number of particles.

Using MATLAB library in C++ is recommended for MATLAB users who are looking for a greater speed, although as illustrated in table 1, the MATLAB code is still 50 times slower than Fortran90 for Monte Carlo type calculations. Fortran 77 has a better efficiency compared to Fortran90 as expected, although in Fortran 90 one does not have Fortran77 restrictions in coding. C++ is likely to have equal or better efficiency compared to Fortran[22] as it is used in VMC++.[1]

TABLE I. Performance of various programming languages for the same Monte Carlo code.

Language	Relative speed
Fortran 77	126
Fortran 90	100
C++ using MATLAB library	2
MATLAB	1

5.6 Conclusions

No single physical calculation is done in the PMC code based on pre-calculated tracks even in the presence of heterogeneities. The pre-calculated data is generated for each particular material and this improves the performance of the code both in terms of accuracy and speed with respect to other fast MC codes based on pre-calculated data. Linear interpolation between grid energies for which pre-calculated data is available provides very accurate results. A new method for generation of pre-calculated data in which only the track of the primary is saved makes the size of the files reasonable and feasible for current computers and ultimately makes it possible to build a code for dose calculation in treatment planning. Careful choice of the electron step size is important to avoid artifacts near boundaries. The speed limit of fast Monte Carlo for "electron" transport is on the order 100 times faster than EGS as long as the code has to do voxel-by-voxel ray tracing. Only by avoiding voxel by voxel ray tracing, a significant improvement on the order of 500 or 1000 can be achieved.

Although the entire track is ready in pre-calculated data, picking up a track from a large pre-calculated data set represents a time-consuming task compared to the more efficient generation of a track from scratch. This is one of the reasons that fast MC codes based on pre-calculated data such as SMC and PMC are not necessarily faster than from scratch MC codes such as DPM and VMC++.

Since all of the physics is handled with a benchmark code (such as, EGSnrc for electrons), the PMC algorithm has the capacity to be used as fast and accurate engine for other particle types, such as protons as long as the pre-calculated tracks can be generated using a well benchmarked general purpose code such as GEANT4[23] or MCNP[24]. The extension of the PMC code for protons using MCNP code will be discussed in the next chapter.

References

1. I. Kawrakow, "VMC++, electron and photon Monte Carlo calculations optimized for Radiation Treatment Planning," *Advanced Monte Carlo for Radiation Physics, Particle Transport Simulation and Applications: Proceedings of the Monte Carlo 2000 Meeting Lisbon*, edited by A. Kling, F. Barao, M. Nakagawa, L. Távora, and P. Vaz (Springer, Berlin, 2001), pp. 229–236.
2. I. Kawrakow and M. Fippel, "VMC++, a MC algorithm optimized for electron and photon beam dose calculations for RTP," in *Proceedings of the 22nd Annual International Conference of the IEEE* (Engineering in Medicine and Biology Society, Piscataway, NJ, 2000).
3. I. Kawrakow, M. Fippel, and K. Friedrich, "3D Electron Dose Calculation using a Voxel based Monte Carlo Algorithm," Med. Phys **23**, 445–457 (1996).
4. P. J. Keall and P. W. Hoban, "Super-Monte Carlo: a 3D electron beam dose calculation algorithm," Med. Phys. **23**, 2023–2034 (1996).
5. P. J. Keall and P. W. Hoban, "Superposition dose calculation incorporating Monte Carlo generated electron track kernels," Med. Phys. **23**, 479–485 (1996).
6. I. Kawrakow and D. W. O. Rogers, "The EGSnrc code system: Monte Carlo simulation of electron and photon transport," NRC, Report PIRS–701, 2000.
7. B. R. B. Walters and D. W. O. Rogers, "DOSXYZnrc Users Manual," NRC Report PIRS 794 (rev B), 2004.
8. F. Verhaegen and J. Seuntjens, "Monte Carlo modelling of external radiotherapy photon beams," Phys. Med. Biol. **48**, R107–R164 (2003).
9. D. W. O. Rogers, B. A. Faddegon, G. X. Ding, C. M. Ma, J. We, and T. R. Mackie, "BEAM: A Monte Carlo code to simulate radiotherapy treatment units," Med. Phys. **22**, 503–524 (1995).
10. I. Kawrakow and A. F. Bielajew, "On the condensed history technique for electron transport," Nucl. Instrum. Methods Phys. Res. B 142, 253–280 (1998).
11. R. L. Siddon, "Prism representation: a 3D ray-tracing algorithm for radiotherapy applications," Phys. Med. Biol. **35**, 2800 (2008).

12. J. Sempau, S. J. Wilderman, and A. F. Bielajew, "DPM, a fast, accurate Monte Carlo code optimized for photon and electron radiotherapy treatment planning dose calculations," Phys. Med. Biol. **45**, 2263–2291 (2000).

13. I. J. Chetty, J. M. Moran, T. S. Nurushev, D. L. McShan, B. A. Fraass, S. J. Wilderman, and A. F. Bielajew, "Experimental validation of the DPM Monte Carlo code using minimally scattered electron beams in heterogeneous media," Phys. Med. Biol. **47**, 1837–1851 (2002).

14. I. J. Chetty, P. M. Charland, N. Tyagi, D. L. Mc Shan, B. A. Fraass, and A. F. Bielajew, "Photon beam relative dose validation of the DPM Monte Carlo code in lung-equivalent media," Med. Phys. **30**, 563–573 (2003).

15. W. R. Nelson, H. Hirayama, and D. W. O. Rogers, "The EGS4 Code System," SLAC Report No. SLAC-265, 1985.

16. E. C. Heath and J. P. Seuntjens, "A direct voxel tracking method for four-dimensional Monte Carlo dose calculations in deforming anatomy," Med. Phys. **33**, 433–445 (2006).

17. M. Goitein, "The cell's-eye view: assessing dose in four dimensions," Int. J. Radiat. Oncol. Biol. Phys. **62**, 951–953 (2005).

18. H. Paganetti, H. Jiang, J. A. Adams, G. T. Chen, and E. Rietzel, "Monte Carlo simulations with time-dependent geometries to investigate effects of organ motion with high temporal resolution," Int. J. Radiat. Oncol., Biol., Phys. **60**, 942–950 (2004).

19. K. K. Brock, D. L. McShan, R. K. Ten Haken, S. J. Hollister, L. A. Dawson, and J. M. Balter, "Inclusion of organ deformation in dose calculations," Med. Phys. **30**, 290–295 (2003).

20. S. Chekanov, "RunMC—an object-oriented analysis framework for Monte Carlo simulation of high-energy particle collisions," Comp. Phys. Comm. **173**, 115–198 (2005).

21. M. Bertini, L. Lönnblad, and T. Sjöstrand, "PYTHIA version 7: A proof-of-concept version," Comp. Phys. Comm. **134**, 365–391 (2001).

22. J. R. Cary, S. G. Shasharina, Cummings J. C., J. V. W. Reynders, and P. J. Hinker, "Comparison of C++ and Fortran 90 for Object-Oriented Scientific Programming," Comp. Phys. Comm. **105**, 20–36 (1997).

23. S. Agostinelli et al., "GEANT4—A simulation toolkit," Nucl. Instrum. Methods Phys. Res. A 506, 250–303 (2003).

24. J. F. Briesmeister, "MCNP-A general Monte Carlo N-particle transport code, Version 4C," Report LA-13709-M, Los Alamos National Laboratory, NM, 2000.

25. T. D. Solberg *et al*., "A review of radiation dosimetry applications using the MCNP Monte Carlo code," Radiochim. Acta. **89**, 337–355 (2001).

Chapter 6

Fast Monte Carlo for Protons based on MCNPX

6.1 Introduction

There is currently a growing interest in using proton beam in radiation therapy because of the particular advantages of these heavy particles over photons and electrons.[1] Figure 6.1 shows medical physics interest in the topic. A major advantage of the proton beam is its relatively low energy deposition in the entrance region, the sharp rise in dose deposition (Bragg peak) and rapid fall-off of dose at the end. These characteristics incorporate the basic role of radiation therapy which is to concentrate a high dose onto the target volume while minimizing any unnecessary radiation dose to the surrounding normal tissues.[2-6]

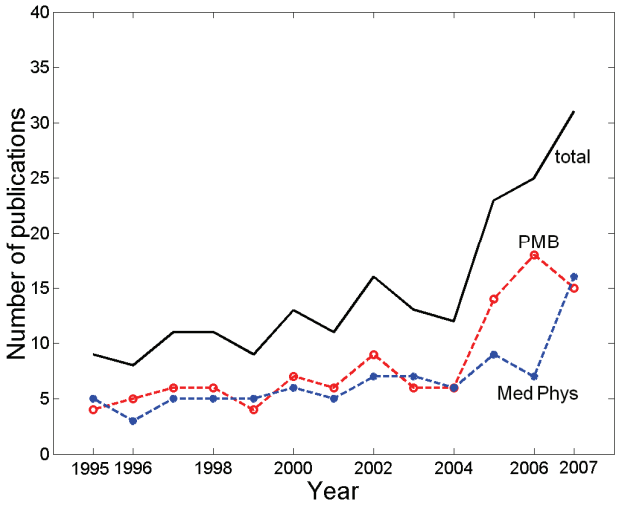

Figure 6.1 Number of publications per year related to proton therapy in 'Medical Physics' and 'Physics in Medicine and Biology' journals.

Treatment planning for radiotherapy that exploits the unique characteristics of proton depth dose to obtain conformal, homogeneous dose distributions within complex target volumes is challenging.

For treatment planning in proton therapy one needs an accurate dose calculation algorithm. In the early versions of dose calculation for protons, a simple and fast methods such as pencil beam algorithm and analytical methods have been used.[7-15] A general problem for these methods is the large discrepancies near the heterogeneities; however, because of their fast performance, they are currently used in treatment planning systems especially for intensity modulated proton therapy. [16-18]

The MC methods generally produce the most accurate results especially for charged particles. Most of the general purpose codes such as GEANT4,[19] FLUKA,[20,21] and MCNPX[22] have capability of the proton transport in clinical conditions and voxel based phantoms. All these general purpose codes with careful choice of approximations produce accurate results for proton transport compared to experiments.[23-29]

This work is an extension of our fast MC code Pre-calculated Monte Carlo (PMC) for protons in which we use pre-generated tracks for particle transport. The PMC code is initially developed for electron transport with capability of being used for other particles. The main difference with other fast MC codes based on pre-generated tracks is that while the other codes generate the tracks for water and modify them for other materials, in PMC the pre-generated data is collected for each particular material. This technique produces very accurate results near heterogeneities and makes the transport algorithm very simple since all the physics is handled by a general purpose code. Another difference of PMC is that only the track of the primary protons is saved and not the track of the secondary particles as they are treated like a primary particle. This technique decreases the size of the pre-calculated data and makes it possible to generate tracks for various materials. In this code MCNPX has been used as a reference and for generation of pre-calculated tracks in various materials and energies.

6.2 Review of fast MC codes for proton transport

As we discussed in Chapter 2, the general purpose codes are very slow and not suitable for day to day clinical treatment planning systems. In recent years, few groups have developed fast MC engine for proton transport in treatment planning such as Fippel and Soukup (VMCpro 2004),[30] Li *et al*.,[31] and Tourovsky *et al.*[32]. Most of these codes have been developed from their early versions for electron transport. [33-37]

6.2.1 VMCpro

Fippel and Soukup in VMCpro[30] have developed fast MC for proton based on the Voxel Monte Carlo code.[33] One component of VMCpro is the algorithm to model the transport of protons with different energies through human tissue. This transport is influenced by elastic and inelastic Coulomb collisions with atomic nuclei and atomic electrons as well as elastic and inelastic nuclear reactions. In this code the transport parameters such as stopping power ratios and cross section of various interactions of protons is formulized considering the specific condition that one has in clinical situation.

The energy range of protons is an the order of 200 MeV and the material range is within water like materials. The proton is transported until it reaches the energy cut off PCUT=0.5 MeV. The transport of the proton is terminated at this energy and the proton is absorbed locally since the range of the proton in this energy is very short (e.g. 0.01 mm in the water). In this code GEANT4 and FLUKA is used as a reference and the dose agreement is within 2%. The speed factor is 13 relative to FLUKA and 35 relative to GEANT4. An example of VMCpro results are illustrated in Fig. 6.2. In this example a monoenergetic proton beam is transported in a homogeneous skeleton and soft tissue. The energy of the proton beam is 100 and 200 MeV.

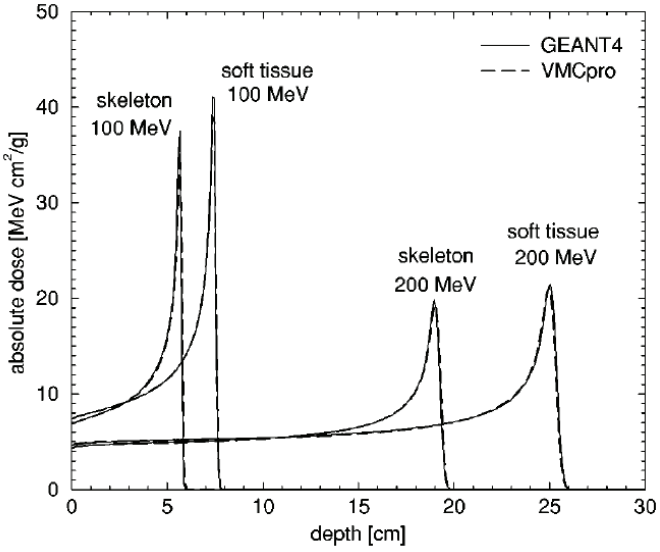

Figure 6.2 Depth dose distributions in soft tissue (ρ=1.03 g/cm3) and adult skeleton (ρ=1.46 g/cm3) for monoenergetic proton pencil beams of 100 MeV and 200 MeV, calculated with GEANT4 and VMCpro. (Figure from Ref.[30])

6.2.2 Track-repeating algorithm

The fast MC code developed by Li *et al*.[32] is based on track-repeating algorithm for proton beam. This code is an extension of MCSIM code[37] which uses pre-generated electron tracks for electron transport. For proton transport, the GEANT[2] is used to create the track of high energy protons in the middle of a large homogeneous water phantom, and tracks of 100000 protons with 250 MeV energy are transported. For each step in the proton track, the location, angle, energy and the energy deposition along the track were recorded for the primary protons and all secondary particles. The cutoff kinetic energy for all the particles was 200 keV and the size of the stored data for 100000 protons was 0.8 Gb.

For transport of the proton, the pre-generated tracks were repeated and the energy was deposited along the path in patient geometry built from CT data with voxel size varying between 2-4 mm. In all other materials such as lung, bone, *etc* the particle tracks in water are picked up and modified. The scattering angles were repeated for air and soft tissue, although they were adjusted properly for bone, based on the scattering power ratios. The particle step lengths were adjusted based on the density of various materials. These techniques were initially used in super position MC code for electron transport developed by Keall and Hoban (1996).

The pre-generated data were obtained by simulating protons with a kinetic energy of 250 MeV. It was necessary to determine where to start track repeating along the proton track if the kinetic energy of an incident proton in a realistic proton beam was lower than 250 MeV. The starting step number (IT) in a recorded proton track history could be found based on the incident proton kinetic energy, *Ein*. One follows energy along the pre-generated track as one reaches the step (number IT) at which the energy of the proton is *Ein*. The energy of the proton at the beginning and end of the step is E(IT) and E(IT+1) respectively. The step length, *lstep*, and the energy deposition, *Edep*, for this step is adjusted according to incident energy *Ein,* using a linear interpolation:

$$Edep = Ein - E(IT+1) \tag{6.1}$$

$$lstep = lstep(IT)\frac{Edep}{Edep(IT)} \tag{6.2}$$

in which lstep(IT) and Edep(IT) are the step length and deposited energy of step number (IT) in pre-generated data. The rest of the track after the first step remains unchanged. The fast proton MC code by Li *et al.* runs 13 times faster than GEANT3 for energies up to 250 MeV.[13]

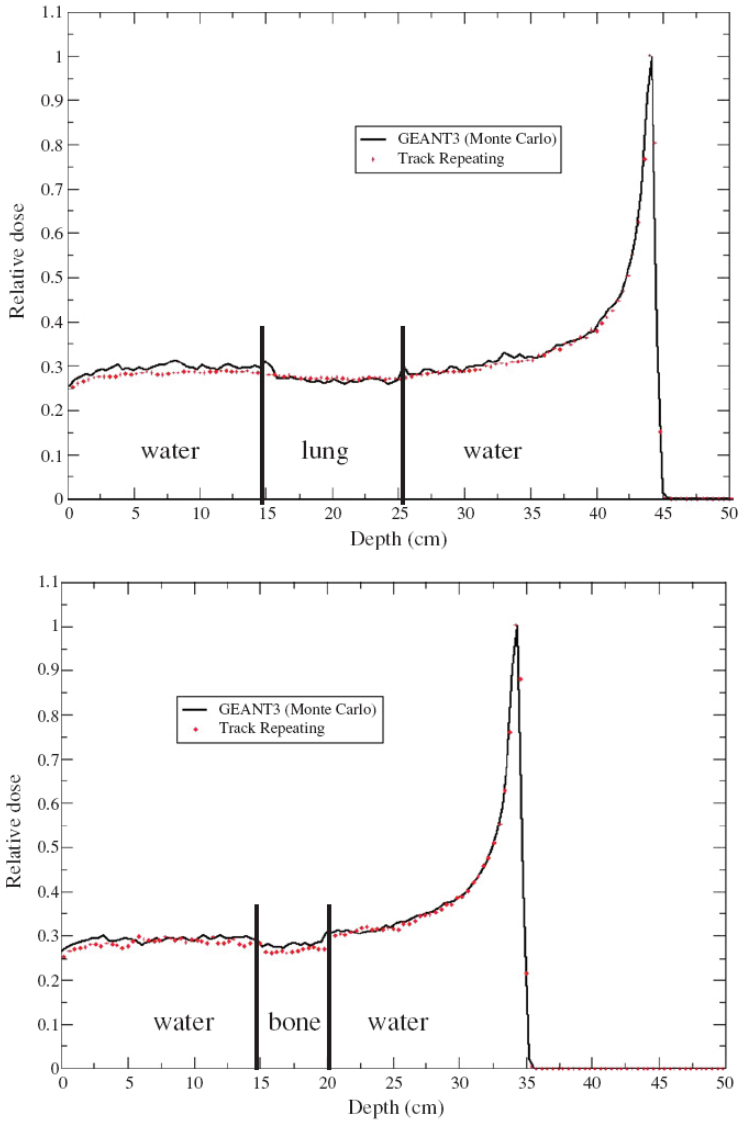

Figure 6.3 Comparison of PDD curves along the central axis at the middle of the lung and bone slab between GEANT3 and track-repeating algorithm for a 250 MeV, 4 × 4 cm^2 parallel proton beam. (Figure from Ref.[31]).

The results of the code in homogeneous materials are generally in good agreement with the reference code within 2 %. However, as illustrated in Fig. 6.3 there exist relatively large discrepancies near the heterogeneities. The shift of the Bragg peak is handled

properly but the magnitude of the error is up to 10 %. Errors of this magnitude are due to various approximation and modification of this code and re-usage of the proton tracks in water for other materials.[37]

6.3 Generation of pre-calculated tracks for proton transport

Our approach in generation of pre-calculated data for proton is similar to that of electron data. The general purpose Monte Carlo code MCNPX[38] is used for generation of the pre-calculated proton tracks. Tracks of 10000 primary protons were generated for various compounds and energies. The proton energy was 20, 40, …220, 240, 250 MeV with an energy cut-off of 200 keV. The protons are transported in the middle of a large homogeneous phantom with various materials such as water, lung, bone, soft tissue.

The `ptrac` routine of MCNPX writes the various events of each particle in an ASCII file in a particular format. The row format of `ptrac` file is complicated and very hard to analyze for beginners; however, it contains the complete information of primary protons and all secondary particles.[39-43] The explanation of the `ptrac` file and the instructions to read such files are discussed in Appendix A.

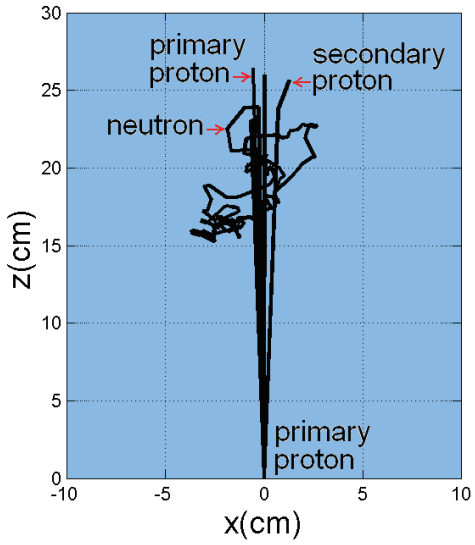

Figure 6.4 Tracks of few 200 MeV protons in a homogeneous water phantom and their secondary particles. The track information is extracted from the `ptrac` output file produced by MCNPX.

. An in-house Fortran code was developed to read and extract the needed information from the ptrac file. This code extracts the position, direction, energy and deposited energy

of a particle in each step. The code also extracts the characteristics of all secondary particles generated by primary protons. Post-processing of the data is needed to handle the physics of the various secondary particles as it is discussed in Section 2.3. The track of a few protons and their secondaries are illustrated in Fig. 6.4.

The composition of different materials is taken from ICRU 44 and given in Table 1.[44] This material comparison is used in MCNPX to fill up the homogeneous phantoms with different materials. The density of materials are: soft tissue ρ= 1.05 g/cm^3, lung ρ=0.3 g/cm^3 and bone ρ=1.92 g/cm^3.

Table 1. Composition of different materials (Soft tissue, Lung tissue and Bone) according to ICRU-44. The numbers are in fraction by weight. The compositions include the atomic number.

	Soft tissue	Lung tissue	Bone
(Z =1) Hydrogen	0.102000	0.103	0.034
(6) Carbon	0.143000	0.105	0.155
(7) Nitrogen	0.034000	0.031	0.042
(8) Oxygen	0.708000	0.749	0.435
(11) Sodium	0.002000	0.002	0.001
(12) Magnesium	-	-	0.002
(15) Phosphorus	0.003000	0.002	0.103
(16) Sulfur	0.003000	0.003	0.003
(17) Chlorine	0.002000	0.003	-
(19) Potassium	0.003000	0.002	-
(20) Calcium	-	-	0.225

6.4 Physics of various secondary particles

Unlike electron and photons, protons produce many different secondary particles such as neutrons, deuterons, tritons, alphas, electrons and secondary protons. From other studies of MC codes for proton transport[30,45-47] one can define three categories for handling secondary particles and these categories were used in PMC:

1- Secondary protons: They are treated like primary protons and explicitly transported in PMC using a track picked up from pre-calculated data. The energy fluence of secondary protons from primary 150 MeV protons in water is illustrated in Fig. 6.5. This is extracted from a `ptrac` file of 200000 protons in MCNPX. The secondary protons have an energy range from zero to the energy of the primary particle. Therefore they should be transported explicitly and their energy cannot be deposited locally or neglected.

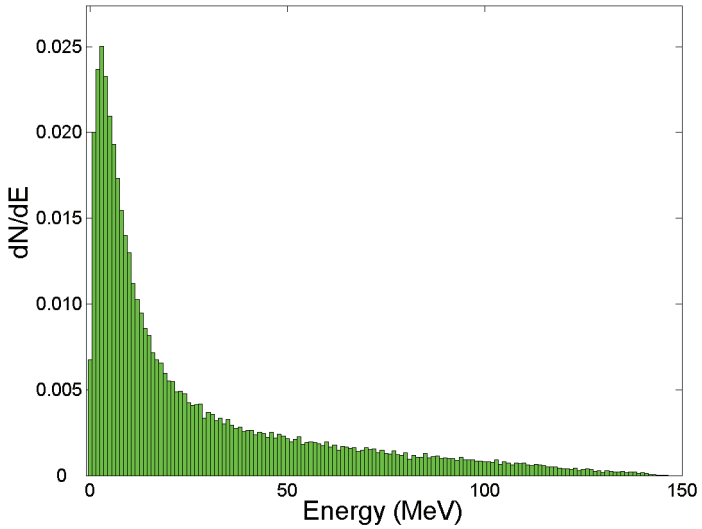

Figure 6.5 Energy fluence of secondary protons produced by 150 MeV protons in water. The spectrum is extracted from a `ptrac` file of a MCNPX run for 2×10^5 protons.

2- Neutrons: Since the energy of the neutron is deposited far from the initial point (as illustrated in 6.4) and their contribution in total dose is less than 0.1 %, they can be neglected. This assumption is verified by several groups[30,31,45] before and is the case for most of the fast MC codes for proton transport.

3- All other secondaries: Since other secondaries have a very short range in clinical range of energy and materials their energy is deposited locally.

An important issue which illustrates the flexibly of PMC code is that even if all the secondary particles have to be transported explicitly, one just needs to include the track of the particle in the pre-calculated data. This information is already available in `ptrac` file and in this case instead of saving just the initial characteristics of secondary particles, the entire track of secondary should be saved in pre-calculated data.

6.5 Transport of protons

The general approach for transport of the particles in PMC is reviewed in Chapter 3. The initial characteristics of the proton, such as energy and position, are taken from the input phase-space file. The one track and the related secondary particle information are picked up from pre-calculated data. After appropriate energy interpolation, the track is rotated and translated to the position of primary proton. In each step of the particle transport, the production of secondary particles is checked. If the secondary particle is a proton and its energy is larger than a user-defined cut-off, it is saved on the stack, otherwise the energy is deposited locally. The energy cut-off for all the simulations of this work is 200 keV. The higher cut-off of up to 500 keV has also given acceptable results in other fast MC code for proton. [30]

If the particle reaches a new material in its path, according to the energy of the proton, a new track from a related material is picked up. For each voxel, the deposited dose is proportional to the fraction of the step inside the voxel. The pre-calculated track of the particle in PMC is saved in Cartesian coordinates (x,y,z). In the case of new materials with different densities, such as lung which has various densities in CT based phantoms, the entire track is scaled proportional to the inverse of density. When the track of the primary particle is terminated, the secondary particles in stack are transported. The neutrons are neglected and the protons are transported one by one like primary proton and other secondary particles are deposited locally. The uncertainties are calculated with the history by history method as it was discussed in Section 3.6.1.

The energy interpolation could have various approaches and we are currently using a combination of methods in PMC and MCDOSE. [31] Given a 95 MeV particle, in this approach, a track with closest higher energy neighbor is picked up (i.e., 100 MeV) and within that track, we move down in energy until the step with an energy closest to 95 MeV is met. We then interpolate that step to the 95 MeV point and the rest of the track is picked up for transport of the particle.

6.6 Physics models of MCNPX

In MCNPX there is an option to choose various physics models through which the particles are transported.[51-53] The default physics model for proton transport is Vavilov model for charged-particle straggling[54] which is chosen for generation of pre-calculated data in this work. The other option in physics model is based on CSDA (Continuous Slowing Down Approximation) model and as a test the pre-calculated data is generated with this option of MCNPX. The result of 150 MeV protons in water phantom has been compared to MCNPX in Fig. 6.6. In this figure the PDD of PMC with Vavilov model, PMC with CSDA model and MCNPX (Vavilov model) are compared. The results of PMC with CSDA models represents generated very sharp peak with respect to the reference, MCNPX.

Other groups[55,56] also have declared such sharp peaks with CSDA model in various homogeneous and heterogeneous mediums. Therefore, although the protons mostly travel trough a straight line, the CSDA model is not an appropriate approach for proton transport in clinical range of energies.

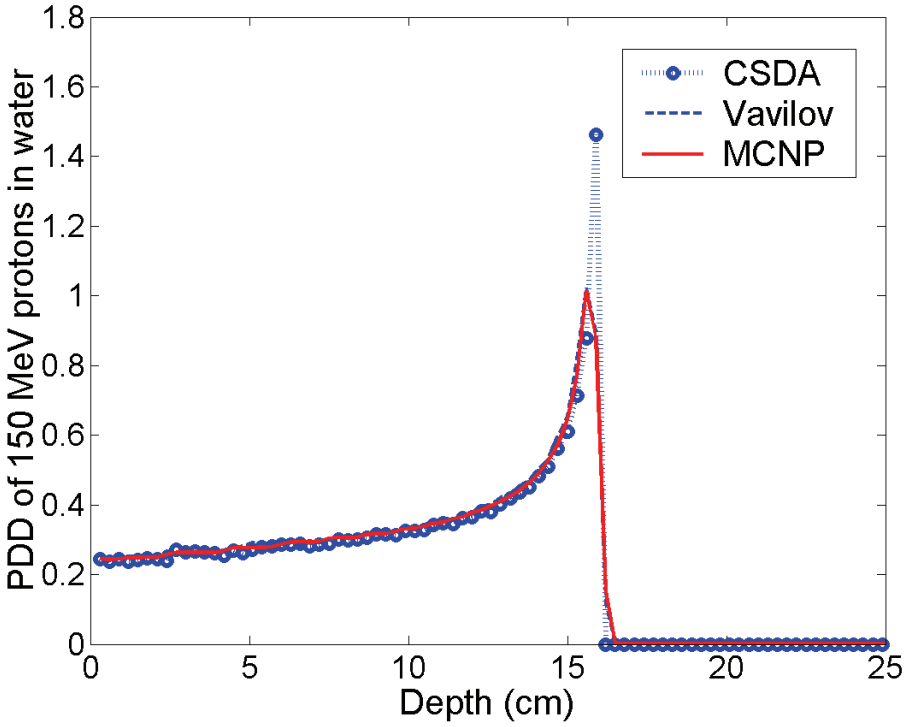

Figure 6.6 Comparison of PMC based on Vavilov model and CSDA model with MCNPX in water phantom. The energy of protons are 150 MeV and the field size is 10×10 cm^2.

6.7 Results and discussion of PMC code for protons

6.7.1 Size of pre-calculated data

The `ptrac` file generated by MCNPX in ASCII format has a very large size since it contains all the detailed information of each step of the primary proton and all secondary particles. For example, the size of the `ptrac` file for 10000 protons with 200 MeV is 235 Mb. Our in-house code to process the `ptrac` file, in the first step, reads the file and deletes the header and converts it into a binary unformatted file which is 66 Mb. In the second step, the code extracts the needed information (such as track of primary proton and initial parameters of secondary particle) from the file. Finally all the information is saved in unformatted file as an input for PMC code and the size of file at this stage is 23 Mb.

For a primary particle, in each step, the code saves five parameters: position (x,y,z), energy of the particle in the beginning of the step and deposited energy during the step. The initial characteristics of secondary particles such as particle type, position, direction and energy are saved in a separate file. The total size of the pre-calculated library for each material is on the order of 100-200 Mb. This compact size of the data is reached since in pre-calculated data of PMC the track of secondary particles is not saved.

6.7.2 Result of the code for homogeneous phantoms

For verification of PMC results the MCNPX code version 2.5 is used as a reference. An important reminder for MCNPX run is that, in the default setting, the maximum energy of the code for all particles is 100 MeV. This number has to be changed manually in the physics part of the code to highest possible energy of the problem (250 MeV in our case) otherwise the physics is wrong. The size of each voxel is 0.3 mm in each direction and the size of the phantom is $21\times21\times30$ cm^3.

The comparison of PMC results with MCNPX for various energies in water is illustrated in Fig. 6.7. A monoenergetic incident proton beam with an energy of 100, 150 and 200 MeV and a field size of 10×10 cm^2 are used. The graph represents the relative percentage depth dose (PDD) along the central axis. There is generally a very good agreement between PMC results and the difference is on the order of 2 %.

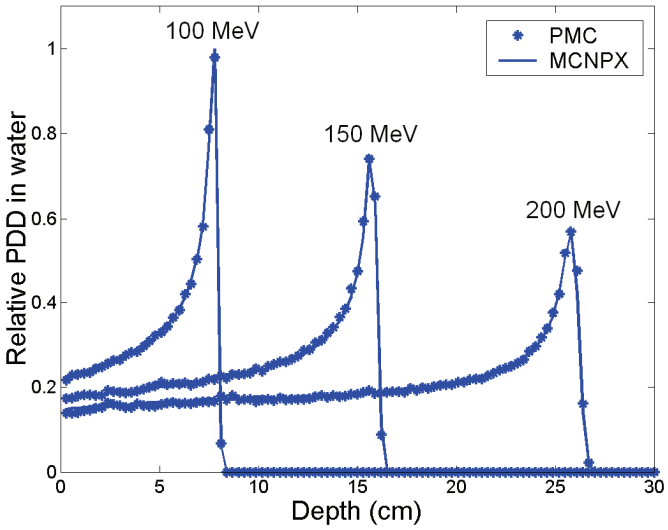

Figure 6.7 The relative PDD of monoenergetic protons in water phantom. The field size is 10×10 cm^2 and the size of the voxel is $(3\ mm)^3$.

The results of PMC code for various materials such as bone, lung and soft tissue are illustrated in Fig. 6.8. The composition of bone, soft tissue and lung have been taken from ICRU 44 with densities of 1.92 g/cm^3, 1.06 g/cm^3 and 0.3 g/cm^3 respectively. There is generally a good agreement between the results with discrepancies up to 2.5 %.

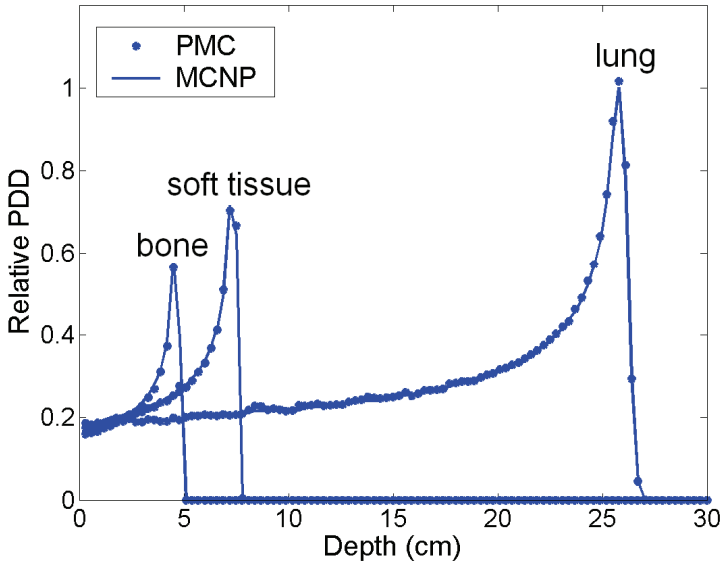

Figure 6.8 Pdd of 100 MeV protons in various materials. The density of materials are 1.92, 1.06 and 0.3 g/cm3 for bone, soft tissue and lung respectively.

6.7.3 Result of the code for in-homogeneous material

Fig. 6.9 illustrates an example of proton transport in heterogeneous phantom. This phantom contains water with a 4 cm slab of bone embedded at a depth of 3 cm. The field size in this case is 4×4 cm^2 and the proton energy is 150 MeV. In this phantom, there are both higher to lower and lower to higher density interfaces. The comparison of PDD with MCNPX for the same geometry but with a lung slab is illustrated in Fig. 6.10. An example of lateral dose profile for a bone and lung slab in water phantom is illustrated in Fig. 6.11 and Fig 6.12. The difference is between 2-3 % and the shift of Bragg peak due to the slab of bone and lung is handled very accurately.

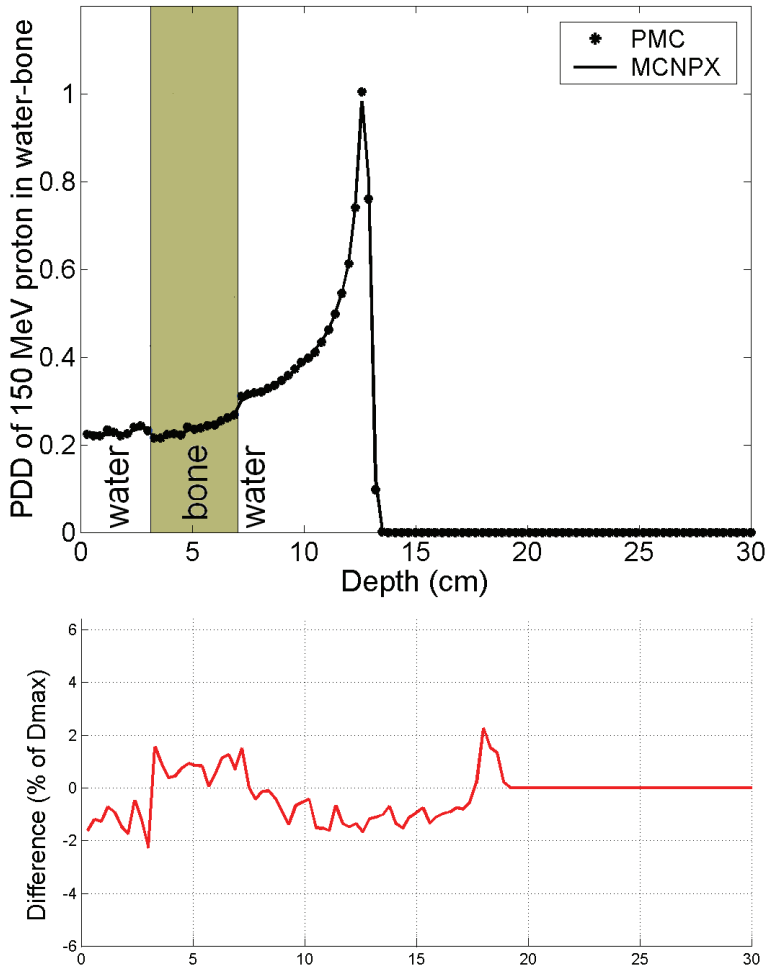

Figure 6.9 PDD of 150 MeV protons in the water phantom in which a 4 cm slab of bone is embedded. Figure (b) illustrates the lateral dose calculation for this phantom.

Transport of 1 million protons with PMC code takes around 60-100s for various homogeneous and inhomogeneous materials in Pentium 1.3 GHz. In terms of speed, the PMC code for protons runs 200 times faster than MCNPX on the same computer. This factor is reasonable considering the fact that MCNP is a relatively slow code.[48] For electron transport the code runs 40-60 times faster than EGSnrc.

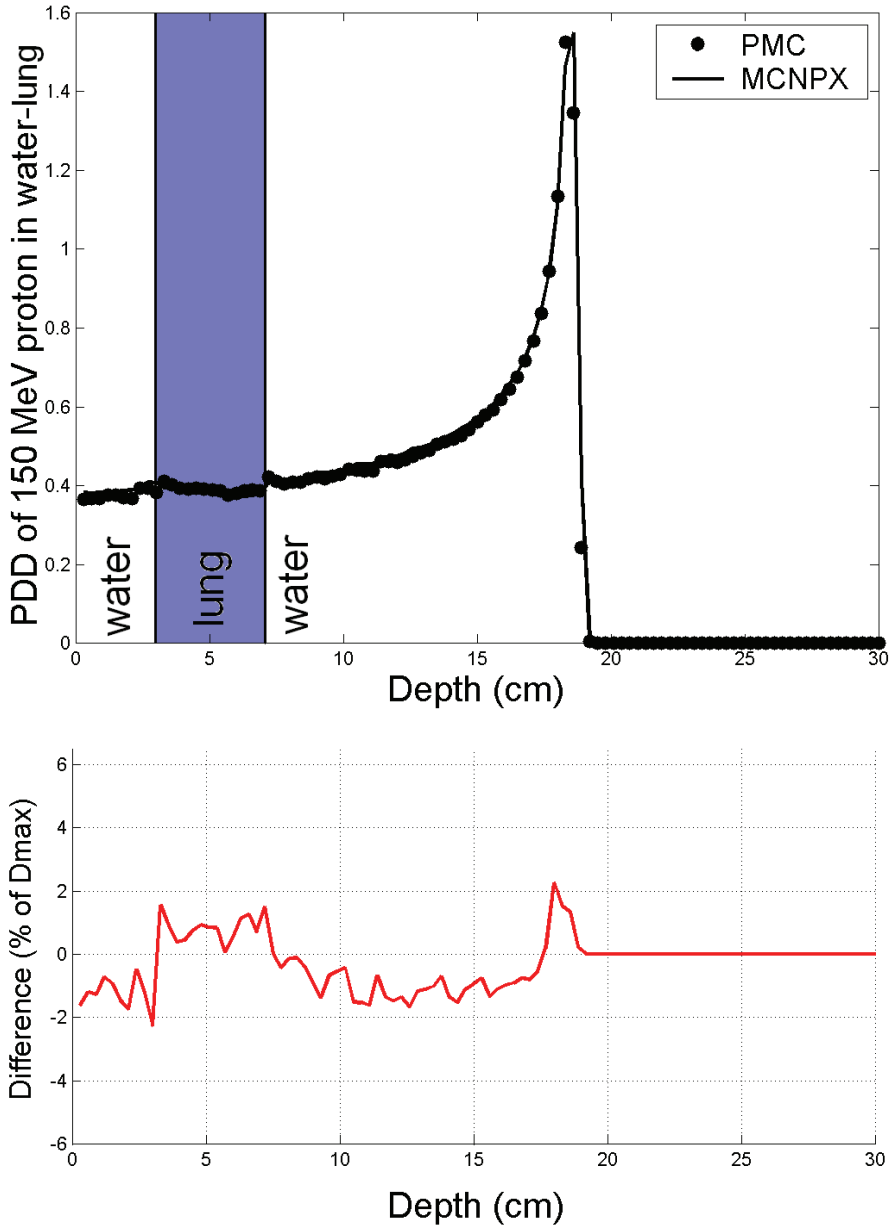

Figure 6.10 PDD of 150 MeV protons in water-lung phantom, and 4×4 cm^2 field size.

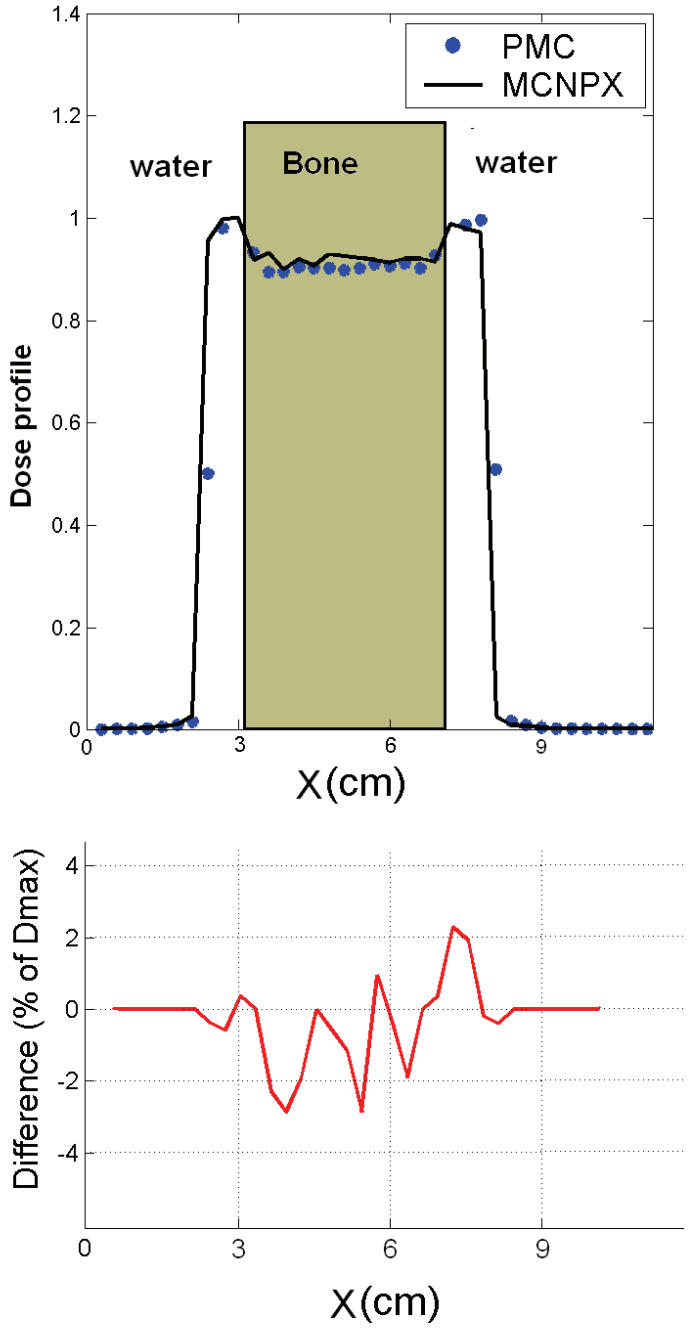

Figure 6.11 The comparison of dose lateral profile at the middle of the bone slab for 6×6 cm^2 field size. The energy of the proton beam is 150 MeV and the profile is compared at depth of 2 cm.

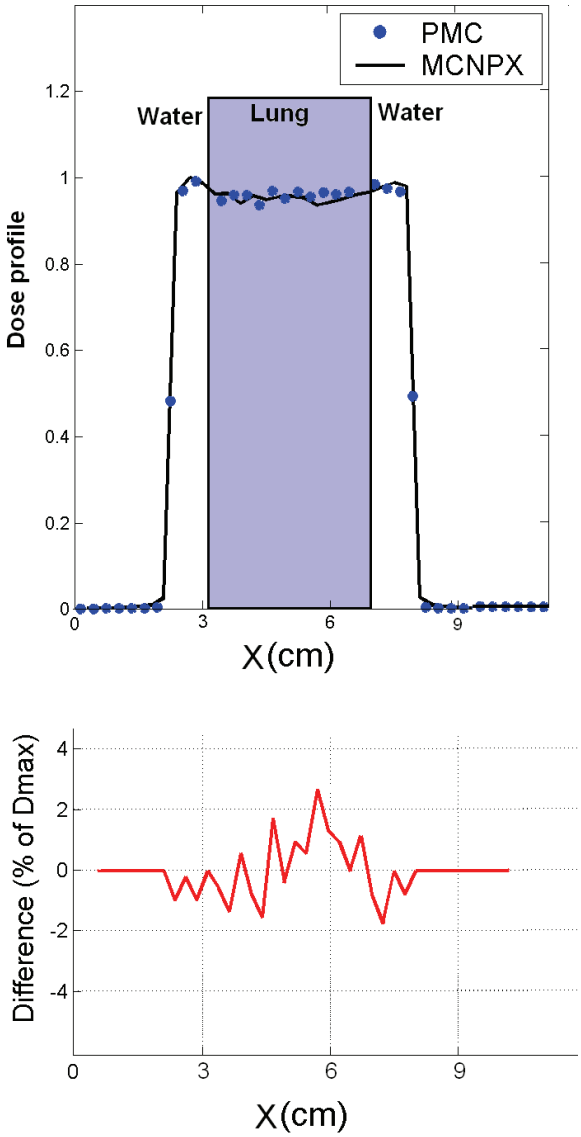

Figure 6.12 The comparison of dose lateral profile at the middle of the lung slab. The energy of the proton beam is 150 MeV and the profile is compared at depth of 2 cm.

6.7.4 Result of dose calculation in a CT based phantom

The PMC code has been employed for proton transport in a CT based head phantom. The head phantom contains various materials such as soft tissue, bone, air cavity. The density of each voxel is determined after appropriate calibration using Hounsfield numbers.[49] Hounsfield numbers are closely related to attenuation coefficients

that range from -1000 (air) to +1000 (dense bone or tooth enamel). CT uses water as its standard value and it is assigned a Hounsfield number of 0.[50]

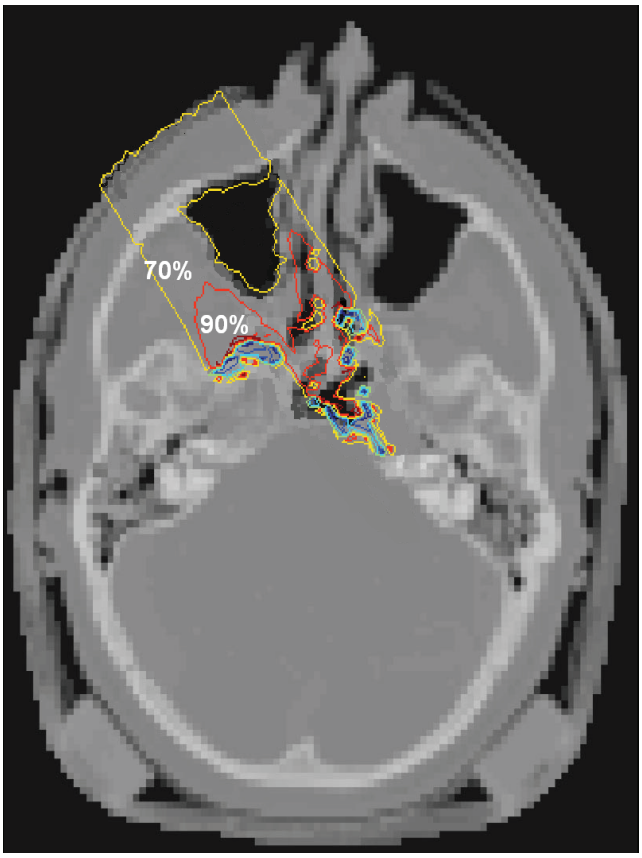

Figure 6.13 Dose distribution in the patients head irradiated with 100 MeV protons. The field size is 5×5 cm^2 and the resolution of the voxels is 2 mm in each dimension.

The input for PMC code is a 3D matrix of real numbers related to the density of each voxel. In a typical phantom we may have different materials with various densities. For example density of bone density in may vary from 1.6-3 g/cm^3. For the proton transport in one material with various densities as mentioned in Section 3.5, the pre-calculated track is scaled using the density of each voxel on the fly. The head phantom is illustrated in Fig. 6.13.The resolution of the phantom is 2 mm^3. The isodose curves represent the dose distribution of 100 MeV protons incident on 5×5 cm^2 field size. The effect of the air cavities and boney structures on the isodose curves are handled properly and can be observed.

6.8 Conclusions

The fast Monte Carlo code, Pre-calculated Monte Carlo has been developed for proton particle. The pre-calculated data is generated by the general purpose MC code, MCNPX. The major difference of PMC code and other fast MC codes based on pre-generated data is that the pre-generated data is calculated for each particular material therefore all the physics is calculated by the general purpose code. This fact makes the physics part of the code very simple especially for proton particles since there are many different types of secondary particles that are produced. The pre-calculated data contains tracks of 10000 protons for various energies and materials and the size of the pre-calculated data is in the order of 100 Mb for each material with the size of the entire data being as high as 1 Gb. The PMC code generally produced accurate results and the transport of protons near the heterogeneities is performed very accurately.

References

1. R. Smith, "Proton therapy" Phys. Med. Biol. **45,** R491–R504 (2006).
2. D. W. Miller "A review of proton beam radiation therapy," Med. Phys. **11**, 1943–1953 (1995).
3. M. Urie, M. Goitein, and M. Wagner, "Compensating for heterogeneities in proton radiation therapy," Phys. Med. Biol. **29**, 553–566 (1984).
4. C. H. Lee, D. Tait, A. E. Nahum, and S. Webb, "Comparison of proton therapy and conformal x-ray therapy in non-small cell lung cancer (nsclc)," Br. J. Radiol. **72**, 1078–1084 (1999).
5. M. Fuss, L. N. Loredo, P. A. Blacharski, R. I. Grove, and J. D. Slater, "Proton radiation therapy for medium and large choroidal melanoma: preservation of the eye and its functionality," Int. J. Radiat. Oncol. Biol. Phys. **49**, 1053–1059 (2001).

6. H. Paganetti, A. Niemierko, M. Ancukiewicz, L. E. Gerweck, J. S. Loeffler, M. Goitein, and H. D. Suit, "Relative biological effectiveness (RBE) values for proton beam therapy," Int. J. Radiat. Oncol. Biol. Phys. **53**, 407–421 (2002).

7. P. L. Petti, "Evaluation of a pencil-beam dose calculation technique for charged particle radiotherapy," Int. J. Radiat. Oncol. Biol. Phys. **35** 1049–57 (1996).

8. L. Hong, M. Goitein, M. Bucciolini, R. Comiskey, B. Gottschalk, S. Rosenthal, C. Serago and M. Urie, "A pencil beam algorithm for proton dose calculations," Phys. Med. Biol. **41,** 1305–1330 (1996).

9. T Bortfeld, "An analytical approximation of the Bragg curve for therapeutic proton beams," Med. Phys. **24,** 2024–33 (1997).

10. H. Szymanowski, A. Mazal, C. Nauraye, S. Biensan, R. Ferrand, M. C. Murillo, S. Caneva, G. Gaboriaud, and J. C. Rosenwald, "Experimental determination and verification of the parameters used in a proton pencil beam algorithm," Med. Phys. **28**, 975–987 (2001).

11. M. J. Berger, "Penetration of proton beams through water II. Three dimensional absorbed dose distributions," Technical Report NISTIR 5330(National Institute of Standards and Technology, Gaithersburg, MD, 1993).

12. M. Lee, A. E. Nahum, and S. Webb, "An empirical method to build up a model of proton dose distribution for a radiotherapy treatment planning package," Phys. Med. Biol. **38**, 989–998 (1993).

13. L. Hong, M. Goitein, M. Bucciolini, R. Comiskey, B. Gottschalk, S. Rosenthal, C. Serago, and M. Urie, "A proton beam algorithm for proton dose calculations," Phys. Med. Biol. **41**, 1305–1330 (1996).

14. K. Russell, U. Isacsson, M. Saxner, A. Ahnesjo, A. Montelius, E. Grusell, C. V. Dahlgren, S. Lorin, and B. Glimelius, "Implementation of pencil kernel and depth penetration algorithms for treatment planning of proton beams," Phys. Med. Biol. **45**, 9–27 (2000).

15. H. Szymanowski and U. Oelfke, "Two-dimensional pencil beam scaling: an improved proton dose algorithm for heterogeneous media," Phys. Med. Biol. **47**, 3313–3330 (2002).

16. M. Soukup, M. Fippel, and M. Alber, "A pencil beam algorithm for intensity modulated proton therapy derived from Monte Carlo simulations," Phys. Med. Biol. **50**, 5089–5104 (2005).

17. S. L. Haisen, H. E. Romeijn, C. Fox, J. R. Palta, and J. F. Dempsey," A computational implementation and comparison of several intensity modulated proton therapy treatment planning algorithms," Med. Phys. **35**, 1103–1112 (2008).

18. A. J. Lomax, T. Bohringer, A. Bolsi, D. Coray, F. Emert, G. Goitein, M. Jermann, S. Lin, E. Pedroni, H. Rutz, O. Stadelmann, B. Timmermann, J. Verwey, and D. C. Weber, "Treatment planning and verification of proton therapy using spot scanning: Initial experiences," Med. Phys. **31**, 3150–3157 (2004).

19. S. Agostinelli *et al*., "GEANT4—A simulation toolkit," Nucl. Instrum. Methods Phys. Res. A 506, 250–303 (2003).

20. A. Fasso, A. Ferrari, and P. R. Sala, ''Electron–photon transport in FLUKA: status,'' in Advanced Monte Carlo for Radiation Physics, Particle Transport Simulation and Applications, Proceedings of the Monte Carlo 2000 Conference, Lisbon, October 23–26, 2000, edited by A. Kling, F. Barao, M. Nakagawa, L. Tavora, and P. Vaz (Springer-Verlag, Berlin, 2000), pp. 159–164.

21. A. Fasso, A. Ferrari, J. Ranft, and P. R. Sala, "FLUKA: Status and Prospective for Hadronic Applications," in Advanced Monte Carlo for Radiation Physics, Particle Transport Simulation and Applications, Proceedings of the Monte Carlo 2000 Conference, Lisbon, October 23–26, 2000, edited by A. Kling, F. Barao, M. Nakagawa, L. Tavora, and P. Vaz (Springer-Verlag, Berlin, 2000) , pp. 955–960.

22. F. B. Brown, "MCNP—A general Monte Carlo-particle transport code, version 5," Report LA-UR-03 1987, Los Alamos National Laboratory, Los Alamos, NM, 2003.

23. K. Parodi, H. Paganetti, E. Cascio, J. B. Flanz, A. A. Bonab, N. M. Alpert, K. Lohmann, and T. Bortfeld, "PET/CT imaging for treatment verification after proton therapy: A study with plastic phantoms and metallic implants," Med. Phys. **34**, 3369–3387 (2007).

24. J.-P. Pignol, P.Cuendet, N. Brassart, G. Fares, F. Colomb, C. M. Diop, R. Sabattier, A. Hachem, and G. Prevot "Combined use of FLUKA and MCNP-4A for the Monte

Carlo simulation of the dosimetry of ^{10}B neutron capture enhancement of fast neutron irradiations," Med. Phys. **25**, 885–891 (1998).

25. C. L. Lee, X. L. Zhou, R. J. Kudchadker, F. Harmon, Y. D. Harker, "A Monte Carlo dosimetry-based evaluation of the 7Li(p,n)7Be reaction near threshold for accelerator boron neutron capture therapy," Med. Phys. **27**, 192–202 (2000).

26. A. Knopf, K. Parodi, H. Paganetti, E. Cascio, A. Bonab, and T. Bortfeld, "Quantitative assessment of the physical potential of proton beam range verification with PET/CT," Phys. Med. Biol. **53**, 4137–4151 (2008).

27. S. Trovati, F. Ballarini, G. Battistoni, F. Cerutti, A. Fassò, A. Ferrari, E. Gadioli, M. V. Garzelli, A. Mairani, A. Ottolenghi, H. G. Paretzke, V. Parini, M. Pelliccioni, L. Pinsky, P. R. Sala, D. Scannicchio, and M. Zankl, " Human exposure to space radiation: role of primary and secondary particles," Human exposure to space radiation: role of primary and secondary particles," Radiat. Prot. Dosimetry 122, 362–366 (2006).

28. P. Kimstrand, N. Tilly, A. Ahnesjö and E. Traneus, "Experimental test of Monte Carlo proton transport at grazing incidence in GEANT4, FLUKA and MCNPX," Phys. Med. Biol. **53**, 1115–1129 (2008).

29. C. Theis, D. Forkel-Wirth, D. Perrin, S. Roesler, and H. Vincke, "Characterisation of ionisation chambers for a mixed radiation field and investigation of their suitability as radiation monitors for the LHC," Radiat. Prot. Dosimetry 116, 170–174 (2005).

30. M. Fippel and M. Soukup, "A Monte Carlo dose calculation algorithm for proton therapy," Med. Phys. **31,** 2263–2273 (2004).

31. J. S. Li, B. Shanine, E. Fourkal and C-M Ma, "A particle track-repeating algorithm for proton beam dose calculation," Phys. Med. Biol. **50,** 1001–1010 (2005).

32. A. Tourovsky, A. J. Lomax, U. Schneider, E. Pedroni, "Monte Carlo dose calculations for spot scanned proton therapy," Phys. Med. Biol. **50,** 971–981 (2005).

33. I. Kawrakow, M. Fippel, and K. Friedrich, "3D Electron Dose Calculation using a Voxel based Monte Carlo Algorithm," Med. Phys. **23**, 445–457 (1996).

34. I. Kawrakow and M. Fippel, "Investigation of variance reduction techniques for Monte Carlo photon dose calculation using XVMC," Phys. Med. Biol. **45**, 2163–2184 (2000).

35. I. Kawrakow and M. Fippel, "VMC++, a MC algorithm optimized for electron and photon beam dose calculations for RTP," in Proceedings of the 22nd Annual International Conference of the IEEE (Engineering in Medicine and Biology Society, Piscataway, NJ, 2000).

36. I. Kawrakow, "VMC++, electron and photon Monte Carlo calculations optimized for Radiation Treatment Planning," Advanced Monte Carlo for Radiation Physics, Particle Transport Simulation and Applications: Proceedings of the Monte Carlo 2000 Meeting Lisbon, edited by A. Kling, F. Barao, M. Nakagawa, L. Távora, and P. Vaz (Springer, Berlin, 2001), pp. 229–236.

37. Ma C-M *et al.* "MCSIM—a Monte Carlo dose calculation tool for radiation therapy," *Proc. 14th ICCR*, (Seoul,Korea, 2004), pp. 123–126.

38. Los Alamos National Laboratory *MCNPX User's Manual* Version 2.4.0, LANL Report LA-CP-02-408 (2002)

39. A. Facure, A. X. da Silva, L. A. da Rosa, S. C. Cardoso and G. F. Rezende, "On the production of neutrons in laminated barriers for 10 MV medical accelerator rooms," Med. Phys. **35,** 3285–3292 (2008).

40. M. Sadeghi, G. Raisali, S. H. Hosseini, and A. Shavar "Monte Carlo calculations and experimental measurements of dosimetric parameters of the IRA-103Pd brachytherapy source," Med. Phys. **35,** 1288–1294 (2008).

41. A. J. Bolewski, M. Ciechanowski, A. Dydejczyk, and A. Kreft, "On the optimization of the isotopic neutron source method for measuring the thermal neutron absorption cross section: advantages and disadvantages of BF3 and 3He counters," Appl. Radiat. Isot. **66**, 457-462 (2008).

42. A. K. Jaradat and P. J. Biggs, "Tenth value layers for 60Co gamma rays and for 4, 6, 10, 15, and 18 MV x rays in concrete for beams of cone angles between 0 degrees and 14 degrees calculated by Monte Carlo simulation," Health Phys. **92**, 456–463 (2007).

43. A. Bozkurt and D. Bor, "Simultaneous determination of equivalent dose to organs and tissues of the patient and of the physician in interventional radiology using the Monte Carlo method," Phys. Med. Biol. **52**, 317–330 (2007).

44. ICRU-Report No. 44 : Tissue substitutes in radiation dosimetry and measurement," in International Commission on Radiation Units and Measurements, 1989. http://physics.nist.gov/PhysRefData/XrayMassCoef/tab2.html

45. F. Verhaegen and H. Palmans "A systematic Monte Carlo study of secondary electron fluence perturbation in clinical proton beams (70–250 MeV) for cylindrical and spherical ion chambers," Med. Phys. **28,** 2088–95 (2001).

46. H. Paganetti, "Nuclear interactions in proton therapy: dose and relative biological effect distributions originating from primary and secondary particles," Phys. Med. Biol. **47**, 747–64 (2002).

47. ICRU-Report No. 63 : Nuclear Data for Neutron and Proton Radiotherapy and for Radiation Protection," in International Commission on Radiation Units and Measurements, 2000.

48. I. Chetty *et al*., "Guidance report on clinical implementation of the Monte Carlo method in external beam radiation therapy treatment planning: Report of the AAPM Task Group No. 105," Med. Phys. **34**, 4818–4853 (2007).

49. J. J. De Marco, T. D. Solberg, and J. B. Smathers, "A CT-based Monte Carlo simulation tool for dosimetry planning and analysis," Med. Phys. **25**, 1–11 (1998).

50. H. Szymanowski and U Oelfke, "CT calibration for two-dimensional scaling of proton pencil beams," Phys. Med. Biol. **48**, 861–874 (2003).

51. K. Hayashi, R. Tayama, K. Shibata, T. Honda, M. Morimoto, T. Izumida, T. Horikawa, S. Kanaya and K Kusakabe, "Development of a simple method to evaluate medical staff radiation dose and its application to a software system supporting PET facility operation," Radiat. Prot. Dosimetry 116, 196–201 (2005).

52. D. M. Duggan, "Improved radial dose function estimation using current version MCNP Monte-Carlo simulation: Model 6711 and ISC3500 125I brachytherapy sources," Appl Radiat Isot. 611, 443–450 (2004).

53. R. Zamenhof, E. Redmond, G. Solares, D. Katz, K. Riley, S. Kiger, and O. Harling, "Monte Carlo-based treatment planning for boron neutron capture therapy using custom designed models automatically generated from CT data," Int. J. Radiat. Oncol. Biol. Phys. **35**, 383–397 (1996).

54. P. V. Vavilov, ”Ionization Losses of High-Energy Heavy Particles,” *Soviet Physics JETP* **5,** 749–51 (1957).

55. G. Ciangaru, J. C. Polf, M. Bues, and A. R. Smith, “Benchmarking analytical calculations of proton doses in heterogeneous matter,” Med. Phys. **31** 3511–23 (2005).

56. Å. K. Carlssonyx, P. Andreoyz, and A. Brahmey, “Monte Carlo and analytical calculation of proton pencil beams for computerized treatment plan optimization,” Phys. Med. Biol. **42,** 1033–1053 (1997)

Chapter 7

Use of orthogonal bremsstrahlung beams for improved radiation therapy imaging

7.1 Introduction to patient imaging

7.1.1 Portal films

An important aspect in radiation therapy, patient positioning is usually achieved with the help of megavoltage portal images.[1-3] In this technique, the image of the patient is obtained by high energy, forward-directed photon beams. This is one of the imaging modalities that enables us to take an image during radiation therapy and produce an online record of the treatment.[4-10] Portal imaging in its early stages was performed with portal films, a special film emulsions sensitive to high energy radiation.[11] The films needed an initial calibration, and after irradiation, the films were scanned and image densities were converted to dose using the previously determined calibration curves.[12-14] A typical portal film setup is illustrated in Fig. 7.1. These exposure conditions depend on the distance between the radiation source and the film, the thickness of the patient and the field size of the beam.

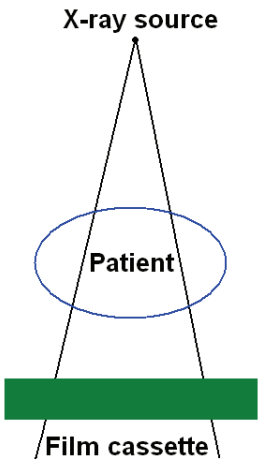

Figure 7.1 Schematic drawing of portal film setup.

For high energy linear accelerators, the quality of portal films, in particular their contrast, is poor because differences in the attenuation coefficient is small for soft tissues at high energies.[15] Another disadvantage of portal films is that the film development and further imaging takes approximately half an hour to complete, making the entire process very time-consuming. The port films which were exposed on identical accelerators were found to differ significantly in appearance because of many factors that affect the final results such as exposure time, cassette geometry, screen material, film emulsion and processor chemistry. Many groups tried to enhance the quality of portal images.[9,13,17] However, advances in technology have led to the development of much more sophisticated and convenient methods, namely electronic portal imaging devices, that are able to produce images using high energy x-rays directly.

7.1.2 Electronic portal imaging devices (EPIDs)

Electronic portal imaging devices (EPIDs) have many potential advantages over traditional x-ray films for portal imaging.[18] In EPID technology, higher contrast images can be obtained with a smaller radiation dose as compared to the older port films. The digitally-obtained images are immediately available for viewing and can be used to adjust patient or field position during radiotherapy interactively. Because of their digital nature, various image processing, contrast enhancement, and image matching techniques can be performed online. Moreover, digital archiving saves space and allows for rapid recall of images over a network.[19-24] There are few types of EPIDs: Camera based EPIDs[25], Matrix ion chamber[19,26-28] and Flat panel EPIDs[29-31].

An example of camera based EPIDs is illustrated in Fig. 7.2. The system consists of an X-ray-to-light converter scintillator, a mirror and a TV camera. The x-ray-to-light converter is usually a metal plate covered with phosphor.

The principles behind ion chamber EPIDs are straight forward and consist of two arrays of 265 chambers.[18] The matrix ion chamber array is read out by applying high voltage (300-500 V) electrodes in succession and measuring the signal generated in each of the 256 signal electrodes.

Flat panel EPID's uses advance technology of amorphous silicon arrays photodiodes and thin film transistors.[29] The photodiodes are electronically read and form the pixels of

the image. This kind of portal imaging has the advantages of requiring short exposure times (i.e., very low number of monitor units), producing images of superior quality and higher contrast relative to older portal films, and providing the ability to verify the proper positioning of the patient prior to dose delivery.

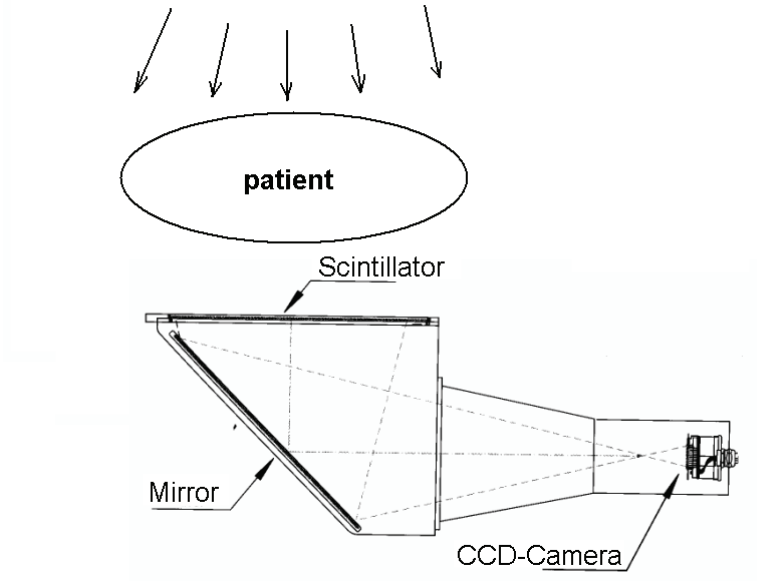

Figure7.2 Electronic portal imaging setup using TV camera.

7.1.3 Cone Beam CT

Currently, there is interest in producing 3-dimensional images using megavoltage beams by developing the megavoltage cone beam CT based technology.[32-38] This system consists of a standard linear accelerator equipped with an amorphous-silicon flat panel electronic portal-imaging device. A cone-beam CT image is reconstructed from a set of open-field projection images acquired at different positions around the patient. An integrated computer workspace provides automated acquisition of projection images, image reconstruction, CT to Cone Beam CT image registration, and couch shift calculation.[32] The EPID readings are first converted to dose using a calibration curve. Subsequently, using image preprocessing and 3D reconstruction, a 256×256×256 voxel reconstruction can be created from 100 projections (256×256 pixels per projection) taken from the patient,.

The cone beam CT scan can be completed in less than one minute with a single complete rotation of the gantry around the patient. Unlike conventional CT, the patient is not moved through the gantry during scanning because of the wide beam used for imaging. Cone beam CT has undergone significant developments in the past few years.[39-46] Current image quality has already proven sufficient for many applications such as Image Guided Radiation Therapy applications (IGRT).

A major advantage of this approach is that the same source is used in the imaging and treatment modes resulting in reduction of errors due to misalignment of the reference coordinates.[37] Another disadvantage of the megavoltage cone beam CT is that a relatively large dose is delivered to the patient to achieve acceptable image quality, discouraging the use of this method on a regular clinical basis.[32] However, as these images are created with megavoltage photons, the images' intrinsic contrast as well as their signal-to-noise ratio are inferior to those obtained with diagnostic kilovoltage beams.[46] A comparison of kilovoltage and megavoltage images is illustrated in Fig. 7.3.

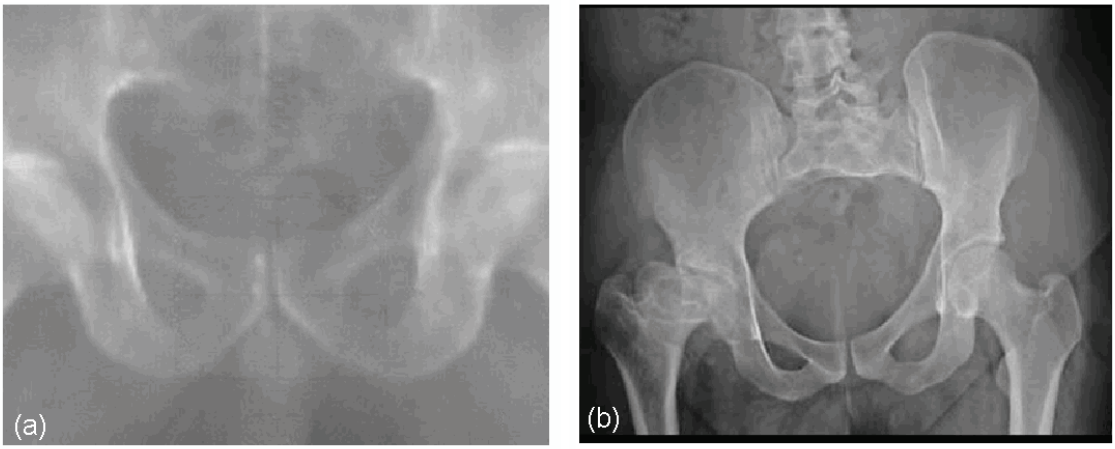

Figure 7.3 Comparison of image contrasts. The megavoltage image of a pelvis is illustrated in (a) and an x-ray pelvis image is illustrated in (b).

7.1.4 Improvement of image contrast

To improve image contrast, the photon energy should be decreased to the energy region where the photoelectric effect becomes important, since in this region the atomic number of the absorbing material has a strong effect on the attenuation coefficient.[47] Several methods have been developed to lower the photon beam energy, such as using low

atomic number materials for targets[47,48] and decreasing the energy of electrons striking the target.[49] In the commercial implementation, a separate x-ray tube and imaging device are mounted on the linac gantry such that the central axis of the x-ray tube is at 90° to that of the linac beam.[37]

Ostapiak *et al*. investigated the performance of various target materials by filming an aluminum contrast object.[48] Beryllium, carbon and conventional target materials were studied and the bremsstrahlung spectra of these materials were also simulated using Monte Carlo techniques. The treatment head of a Siemens linear accelerator has been modified to accommodate a low Z target for investigational use. In this study, a factor of 2 improvement in contrast is gained by using the low Z technique over conventional therapy imaging.

7.2 Previous studies of bremsstrahlung beams

Several groups have studied the energy spectrum and angular distribution of the bremsstrahlung beams produced by various target materials.[49-58] Based on Monte Carlo calculations as well as experimental results, the study by Faddegon *et al*. provides a detailed look at the measured mean energy, angular distribution and spectrum of bremsstrahlung beams. The experimental setup of this work is illustrated in Fig. 7.4.

In this setup, the electron beam emerges from the beam tube through a thin Ti window, passes through a detector used for monitoring of the beam current, and impinges on the target. Measurements were performed at θ= 0°, 1°, 2°, 4 °, 10°, 30°,60°,90°. The nominal distance from the target to the NaI detector was 300 cm and the diameter of the electron beam was focused to be 0.35 mm. The targets were cylinders of wide range of atomic numbers: Be (7.7 cm thick, 4.2 cm radius), Al (3.6 cm thick, 3.6 cm radius), and Pb(0.8 cm thick, 1.5 cm radius). The NaI detector and the photomultiplier tube (PMT) used in this experiment are modified to improve the detector sensitivity and are shielded by Pb housing as illustrated in Fig. 7.4.[53]

The bremsstrahlung yield is defined as the number of photons of particular energy from the target that reach a given point in vacuum per unit solid angle. The solid angle is defined from the point of intersection of the beam axis with the upstream surface of the target (Fig. 7.4).

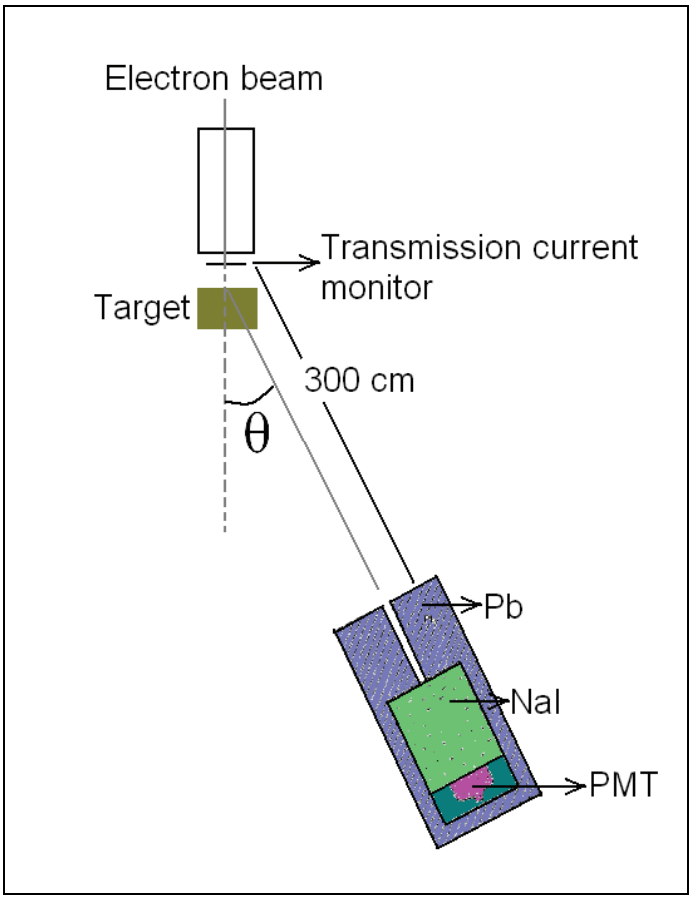

Figure 7.4 Experimental setup used by Faddegon *et al.* for measurement of bremsstrahlung yield of various targets. The range of the angle, θ, is between 1°-90°.

In the MC calculation part of this work, EGSnrc along with PRESTA electron transport algorithms are used. The energy of the primary electrons was restricted to 15 MeV and the energy cutoffs for Monte Carlo calculations were 0.145 MeV and 0.1 MeV for electrons and photons, respectively.

The angle of interest in this study is extended to 90 degrees, so it includes the mean energy, spectrum and relative fluence of the orthogonal beam. The energy of the primary electrons was restricted to 15 MeV and the energy cutoffs for Monte Carlo calculations were 0.145 MeV and 0.1 MeV for electrons and photons, respectively. Faddegon *et al* found good agreements between the Monte Carlo simulations and the measured data. Using their data as an initial benchmark, the same geometry (Fig. 7.4) with 15 MeV incident

electrons were simulated and the same results were obtained, discussed in the following sections.

Our study evaluated various parameters of orthogonal beams relevant for imaging including their basic characteristics, such as energy and relative fluence for various target materials. Using Monte Carlo calculations, we carried out an optimization of target dimensions and used the results to build the targets for our experiments. We found a good agreement between calculated and measured image contrast for the various target materials, and concluded that orthogonal bremsstrahlung beams produced by megavoltage electron beams striking low atomic number targets are suitable for clinical imaging in radiotherapy.

7.3 Use of the orthogonal x-ray beams for imaging

In this work we show that by placing a specially designed target in the linac head and using the orthogonal component of the bremsstrahlung beam, kilovoltage x-ray quality images can be obtained because of the much reduced mean energy of the bremsstrahlung beams in this direction. The orthogonal beam can be used as the source for the kilovoltage portal and 3-D imaging, thereby allowing the imaging and the clinical beam to emanate from the same focal spot.

Figure 1 shows schematically a linac in the standard treatment mode (a), and the proposed setup for a linac in the imaging mode equipped with the orthogonal bremsstrahlung beam capability (b). In the standard mode, a 270° bending magnet is used to bend the electron beam produced by the accelerator tube in order to reduce the focal spot size.[61] For each electron energy, the strength of the magnetic field has to be set to a specific level. Changing the magnetic field strength is done by changing the electric current through the bending magnets.

In the standard treatment mode, a parallel circular electron beam with a radius of about 1 mm hits the target surface and bremsstrahlung photons are created and emitted in all directions, although the greatest fluence is in the forward direction. These photons will then pass through the Beryllium window, the flattening filter, the monitor chamber and the mirror. The role of the following secondary collimators is to block the radiation.[62-64]

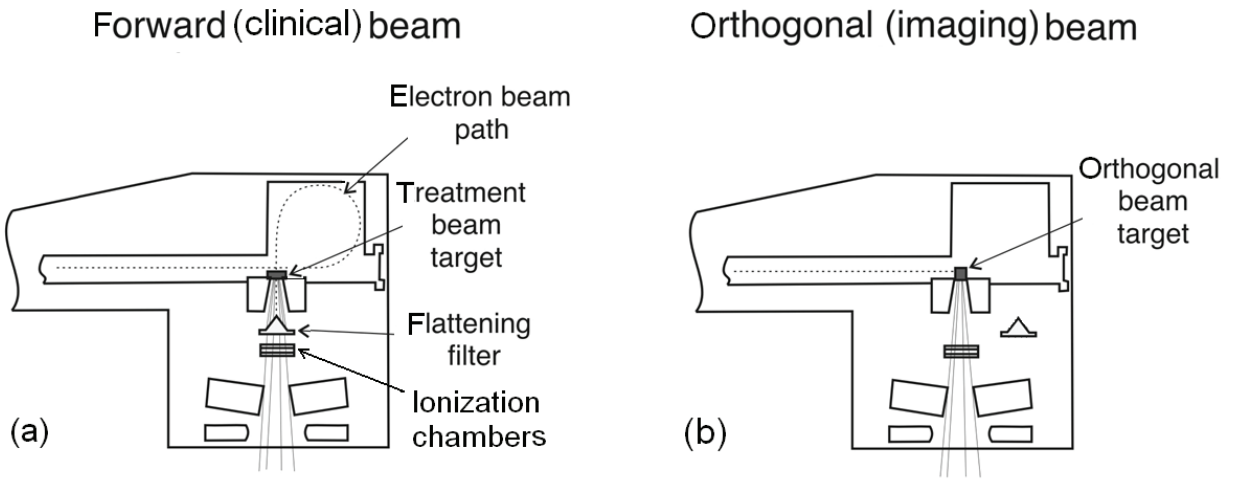

Figure 7.5 Generation of low energy bremsstrahlung beams in the imaging mode: (a) Standard treatment clinical beam setup; (b) Configuration for imaging beam setup in which the bending magnet is turned off and the electron beam hits the modified target from the side. The orthogonal bremsstrahlung beam is used for imaging.

In the imaging mode, the bending magnet of the linac beam transport system is turned off, and the electrons that exit the waveguide hit the modified target directly. The much reduced effective energy orthogonal component of the bremsstrahlung beam is then used to produce a kV-quality image. Although the mean energy of the orthogonal component of the bremsstrahlung beam is always less than the forward-directed beam, this difference in mean energy is more pronounced when the beam is produced in a low atomic number target (i.e., it has a significant spectral contribution in the low x-ray energy range).[50] Hence, an image produced with the orthogonal beam has the potential to have a higher contrast and better quality compared to that obtained with the high energy forward beam. We surmise that orthogonal beams could produce kilovoltage cone-beam CT for use in image-guided radiotherapy without the need for a separate x-ray source mounted on the linac gantry.

7.4 Monte Carlo calculations and optimization

7.4.1 Introduction to BEAMnrc

The BEAMnrc[66] code is usually used to simulate radiation therapy accelerators, and it has fine graphic interfaces. In the BEAMnrc user code, the geometry of the particle accelerator, the source unit (or another physical system to be modeled) is fixed using completely independent and re-usable "geometrical blocks", centered on the longitudinal symmetry axis of the system (*i.e.* z-axis). These blocks are named component modules (CMs) and each part of the system is considered to be a single CM.

A typical accelerator model simulated by BEAMnrc is illustrated in Fig. 7.6. To simulate a linear accelerator, every component module (e.g. SLABS, CONS3R, CONESTAK, FLATFILT, CHAMBERS, JAWS, APPLICAT) contains one or more regions in which different quantities of interest like absorbed dose can be scored. The original names of the CMs are related by the various accelerator components, but BEAMnrc is a very versatile code and can be used in a wide variety of applications beyond radiotherapy applications.[67-73]

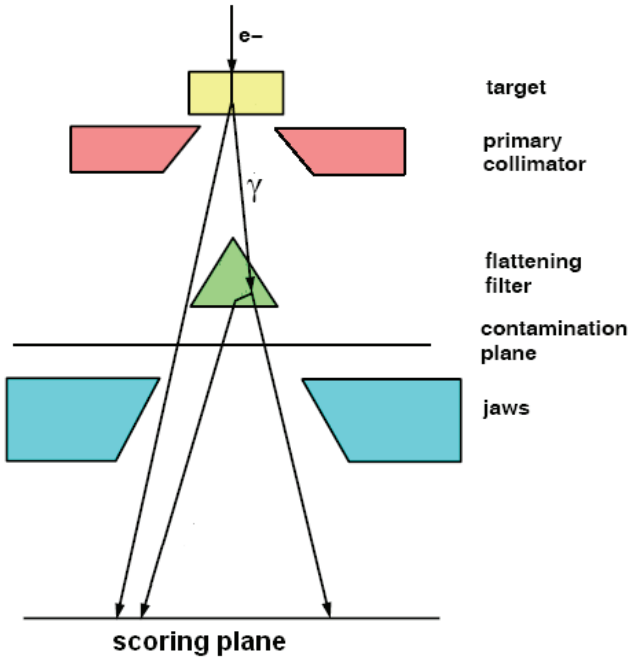

Figure 7.6 A typical accelerator model in BEAMnrc in photon mode using different component modules.

One of the most important design features of the BEAMnrc is the possibility of defining a certain number of scoring planes between two consecutive CMs or at the end of the last CM. These planes are always perpendicular to the *z* axis. The complete information (charge, energy, position, direction, history) of each particle crossing a user defined scoring plane is recorded in a phase space data file that can be re-used in BEAMnrc or as an input in other Monte Carlo codes (like BEAMDP[67]) in order to determine the particles characteristics (fluence, angular distributions or energy spectra, etc.) or to calculate dose distributions in phantoms.

7.4.2 Optimization of the target dimensions

The BEAMnrc code was used to design the targets and to simulate configurations for the creation of orthogonal beams. The reliability of our simulation was confirmed by calculating the spectra for the setup of the experiments performed by Faddegon *et al*.[50] As mentioned in Section 7.3, Faddegon used a 15 MeV electron beam incident on thick targets of various materials and measured the mean energy and energy spectrum with a sodium iodide detector placed 300 cm away from the target at various angles with respect to the incident electron beam. The mean energies of the orthogonal photon beams created by the 15 MeV electrons were 1.8, 0.6, and 0.4 MeV for lead (Pb), aluminum (Al), and beryllium (Be) targets, respectively.

Table 1 R_{CSDA} of 4-18 MeV electrons in various materials in *cm*.

	W ρ=19.3 g/cm^3	Pb ρ=11.3 g/cm^3	Al ρ=2.67 g/cm^3	C ρ=1.7 g/cm^3	Be ρ=1.85g/cm^3
4 MeV	0.16	0.27	0.92	1.36	1.39
6 MeV	0.22	0.37	1.36	1.89	2.09
12 MeV	0.36	0.60	2.55	3.64	4.40
15 MeV	0.42	0.70	3.08	4.82	5.01
18 MeV	0.47	0.79	3.61	5.68	5.92

In experiments carried out by Faddegon *et al.* the targets were cylinders with approximately 110% of R_{CSDA} (the continuous-slowing-down approximation range) in

height as well as radius, and the beam hit the target along the axis of the cylinder. The R_{CSDA} of various materials at various energies is illustrated in Table.1 Although the thickness of 110% of R_{CSDA} in the forward direction is sufficient to achieve a high photon intensity while eliminating electron contamination, this is not necessarily true for the radius in the orthogonal beam direction.

The targets are simulated by using XTUBE component module in the BEAMnrc code, Fig. 7.7(a). This component module is usually used to simulate the target in the x-ray tube and the primary electron beam is incident on the target from the side.[57] XTUBE may have an arbitrary number of layers, each with different thickness and materials. We irradiated the target from the side, by setting the angle of declined surface of the component (θ in Fig. 7.7(a)) to zero. Details of the accelerator head were not considered in the initial simulations, since the first goal was to study the characteristics of the orthogonal bremsstrahlung beam emerging from the target. Photon yields and spectra of various targets, composed of materials covering a wide range of atomic numbers (Be, carbon (C), Al, copper (Cu), Pb, tungsten (W)) were investigated. The energy of the incident electrons was 6 and 12 MeV, and the energy cutoffs were set at 0.1 MeV for both electrons and photons. The diameter of the beam was set to 1.2 mm, which is a typical diameter of the electron pencil beam produced by a linac and emerging through the exit window.[53]

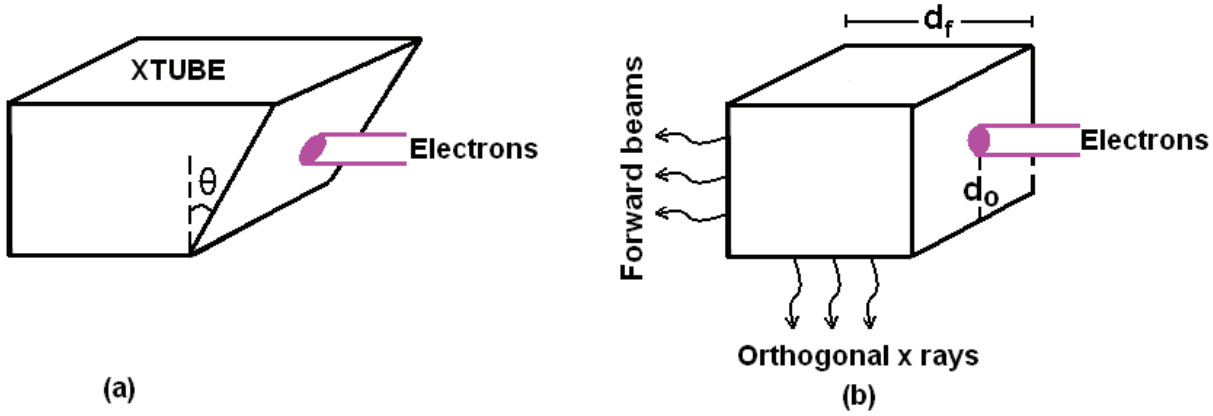

Figure 7.7 Simulation geometry and parameters used for targets used in the Monte Carlo calculations: (a) Illustration of the XTUBE component in BEAMnrc. The target angle in (a) is set to zero resulting in the geometry shown (b) where d_f represents the thickness of the target in the forward direction and d_o represents the distance between the edge of the source and edge of the target in the orthogonal direction.

The first set of simulations was carried out to compare the photon energy and the relative photon fluence produced by the various targets as well as to optimize the target dimension in the orthogonal direction. The target thickness in the forward direction (d_f in Fig. 7.7(b)) was set to 110% of R_{CSDA} in order to stop transmission of all electrons striking the target in the forward direction and to obtain the maximum photon yield in the orthogonal direction.

Through our work, the term "target thickness" in the orthogonal direction is referred to as d_o in Fig. 7.7(b). The optimal target thickness in the direction perpendicular to the incident electron beam was calculated by simulating targets of the same material with d_o that varied from 30% to 120% of R_{CSDA} for each target material. Phase space files were recorded in a 20×20 cm^2 scoring area, 50 cm below the target. The yield of the forward directed bremsstrahlung fluence for the same setup and materials was also calculated to obtain a ratio of the photon fluence yield in the orthogonal direction to that in the forward direction. Over 100 runs with each run having a minimum of two million incident electrons were simulated to study the effects of the target atomic number Z and target thickness on the orthogonal component of the bremsstrahlung beam.

7.4.3 Calculation of image contrast and beam profile

To evaluate the contrast of the images created by the orthogonal bremsstrahlung beam a simple contrast object was simulated. The object was made of Lucite with three steps of incremental 1 cm thicknesses, and an object with the same characteristics and material was used in the experimental setup. In the BEAMnrc code the steps were built with three successive 'block' component modules and the phase space file was stored after the third block. The setup is illustrated in Fig. 7.8 with the object placed 12 cm from the target. Using a home-developed MATLAB code, the intensity map of the particles was extracted from the resulting phase space file in the scoring plane. The MATLAB code uses an ASCII file which is generated by BEAMDP.[74] The BEAMDP program is used for processing of phase-space files and to derive spectral distributions, energy fluence distributions and energy fluence as a function of the position of the photon beam. BEAMDP is an interactive program which can analyze the results of BEAMnrc and generates an out put of various parameters such as:

1. a phase-space data file for beam characterization models;
2. fluence vs. position from a phase-space data file;
3. energy fluence vs. position from a phase-space data file;
4. spectral distributions from a phase-space data file;
5. an energy fluence distribution from a phase-space data file;
6. mean energy distributions from a phase-space data file;
7. angular distributions from a phase-space data file;
8. *x* and *y* scatter plot of particles from a phase-space data file;
9. the distribution of particle weights from the phase-space data file;
10. to combine two phase-space files into one;
11. to list the parameters of phase-space particles on the screen.

We used "x and y scatter plot of particles" with which the BEAMDP produced a large size file containing the position of all particles in the phase space file.

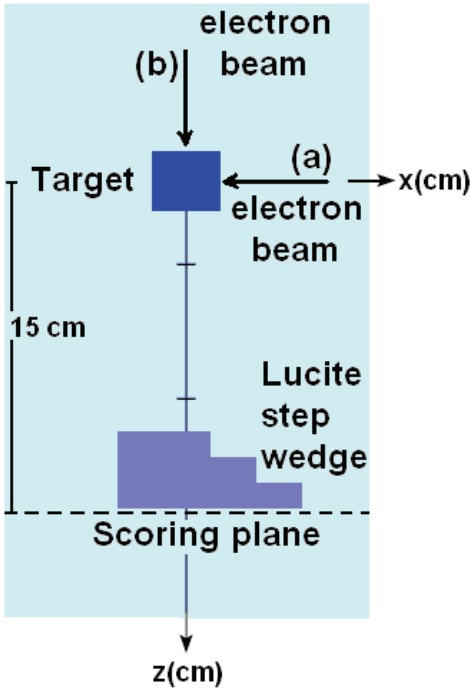

Figure 7.8 The simulated setup with BEAMnrc to compare the image contrast created with orthogonal photons (a) and forward photons (b). The target is XTUBE and the wedge is BLOCK component module of BEAMnrc and the energy of incident electron on the target is 6 and 12 MeV. The phase space file is gathered in a $5\times5cm^2$ square placed in the x-y plane right below the Lucite step wedge.

The contrast is defined as the ratio of the maximum change in intensity in an image to the maximum intensity[76] or

$$C = \frac{I_0 - I}{I_0} \tag{7.1}$$

where I_0 and I are the intensities of the brightest and darkest point in the image. This definition is used to compare the contrast of images in the forward and orthogonal direction for various target materials. The relative contrast calculated in this manner was compared with the measured contrast from the experiment.

An important characteristic of photons generated by the target in the orthogonal direction is the beam profile. The beam profile is a key parameter for the design of a flattening filter and Monte Carlo simulations have been a powerful tool for this purpose.[77-81] The shape of the profile depends mainly on the distribution of the electrons in the target. A review of the distribution of the electrons in the target and the relative photon beam spot size has been performed by Verhaegen and Seuntjens (2003).[82] For calculation of the beam profile the setup and the coordinate system are the same as in Fig. 7.8 but the contrast object was removed. The beam profile is calculated for distances of 50 cm and 100 cm from the target.

7.5 Equipment and experimental techniques

A Clinac-18 linac (Varian, Palo Alto, CA) installed at the Montreal General Hospital (Fig. 7.9) was used in the experimental study of the imaging characteristics of the orthogonal component of the bremsstrahlung beam.

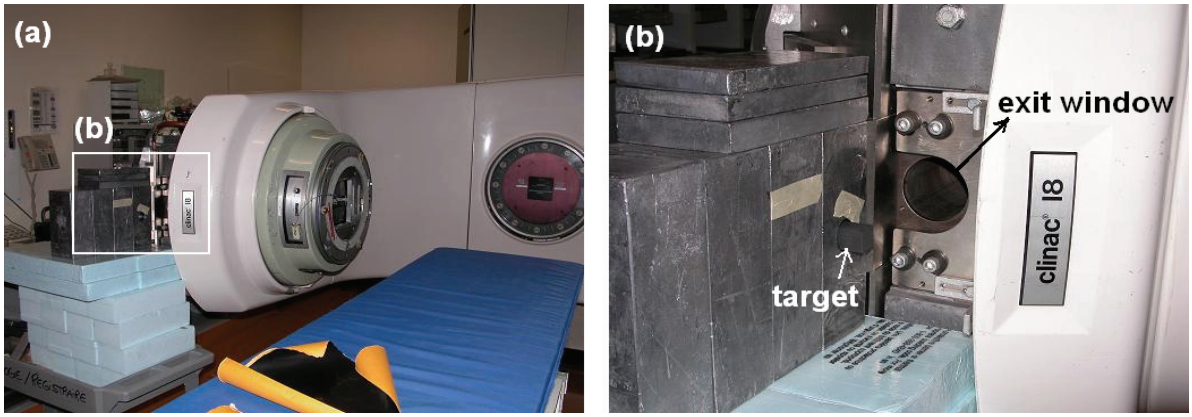

Figure 7.9 (a) Clinac-18 and experimental setup for contrast measurement. (b) The target is placed after the exit window to produce orthogonal bremmstrahlung beam from primary electron beam of the linac.

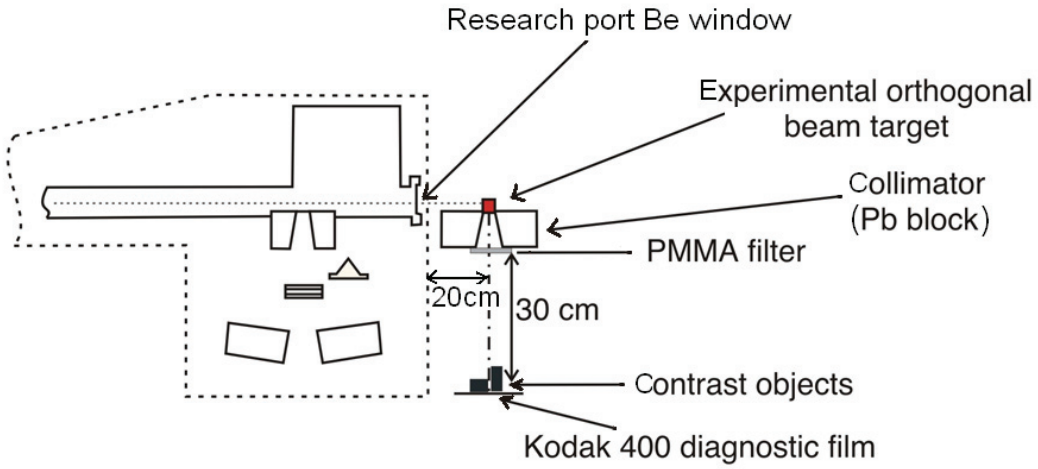

Figure 7.10 Setup for the study of the orthogonal beam on the Varian Clinac-18 linac. The bending magnet is turned off, and the primary electron beam exits through the research port and impinges on an x-ray target.

The Clinac-18 is equipped with a research port which allows the electron beam to exit the accelerator without traversing the bending magnet, as illustrated in Fig. 7.10. To create the primary electron beam, the 270° bending magnet in the beam transport system was turned off, the monitor chambers were disabled, and the primary electron beam was made to exit through a beryllium window via the research port in the forward direction. To allow the electron beam to exit centered on the exit window and in a scatter-free manner, the bending magnet was demagnetized by briefly powering the magnet with a reverse current prior to the experiment.

For determining the position and the diameter of the primary electron beam radiation exposure of thin radiation sensitive paper was used. The diameter of the beam at the linac research port window was on the order of 1 mm. Because of space constraints the target was placed 20 cm away from the exit window in air, as illustrated in Fig. 7.10. The 20 cm air path caused a broadening of the electron pencil beam and the spot size had a diameter of 15 mm when it hit the experimental targets. The targets were made of C, Al and Pb, with cubical shape as illustrated in Fig. 2.b with thicknesses of 80% of R_{CSDA} in orthogonal direction and 110% of R_{CSDA} in forward direction (d_o and d_f in Fig. 2.b respectively).

A lead collimator was attached to the targets to collimate the beam emerging in the orthogonal direction. As it is illustrated in Fig. 7.9(b) extensive lead shielding was also placed around the experimental setup to eliminate contamination and backscattered-photons from the forwardly directed beam. The primary electron beam of the linac was available in electron and photon mode of the linear accelerator. The photon intensity in the photon mode was so high that all films were overexposed even at the lowest possible irradiation time (0.6 s). The electron mode was found to provide a sufficiently high photon fluence rate in the orthogonal direction and for experiments reported in this work an electron energy of 6 MeV in the electron mode of the linac was used.

Two simple Lucite objects (a step wedge and a cylinder with three axial holes) as shown in Fig. 7.11, were used to study image contrast with radiological film (Agfa 400) which was placed behind the objects. The photograph of the Lucite objects inside the lead collimator is also illustrated in Fig. 7.11. This setup was also placed in the forward direction to compare the contrast of forward beam images with those obtained with orthogonal beams. In the forward direction set-up (similar to the setup which is illustrated in Fig 7.8.(b)) , the electron beam hit the target from the front and the collimator as well as the Lucite objects and the film were placed on the opposite side of the target in the direction of the incident electron beam. Typical irradiation times amounted to between 10 s and 30 s in the 6 MeV electron beam mode.

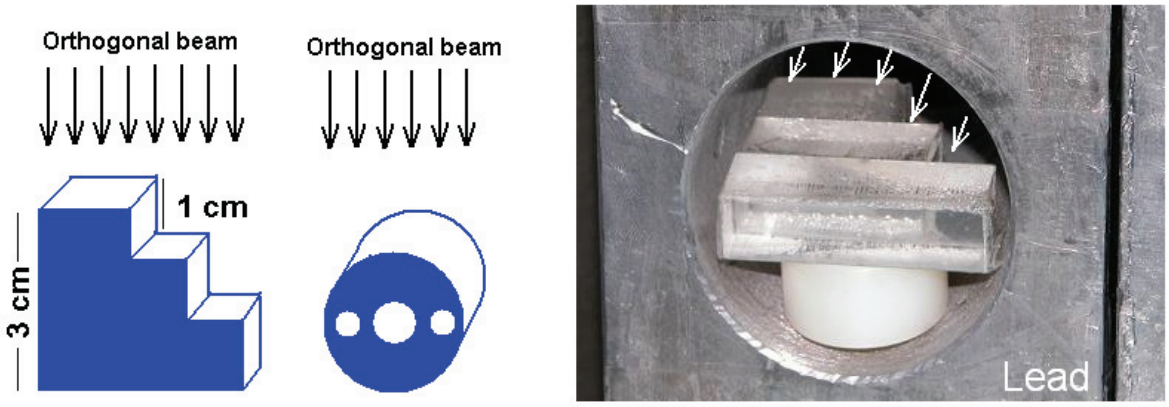

Figure 7.11 Two contrast objects (step wedge and cylinder) used to evaluate the characteristics of the orthogonal beams. The central opening of the cylindrical object has a screw thread groove inside. The objects were placed inside the lead collimator and shielding to eliminate contamination.

7.6 Results and discussion

7.6.1 Optimization of target dimensions

The results of the optimization of the target dimensions in the orthogonal direction are illustrated in Fig. 7.12(a). The figure represents the relative electron fluence (normalized to 1 for the Al target) in the phase space versus target thickness, d_o, expressed as percentage of the CSDA range. For all target materials a thickness d_o of 80% of R_{CSDA} is sufficient to stop all electrons from exiting the target in the orthogonal direction. To verify whether or not this is the optimal thickness, the relative number of photons in the same setup is provided in Fig. 7.12(b). Since the relative number of photons in the orthogonal direction decreases steadily as a function of the target thickness as a result of the self-absorption of photons in the target; we conclude that the 80 % of R_{CSDA} is the optimal target thickness required to stop majority of electrons and concurrently provide the highest number of photons. In 80 % of R_{CSDA}, the photon orthogonal fluence for high atomic number targets was determined to be larger compared to low Z targets (Fig. 7.12 (b)) by a factor of 20 for W compared to Be.

Similar simulations were repeated for 12 MeV electrons and the same cut-off, 80% R_{CSDA}, was found. The simulations were also done for a different pencil beam diameter of 10 mm instead of 1.2 mm, to check whether the conclusion of 80% R_{CSDA} will change for beam diameters more realistic than pencil beams and the same cutoff was also found. Henceforth, in further simulations and experiments 80% of R_{CSDA} was used as the minimal distance between the edge of the electron pencil beam and the edge of the target (d_o in Fig. 7.7) to minimize electron contamination and to maximize photon output.

7.6.2 Energy and photon fluence

Figure 7.13 illustrates the calculated mean energy of the photon beams versus target thickness in the orthogonal direction for various target materials. As expected the beam becomes harder for larger target thicknesses, d_o, and the mean photon energy for low-Z target is significantly lower (320 keV for Al and 150 keV for Be) compared to higher Z targets (980 keV for Pb). Considering the results from figures 7.12 and 7.13, lowering the Z of the target can be done at the expense of photon intensity in the orthogonal direction

and, hence, the choice of the target is a balance between image quality in the orthogonal direction and beam intensity.

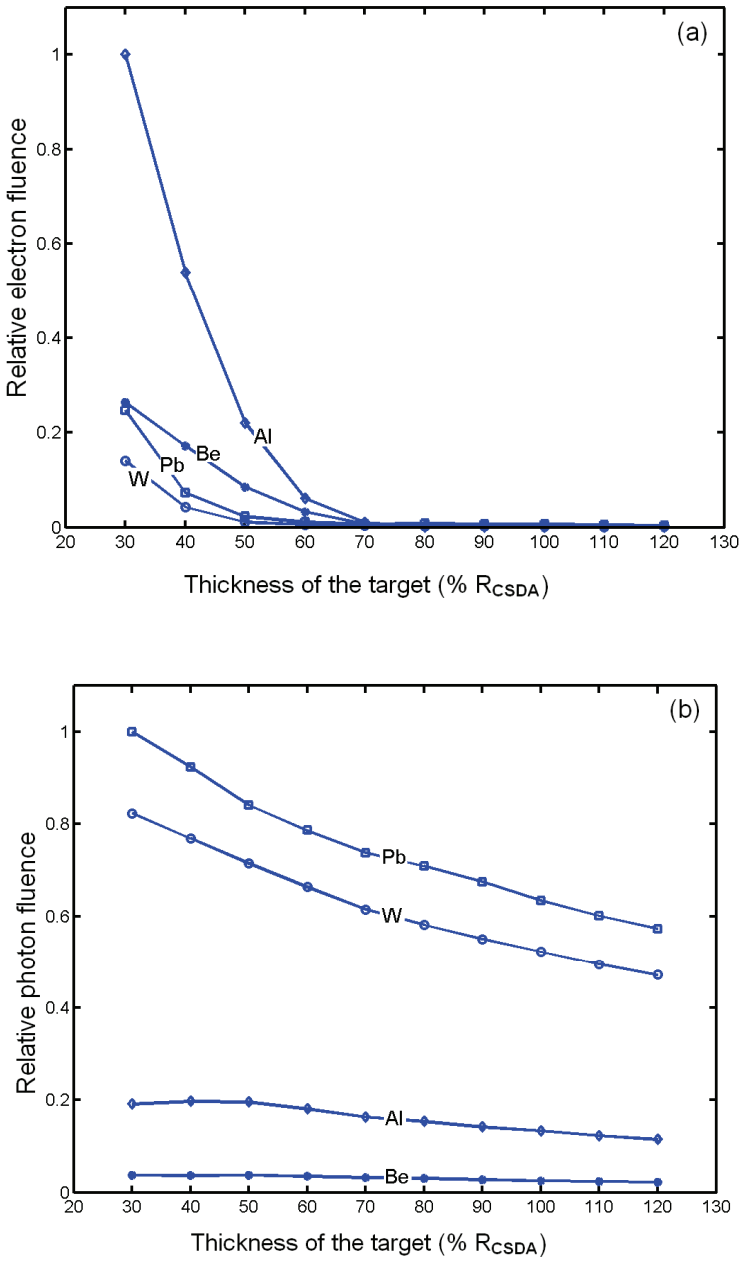

Figure 7.12 (a) Relative electron fluence in the orthogonal direction as a function of target thickness (d_0 in Fig. 2(b)) for various target materials. The numbers are normalized to 1 for the Al fluence at 30 % of R_{CSDA}. The field is 20×20 cm^2 placed 50 cm below the target. (b) Relative photon fluence in the orthogonal direction for the same setup as in (a) versus thickness of the target. The data in both figures are normalized to 1 for the photon fluence produced the Pb target at 30% of R_{CSDA} .

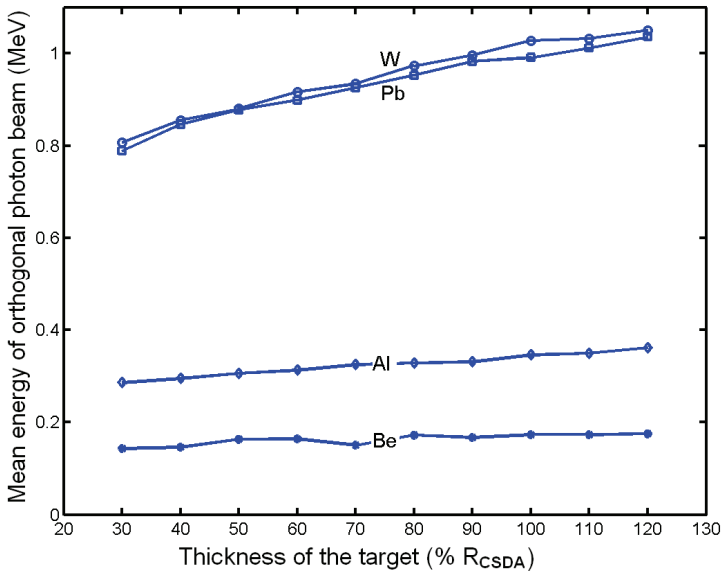

Figure 7.13 Mean energy (MeV) in the orthogonal direction for various target materials

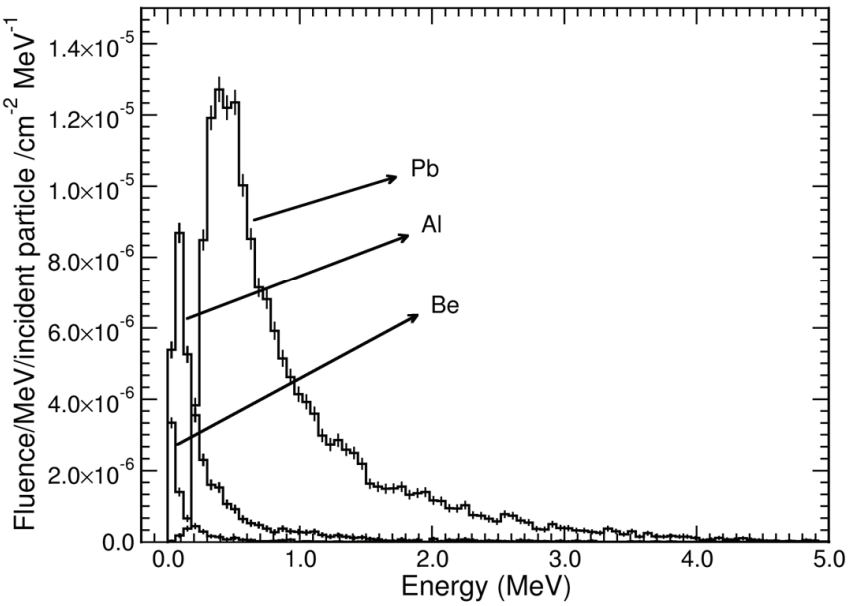

Figure 7.14 Simulated photon fluence spectra in the orthogonal direction for three target materials: Be, Al, and Pb.

Figure 7.14 summarizes the photon fluence spectra in the orthogonal direction for various targets. The photon spectrum moves toward lower energy for lower Z target materials, but the beam intensity also decreases.

The idea of a target with multiple layers was also investigated. The target in this case had a core with a low Z material surrounded by a high Z material and vice-versa. Many combinations, such as Be and Pb, with various thicknesses of the core and various surrounding material were investigated. The results of the photon intensity and mean energy produced in such a target were similar to an average Z material, such as Al, so having a target with multiple layers was not found to provide any real advantage.

The photon yield in the orthogonal direction was compared to the yield in the forward direction along d_f, and it was calculated to be smaller by a factor of 6 to 8 for a given target material. This is due to the forward-directed angular distribution of the bremsstrahlung created by high-energy electrons in the target.

7.6.3 Beam profile and image contrast

There is a major difference between the source shape in the forward direction compared to that in the orthogonal direction. For a circular electron beam spot, the photon distribution in the azimuthal direction is uniformly distributed since the electrons hit the target and scatter through a random azimuthal angle.[82] However, in the forward direction (along the-x axis in Fig. 7.8) the electron fluence reduces roughly exponentially and, consequently, the photon source weakens with depth. Thus the generated orthogonal beam is more intense in the upstream portion of the field compared to the downstream portion (the right side of the target compared to the left side in Fig. 7.8), although for large distances this effect might be negligible.

Several simulated orthogonal beam profiles are illustrated in Fig. 7.15. The profile of the orthogonal beam is not symmetric in x and y direction (see Fig. 7.15) and the asymmetry depends on the source geometry and the target geometry. Assuming the source to have a cylindrical shape, the shape of the source is represented by a rectangle which is the projection of a cylinder on a plane tangential to the cylinder outer surface (Fig. 7.15). The intensity map, shown in Fig. 7.15(a), is extracted with a MATLAB routine from a

40×40 cm^2 phase space file at an SSD of 50 cm below the target. The beam profiles for a central line in the *x* and *y* direction for two SSDs (50 cm and 100 cm) are illustrated in Fig. 7.15(b). There is an apparent asymmetry between the *x* and *y* direction as the beam profile is wider in the *y* direction than it is in the *x* direction. This agrees with the shape of the source of the photons and the distribution of the electrons in the target.

As illustrated in Fig. 7.7, the size of the target in the forward direction (*x* direction in Fig. 7.15) is 110% of RCSDA while in the orthogonal direction (along the y axis) it is approximately 160% of RCSDA (a rectangle with half width of 80 % of RCSDA). So the size of the target is smaller in the x direction and the beam profile is sharper, as illustrated in Fig. 7.15(b) for an SSD of 50 cm. Both x and y profiles flatten at an SSD of 100 cm but the x profile is still sharper. In Fig. 7.15(b) at an SSD of 50 cm one also clearly sees the effect of the electron fluence reduction in the target on the x profile, while the y profile is mostly symmetric. The beam hits the target along the x direction from the right hand side and is reduced toward the left-hand side. This creates a broader and sharper profile on the right-hand side compared to the left hand side. The relative difference of the beam profiles in both sides (R and L in Fig. 7.15) are 27% for SSD = 50 cm and 2% for SSD = 100 cm.

The simulated intensity maps of the contrast object are illustrated in Fig. 7.16(a). Three of the maps are created with orthogonal beams with Pb, Al and Be targets, and one is created with a forward beam produced by the Al target. Since a large area (5×5 cm^2) is used, a large number of histories were needed to get sufficient intensity in each pixel of these images particularly for low *Z* targets. For example, for the Al target 800 million electrons were used.

7.6.4 Experimental results

Figure 7.16(b) illustrates the images on diagnostic film of the two simple Lucite objects shown in Fig. 7.11. The images were created by photon beams emanating from the Pb, Al and C targets in the orthogonal direction as well as in the forward direction for the Al target. The primary electron energy striking the target was 6 MeV. It is clear that the lower *Z* materials with calculated mean energies of 300 keV or less provide better contrast than the high Z targets. For the image created with the C target even the screw thread of the cylindrical object is recognizable.

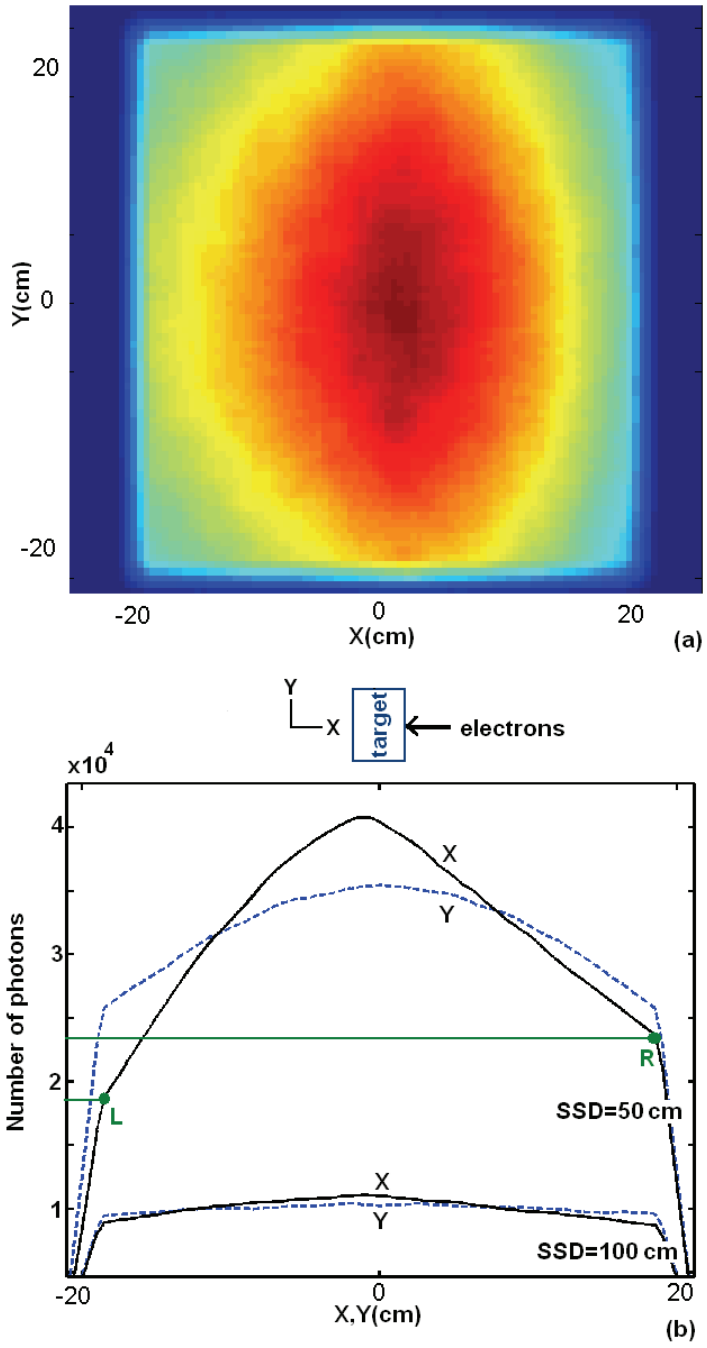

Figure 7.15 (a) Intensity map of the orthogonal photons in 40×40cm^2 plane placed 50 cm below the target. (b) The beam profile in X (solid line) and Y (dashed line) direction, in SSD=50cm for the upper pair and SSD=100cm for lower pair. The primary electron beam hits the target from the positive X direction, right side, and attenuates as it penetrates through the left side. The effect is visible in the X profile as the intensity in right side (R) is higher than the left side (L).

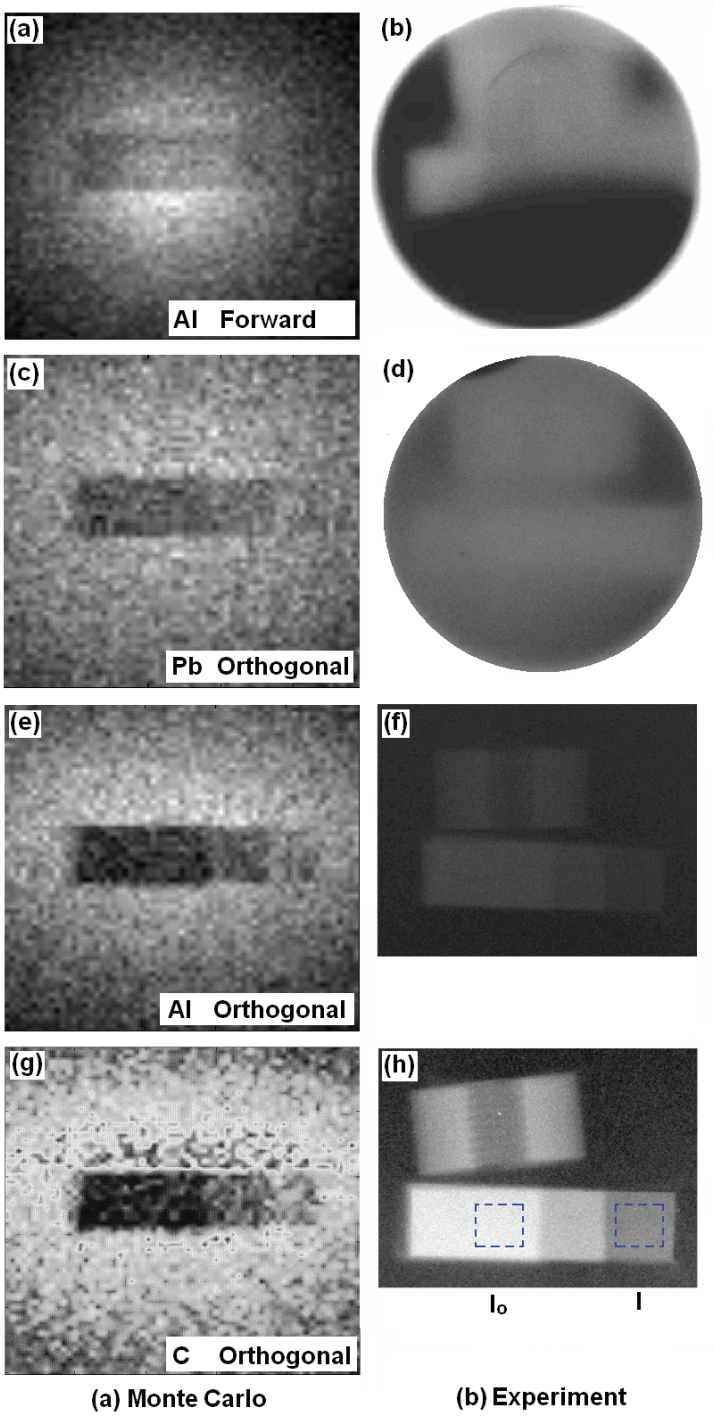

Figure 7.16 Calculated contrast images (left column images) and experimental contrast images (right column imaes) of step wedge and cylinder contrast objects. The images were obtained under the following condition: (a) and (b) for Al target/forward beam; (c) and (d) for Pb target/orthogonal beam; (e) and (f) for Al target /orthogonal beam; (g) and (h) for C target /orthogonal beam. The energy of the incident electron beam striking the target is 6 MeV. The setup is illustrated in Figures 3 and 4. The dashed squares, I and I_0, are examples of the regions used for numerical calculation of the image contrast.

The relative contrast of the images in Fig. 7.16 is calculated using Eq. (7.1) and the results are represented in Fig. 7.17. An example of the regions for which the I_o and I are calculated for one image is illustrated in Fig. 7.16(b). The results of both Monte Carlo calculations and experiments show a superior contrast of images created with orthogonal beams compared to those with forward beams. There is also agreement of contrast improvement for lower Z target materials between Monte Carlo calculation and experiment.

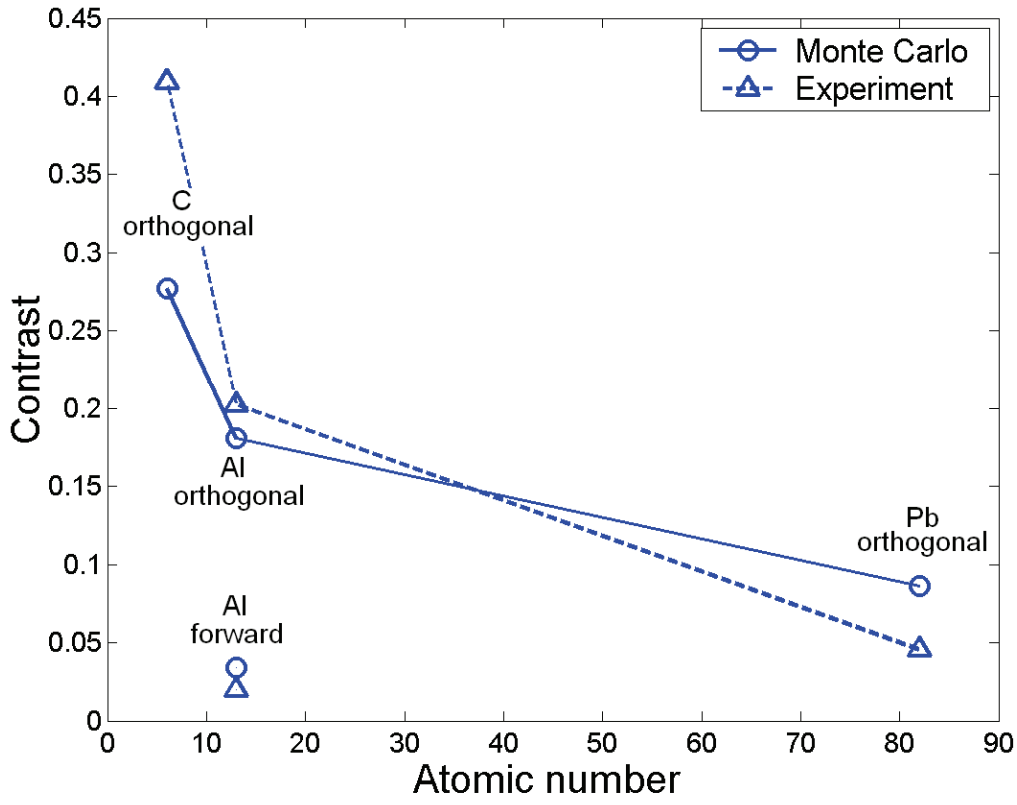

Figure 7.17 Calculated and measured image contrast for three targets materials: carbon, aluminum and lead. For the aluminum target, data for both forward and orthogonal beams are shown, and for carbon and lead targets, data for orthogonal beams only are shown.

7.7 Conclusions and future work

Orthogonal bremsstrahlung beams have a lower mean energy compared to associated forward beams. Higher Z targets create higher intensity, while lower Z targets provide a more desirable low energy spectrum. In experiments and simulations we have

shown that the images created with the orthogonal beams have a higher contrast compared to the images created in the forward beam. The intensity in the orthogonal direction provided by an Al target is sufficient to create images within a reasonable exposure time with a clinical accelerator run in the electron mode. The fact that all images in this work were obtained with the accelerator run in the electron mode for reasonable exposure times demonstrates the feasibility of orthogonal beams for imaging in radiation therapy. For a practical implementation of portal imaging using very low *Z* materials, such as carbon, one could envisage using the accelerator photon mode where the intensity of the primary electron beam is two to three orders of magnitude higher than in electron modes.

This work was followed up by A. Sarfehnia as an M. Sc. project. [83-84] The similar experimental setup and targets were used for further investigation of bremmstrahlung beam characteristics. A 10 MeV electron beam emerging through linac was made to strike targets of carbon, aluminum, and copper. In these set of experiments, the linac was operated in the "photon mode" producing a high fluence rate of 10 MeV electrons at the same beam current as that used in radiotherapy. The PDD and attenuation measurements of both the forward and orthogonal beams were carried out, and the results were also used to estimate the effective and mean energy of the beams. The mean energy of a spectrum produced by a carbon target dropped from 1300 keV in the forward direction to 220 keV in the orthogonal direction, while for an aluminum target it dropped from 1670 to 410 keV, and for a copper target the mean energy dropped from 1790 to 790 keV. An in-depth Monte Carlo study of photon yield and electron contamination was also performed. In this work effect of various parameters in bremmstrahlung yield were investigated such as: Spectral calculation, dependence of yield and contamination on target material, and dependence of yield on target thickness and radius.

Our work mainly verified the basic characteristics of the photon beams generated by the target in the orthogonal direction. Future work may establish the practical implementation of this method. This involves a target design in which orthogonal beam spot size is optimized. This could be accomplished in various ways. One way could be to design a collimator to shield the spread-out spot whereas another way could be to reduce the physical dimensions of the target. Reducing the dimensions of the target in the forward direction will reduce the spot size of the beam as well as intensity of the beam in the

orthogonal direction and this could be done as long as there is enough primary electron intensity. Reducing the size of the target in the forward direction also reduces the asymmetry of the beam in a plane parallel to the primary beam axis and generates a flatter orthogonal beam. A target for orthogonal imaging has a larger size compared to a standard treatment target and implementation of the new target could present technical problems of space, if the size of the target region in the vacuum system is inadequate. Another possibility for reducing spot size is to reduce the size of the target in all directions except in the downward orthogonal direction and placing appropriate shielding around the target.

We investigated the design of a target with two different materials; low Z material surrounded by a high Z material and arrived at the same conclusions as for average Z material regarding energy and intensity. In any target design, the distance between the edge of the primary electron beam and the edge of the target in downward direction should be at least 80% of R_{CSDA} to minimize the electron contamination. Finally, the design of a new target should also be accompanied by a flattering filter and shielding to stop the strong forward-peaked photon beam in such a way that minimal modification of the linac is required. This work suggests that in comparison to megavoltage CT, an integrated, linac-based, cone beam imaging system with enhanced contrast obtained with orthogonal x-ray beam is feasible.

References

1. M. G. Herman, J. M. Balter, D. A. Jaffray, K. P. McGee, P. Munro, S. Shalev, M. Ven Herk, and J. W. Wong, "Clinical use of electronic portal imaging: Report of AAPM Radiation Therapy Committee Task Group 58," Med. Phys. **28**, 712-737 (2001).
2. C. L. Creutzberg, V. G. Althof, H. Huizenga, A. G. Visser, and P. C. Levendag, "Quality assurance using portal imaging: The accuracy of patient positioning in irradiation of breast cancer," Int. J. Radiat. Oncol., Biol., Phys. **25**(3), 529–539 (1993).
3. S. A. Rosenthal, J. M. Galvin, J. W. Goldwein, A. R. Smith, and P. H. Blitzer, "Improved methods for determination of variability in patient positioning for radiation therapy using simulation and serial portal film measurements," Int. J. Radiat. Oncol., Biol., Phys. **23**, 621–625 (1992).

4. N. A. Baily, R. A. Horm, and T. D. Kampp, "Fluoroscopic visualization of megavoltage therapeutic X-ray beams," Int. J. Radiat. Oncol. Biol. Phys. **6**, 935–939 (1980).
5. H. Meertens, M. van Herk, and J. Weeda, "A liquid ionization detector for digital radiography of therapeutic megavoltage photon beams," Phys. Med. Biol. **30**, 313–321 (1985).
6. J. W. Motz and M. Donas, "Image information content and patient exposure," Med. Phys. **5,** 8–22 (1978).
7. S. Brenner, B. Rosengren, H. Wallman, and O. Netteland, "Television monitoring of a 30 MV x-ray beam," Phys. Med. Biol. **7**, 29–34 (1962).
8. M. Van Herk and H. Meertens, "A matrix ionization chamber imaging device for on-line patient setup verification during radiotherapy," Radiother. Oncol. **11**(4), 369–378 (1988).
9. B. Wowk, T. Radcliffe, K. W. Leszczynski, S. Shalev, and R. Rajapakshe, "Optimization of metal/phosphor screens for on-line portal imaging," Med. Phys. **21**, 227–235 (1994).
10. D. A. Fein, K. P. McGee, T. E. Schultheiss, B. L. Fowble, and G. E. Hanks, "Intra- and interfractional reproducibility of tangential breast fields: A prospective on-line portal imaging study," Int. J. Radiat. Oncol. Biol. Phys. **34**, 733–740 (1996).
11. J. E. Marks, A. G. Haus, H. G. Sutton, and M. L. Griem, "The value of frequent treatment (N.Y.) verification films in reducing localization error in the irradiation of complex fields," Cancer (N.Y.) **37**, 2755–2761 (1976).
12. H. I. Amols, L. E. Reinstein, and B. Lagueux, "A quantitative assessment of portal film contrast as a function of beam energy," Med. Phys. **13**, 711-716 (1986).
13. S. A. Rosenthal, J. M. Galvin, J. W. Goldwein, A. R. Smith, and P. H. Blitzer, "Improved methods for determination of variability in patient positioning for radiation therapy using simulation and serial portal film measurements," Int. J. Radiat. Oncol. Biol. Phys. **23**, 621–625 (1992).
14. J. W. Denham, M. J. Dally, K. Hunter, J. Wheat, P. P. Fahey, and C. S. Hamilton, "Objective decision-making following a portal film: The results of a pilot study," Int. J. Radiat. Oncol. Biol. Phys. **26**, 869–876 (1993).

15. L. E. Reinstein, M. Durham, M. Tefft, A. Yu, A. S. Glicksman, and W. Eaton, "Portal film quality: A multiple institutional study," Med. Phys. **11**, 555 (1984).
16. L. E. Reinstein, L. Alquist, H. I. Amols, and B. Lagueux, "Quantitative evaluation of a portal film contrast enhancement technique," Med. Phys. **14**, 309 (1987).
17. J. Leong, "Digital image processing system for high energy x-ray portal images," Phys. Med. Biol. **20**, 1527–1535 (1984).
18. P. Munro, "Portal imaging Technology, past present and future," Seminars in Radiation Therapy **5**, 115-133 (1995).
19. M. Van Herk and H. Meertens, "A matrix ionization chamber imaging device for on-line patient setup verification during radiotherapy," Radiother. Oncol. **11**(4), 369–378 (1988).
20. A. L. Boyer, L. Antonuk, A. Fenster, M. Van Herk, H. Meertens, P. Munro, L. E. Reinstein, and J. Wong, "A review of electronic portal imaging devices (EPIDs)," Med. Phys. **19**, 1–16 (1992).
21. B. J. Heijmen, K. L. Pasma, M. Kroonwijk, V. G. Althof, J. C. de Boer, A. G. Visser, and H. Huizenga, "Portal dose measurement in radiotherapy using an electronic portal imaging device (EPID)," Phys. Med. Biol. **40**, 1943–1955 (1995).
22. L. Dong, A. Shiu, S. Tung, and A. Boyer, "Verification of radiosurgery target point alignment with an electronic portal imaging device (EPID)," Med. Phys. **24**, 263–267 (1997).
23. J. Balter, A. Thompson, and R. K. Ten Haken, "Automated quality assurance of mechanical components of a computer controlled accelerator using and EPID," Fourth International Workshop on Electronic Portal Imaging, Amsterdam, 1996.
24. D. Verellen, W. De Neve, F. Van den Heuvel, M. Coghe, O. Louis, and G. Storme, "On-line portal imaging: Image quality defining parameters for pelvic fields—a clinical evaluation," Int. J. Radiat. Oncol., Biol., Phys. **27** (4), 945–952 (1993).
25. P. Munro, J. A. Rawlinson, and A. Fenster, "A digital fluoroscopic imaging device for radiotherapy localization," Int. J. Radiat. Oncol. Biol., Phys. **18**, 641–649 (1990).
26. H. Meertens, M. van Herk, and J. Weeda, "A liquid ionization detector for digital radiography of therapeutic megavoltage photon beams," Phys. Med. Biol. **30**, 313–321 (1985).

27. M. van Herk, W. Fencl, and A. van Dalen, "Design and implementation of a high speed matrix ionization chamber system," Med. Phys. **22**, 991 (1995).
28. Y. Zhu, X. Q. Jiang, and J. Van Dyk, "Portal dosimetry using a liquid ion chamber matrix: Dose response studies," Med. Phys. **22**, 1101–1106 (1995).
29. L. E. Antonuk, J. Boudry, Y. El-Mohri, W. Huang, J. H. Siewerdsen, J. Yorkston, and R. A. Street, "A high resolution, high frame rate, flatpanel TFT array for digital x-ray imaging," Proc. SPIE 2163, 118–128 (1994).
30. W. Zhao and J. A. Rowlands, "X-ray imaging using amorphous selenium: Feasibility of a flat panel self-scanned detector for digital radiology," Med. Phys. **22**, 1595–1604 (1995).
31. L. E. Antonuk, J. Yorkston, W. Huang, H. Sandler, J. H. Siewerdsen, and Y. el-Mohri, "Megavoltage imaging with a large-area, flat-panel, amorphous silicon imager," Int. J. Radiat. Oncol., Biol., Phys. **36**, 661–672 (1996).
32. J. Sillanpaa, J. Chang, G. Mageras, H. Riem, J. Ford, D. Todor, C. C. Ling, and H. Amols, "Developments in megavoltage cone beam CT with an amorphous silicon EPID: reduction of exposure and synchronization with respiratory gating," Med. Phys. **32**, 819–829 (2005).
33. W. Swindell, R. G. Simpson, and J. R. Oleson, "Computed tomography with a linear accelerator with radiotherapy applications," Med. Phys. **10**, 416–420 (1983).
34. D. G. Lewis, W. Swindell, E. J. Morton, P. M. Evans, and Z. R. Xiao, "A megavoltage CT scanner for radiotherapy verification," Phys. Med. Biol. **37**, 1985–1999 (1992).
35. K. J. Ruchala, G. H. Olivera, E. A. Schloesser, and T. R. Mackie, "Megavoltage CT on a tomotherapy system," Phys. Med. Biol. **44**, 2597–2621 (1999).
36. M. A. Mosleh-Shirazi, P. M. Evans, W. Swindell, S. Webb, and M. Partridge, "A cone-beam megavoltage CT scanner for treatment verification in conformal radiotherapy," Radiother. Oncol. **48**, 319–328 (1998).
37. D. A. Jaffray, J. H. Siewerdsen, J. W. Wong, and A. A. Martinez, "Flat-panel cone beam computed tomography for image-guided radiation therapy," Int. J. Radiat. Oncol., Biol., Phys. **53**, 1337–1349 (2002).

38. B. A. Groh, J. Siewerdsen, D. G. Drake, J. W. Wong, and D. A. Jaffray, "A performance comparison of flat-panel imager-based MV and kV cone-beam CT," Med. Phys. **29**, 967–975 (2002).

39. J. R. Sykes, R. Lindsay, C. J. Dean, D. S. Brettle, D. R. Magee, and D. I. Thwaites, "Measurement of cone beam CT coincidence with megavoltage isocentre and image sharpness using the QUASARtrade mark Penta-Guide phantom," Phys. Med. Biol. **53**, 5275–5293 (2008).

40. S. F. Petit, W. J. van Elmpt, S. M. Nijsten, P. Lambin, and A. L. Dekker "Calibration of megavoltage cone-beam CT for radiotherapy dose calculations: correction of cupping artifacts and conversion of CT numbers to electron density," Med. Phys. **35**, 849–865 (2008).

41. I. S. Grills, G. Hugo, L. L. Kestin, A. P. Galerani, K. K. Chao, J. Wloch, and D. Yan, "Image-guided radiotherapy via daily online cone-beam CT substantially reduces margin requirements for stereotactic lung radiotherapy," Int. J. Radiat. Oncol. Biol. Phys. **70**(3), 1045–1056 (2008).

42. A. Khoury, C. M. Whyne, M. Daly, D. Moseley, G. Bootsma, T. Skrinskas, J. Siewerdsen, and D. Jaffray, "Intraoperative cone-beam CT for correction of periaxial malrotation of the femoral shaft: a surface-matching approach," Med. Phys. **34**, 1380–1387 (2007).

43. D. Létourneau, R. Wong, D. Moseley, M. B. Sharpe, S. Ansell, M. Gospodarowicz, and D. A. Jaffray, "Online planning and delivery technique for radiotherapy of spinal metastases using cone-beam CT: image quality and system performance," Int. J. Radiat. Oncol., Biol., Phys. **67**(4), 1229–1237 (2007).

44. J. Boda-Heggemann, C. Walter, A. Rahn, H. Wertz, I. Loeb, F. Lohr, and F.Wenz, "Repositioning accuracy of two different mask systems-3D revisited: comparison using true 3D/3D matching with cone-beam CT," Int. J. Radiat. Oncol., Biol., Phys. **66**(5), 1568–1575 (2006).

45. M. J. Daly, J. H. Siewerdsen, D. J. Moseley, D. A. Jaffray, J. C. Irish, "Intraoperative cone-beam CT for guidance of head and neck surgery: Assessment of dose and image quality using a C-arm prototype," Med. Phys. **33**, 3769–3780 (2006).

46. F. Verhaegen, B. Reniers, F. Deblois, S. Devic, J. Seuntjens and D. Hristov, "Dosimetric and microdosimetric study of contrast-enhanced radiotherapy with kilovolt x-rays," Phys. Med. Biol. **50**, 3555–3369 (2005).

47. S. Flampouri, P. M. Evans, F. Verhaegen, A. E. Nahum, E. Spezi, and M. Partridge, "Optimization of accelerator target and detector for portal imaging using Monte Carlo simulation and experiment," Phys. Med. Biol. **47**, 3331–3349 (2002).

48. O. Z. Ostapiak, P. F. O'Brien, and B. A. Faddegon, "Megavoltage imaging with low Z targets: Implementation and characterization of an investigational system," Med. Phys. **25**, 1910–1918 (1998).

49. D. W. Mah, D. M. Galbraith, and J. A. Rawlinson, "Low-energy imaging with high-energy bremsstrahlung beams: Analysis and scatter reduction," Med. Phys. **20**, 653–665 (1993).

50. B. A. Faddegon, C. K. Ross, and D. W. O. Rogers, "Angular distribution of bremsstrahlung from 15-MeV electrons incident on thick targets of Be, Al, and Pb," Med. Phys. **18**, 727-739 (1991).

51. E. B. Podgorsak, J. A. Rawlinson, M. Glavinovic, and H. E. Johns, "Design of x-ray targets for high energy linear accelerators in radiotherapy," Am. J. Roentgenol., Radium Ther. Nucl. Med. **121**, 873–882 (1974).

52. L. B. Levy, R. G Waggener, and A. E. Wright, "Measurement of primary bremsstrahlung spectrum from an 8-MeV linear accelerator," Med. Phys. **3**, 173–175 (1976).

53. B. A. Faddegon, C. K. Ross, and D. W. O. Rogers, "Forward-directed bremsstrahlung of 10- to 30-MeV electrons incident on thick targets of Al and Pb," Med. Phys. **17**, 773–785 (1990).

54. G. X. Ding, "Energy spectra, angular spread, fluence profiles and dose distributions of 6 and 18 MV photon beams: results of Monte Carlo simulations for a varian 2100EX accelerator," Phys. Med. Biol. **47**, 1025–1046 (2002).

55. B. Faddegon, B. Egley, and T. Steinberg, "Comparison of beam characteristics of a gold x-ray target and a tungsten replacement target," Med. Phys. **31**, 91–97 (2004).

[56] S. W. Lee, J. Y. Jin, H. Guan, F. Martin, J. H. Kim, and F. F. Yin, "Clinical assessment and characterization of a dual tube kilovoltage X-ray localization system in the radiotherapy treatment room," J. Appl. Clin. Med. Phys. **9,** 2318 (2008).

[57] K. Aljarrah, G. C. Sharp, T. Neicu, and S. B. Jiang "Determination of the initial beam parameters in Monte Carlo linac simulation," Med. Phys. **33**, 3767–3780 (2006).

[58] B. De Smedt, N. Reynaert, F. Flachet, M. Coghe, M. G. Thompson, L. Paelinck, G, Pittomvils, C. De Wagter, W. De Neve, and H. Thierens, "Decoupling initial electron beam parameters for Monte Carlo photon beam modelling by removing beam-modifying filters from the beam path," Phys. Med. Biol. **50**, 5935–5951 (2005).

[59] W. R. Nelson, H. Hirayama, and D. W. O. Rogers, "The EGS4 Code System," SLAC Report No. SLAC-265, 1985.

[60] A. F. Bielajew and D. W. O. Rogers, "PRESTA—'The parameter reduced electron step algorithm' for electron Monte Carlo transport," Nucl. Instrum. Meth. B **18**, 165–181 (1987).

[61] C. J. Karzmark, "Advances in linear accelerator design for radiotherapy," Med. Phys. **11**, 105–128 (1984).

[62] M. K. Fix, P. J. Keall, and J. V. Siebers, "Photon-beam subsource sensitivity to the initial electron-beam parameters," Med. Phys. **32**, 1164–1175 (2005).

[63] B. Libby, J. Siebers, and R. Mohan, "Validation of Monte Carlo generated phase-space descriptions of medical linear accelerators," Med. Phys. **26**, 1476–1483 (1999).

[64] E. L. Chaney, T. J. Cullip, and T. A. Gabriel, "A Monte Carlo study of accelerator head scatter," Med. Phys. **21**, 1383–1390 (1994).

[65] D. M. Lovelock, C. S. Chui, and R. Mohan, "A Monte Carlo model of photon beams used in radiation therapy," Med. Phys. **22**, 1387–1394 (1995).

[66] D. W. O. Rogers, B. Walters, and I. Kawrakow, "BEAMnrc Users Manual," NRC Report PIRS 509(a)revH, 2004.

[67] P. Edimo, C. Clermont, M. G. Kwato, and S. Vynckier, "Evaluation of a commercial VMC++ Monte Carlo based treatment planning system for electron beams using EGSnrc/BEAMnrc simulations and measurements," Med. Phys. **22**, August (2008).

[68] T. Kairn, D. Cassidy, P. M. Sandford, and A. L. Fielding. "Radiotherapy treatment verification using radiological thickness measured with an amorphous silicon electronic

portal imaging device: Monte Carlo simulation and experiment," Phys. Med. Biol. **53**, 3903–3919 (2008).

69. E. Heath and J. Seuntjens, "Development and validation of a BEAMnrc component module for accurate Monte Carlo modelling of the Varian dynamic millennium multileaf collimator," Phys. Med. Biol. **48**, 4045–4063 (2003).

70. I. Kawrakow, D. W. O. Rogers, and B. R. B. Walters, "Large efficiency improvements in BEAMnrc using directional bremsstrahlung splitting," Med. Phys. **31**, 2883–2898 (2004).

71. M. McEwen, H. Palmans, and A. Williams, "An empirical method for the determination of wall perturbation factors for parallel-plate chambers in high-energy electron beams," Phys. Med. Biol. **51**, 5167–5181 (2006).

72. H. M. Deloar, E. Kunieda, T. Kawase, T. Tsunoo, H. Saitoh, M. Ozaki, K. Saito, S. Takagi, O. Sato, T. Fujisaki, A. Myojoyama, and G. Sorell, "Investigations of different kilovoltage X-ray energy for three-dimensional converging stereotactic radiotherapy system: Monte Carlo simulations with CT data," Med. Phys. **33**, 4635–4642 (2006).

73. M. Pacilio, D. Aragno, R. Rauco, S. D'Onofrio, M. C. Pressello, L. Bianciardi, and Santini E. , "Monte Carlo dose calculations using MCNP4C and EGSnrc/BEAMnrc codes to study the energy dependence of the radiochromic film response to beta-emitting sources," Phys. Med. Biol. **52**, 3931–3848 (2007).

74. C.-M. Ma and D. W. O. Rogers, "BEAMDP Users Manual," NRC Report PIRS-0509 (D), 1995.

75. F. Ubrich, J. Wulff, R. Kranzer, and K. Zink, "Thimble ionization chambers in medium-energy x-ray beams and the role of constructive details of the central electrode: Monte Carlo simulations and measurements," Phys. Med. Biol. **53**, 4893–4906 (2008).

76. R. C. Gonzales and R. E. Woods, *Digital Image Processing* (Addison-Wesley, Reading, MA, 1992).

77. J. L. Robar, Riccio S. A., and M. A. Martin, "Tumour dose enhancement using modified megavoltage photon beams and contrast media," Phys. Med. Biol. **47**, 2433–2449 (2002).

78. B. A. Faddegon, P. O'Brien, and D. L. Mason, "The flatness of Siemens linear accelerator x-ray fields," Med. Phys. **26**, 220–228 (1999).

79. M. R. Bieda, J. A. Antolak, and K. R. Hogstrom, "The effect of scattering foil parameters on electron-beam Monte Carlo calculations," Med. Phys. **28**, 2527–2534 (2001).

80. D. Sheikh-Bagheri and D. W. O. Rogers, "Sensitivity of megavoltage photon beam Monte Carlo simulations to electron beam and other parameters," Med. Phys. **29**, 379–390 (2002).

81. A. Tzedakis, J. E. Damilakis, M. Mazonakis, J. Stratakis, H. Varveris, and N. Gourtsoyiannis, "Influence of initial electron beam parameters on Monte Carlo calculated absorbed dose distributions for radiotherapy photon beams," Med. Phys. **31**, 907–913 (2004).

82. F. Verhaegen and J. Seuntjens, "Monte Carlo modelling of external radiotherapy photon beams," Phys. Med. Biol. **48**, R107-R164 (2003).

83. K. Jabbari, A. Sarfehnia, E. B. Podgorsak, and J. P. Seuntjens, "Monte Carlo feasibility study of using orthogonal bremsstrahlung beams for improved radiation therapy imaging," Phys. Med. Biol. **52**, 1171–1184 (2006).

84. A. Sarfehnia, K. Jabbari, J. P. Seuntjens, and E. B. Podgorsak, "Experimental verification of beam quality in high-contrast imaging with orthogonal bremsstrahlung photon beams," Med. Phys. **34**, 2896–2906 (2007).

Chapter 8

Summary and future work

Treatment planning systems in radiation therapy require a fast and accurate method for dose calculation. Currently, Monte Carol techniques produce the most accurate dose-calculation results and treatment planning systems based on these techniques are becoming the dominant systems in radiation therapy. One of the most important issues in day to day use of MC-based treatment planning systems in radiation therapy clinics is their slow speeds. Fast MC enables these systems to perform dose calculation in a reasonable amount of time.

Our approach for development of fast MC code was based on pre-calculated data. The PMC (Pre-calculated MC) code uses the pre-calculated tracks generated by a reliable general propose MC code. The pre-calculated tracks are generated for each particular material. This in turn makes the physics of the code very simple, and enables the code to transport various particles such as electrons and protons with the same transport algorithm. The first version of PMC code was developed for electron transport, and it was tested in several homogeneous and heterogeneous cases, producing very accurate results. The first version of PMC runs 40-60 times faster than EGSnrc and the errors were within 1-3 % relative to EGSnrc. The size of the pre-calculated data for various materials (water, lung, bone) is in the order of 300-400 Mb. This memory size is easily available in most current computers with 4-8 Gb RAM. However the size of the pre-calculated data can be optimized. For example, in the current version, all variables are saved in real arrays while 30 % of parameters (such as secondary particle types and some of the indices) can be saved as integer(2) or integer(1) values.

PMC code is developed in Fortran language and for greater flexibility the code can be translated to C++. Although the code is tested in various heterogeneous cases, its

potential implementation in treatment planning systems will require several standard tests that have to be performed. The large size of the pre-calculated data limits the application of this method in parallel processing in current processors. To solve this problem, a major development and improvement in the available cash of CPUs is required.

As for the second goal of the project, we focused on improving the speed of the code by using several old and novel techniques in order to enhance the code's efficiency. The major obstacle for speed up in fast MC was observed to be the boundary crossing and ray tracing algorithms. The fast MC codes are typically 10-50 times faster than the reference code (EGS4/EGSnrc), while according to our time profile of the code, as long as the ray tracing algorithm in performed, the speed factor is limited to 100. We finally were able to develop a Fast MC code which avoids ray tracing and boundary crossing calculations. In this method, the ray tracing is included in the pre-calculated data and the electron is transported in a voxel-by-voxel manner (as compared to the step-by step manner in a standard fast MC code). In this method the related parameters of the electron which enters the surface of a voxel are categorized and digitized. The discretization of entrance parameters such as incident angle, produces an error and with appropriate optimization, the error can be reduced. For example in the current stage of the code, the polar angle of the incident electrons are discretized to 0, 10, 20 … degrees and for the electron with incident angle of 8 degree the pre-calculated data with 10 degree angle is picked up. There are other possible options that may improve the results of the code such as:

a) Taking a random number and according to the value of the number with appropriate threshold we pick up a track from 0 degree set or 10 degree set.

b) Modifying the 10 degree track of the particle. This modification is restricted to change of deposited energy and the track of the voxels. A possible modification technique is that for the angles close to 10 degree, e.g. 9 or 11 as long as the track passes through the same voxels as the 10 degree track, we include deposited energy of the electrons in the pre-calculated data for each angle. This information (an array of real numbers representing the deposited energy in each voxel) does not require a large amount of data.

c) Interpolation between the 0 degree and 10 degree angle. The advantage of interpolation between the two tracks is that the ray tracing parameters in pre-calculated data such as the position of the exited electron from each voxel can be modified.

Although the size of the pre-calculated data in this case is vary large (1-2 Gb), it was demonstrated that the code can run 560 times faster than EGSnrc which is a new speed limit for the electron transport.Further improvements and developments are required to improve the accuracy of the results in heterogeneous phantoms. A reduction in the size of the pre-calculated data can also improve the overall performance of the code.

The PMC code is further developed for proton transport based on the MCNPX code. The pre-calculated tracks of protons are generated with MCNPX, while the same transport algorithm as that used for the electrons is used for the protons. The PMC code produced accurate results for proton transport which illustrates the flexibility of the code. The physics of various secondary particles produced by protons is handled properly, while in terms of the speed, PMC runs 100 times faster than MCNPX.

In PMC for proton the pre-calculated data is calculated in energy range of 20-250 MeV with 20 MeV bins. The smaller energy bin may improve the accuracy of the results on the expense of the larger size of the pre-calculated data. Future work improving the results of the code,can evaluate various energy interpolation methods. In the current version of the PMC for proton transport, given a 145 MeV particle a track with closest higher energy neighbor is picked up (i.e., 150 MeV) and within that track, we move down in energy until the step with an energy closest to 145 MeV is met. We interpolate that step to reach 145 MeV point and the rest of the track is picked up for transport of the particle. There are options for optimizing each step of the above process. For example, in the current version linear interpolation is used and other type of interpolations can be evaluated. Instead of interpolation of the first step it is possible to rescale the entire track with respect to the energy.

The track of the protons are almost linear and it is possible to approximate the track of the proton as a line for a faster ray tracing. However, we still have to move the proton through the small steps since the deposited energy in not distributed uniformly along the proton track. The transport of the particle without ray tracing as it is applied for electrons (in which the boundary crossing is included in the pre-calculated data) could also be used for proton transport. This method for proton transport should have more accurate results compared to electrons because of the relatively straight path of the proton and less scattering compare to electron.

In-house MATLAB subroutines have been developed in various stages of this work and most of the graphs and the results are processed with these softwares. The MATLAB subroutines are particularly helpful for EGSnrc, BEAMnrc results in windows machines since the available softwares for processing of the results are commonly developed for Unix machines. The significant advantage of MATLAB is that the user can use very powerful toolboxes such as Image processing toolbox to analyze various parameters and apply many image registration techniques. For example, one of our MATLAB codes automatically reads the output file of the EGSnrc for dose calculation in a voxel based phantom and generates a 3D matrix of the dose. Isodose lines and 3D isodose surfaces can subsequently be generated using simple MATLAB commands. Moreover, the images can be easily registered with CT or other images for further comparison.

Another useful MATLAB code is developed for processing of the `ptrac.f` output file of MCNPX. The MCNPX code is capable of saving complete information of the primary particles (protons in our case) and all secondary particles in the `ptrac.f` output file. The results of MCNPX is pre-processed with a Fortran code, and using MATLAB, the tracks of all particles can be analyzed and investigated for various purposes. One of the interesting tasks that can be performed as a future work, is the development of an educational software for demonstration of the proton tracks, secondary particles and various interactions in an interactive environment.

In this work, we have focused on various techniques to speed up the electron transport, while, in the future, the code can be expanded to include photon transport. In a treatment planning system, in case of photon particle we can call one the available codes for photon transport (such as XVMC). The transport algorithm for photons is much simpler than that of charged particles (electrons and protons) because photons take much longer steps in the medium. Therefore, different variance reduction techniques are required to improve the efficiency of photon transport. Because of the straight path of the photons in a medium, it is possible to apply mathematical techniques for efficient transport of the particle. The pre-calculated data for photons can contain relatively larger number of photons. EGSnrc can be used for generation of Size of the pre-calculated data inclusing about 50000 photons for each energy (0.2-20MV) would be around 200 Mb. The transport of a ‘group’ of the particles must be more promising for photons (compared to electrons

and protons). In such a case for each photon in phase-space file, we can pick up a few photon tracks from pre-recalculated data with the same energy and transport the photons different weights.

Because of the straight path of the photons in a medium, it is possible to apply mathematical techniques for efficient transport of the particle. The pre-calculated data for photons can contain relatively larger number of photons. EGSnrc can be used for generation of Size of the pre-calculated data inclusing about 50000 photons for each energy (0.2-20MV) would be around 200 Mb.

Photons deposit the energy in the medium in-directly with setting the electrons in motion. Therefore, a time consuming part of the photon transport in Monte Carlo is the transport of the secondary electrons for which the PMC code already has the pre-calculated tracks of electrons.

.

Appendix A

Format of `ptrac` file from MCNPX

The `ptrac` card in MCNPX code generates an output file containing the information of various events of the particle. The user can control the output with three type of keywords: output-control keywords, event-filter keywords, and history-filter keywords. A typical `ptrac` file which we used in this work is :

```
PTRAC file=asc max=9000000 write=all
```

1- `file=asc`: The `file` controls the output format. There are two options: `asc` which generates and ASCII output file and `bin` which generates the output in binary format.
2- `max=9000000`: Maximum number of the events which is written in the output file. The code automatically terminates the simulation after this number is reached. This number is used to prevent the code from long runs or generation of an output file with very large size. However, since the generation of pre-calculated data requires information of all particles and events, a very large `max` is selected.
3- `write=all`: If *write= pos*, the three coordinates of the events (*x*,*y*,*z*) are written in the output file. This option is useful for demonstration purposes. With *write=all* for each event as well as the position, other parameters are written in the output file such as material numbers and the direction cosines(u, v, w), particle energy, weight, and time.

The output of `ptrac` card is flexible and it is also possible to filter specific types of events in particular range of geometry or energy with other available keywords such as `event`, `filter`, `surface`, and `type`. For example with `FILTER=100,150,ERG` one can just keep the events in which the energy of the particle is between 100 and 150 MeV or with `FILTER=15,20,z` the events with depth (coordinate of the particle in *z* direction) of 15 to 20 *cm* are written in the output file.

PTRAC.f output: Ptrac card produces a ptrac.f output which contains two groups of numbers, a header and the track information. Unfortunately the explanation of the output file (ptrac.f) in the MCNPX manual is very confusing and time consuming to understand with no example. In this section, we tried to explain a ptrac file of MCNPX which contains proton tracks. An example of a ptrac.f file is illustrated in Fig. A.1. In this figure, no explanations or comments are added to maintain clarity and to help the reader see the general look of the file. This file will be discussed step by step and various parameters of the header and track information are explained.

```
  -1

test  input
   1.3000E+01  1.0000E+00  1.0000E+02  0.0000E+00  0.0000E+00  1.0000E+00  1.0000E+00  0.0000E+00  1.0000E+00  1.0000E+06
   0.0000E+00  0.0000E+00  0.0000E+00  0.0000E+00  0.0000E+00  0.0000E+00  1.0000E+00  2.0000E+00  0.0000E+00  0.0000E+00
     2    7    9    8    9    8    9    8    9    8    9    0    4    0    0    0    0    0    0    0
    1   2   7   8   9  16  17  18  19  20  21  22  23  24  25  26  27  28   7   8  10  11  16  17  18  19  20  21  22  23
   24  25  26  27  28   7   8  12  13  16  17  18  19  20  21  22  23  24  25  26  27  28   7   8  10  11  16  17  18  19
   20  21  22  23  24  25  26  27  28   7   8  14  15  16  17  18  19  20  21  22  23  24  25  26  27  28
         1      1000
      4000         1        40         9         1         1         0
  0.00000E+00  0.00000E+00  0.00000E+00  0.00000E+00  0.00000E+00  0.10000E+01  0.20000E+03  0.10000E+01  0.00000E+00
      4000         1      8016         2         9         1         1        49
  0.34792E+00  0.72012E+00  0.23767E+02  0.14395E+00  0.33793E+00  0.93010E+00  0.46857E+02  0.10000E+01  0.16930E+00
      5000         1      8016         2         9         1         1        49
  0.34792E+00  0.72012E+00  0.23767E+02  0.14395E+00  0.33793E+00  0.93010E+00  0.46857E+02  0.10000E+01  0.16930E+00
      9000         1         2         1         9         1         1       187
  0.65529E+00  0.12817E+01  0.25673E+02  0.28468E+00  0.33266E+00  0.89905E+00  0.10000E+01  0.10000E+01  0.19883E+00
         2      1000
      5000         1        40         9         1         1         0
  0.00000E+00  0.00000E+00  0.00000E+00  0.00000E+00  0.00000E+00  0.10000E+01  0.20000E+03  0.10000E+01  0.00000E+00
      9000         1         2         1         9         1         1       179
 -0.61483E+00 -0.25048E+00  0.26526E+02 -0.24116E+00 -0.48116E-01  0.96929E+00  0.10000E+01  0.10000E+01  0.20326E+00
         3      1000
      5000         1        40         9         1         1         0
  0.00000E+00  0.00000E+00  0.00000E+00  0.00000E+00  0.00000E+00  0.10000E+01  0.20000E+03  0.10000E+01  0.00000E+00
      9000         1         2         1         9         1         1       179
  0.10696E+01 -0.36125E+00  0.26200E+02 -0.22800E+00 -0.23977E-01  0.97336E+00  0.10000E+01  0.10000E+01  0.20113E+00
         4      1000
      4000         1        40         9         1         1         0
  0.00000E+00  0.00000E+00  0.00000E+00  0.00000E+00  0.00000E+00  0.10000E+01  0.20000E+03  0.10000E+01  0.00000E+00
      5000         3      8016         5         9         1         1        35
  0.76245E+00  0.56926E+00  0.21511E+02  0.96960E+00 -0.24423E+00  0.15339E-01  0.12023E+02  0.10000E+01  0.14722E+00
      2007         3        17         1         9         1         1        35
  0.76245E+00  0.56926E+00  0.21511E+02  0.96960E+00 -0.24423E+00  0.15339E-01  0.71653E+02  0.10000E+01  0.14722E+00
      5000         3      8016      -101         9         1         1        35
  0.76245E+00  0.56926E+00  0.21511E+02  0.96960E+00 -0.24423E+00  0.15339E-01  0.12023E+02  0.10000E+01  0.14722E+00
      2007         3         2         2         9         1         1       122
  0.92904E+00  0.53038E+00  0.21515E+02  0.96849E+00 -0.24745E+00 -0.28297E-01  0.10000E+01  0.10000E+01  0.15199E+00
      5000         2      8016      -101         9         1         1        35
  0.76245E+00  0.56926E+00  0.21511E+02 -0.49962E+00  0.44221E+00  0.74487E+00  0.48621E+02  0.10000E+01  0.14722E+00
      9000         2         2         3         9         1         1       169
 -0.31296E+00  0.15663E+01  0.23117E+02 -0.43777E+00  0.54307E+00  0.71654E+00  0.10000E+01  0.10000E+01  0.17863E+00
         5      1000
      4000         1        40         9         1         1         0
  0.00000E+00  0.00000E+00  0.00000E+00  0.00000E+00  0.00000E+00  0.10000E+01  0.20000E+03  0.10000E+01  0.00000E+00
      4000         1      1001         2         9         1         1        43
 -0.78781E+00 -0.66411E+00  0.23031E+02  0.28205E-01  0.83219E+00  0.55378E+00  0.14965E+02  0.10000E+01  0.16105E+00
      5000         1      1001         2         9         1         1        43
 -0.78781E+00 -0.66411E+00  0.23031E+02  0.28205E-01  0.83219E+00  0.55378E+00  0.14965E+02  0.10000E+01  0.16105E+00
      9000         1         2         1         9         1         1       138
 -0.76482E+00 -0.44548E+00  0.23158E+02  0.12388E+00  0.91162E+00  0.39192E+00  0.10000E+01  0.10000E+01  0.16750E+00
```

Figure A.1 An example of ptrac.f output file generated by MCNPX code.

First, we describe the overall structure of the `ptrac.f` file. As it is illustrated in Fig. A.2, the file contains a header file followed by the track of each history (proton). The header contains a meaningless '-1' at the beginning, name of the input file and a block of real and integer numbers.

After header, the track information for each history begins which contains the track of the primary particle and all of the secondaries. The divider is the number "1000" after each history number. In this example we have 4 histories in the track section. The details of header and history tracks are discussed in the next steps.

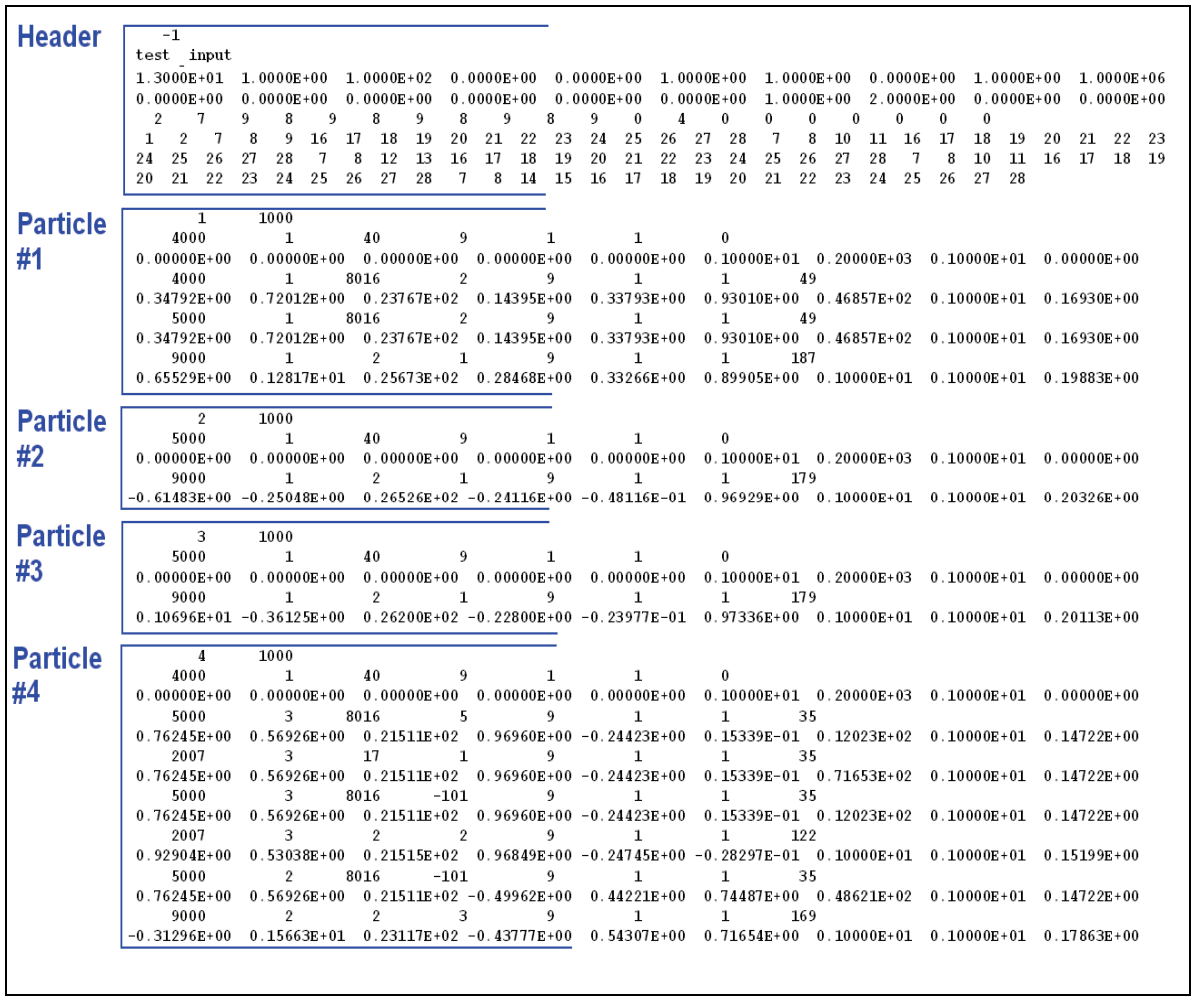

Figure A.2 Review of overall structure of the `ptrac.f` file including the header file and the data for 4 histories.

First section of header file which includes a list of real numbers is explained in Fig. A.3. The first number (*m*) is always 13 and the rest of the numbers are entries for n1- n13. If

user has no entry for *ni* that number would be *0* (i.e. *n2=0*), otherwise the entry of user is the number right after *ni*. For example, *n1= 1* means that the next number , which is related to *n1,* is 100. The n1-n13 are explained in Table A.1.

Table A.2 The description of n1-n13 in header file

n1	n2	n3	n4	n5	n6	n7	n8	n9	n10	n11	n12	n13
buffer	cell	event	file	filter	max	menp	nps	surface	tally	type	value	write

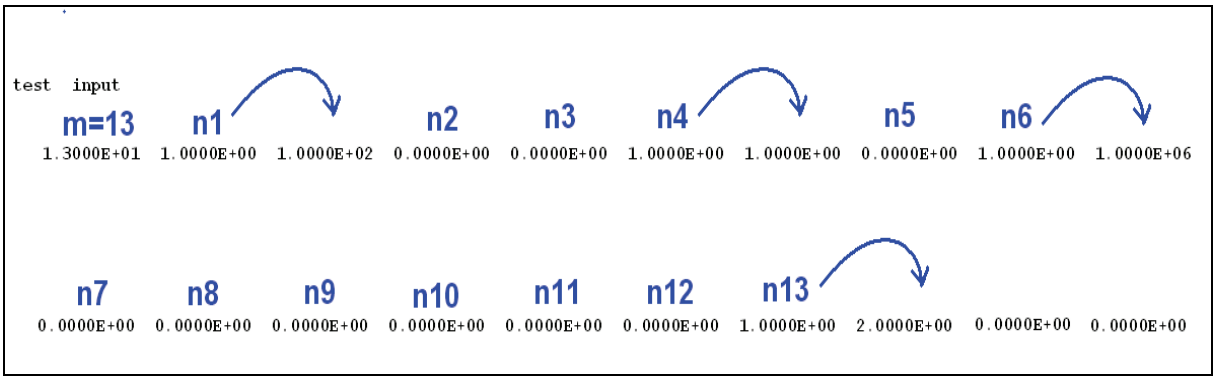

Figure A.3 The parameters related to first part of the header file.

The second part of the header file is illustrated in Fig. A.4. This is divided to two sub-sections. The first subsection is the explanation of the second subsection. As we see in Fig. A.4, the first sub-section, which is one line of integer numbers, contains the number of variables related to N1-N11 in the second subsection. For example, in the first line N1 and N2 are 2 and 7 respectively. This means that in the second sub-section first two numbers are related to N1 and next 7 numbers are related to N2. The second section is the description of the track section of the file and the definition of indices related to N1 –N12 are described in Table A.2 (Table I-3 in MCNP Manual). However these numbers are connected to track section of the `ptrac.f` file in three steps which is very confusing. We follow the discussion through an example in order to avoid confusion.

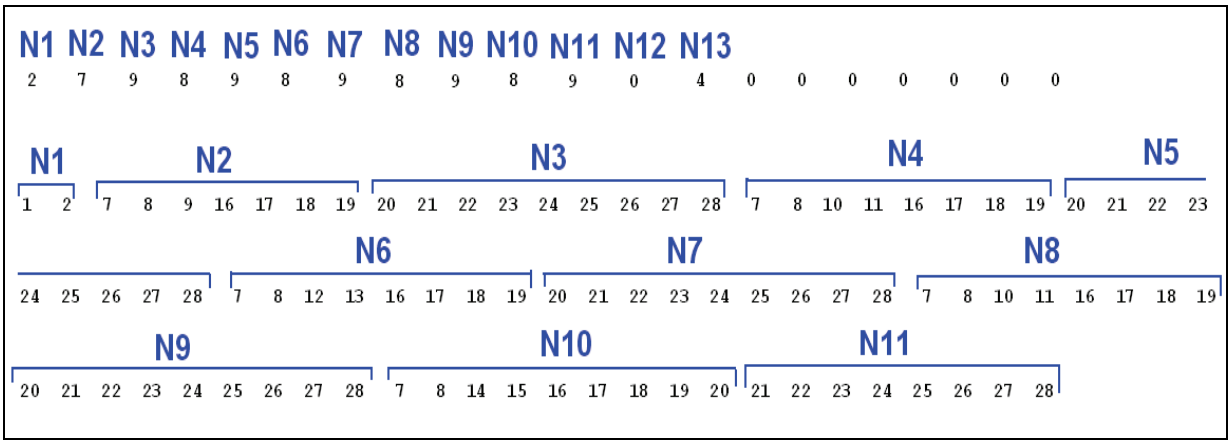

Figure A.4 Second part of the header which is related to the track information

N1 (According to Table I.3 in MCNPX manual) is related to the first line of the track information of the history as illustrated in Fig. A.5. N1 in Fig. A.4 has two variables which can be seen in the first line of the track information in Fig. A.4. The two indices are indicated in the header, Fig. A.4, which are (1 and 2). For meaning of 1 and 2 it is referred to Table I-4 in which MCNPX manual (Table A.2) and we just see: "NPS: see the developers guide !". After checking the developers guide we finally realize that NPS is number of history. Now we understand that the first number in the track section indicates the number of history followed up by "1000".

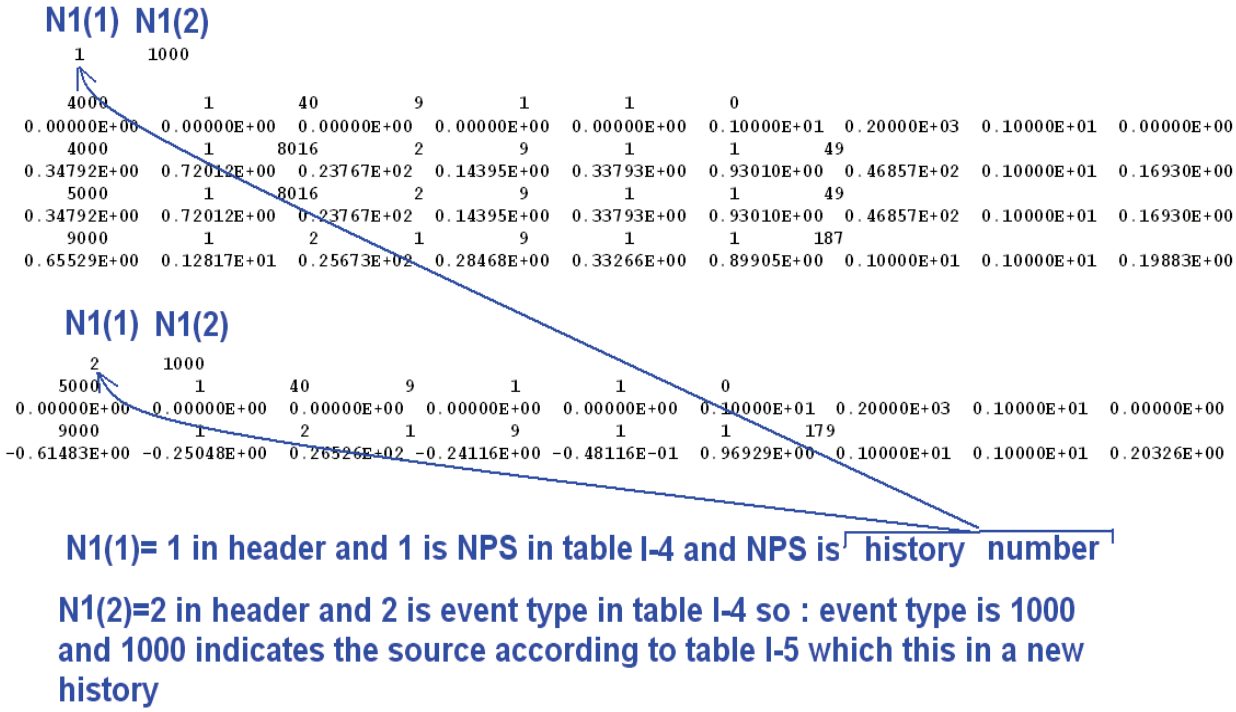

Figure A.5 Description of N(1) variable

Table A.2 Description of Variable IDs (From MCNPX manual).

Variable ID	MCNPX Name	Description
NPS LINE		
1	NPS	See the developer's guide
2	---	Event type of 1st event (see Table I-5)
3	NCL(ICL)	See the developer's guide
4	NSF(JSU)	See the developer's guide
5	JPTAL(1,ITAL)	See the developer's guide
6	TAL(JPTAL(7,ITAL))	See the developer's guide
EVENT LINE		
7		Event type of next event (see Table I-5)
8	NODE	See the developer's guide
9	NSR	See the developer's guide
10	NXS(2,IEX)	See the developer's guide
11	NTYN/MTP	Reaction type (see Table I-7). NTYN for bank event; MTP for collision event
12	NSF(JSU)	Surface number

Table A.3 Event type description (from MCNPX manual).

Location	Variable ID	Event Type					Flag†
		src	bnk‡	sur	col	ter	
I_2 or J_1	7	1000	±(2000+L)	3000	4000	5000	9000

† When I_2 or J_1 = 9000, this event is the last event for this history.
‡ When I_2 or J_1 < 0, the next event has been rejected and is included for creation information only. The value L is given in Table I-6.

The second number (1000) is related to N(2)=2 in the header (Fig. A.4) and this index in Table A.2 (Table I-3 MCNPX manual) is related to the event type. So the event type is 1000 and using Table A.3 (Table I-5 MCNPX manual) this number means "source" (this particle start from the source which means it's a new history).

Description of N2 is similar to N1 but much more important since in N2 set, the actual characteristics of the particle are determined. N2 is related to the line 2 in Fig. A.6 of the track information (line 1 in Fig. A.6 was described by N1). As shown in Fig. A.4 in the first sentence, N2 has 7 indices and they are described in the second line of the track section (line 2 Fig.A.6).

First number related to N2 , (N2(1) in Fig. . A.6) according to Fig. A.4 has the index of 7 (please note that this '7' has nothing to do with the '7' that we have in the last

paragraph) and index of 7 in Table A.2 is "Event type of **next** event". This is one the most confusing part in `ptrac.f` output. Since all of the parameters (N(2) -N(7)) of this line 2 is for related event (#1) in line 3 but the first parameter determines the event number 2 in Fig. A.6. In Fig. A.6 for first history, line2, N(1) is 4000 as it is pointed with a circle. This means that **next** event (event#2) is 4000 type and according to Table A.3, 4000 means a collision. So event number 2 is a collision. Everything else in line 2 and line 3 are related to event number 1, but the first number shows the type of the next event, event #2.

The same role is shown in history number 2. N2(1) in 5000 which according to Table A.3 is termination and this means that the next event in this history, event #2 is the termination event in which the particle track is terminated. We will see that 9000 at the end of the track is not like the 4000 and 5000, and it is not related to the event type of the "next" event.

The rest of the variables of N2 are straight forward which are related to current event (event #1). At first we check that the related indices of N(2) – N(7) from Fig. A.4 and the related numbers that we see in track in Fig. A.6 are described in Table A.2 (Table I.4 in MCNPX manual and as one would notice, in the MCNPX manual, instead of explaining the variables, a referral to "See the developer's guide" is made). Finally using Tables and descriptions, the related parameters to N(2) – N(7) for our example are shown in Table A.4.

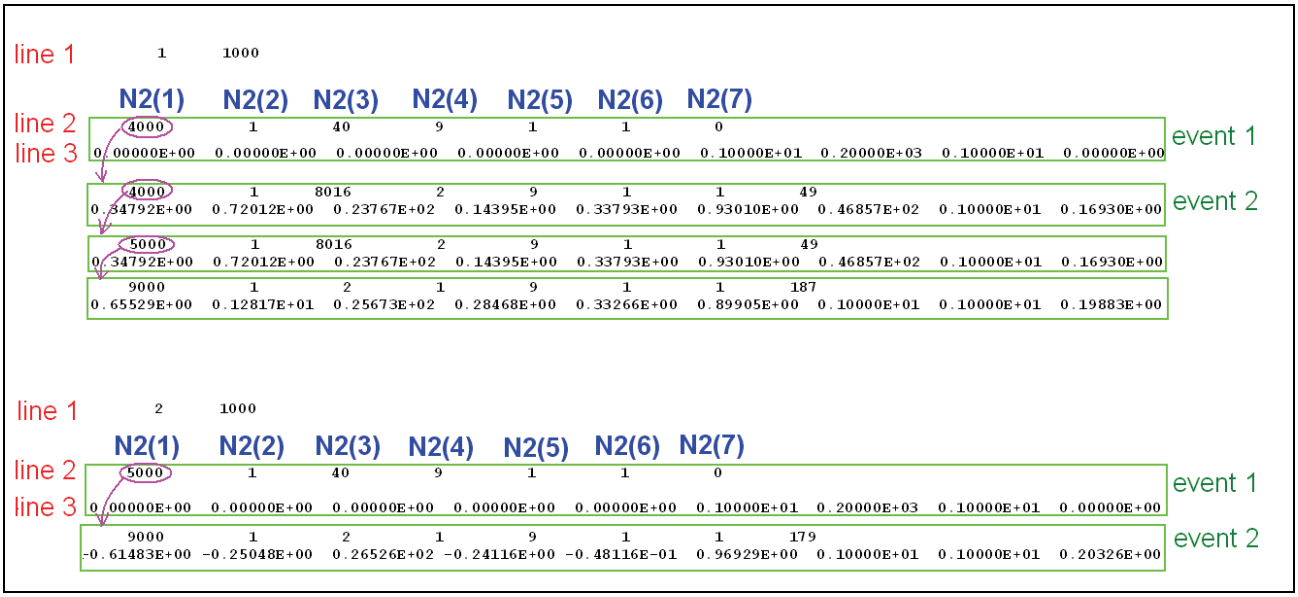

Figure A.6 Description of N2 set and N2(1) which means the event type of the "next" event .

Table A.4 Explanation of N2 parameters in Fig. A.6.

	Related index in header (Fig.A.4)	Related number in the track (Fig.A.6)	Final description
N2(2)	8	1	Number of the nodes in the track
N2(3)	9	40	Source type
N2(4)	16	9	Particle type (9 for proton)
N2(5)	17	1	Number of the related cell
N2(6)	18	1	Perturbation material number
N2(7)	19	0	Count of the collisions per track

In the next step, we discuss the parameters related to N3 set .N3 directly describes the physical parameter of the proton in each step. According to the first line of header in Fig. A.4, N3 has 9 indices and those indices are mentioned in the second section of the header. N3 set of the numbers in track line (Fig. A.7 and Table A.5) is related to initial characteristics of the particle such as position (*x*,*y*,*z*), direction cosine (*u*,*v*,*w*) and energy of the proton. The unit of position in `ptrac` file is *cm* and unit of energy is MeV.

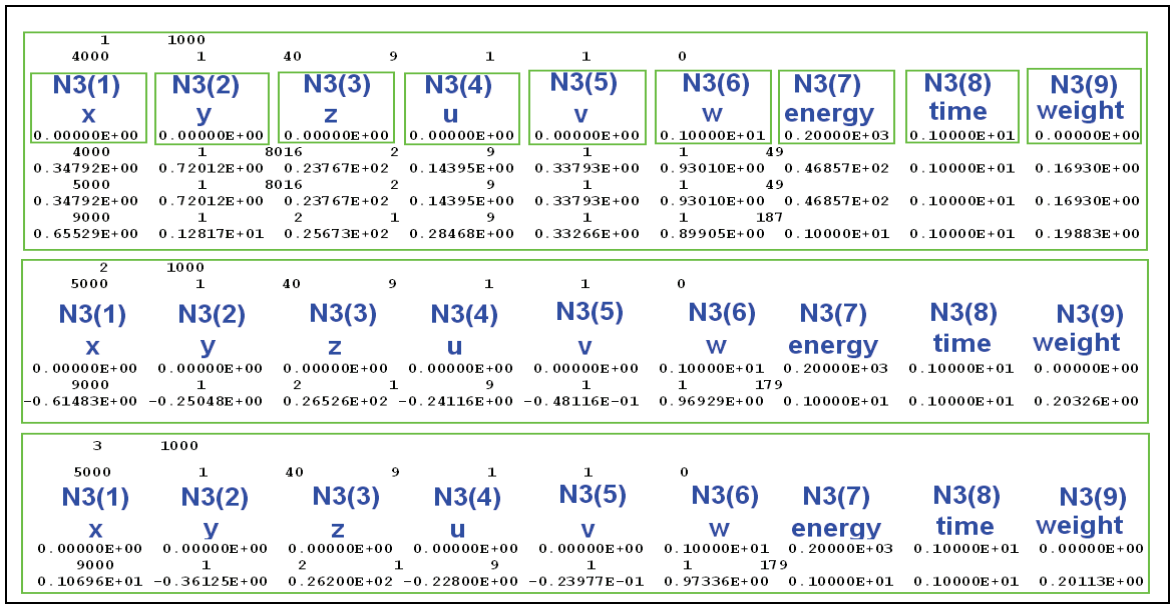

Figure A.7 Description of the first event related to N3 set of numbers.

Table A.5 The physical parameters related to N3.

	Related index in header (Fig. A.4)	Related number in the track (Fig. A.6)	Final description
N3(1)	20	0	x (position, cm)
N3(2)	21	0	y
N3(3)	22	0	z
N3(4)	23	0	u (direction)
N3(5)	24	0	v
N3(6)	25	1	w
N3(7)	26	200	Energy (MeV)
N3(8)	27	1	weight
N3(9)	28	0	time

The numbers N2 and N3 were related to the first event which is an event from the source and describes the initial characteristics of the particle. We have similar relations for each set of "two" numbers (N4,N5) and (N6,N7) and (N8,N9) depending on the reaction type (Table I.3 in MCNPX manual). For example, (N8,N9) is related to the collision type (number 4000 in Table A.3). In our example, as we saw in Fig. A.6, for particle number 1 in line 2, first number (4000) indicates the reaction type of the next event. Hence, the next event (event number 2) is a collision.

We describe this event (event # 2) in Fig. A.8. Since this event is a collision type, the related numbers are N8 and N9. N8 according to the header, Fig. 8.4 line1, has 8 indices. The index of the first number, N8(1), is 7 which according to Table A.2 is the event type of the next line. This means that event number 3 is also a collision event. As we discussed earlier, this number has nothing to do with the event # 2. The rest of the numbers (N8(2)-N8(8)) are related to the current event, event #2, and they are described in Table A.6.

The set of the N9 numbers are related to physical parameters of the particle at this point and are similar to the description of A3 in Table A.4. The related parameters to N9(1)-N(9) are also illustrated in Fig. A.8. In the event number 3, Fig. A.8, as we see the

N8(1)=5000 which means the event type of the next event . Event type “5000” according to Table A.3 is termination type and this means that next event , event number 4 is the last event of the particle.

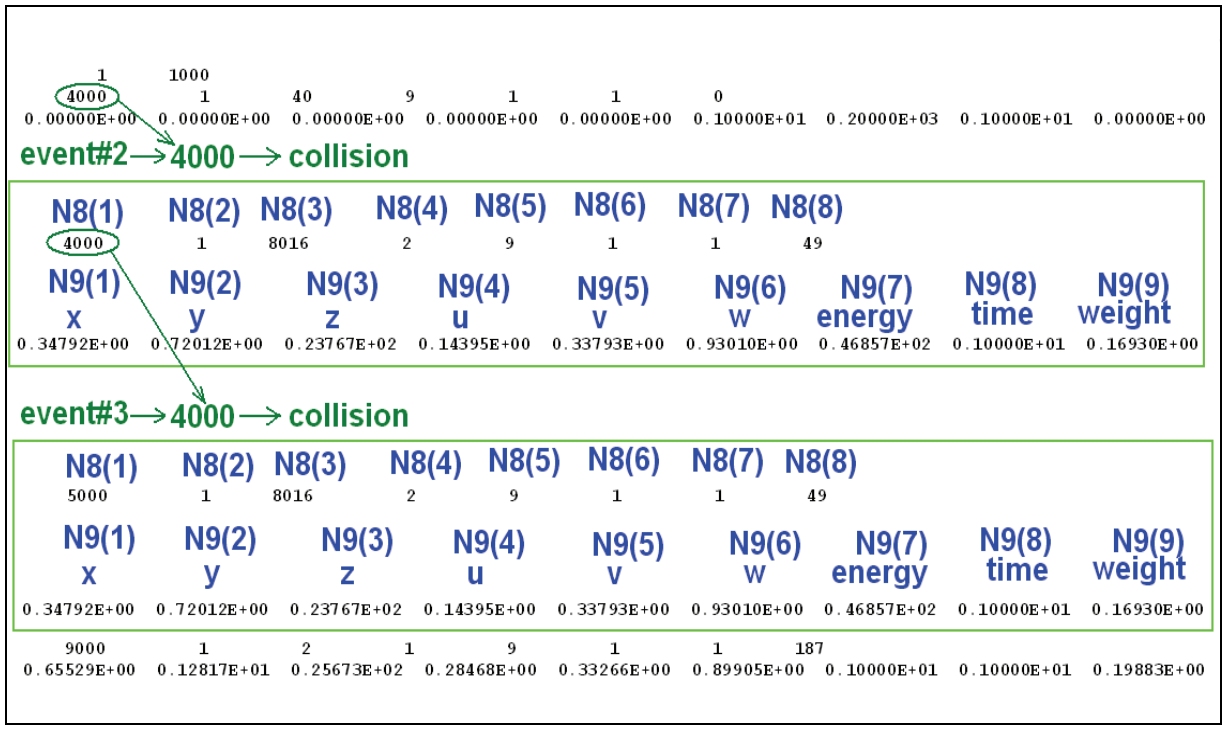

Figure A.8. N(8) and N(9) which are related to collision event.
Table A.6 Explanation of N8 parameters.

	Related index in header (Fig. A.4)	Related number in the track (Fig. A.8)	Final description
N8(2)	8	1	Number of the nudes in the track
N8(3)	10	8016	1000×Z+A (oxygen)
N8(4)	11	2	Reaction type (elastic)
N8(5)	16	9	Particle type (proton)
N8(6)	17	1	Cell number
N8(7)	18	1	Perturbation material number
N8(8)	19	49	Count of the collisions per track

The last event (event #4) in particle number 1 is illustrated in Fig. A.9. N10(1)=9000 is a flag which says this is the last event for this 'history'. Please note that 9000 is not necessarily a flag for the last event of the particle since we might have a secondary. 9000 is the last event of the last particle. N10(3) indicates the termination type and is related to the parameter NTER. NTER=2 according to Table A.7 (Table I.7 in MCNPX manual) is the energy cutoff. The proton at this point reaches the user defined energy cut-off (0.1 MeV) and the transport is terminated by MCNPX.

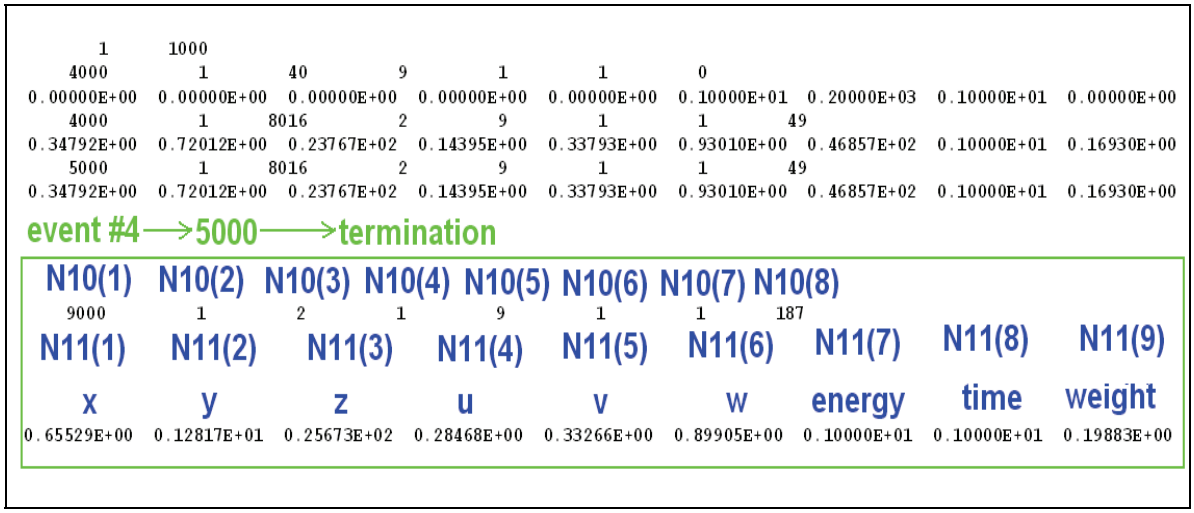

Figure 8.9 Last event for particle number one. The termination type is "energy cut-off".
Table A.7 Definition of various types of termination (NTER)

NTER	Description	MTP	NTYN	Description
1	Escape			**NEUTRON**
2	Energy cutoff	4	1	Inelastic $S(\alpha,\beta)$
3	Time cutoff	2	2	Elastic $S(\alpha,\beta)$
4	Weight window	>0	-99	Elastic scatter / Inelastic scatter
5	Cell importance		>5	ENDF Reaction ID
6	Weight cutoff			
7	Energy importance			
8	DXTRAN			**PHOTON**
9	Forced collision	-1	1	Incoherent scatter
10	Exponential transform	-2	2	Coherent scatter

Finally we explain an example of the track with secondary particles. In our example particle number 4 generates secondary particles as illustrated in Fig. 8.10 . In this section the proton has an interaction and the track of the particle is terminated at the interaction point. The position of interaction is (x,y,z)=(0.762,0.569,21.51) in *cm* and the proton

interacts with an oxygen atom (8016). Then we have the track of the primary proton as one particle (the one with the larger energy) and another secondary particle. The number 2007 according to Table A.3 indicates that the next event in the beginning of a secondary particle (2000+L, L=7, and the definition of secondary particle (L value) is indicated in Table I.6 MCNPX manual) .

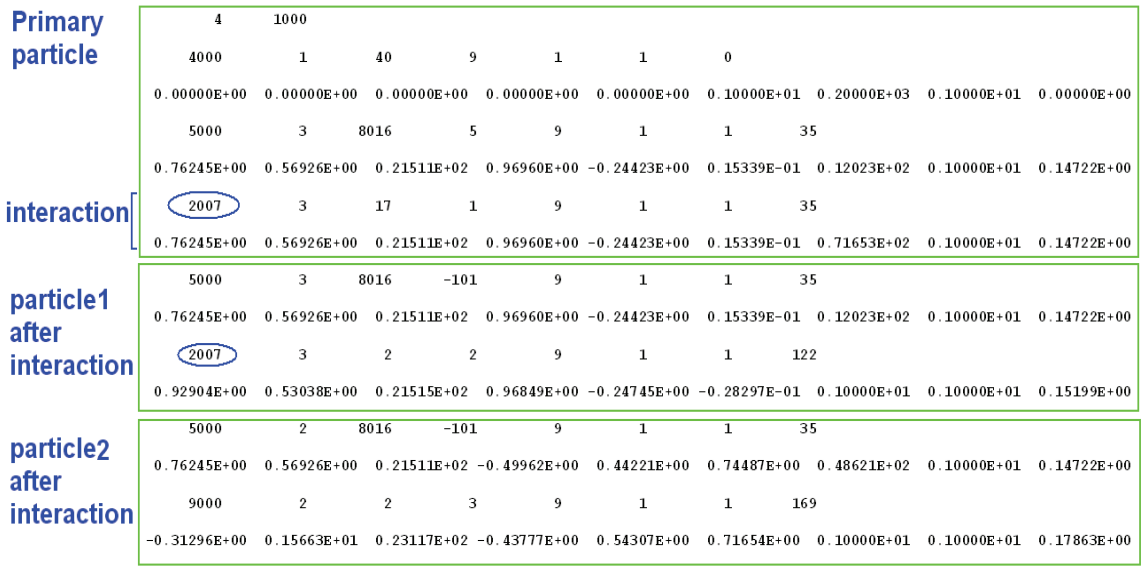

Figure A.10 This is history number 4 in which the proton interacts with an oxygen atom and generates a secondary particle.

As we see in Fig. A.10, both particles (particle1 and particle2) have the same position (x,y,z)=(0.762,0.569,21.51) but different directions. The direction cosines for particle 1 are (u,v,w)=(0.969,-0.244,0.153E-1) and for particle 2 (u,v,w)=(-0.499,-0.442,0.744). The energy of the particles is 12.02 and 48.62 MeV for particle 1 and 2, respectively. Both particles are protons (NPS=9) and they are terminated in the second step by the energy cut-off. Particle 1 come to rest after 122 collisions and particle2 comes to rest after 169 collisions.

An example of `ptrac.f` for 150 MeV protons : Another example of `ptrac.f` output file is illustrated in Fig. A.11 which corresponds to the track of a 150 MeV proton beam in water. This file contains the header file and the track information of two protons. The detail information of first particle is described step by step. Note that in some part of the following explanations we used the information of the header file which is discussed before.

```
test  input
 1.3000E+01  1.0000E+00  1.0000E+02  0.0000E+00  0.0000E+00  1.0000E+00  1.0000E+00  0.0000E+00  1.0000E+00  1.0000E+06
 0.0000E+00  0.0000E+00  0.0000E+00  0.0000E+00  0.0000E+00  0.0000E+00  0.0000E+00  1.0000E+00  2.0000E+00  0.0000E+00  0.0000E+00
   2   7   9   8   9   8   9   8   9   8   9   0   4   0   0   0   0   0   0   0
  1  2  7  8  9 16 17 18 19 20 21 22 23 24 25 26 27 28  7  8 10 11 16 17 18 19 20 21 22 23
 24 25 26 27 28  7  8 12 13 16 17 18 19 20 21 22 23 24 25 26 27 28  7  8 10 11 16 17 18 19
 20 21 22 23 24 25 26 27 28  7  8 14 15 16 17 18 19 20 21 22 23 24 25 26 27 28

Line#          1      1000
1           4000         1        40         9         1         1         0
2     0.00000E+00  0.00000E+00  0.00000E+00  0.00000E+00  0.00000E+00  0.10000E+01  0.15000E+03  0.10000E+01  0.00000E+00
3           4000         1      1001         2         9         1         1         6
4    -0.19869E-01 -0.44568E-01  0.40884E+01 -0.33149E+00  0.35893E+00  0.87251E+00  0.96298E+02  0.10000E+01  0.27694E-01
5           5000         1      1001         2         9         1         1         6
6    -0.19869E-01 -0.44568E-01  0.40884E+01 -0.33149E+00  0.35893E+00  0.87251E+00  0.96298E+02  0.10000E+01  0.27694E-01
7           2031         1         2         1         9         1         1       221
8    -0.23774E+01  0.24571E+01  0.10484E+02  0.26982E-02  0.52141E+00  0.85331E+00  0.20000E+00  0.10000E+01  0.10419E+00
9           5000         2      1001       -99         9         1         1         0
10   -0.19869E-01 -0.44568E-01  0.40884E+01  0.55628E+00 -0.67269E+00  0.48790E+00  0.29651E+02  0.10000E+01  0.27694E-01
11          9000         2         2         2         9         1         1       171
12    0.43907E+00 -0.66222E+00  0.45111E+01  0.42053E+00 -0.69268E+00  0.58595E+00  0.20000E+00  0.10000E+01  0.43904E-01
             2      1000
            5000         1        40         9         1         1         0
      0.00000E+00  0.00000E+00  0.00000E+00  0.00000E+00  0.00000E+00  0.10000E+01  0.15000E+03  0.10000E+01  0.00000E+00
            9000         1         2         1         9         1         1       225
     -0.33490E+00  0.63449E-01  0.15844E+02 -0.19594E+00 -0.12293E+00  0.97288E+00  0.20000E+00  0.10000E+01  0.13751E+00
```

Figure A.11 `ptrac.f` file for 150 MeV protons in water.

Table A.8 Description of the numbers is line 1.

4000	type of the next event, line 3 and 4 (related to next event) are a collision type.
1	the number of nudes
40	Source type (NSR)
9	Particle type (IPT) , proton
1	Number of the cell in the problem. Particle is in the cell #1.
1	Perturbation material number
0	Count of collision per track. (It is the beginning of the track an no collision yet)

Line # 2 is explained in Table A.5 exactly in the same order. The column 7 is relates to energy of the proton , 150 MeV. Table A.9 is related to line 3.

Table A.9 Description of the numbers is line 3.

4000	Type of the next event, line 5 and 6 (related to next event) are a collision type.
1	The number of nudes
1001	Table A.2, NXS(2) , and from table F-1 MCNPX manual NSX(2) =1000×Z+A . The proton has a collision with a helium atom at this point.
2	MTP, Reaction type: Table I-7 MCNPX ,NTYN=2 is an elastic collision.
9	Particle type (IPT) , proton
1	Number of the cell in the problem. Particle is in the cell #1.
1	Perturbation material number
6	Count of collision per track. 6 collision until this point .

Since it is an elastic collision for some reason, MCNPX writes the same parameters twice and all the numbers are repeated again in line 5 and 6 (except number 5000). '5000' means in the next event, the transport of the current particle is terminated. Since it is '5000' and not '9000,' there are other secondary particles to be transported. Number of line 7 related to termination event is described in Table A.10 .The secondary particle is described in line 9 and 10 with energy = 29.6 MeV.

Table A.10 Description of the numbers is line 7.

2031	type of the next event, 2000=secondary particle, 2000+L, L=31, and Table (I-6, MCNPX) it is light ions from protons.
1	The number of nudes
2	NTER, termination type , 2= energy cut off (0.2 MeV)
1	Branch number of the history .
9	Particle type (IPT) , proton
1	Number of the cell in the problem. Particle is in the cell #1.
1	Perturbation material number
221	Count of collision per track, 221 collisions until this point .

Table A.11 Description of the numbers is line 9.

5000	type of the next event, termination event.
2	the number of nudes
1001	Table A.2, NXS(2) , and from table F-1 MCNPX manual NSX(2) =1000×Z+A . The proton has a collision with a helium atom at this point.
-99	NTYN, Reaction type: Table I-7 MCNPX ,NTYN=2 is an elastic collision.
9	Particle type (IPT) , proton
1	Number of the cell in the problem. Particle is in the cell #1.
1	Perturbation material number
0	Count of collision per track, 221 collisions until this point .

Bibliography

W. Abdel-Rahman, J. P. Seuntjens, F. Verhaegen, and E. B. Podgorsak, "Radiation induced currents in parallel plate ionization chambers: measurement and Monte Carlo simulation for megavoltage photon and electron beams," Med. Phys. **33**, 3094–3104 (2006).

S. Agostinelli *et al*., "GEANT4—A simulation toolkit," Nucl. Instrum. Methods Phys. Res. A 506, 250–303 (2003).

K. Aljarrah, G. C. Sharp, T. Neicu, and S. B. Jiang "Determination of the initial beam parameters in Monte Carlo linac simulation," Med. Phys. **33**, 3767–3780 (2006).

H. I. Amols, L. E. Reinstein, and B. Lagueux, "A quantitative assessment of portal film contrast as a function of beam energy," Med. Phys. **13**, 711-716 (1986).

P. Andreo, "Monte Carlo techniques in medical radiation physics," Phys. Med. Biol. **36**, 861–920 (1991).

L. E. Antonuk, J. Boudry, Y. El-Mohri, W. Huang, J. H. Siewerdsen, J. Yorkston, and R. A. Street, "A high resolution, high frame rate, flatpanel TFT array for digital x-ray imaging," Proc. SPIE 2163, 118–128 (1994).

L. E. Antonuk, J. Yorkston, W. Huang, H. Sandler, J. H. Siewerdsen, and Y. el-Mohri, "Megavoltage imaging with a large-area, flat-panel, amorphous silicon imager," Int. J. Radiat. Oncol., Biol., Phys. **36**, 661–672 (1996).

F. Araki, " Monte Carlo study of a Cyberknife stereotactic radiosurgery system," Med. Phys. **33**,2955–2963 (2006).

H. Attix, Introduction to radiological physics and radiation dosimetry (Whily & Son, New York, NY, 1986).

N. A. Baily, R. A. Horm, and T. D. Kampp, "Fluoroscopic visualization of megavoltage therapeutic X-ray beams," Int. J. Radiat. Oncol. Biol. Phys. **6**, 935–939 (1980).

J. Balter, A. Thompson, and R. K. Ten Haken, "Automated quality assurance of mechanical components of a computer controlled accelerator using and EPID," Fourth International Workshop on Electronic Portal Imaging, Amsterdam, 1996.

J. Baro, J. Sempau, J. M. Fernandez-Varea, and F. Salvat, "PENELOPE: an algorithm for Monte Carlo simulation of the penetration and energy loss of electrons and positrons in matter," Nucl. Instrum. Methods Phys. Res. B 100, 31–46 (1995).

M. Berger and S. Seltzer, "ETRAN Monte Carlo code system for electron and photon transport through extended media," Radiation Shielding Information Center (RSIC) Report CCC-107, Oak Ridge National Laboratory, Oak Ridge, TN, 1973.

M. J. Berger, in *Methods in Computational Physics*, edited by S. Fernbach, B. Alder, and M. Rothenberg (Academic, New York, 1963), Vol. 1.

M. J. Berger, "Penetration of proton beams through water II. Three dimensional absorbed dose distributions," Technical Report NISTIR 5330(National Institute of Standards and Technology, Gaithersburg, MD, 1993).

M. Bertini, L. Lönnblad, and T. Sjöstrand, "PYTHIA version 7: A proof-of-concept version," Comp. Phys. Comm. **134**, 365–391 (2001).

M. R. Bieda, J. A. Antolak, and K. R. Hogstrom, "The effect of scattering foil parameters on electron-beam Monte Carlo calculations," Med. Phys. **28**, 2527–2534 (2001).

A. F. Bielajew and D. W. O. Rogers, "PRESTA—'The parameter reduced electron step algorithm' for electron Monte Carlo transport," Nucl. Instrum. Meth. B **18**, 165–181 (1987).

A. F. Bielajew, D. W. Rogers, J. Cygler, and J. J. Battista, "A comparison of electron pencil beam and Monte Carlo calculation methods," in: The Use of Computers in Radiation Therapy, edited by A.D. Bruinvis (Elsevier, Amestrdam, 1987).

A. F. Bielajew, ''HOWFAR and HOWNEAR: geometry modelling for Monte Carlo particle transport,'' Technical Report PIRS-0341, National Research Council of Canada, Ottawa, 1995. (http://www.slac.stanford.edu/egs/docs/pdf/nrc-pirs0341.pdf.)

M. Blomquist, J. Li, C. M. Ma, B. Zackrisson, and M. Karlsson, "Comparison between a conventional treatment energy and 50 MV photons for the treatment of lung tumors," Phys. Med. Biol. **47**, 889–897 (2002).

J. Boda-Heggemann, C. Walter, A. Rahn, H. Wertz, I. Loeb, F. Lohr, and F.Wenz, "Repositioning accuracy of two different mask systems-3D revisited: comparison using true 3D/3D matching with cone-beam CT," Int. J. Radiat. Oncol., Biol., Phys. **66**(5), 1568–1575 (2006).

A. J. Bolewski, M. Ciechanowski, A. Dydejczyk, and A. Kreft, ”On the optimization of the isotopic neutron source method for measuring the thermal neutron absorption cross section: advantages and disadvantages of BF3 and 3He counters,” Appl. Radiat. Isot. **66**, 457-462 (2008).

J. Borg, I. Kawrakow, D. W. O. Rogers, and J. P. Seuntjens, ‘‘Monte Carlo study of correction factors for Spencer–Attix cavity theory at photon energies at or above 100 keV,’’ Med. Phys. **27**, 1804–1813 (2000).

T Bortfeld, “An analytical approximation of the Bragg curve for therapeutic proton beams,” Med. Phys. **24,** 2024–33 (1997).

A. L. Boyer, L. Antonuk, A. Fenster, M. Van Herk, H. Meertens, P. Munro, L. E. Reinstein, and J. Wong, “A review of electronic portal imaging devices (EPIDs),” Med. Phys. **19**, 1–16 (1992).

S. Brenner, B. Rosengren, H. Wallman, and O. Netteland, “Television monitoring of a 30 MV x-ray beam,” Phys. Med. Biol. **7**, 29–34 (1962).

F. B. Brown, “MCNP—A general Monte Carlo-particle transport code, version 5,” Report LA-UR-03 1987, Los Alamos National Laboratory, Los Alamos, NM, 2003.

A. L. Boyer and E. C. Mok, “A photon beam distribution model employing convolution calculation,” Med. Phys. **12**, 169–177 (1985).

J. F. Briesmeister, “MCNP-A general Monte Carlo N-particle transport code, Version 4C,” Report LA-13709-M, Los Alamos National Laboratory, NM, 2000.

K. K. Brock, D. L. McShan, R. K. Ten Haken, S. J. Hollister, L. A. Dawson, and J. M. Balter, “Inclusion of organ deformation in dose calculations,” Med. Phys. **30**, 290–295 (2003).

A. Bozkurt and D. Bor, “Simultaneous determination of equivalent dose to organs and tissues of the patient and of the physician in interventional radiology using the Monte Carlo method,” Phys. Med. Biol. **52**, 317–330 (2007).

Å. K. Carlssonyx, P. Andreoyz, and A. Brahmey, “Monte Carlo and analytical calculation of proton pencil beams for computerized treatment plan optimization,” Phys. Med. Biol. **42,** 1033–1053 (1997).

J. R. Cary, S. G. Shasharina, Cummings J. C., J. V. W. Reynders, and P. J. Hinker, "Comparison of C++ and Fortran 90 for Object-Oriented Scientific Programming," Comp. Phys. Comm. **105**, 20–36 (1997).

E. L. Chaney, T. J. Cullip, and T. A. Gabriel, "A Monte Carlo study of accelerator head scatter," Med. Phys. **21**, 1383–1390 (1994).

S. Chekanov, "RunMC—an object-oriented analysis framework for Monte Carlo simulation of high-energy particle collisions," Comp. Phys. Comm. **173**, 115–198 (2005).

I. J. Chetty, J. M. Moran, T. S. Nurushev, D. L. McShan, B. A. Fraass, S. J. Wilderman, and A. F. Bielajew, "Experimental validation of the DPM Monte Carlo code using minimally scattered electron beams in heterogeneous media," Phys. Med. Biol. **47**, 1837–1851 (2002).

I. J. Chetty, P. M. Charland, N. Tyagi, D. L. McShan, B. Fraass, and A. F. Bielajew, "Experimental validation of the DPM Monte Carlo code for photon beam dose calculations in inhomogeneous media," Med. Phys. **29**, 1351 (abstract) (2002).

I. J. Chetty, P. M. Charland, N. Tyagi, D. L. Mc Shan, B. A. Fraass, and A. F. Bielajew, "Photon beam relative dose validation of the DPM Monte Carlo code in lung-equivalent media," Med. Phys. **30**, 563–573 (2003).

I. J. Chetty, N. Tyagi, M. Rosu, P. M. Charland, D. L. McShan, R. K. Ten Haken, B. A. Fraass, and A. F. Bielajew, "Clinical implementation, validation and use of the DPM Monte Carlo code for radiotherapy treatment planning," in Nuclear Mathematical and Computational Sciences: A Century in Review, A Century Anew, Gatlinburg, TN (American Nuclear Society, LaGrange Park, IL, 2003), Vol. 119, pp. 1–17.

I. J. Chetty, "Monte Carlo treatment planning: The influence of 'variance reduction' techniques (ECUT, PCUT, ESTEP) on the accuracy and speed of dose calculations," Med. Phys. **32**, 2018 (abstract) (2005).

I. Chetty *et al*., "Guidance report on clinical implementation of the Monte Carlo method in external beam radiation therapy treatment planning: Report of the AAPM Task Group No. 105," Med. Phys. **34**, 4818–4853 (2007).

O. Chibani and X. A. Li, "Monte Carlo dose calculations in homogeneous media and at interfaces: A comparison between GEPTS, EGSnrc, MCNP, and measurements," Med. Phys. **29**, 835–847 (2002).

S. H. Cho, O. N. Vassiliev, S. Lee, H. H. Liu, G. S. Ibbott, and R. Mohan," Reference photon dosimetry data and reference phase space data for the 6 MV photon beam from varian clinac 2100 series linear accelerators," Med. Phys. **32**, 137–148 (2005).

L. E. Court, L. Jahnke, D. Chin, J. Song, R. Cormack, P. Zygmanski, R. B. Tishler, and L. Chin, "Dynamic IMRT treatments of sinus region tumors: comparison of Monte Carlo calculations with treatment planning system calculations and ion chamber measurements," Technol. Cancer Res. Treat. **5**, 489–95 (2006).

J. C. Chow, M. K. Leung, M. K. Islam, B. D. Norrlinger, and D. A. Jaffray, "Evaluation of the effect of patient dose from cone beam computed tomography on prostate IMRT using Monte Carlo simulation," Med. Phys. **35**, 52–60 (2008).

G. Ciangaru, J. C. Polf, M. Bues, and A. R. Smith, "Benchmarking analytical calculations of proton doses in heterogeneous matter," Med. Phys. **31** 3511–23 (2005).

C. L. Creutzberg, V. G. Althof, H. Huizenga, A. G. Visser, and P. C. Levendag, "Quality assurance using portal imaging: The accuracy of patient positioning in irradiation of breast cancer," Int. J. Radiat. Oncol., Biol., Phys. **25**(3), 529–539 (1993).

F. Crop, N. Reynaert, G. Pittomvils, L. Paelinck, W. De Gersem, C. De Wagter, L. Vakaet, W. De Neve, and H. Thierens, "Monte Carlo modeling of the ModuLeaf miniature MLC for small field dosimetry and quality assurance of the clinical treatment planning system," Phys. Med. Biol. **52**, 3275–3290 (2007).

C. Cris, E. Born, R. Mini, H. Neuenschwander, and W. Volken, "A scaling method for multiple source models," in Proceedings of the 13th ICCR, edited by T. Bortfeld and W. Schlegel (Springer-Verlag, Heidelberg, 2000), pp. 411–413.

J. Cygler, J. J. Battista, J. W. Scrimger, E. Mah, and J. Antolak, "Electron dose distributions in experimental phantoms: a comparison with 2D pencil beam calculations," Phys. Med. Biol. **32**, 1073–1086 (1987).

J. J. DeMarco, T. D. Solberg, and J. B. Smathers, "A CT-based Monte Carlo simulation tool for dosimetry planning and analysis," Med. Phys. **25**, 1–11 (1998).

B. De Smedt, N. Reynaert, F. Flachet, M. Coghe, M. G. Thompson, L. Paelinck, G, Pittomvils, C. De Wagter, W. De Neve, and H. Thierens, "Decoupling initial electron beam parameters for Monte Carlo photon beam modelling by removing beam-modifying filters from the beam path," Phys. Med. Biol. **50**, 5935–5951 (2005)

M. J. Daly, J. H. Siewerdsen, D. J. Moseley, D. A. Jaffray, J. C. Irish, "Intraoperative cone-beam CT for guidance of head and neck surgery: Assessment of dose and image quality using a C-arm prototype," Med. Phys. **33**, 3769–3780 (2006).

J. W. Denham, M. J. Dally, K. Hunter, J. Wheat, P. P. Fahey, and C. S. Hamilton, "Objective decision-making following a portal film: The results of a pilot study," Int. J. Radiat. Oncol. Biol. Phys. **26**, 869–876 (1993).

J. Deng, S. B. Jiang, P. Pawlicki, J. Li, and C.-M. Ma, "Electron beam commissioning for Monte Carlo dose calculation," in Proceedings of the 13th ICCR, edited by T. Bortfeld and W. Schlegel (Springer-Verlag, Heidelberg, 2000), pp. 431–433.

H. M. Deloar, E. Kunieda, T. Kawase, T. Tsunoo, H. Saitoh, M. Ozaki, K. Saito, S. Takagi, O. Sato, T. Fujisaki, A. Myojoyama, and G. Sorell, "Investigations of different kilovoltage X-ray energy for three-dimensional converging stereotactic radiotherapy system: Monte Carlo simulations with CT data," Med. Phys. **33**, 4635–4642 (2006).

G. X. Ding, J. E. Cygler, G. G. Zhang, and M. K. Yu, "Evaluation of a commercial three dimensional electron beam treatment planning system," Med. Phys. **26**, 2571–2580 (1999).

G. X. Ding, "Energy spectra, angular spread, fluence profiles and dose distributions of 6 and 18 MV photon beams: Results of Monte Carlo simulations for a Varian 2100EX accelerator," Phys. Med. Biol. **47**, 1025–1046 (2002).

G. X. Ding, J. E. Cygler, C. W. Yu, N. I. Kalach, and G. Daskalov, "A comparison of electron beam dose calculation accuracy between treatment planning systems using either a pencil beam or a Monte Carlo algorithm," Int. J. Radiat. Oncol. Biol. Phys. **63,** 622–633(2005).

G. X. Ding, D. M. Duggan, C. W. Coffey, P. Shokrani, and J. E. Cygler, "First macro Monte Carlo based commercial dose calculation module for electron beam treatment planning--new issues for clinical consideration," Phys. Med. Biol. **51**, 2781–2799 (2006).

G. X. Ding, D. M. Duggan, and C. W. Coffey, "A theoretical approach for non-equilibrium radiation dosimetry." Phys. Med. Biol. **53**, 3493–3499 (2008).

L. Dong, A. Shiu, S. Tung, and A. Boyer, "Verification of radiosurgery target point alignment with an electronic portal imaging device (EPID)," Med. Phys. **24**, 263–267 (1997).

R. Doucet, M. Olivares, F. DeBlois, E. B. Podgorsak, I. Kawrakow, and J. Seuntjens, "Comparison of measured and Monte Carlo calculated dose distributions in inhomogeneous phantoms in clinical electron beams," Phys. Med. Biol. **48**, 2339–2354 (2003).

D. M. Duggan, "Improved radial dose function estimation using current version MCNP Monte-Carlo simulation: Model 6711 and ISC3500 125I brachytherapy sources," Appl Radiat Isot. 611, 443–450 (2004).

P. Edimo, C. Clermont, M. G. Kwato, and S. Vynckier, "Evaluation of a commercial VMC++ Monte Carlo based treatment planning system for electron beams using EGSnrc/BEAMnrc simulations and measurements," Med. Phys. **22**, August (2008).

K. Eklund and A. Ahnesjö, "Fast modelling of spectra and stopping-power ratios using differentiated fluence pencil kernels," Phys. Med. Biol. **53**, 4231–4247 (2008).

A. Facure, A. X. da Silva, L. A. da Rosa, S. C. Cardoso and G. F. Rezende, "On the production of neutrons in laminated barriers for 10 MV medical accelerator rooms," Med. Phys. **35,** 3285–3292 (2008).

B. A. Faddegon, C. K. Ross, and D. W. O. Rogers, "Forward-directed bremsstrahlung of 10- to 30-MeV electrons incident on thick targets of Al and Pb," Med. Phys. **17**, 773–785 (1990).

B. A. Faddegon, C. K. Ross, and D. W. O. Rogers, "Angular distribution of bremsstrahlung from 15-MeV electrons incident on thick targets of Be, Al, and Pb," Med. Phys. **18**, 727-739 (1991).

B. A. Faddegon, P. O'Brien, and D. L. Mason, "The flatness of Siemens linear accelerator x-ray fields," Med. Phys. **26**, 220–228 (1999).

B. Faddegon, B. Egley, and T. Steinberg, "Comparison of beam characteristics of a gold x-ray target and a tungsten replacement target," Med. Phys. **31**, 91–97 (2004).

A. Fasso, A. Ferrari, and P. R. Sala, ''Electron–photon transport in FLUKA: status,'' in Advanced Monte Carlo for Radiation Physics, Particle Transport Simulation and Applications, Proceedings of the Monte Carlo 2000 Conference, Lisbon, October 23–26, 2000, edited by A. Kling, F. Barao, M. Nakagawa, L. Tavora, and P. Vaz (Springer-Verlag, Berlin, 2000), pp. 159–164.

D. A. Fein, K. P. McGee, T. E. Schultheiss, B. L. Fowble, and G. E. Hanks, "Intra- and interfractional reproducibility of tangential breast fields: A prospective on-line portal imaging study," Int. J. Radiat. Oncol., Biol., Phys. **34**, 733–740 (1996).

B. Fraass, K. Doppke, M. Hunt, G. Kutcher, G. Starkschall, R. Stern, and J. Van Dyke, "American Association of Physicists in Medicine Radiation Therapy Committee Task Group 53: Quality assurance for clinical radiotherapy treatment planning," Med. Phys. **25**, 1773–1829 (1998).

W. Feller, *An Introduction to Probability Theory and Its Applications*, 3rd ed.)Wiley, New York, 1967), Vol. I.

M. Fippel, I. Kawrakow, and K. Friedrich, "Electron beam dose calculations with the VMC algorithm and the verification data of the NCI working group," Phys. Med. Biol. **42**, 501–520 (1997).

M. Fippel, "Fast Monte Carlo dose calculation for photon beams based on the VMC electron algorithm," Med. Phys. **26**, 1466–1475 (1999).

M. Fippel and M. Soukup, "A Monte Carlo dose calculation algorithm for proton therapy," Med. Phys. **31,** 2263–2273 (2004).

M. K. Fix, P. J. Keall, and J. V. Siebers, "Photon-beam subsource sensitivity to the initial electron-beam parameters," Med. Phys. **32**, 1164–1175 (2005).

S. Flampouri, P. M. Evans, F. Verhaegen, A. E. Nahum, E. Spezi, and M. Partridge, "Optimization of accelerator target and detector for portal imaging using Monte Carlo simulation and experiment," Phys. Med. Biol. **47**, 3331–3349 (2002).

S. Flampouri, S. B. Jiang, G. C. Sharp, J. Wolfgang, A. A. Patel, and N. C. Choi , "Estimation of the delivered patient dose in lung IMRT treatment based on deformable registration of 4D-CT data and Monte Carlo simulations," Phys. Med. Biol. **51**, 2763–2779 (2006).

A. Fogliata, E. Vanetti, D. Albers, C. Brink, A. Clivio, T. Knöös, G. Nicolini, and L. Cozzi, "On the dosimetric behaviour of photon dose calculation algorithms in the presence of simple geometric heterogeneities: comparison with Monte Carlo calculations," Phys. Med. Biol. **52**, 1363–1385 (2007).

A. Fogliata, G. Nicolini, E. Vanetti, A. Clivio, P. Winkler, and L. Cozzi, "The impact of photon dose calculation algorithms on expected dose distributions in lungs under different respiratory phases," Phys. Med. Biol. **53**, 2375–2390 (2008).

M. Fragoso, F. Verhaegen, and A. Nahum, "A comparison of Monte Carlo (EGSnrc, PENELOPE) and commercial treatment planning system (PLATO) calculations of the dose distribution delivered by low dose-rate 137Cs sources in intracavitary brachytherapy," Med. Phys. (abstract) **29**, 1350 (2002).

M. Fuss, L. N. Loredo, P. A. Blacharski, R. I. Grove, and J. D. Slater, "Proton radiation therapy for medium and large choroidal melanoma: preservation of the eye and its functionality," Int. J. Radiat. Oncol. Biol. Phys. **49**, 1053–1059 (2001).

I. M. Gagné and D. M. Robinson, "The impact of tumor motion upon CT image integrity and target delineation" Med. Phys. **31**, 3378 (2004).

J. Gardner, J. Siebers, and I. Kawrakow, "Dose calculation validation of VMC++ for photon beams," Med. Phys. **34**, 1809–1818 (2007).

J. K. Gardner, J. V. Siebers, and I. Kawrakow, "Comparison of two methods to compute the absorbed dose to water for photon beams," Phys. Med. Biol. **52**, 439–447 (2007).

M. Goitein and J. Busse, "Immobilization error: Some theoretical considerations," Radiology **117**, 407–412 (1975).

M. Goitein, "The cell's-eye view: assessing dose in four dimensions," Int. J. Radiat. Oncol. Biol. Phys. **62**, 951–953 (2005).

R. C. Gonzales and R. E. Woods, *Digital Image Processing* (Addison-Wesley, Reading, MA, 1992).

I. S. Grills, G. Hugo, L. L. Kestin, A. P. Galerani, K. K. Chao, J. Wloch, and D. Yan, "Image-guided radiotherapy via daily online cone-beam CT substantially reduces margin requirements for stereotactic lung radiotherapy," Int. J. Radiat. Oncol., Biol., Phys. **70**(3), 1045–1056 (2008).

B. A. Groh, J. Siewerdsen, D. G. Drake, J. W. Wong, and D. A. Jaffray, "A performance comparison of flat-panel imager-based MV and kV cone-beam CT," Med. Phys. **29**, 967–975 (2002).

S. L. Haisen, H. E. Romeijn, C. Fox, J. R. Palta, and J. F. Dempsey," A computational implementation and comparison of several intensity modulated proton therapy treatment planning algorithms," Med. Phys. **35**, 1103–1112 (2008).

F. Hasenbalg, H. Neuenschwander, R. Mini, and E. J. Born, "Collapsed cone convolution and analytical anisotropic algorithm dose calculations compared to VMC++ Monte Carlo simulations in clinical cases," Phys. Med. Biol. **52**, 3679–3691 (2007).

F. Hasenbalg, M. K. Fix, E. J. Born, R. Mini, and I. Kawrakow, "VMC++ versus BEAMnrc: A comparison of simulated linear accelerator heads for photon beams," Med. Phys. **35**, 1521 (2008).

K. Hayashi, R. Tayama, K. Shibata, T. Honda, M. Morimoto, T. Izumida, T. Horikawa, S. Kanaya and K Kusakabe, "Development of a simple method to evaluate medical staff radiation dose and its application to a software system supporting PET facility operation," Radiat. Prot. Dosimetry 116, 196–201 (2005).

B. J. Heijmen, K. L. Pasma, M. Kroonwijk, V. G. Althof, J. C. de Boer, A. G. Visser, and H. Huizenga, "Portal dose measurement in radiotherapy using an electronic portal imaging device (EPID)," Phys. Med. Biol. **40**, 1943–1955 (1995).

M. G. Herman, J. M. Balter, D. A. Jaffray, K. P. McGee, P. Munro, S. Shalev, M. Ven Herk, and J. W. Wong, "Clinical use of electronic portal imaging: Report of AAPM Radiation Therapy Committee Task Group 58," Med. Phys. **28**, 712-737 (2001).

E. Heath and J. Seuntjens, "Development and validation of a BEAMnrc component module for accurate Monte Carlo modelling of the Varian dynamic millennium multileaf collimator," Phys. Med. Biol. **48**, 4045–4063 (2003).

W. Huda, S. C. Bushong, and W. R. Hendee, "In x-ray computed tomography, technique factors should be selected appropriate to patient size," Med. Phys. **28**, 1543 (2001).

K. R. Hogstrom, "Evaluation of electron pencil beam dose calculation," Med. Phys. **12**(4), 554 (1985).

L. Hong, M. Goitein, M. Bucciolini, R. Comiskey, B. Gottschalk, S. Rosenthal, C. Serago and M. Urie, "A pencil beam algorithm for proton dose calculations," Phys. Med. Biol. **41,** 1305–1330 (1996).

International Commission on Radiological Protection. *Report of the Task Group on Reference Man,* Vol. 23 (Pergamon, New York, 1974).

ICRU-Report No. 44 : Tissue substitutes in radiation dosimetry and measurement," in International Commission on Radiation Units and Measurements, 1989.

http://physics.nist.gov/PhysRefData/XrayMassCoef/tab2.html

ICRU-Report No. 63 : Nuclear Data for Neutron and Proton Radiotherapy and for Radiation Protection," in International Commission on Radiation Units and Measurements, 2000.

A. Ito, in *Monte Carlo Transport of Electrons and Photons*, edited by W. R. Nelson, T. M. Jenkins, A. Rindi, A. E. Nahum, and D. W. O. Rogers (Plenum, New York, 1988), pp. 573–598.

K. Jabbari and S. Pistorius, "A novel method for automatic detection of patient out-of-plane rotation by comparing a single portal image to a reference image," Med. Phys. **32**, 3678–3687 (2005).

K. Jabbari, A. Sarfehnia, E. B. Podgorsak, and J. P. Seuntjens, "Monte Carlo feasibility study of using orthogonal bremsstrahlung beams for improved radiation therapy imaging," Phys. Med. Biol. **52**, 1171–1184 (2006).

D. A. Jaffray, J. H. Siewerdsen, J. W. Wong, and A. A. Martinez, "Flat-panel cone beam computed tomography for image-guided radiation therapy," Int. J. Radiat. Oncol., Biol., Phys. **53**, 1337–1349 (2002).

A. K. Jaradat and P. J. Biggs, "Tenth value layers for 60Co gamma rays and for 4, 6, 10, 15, and 18 MV x rays in concrete for beams of cone angles between 0 degrees and 14 degrees calculated by Monte Carlo simulation," Health Phys. **92**, 456–463 (2007).

R. Jeraj and P. Keall, "The effect of statistical uncertainty on inverse treatment planning based on Monte Carlo dose calculation," Phys. Med. Biol. **45**, 3601–3613 (2002).

R. Jeraj and P. J. Keall, "Monte Carlo-based inverse treatment planning," Phys. Med. Biol. **44**, 1885–1896 (1999).

S. B. Jiang, J. Deng, J. Li, P. Pawlicki, A. Boyer, and C.-M. Ma, "Modeling and commissioning of clinical photon beams for Monte Carlo treatment planning," in Proceedings of the 13th ICCR, edited by T. Bortfeld and W. Schlegel (Springer-Verlag, Heidelberg, 2000), pp. 434–436.

C. P. Joshi, J. Darko, P. B. Vidyasagar, and L. J Schreiner, "Investigation of an efficient source design for Cobalt-60-based tomotherapy using EGSnrc Monte Carlo simulations," Phys. Med. Biol. **53**, 575–592 (2008).

T. Kairn, D. Cassidy, P. M. Sandford, and A. L. Fielding. "Radiotherapy treatment verification using radiological thickness measured with an amorphous silicon electronic portal imaging device: Monte Carlo simulation and experiment," Phys. Med. Biol. **53**, 3903–3919 (2008).

C. J. Karzmark, "Advances in linear accelerator design for radiotherapy," Med. Phys. **11**, 105–128 (1984).

I. Kawrakow, M. Fippel, and K. Friedrich, "3D Electron Dose Calculation using a Voxel based Monte Carlo Algorithm," Med. Phys **23**, 445–457 (1996).

I. Kawrakow, "Improved modeling of multiple scattering in the Voxel Monte Carlo model," Med. Phys. **24**, 505–517 (1997).

I. Kawrakow and A. F. Bielajew, "On the representation of electron multiple elastic-scattering distributions for Monte Carlo calculations," Nucl. Instrum. Methods Phys. Res. B 134, 325–336 (1998).

I. Kawrakow and D. W. O. Rogers, "The EGSnrc code system: Monte Carlo simulation of electron and photon transport," NRC, Report PIRS–701, 2000.

I. Kawrakow, "Accurate condensed history Monte Carlo simulation of electron transport. I. EGSnrc, the new EGS4 version," Med. Phys. **27**, 485–498 (2000).

I. Kawrakow and M. Fippel, "VMC++, a MC algorithm optimized for electron and photon beam dose calculations for RTP," in *Proceedings of the 22nd Annual International Conference of the IEEE* (Engineering in Medicine and Biology Society, Piscataway, NJ, 2000).

I. Kawrakow, D. W. O. Rogers, and B. R. B. Walters, "Large efficiency improvements in BEAMnrc using directional bremsstrahlung splitting," Med. Phys. **31**, 2883–2898 (2004).

I. Kawrakow and B. Walters, "Efficient photon beam dose calculations using DOSXYZnrc with BEAMnrc," Med. Phys. **33**, 3046–3056 (2006).

I. Kawrakow and B. R. B. Walters, "Technical note: Overprediction of dose with default PRESTA-I boundary crossing in DOSXYZnrc and BEAMnrc," Med. Phys. **34**, 547–650 (2007).

P. J. Keall and P. W. Hoban, "Super-Monte Carlo: a 3D electron beam dose calculation algorithm," Med. Phys. **23**, 2023–2034 (1996).

P. J. Keall and P. W. Hoban, "Superposition dose calculation incorporating Monte Carlo generated electron track kernels," Med. Phys. **23**, 479–485 (1996).

P. J. Keall, J. V. Siebers, R. Jeraj, and R. Mohan, "The effect of dose calculation uncertainty on the evaluation of radiotherapy plans," Med. Phys. **27**, 478–484 (2000).

P. J. Keall, J. V. Siebers, S. Joshi, and R. Mohan, "Monte Carlo as a four-dimensional radiotherapy treatment-planning tool to account for respiratory motion," Phys. Med. Biol. **49**, 3639–3648 (2004).

F. M. Khan, *The Physics of Radiation Therapy* (Lippincott, Williams & Wilkins,Philadelphia, PA, 2003).

F. M. Khan, *Treatment Planning in Radiation Oncology* (Lippincott, Williams & Wilkins, Philadelphia, PA, 2003).

A. Khoury, C. M. Whyne, M. Daly, D. Moseley, G. Bootsma, T. Skrinskas, J. Siewerdsen, and D. Jaffray, "Intraoperative cone-beam CT for correction of periaxial malrotation of the femoral shaft: a surface-matching approach," Med. Phys. **34**, 1380–1387 (2007).

P. Kimstrand, N. Tilly, A. Ahnesjö and E. Traneus, "Experimental test of Monte Carlo proton transport at grazing incidence in GEANT4, FLUKA and MCNPX," Phys. Med. Biol. **53**, 1115–1129 (2008).

A. Kling, F. Barao, M. Nakagawa, L. Távora, and P. Vaz (Springer, Berlin, 2001), pp. 229–236.

B. R. B. Walters and D. W. O. Rogers, "DOSXYZnrc Users Manual," NRC Report PIRS 794 (rev B), 2004.

T. Knoos, A Ahnesjo, P. Nilsson, and L. Weber, "Limitation of pencil beam approach to photon dose calculation in lung tissue," Phys. Med. Biol. **40**, 1411–1420 (1995).

A. Knopf, K. Parodi, H. Paganetti, E. Cascio, A. Bonab, and T. Bortfeld, "Quantitative assessment of the physical potential of proton beam range verification with PET/CT," Phys. Med. Biol. **53**, 4137–4151 (2008).

D. J. La Russa, M. McEwen, and D. W. Rogers, "An experimental and computational investigation of the standard temperature-pressure correction factor for ion chambers in kilovoltage x rays." Med. Phys. **34**, 4690–4699 (2007).

E. W. Larsen, "A theoretical derivation of the condensed history algorithm," Ann. Nucl. Energy 19, 701–714 (1992).

I. Lax, "Inhomogeneity corrections in electron beam dose planning. Limitations with the semi-infinite slab approximation," Phys. Med. Biol. **31**, 879-892 (1986).

M. Lee, A. E. Nahum, and S. Webb, "An empirical method to build up a model of proton dose distribution for a radiotherapy treatment planning package," Phys. Med. Biol. **38**, 989–998 (1993).

C. H. Lee, D. Tait, A. E. Nahum, and S. Webb, "Comparison of proton therapy and conformal x-ray therapy in non-small cell lung cancer (nsclc)," Br. J. Radiol. **72**, 1078–1084 (1999).

C. L. Lee, X. L. Zhou, R. J. Kudchadker, F. Harmon, Y. D. Harker, "A Monte Carlo dosimetry-based evaluation of the 7Li(p,n)7Be reaction near threshold for accelerator boron neutron capture therapy," Med. Phys. **27**, 192–202 (2000).

M. C. Lee, S. B. Jiang, and C. M. Ma, "Monte Carlo and experimental investigations of multileaf collimated electron beams for modulated electron radiation therapy," Med. Phys. **27**, 2708–2708 (2000).

S. Lee, G. Fichtinger, and G. S. Chirikjian, "Numerical algorithms for spatial registration of line fiducials from cross-sectional images," Med. Phys. **29**, 1881 (2002).

T. K. Lee and G. A. Sandisonm, "The energy-dependent electron loss model: backscattering and application to heterogeneous slab media," Phys. Med. Biol. **48**, 259–273 (2003).

S. W. Lee, J. Y. Jin, H. Guan, F. Martin, J. H. Kim, and F. F. Yin, "Clinical assessment and characterization of a dual tube kilovoltage X-ray localization system in the radiotherapy treatment room," J. Appl. Clin. Med. Phys. **9,** 2318 (2008).

J. Leong, "Digital image processing system for high energy x-ray portal images," Phys. Med. Biol. **20**, 1527–1535 (1984).

D. Létourneau, R. Wong, D. Moseley, M. B. Sharpe, S. Ansell, M. Gospodarowicz, and D. A. Jaffray, "Online planning and delivery technique for radiotherapy of spinal metastases using cone-beam CT: image quality and system performance," Int. J. Radiat. Oncol., Biol., Phys. **67**(4), 1229–1237 (2007).

L. B. Levy, R. G Waggener, and A. E. Wright, "Measurement of primary bremsstrahlung spectrum from an 8-MeV linear accelerator," Med. Phys. **3**, 173-175 (1976).

D. G. Lewis, W. Swindell, E. J. Morton, P. M. Evans, and Z. R. Xiao, "A megavoltage CT scanner for radiotherapy verification," Phys. Med. Biol. **37**, 1985–1999 (1992).

H. W. Lewis, "Multiple scattering in an infinite medium," Phys. Rev. **78**, 526–529 (1950).

J. S. Li, B. Shanine, E. Fourkal, and C.-M. Ma, "A particle track-repeating algorithm for proton beam dose calculation," Phys. Med. Biol. **50**, 1001–1010 (2005).

B. Libby, J. Siebers, and R. Mohan, "Validation of Monte Carlo generated phase-space descriptions of medical linear accelerators," Med. Phys. **26**, 1476–1483 (1999).

A. J. Lomax, T. Bohringer, A. Bolsi, D. Coray, F. Emert, G. Goitein, M. Jermann, S. Lin, E. Pedroni, H. Rutz, O. Stadelmann, B. Timmermann, J. Verwey, and D. C. Weber, "Treatment planning and verification of proton therapy using spot scanning: Initial experiences," Med. Phys. **31**, 3150–3157 (2004).

Los Alamos National Laboratory *MCNPX User's Manual* Version 2.4.0, LANL Report LA-CP-02-408 (2002).

P. E. Lindsay, I. El Naqa, A. J. Hope, M. Vicic, J. Cui, J. D. Bradley, and J. O. Deasy, "Retrospective monte carlo dose calculations with limited beam weight information," Med. Phys. **34**, 334–346 (2007).

D. M. Lovelock, C. S. Chui, and R. Mohan, "A Monte Carlo model of photon beams used in radiation therapy," Med. Phys. **22**, 1387–1394 (1995).

C. M. Ma and S. B. Jiang, "Monte Carlo modelling of electron beams from medical accelerators," Phys. Med. Biol. **44**, R157–R189 (1999).

C. M. Ma, E. Mok, A. Kapur, T. Pawlicki, D. Findley, S. Brain, K. Forster, and A. L. Boyer, "Clinical implementation of a Monte Carlo treatment planning system," Med. Phys. **26**, 2133–2143 (1999).

C. M. Ma, B. A. Faddegon, D. W. O. Rogers, and T. R. Mackie, "Accurate characterization of Monte Carlo calculated electron beams for radiotherapy," Med. Phys. **24**, 401–416 (1997).

C. M. Ma, J. S. Li, T. Pawlicki, S. B. Jiang, and J. Deng, "MCDOSE—A Monte Carlo dose calculation tool for radiation therapy treatment planning," in Proceedings of the 13th

ICCR, edited by T. Bortfeld and W.Schlegel (Springer-Verlag, Heidelberg, 2000), pp. 411–413.

C. M. Ma, J. S. Li, T. Pawlicki, S. B. Jiang, J. Deng, M. C. Lee, T. Koumrian, M. Luxton, and S. Brain, "A Monte Carlo dose calculation tool for radiotherapy treatment planning," Phys. Med. Biol. **47,** 1671–1689 (2002).

C. Ma, J. S. Li, T. Pawlicki, S. B. Jiang, J. Deng, M. C. Lee, T. Koumrian, M. Luxton, and S. Brain, "MCDOSE - A Monte Carlo dose calculation tool for radiation therapy treatment planning," Phys. Med. Biol. **47**, 1671–1689 (2002).

C-M Ma *et al.* "MCSIM—a Monte Carlo dose calculation tool for radiation therapy," *Proc. 14th ICCR*, (Seoul,Korea, 2004), pp. 123–126.

C. Ma, J. Li, J. Deng, and J. Fan, "Investigation of Fast Monte Carlo Dose Calculation for CyberKnife SRS/SRT Treatment Planning," Med. Phys. **34**, 2589–2590 (2007).

T. R. Mackie, J. W. Scrimger, and J. J. Battista, "A convolution method of calculating dose for 15-MV x rays," Med. Phys. **12**, 188–196 (1985).

E. Mah, J. Antolak, J. W. Scrimger, and J. J. Battista, "Experimental evaluation of 2D and 3D electron pencil beam algorithm," Phys. Med. Biol. **34**, 1179–1194 (1989).

D. W. Mah, D. M. Galbraith, and J. A. Rawlinson, "Low-energy imaging with high-energy bremsstrahlung beams: Analysis and scatter reduction," Med. Phys. **20**, 653–665 (1993).

J. E. Marks, A. G. Haus, H. G. Sutton, and M. L. Griem, "The value of frequent treatment (N.Y.) verification films in reducing localization error in the irradiation of complex fields," Cancer (N.Y.) **37**, 2755–2761 (1976).

M. McEwen, H. Palmans, and A. Williams, "An empirical method for the determination of wall perturbation factors for parallel-plate chambers in high-energy electron beams," Phys. Med. Biol. **51**, 5167–5181 (2006).

H. Meertens, M. van Herk, and J. Weeda, "A liquid ionization detector for digital radiography of therapeutic megavoltage photon beams," Phys. Med. Biol. **30**, 313–321 (1985).

D. W. Miller "A review of proton beam radiation therapy," Med. Phys. **11**, 1943–1953 (1995).

R. Mohan, C. Chui, and L. Lidofsky, "Energy and angular distributions of photons from medical linear accelerators," Med. Phys. **12**, 592–597 (1985).

R. Mohan, C. Chui, and L. Lidofsky, "Differential pencil beam dose computation model for photons," Med. Phys. **13**, 64–73 (1986).

M. A. Mosleh-Shirazi, P. M. Evans, W. Swindell, S. Webb, and M. Partridge, "A cone-beam megavoltage CT scanner for treatment verification in conformal radiotherapy," Radiother. Oncol. **48**, 319–328 (1998).

J. W. Motz and M. Donas, "Image information content and patient exposure," Med. Phys. **5,** 8–22 (1978).

P. Munro, "Portal imaging Technology, past present and future," Seminars in Radiation Therapy **5**, 115-133 (1995).

P. Munro, J. A. Rawlinson, and A. Fenster, "A digital fluoroscopic imaging device for radiotherapy localization," Int. J. Radiat. Oncol., Biol., Phys. **18**, 641–649 (1990).

A. E. Nahum, in *Monte Carlo Transport of Electrons and Photons*, edited by W. R. Nelson, T. M. Jenkins, A. Rindi, A. E. Nahum, and D. W. O. Rogers (Plenum, New York, 1988), pp. 3–20.

W. R. Nelson, H. Hirayama, and D. W. O. Rogers, "The EGS4 Code System," SLAC Report No. SLAC-265, 1985.

H. Neuenschwander and E. J. Born, "A Macro Monte Carlo method for electron beam dose calculations," Phys. Med. Biol. **37**, 107–125 (1992).

H. Neuenschwander, T. R. Mackie, and P. J. Reckwerdt, "MMC— A high-performance Monte Carlo code for electron beam treatment planning," Phys. Med. Biol. **40**, 543–574 (1995).

J. E. O Connor, "The variation of scattered x-rays with density in an irradiated body," Phys. Med. Biol. **1**, 352-369 (1957).

M. Oliver, R. Staruch, A. Gladwish, J. Craig, J. Chen, and E. Wong, "Monte Carlo dose calculation of segmental IMRT delivery to a moving phantom using dynamic MLC and gating log files," Phys. Med. Biol. **53**, 187–196 (2008).

E. K. Osei, J. Darko, A. Mosseri, and J. Jezioranski, "EGSNRC Monte Carlo study of the effect of photon energy and field margin in phantoms simulating small lung lesions," Med. Phys. **30**, 2706–2714 (2003).

O. Z. Ostapiak, P. F. O'Brien, and B. A. Faddegon, "Megavoltage imaging with low Z targets: Implementation and characterization of an investigational system," Med. Phys. **25**, 1910–1918 (1998).

M. Pacilio, D. Aragno, R. Rauco, S. D'Onofrio, M. C. Pressello, L. Bianciardi and E.Santini, "Monte Carlo dose calculations using MCNP4C and EGSnrc/BEAMnrc codes to study the energy dependence of the radiochromic film response to beta-emitting sources," Phys. Med. Biol. **52**, 3931–3948 (2007).

H. Paganetti, "Nuclear interactions in proton therapy: dose and relative biological effect distributions originating from primary and secondary particles," Phys. Med. Biol. **47**, 747–64 (2002).

H. Paganetti, A. Niemierko, M. Ancukiewicz, L. E. Gerweck, J. S. Loeffler, M. Goitein, and H. D. Suit, "Relative biological effectiveness (RBE) values for proton beam therapy," Int. J. Radiat. Oncol. Biol. Phys. **53**, 407–421 (2002).

H. Paganetti, H. Jiang, J. A. Adams, G. T. Chen, and E. Rietzel, "Monte Carlo simulations with time-dependent geometries to investigate effects of organ motion with high temporal resolution," Int. J. Radiat. Oncol., Biol., Phys. **60**, 942–950 (2004).

K. Parodi, H. Paganetti, E. Cascio, J. B. Flanz, A. A. Bonab, N. M. Alpert, K. Lohmann, and T. Bortfeld, "PET/CT imaging for treatment verification after proton therapy: A study with plastic phantoms and metallic implants," Med. Phys. **34**, 3369–3387 (2007).

P. Pemler, J. Besserer, U. Schneider, and H. Neuenschwander, "Evaluation of a commercial electron treatment planning system based on Monte Carlo techniques (eMC) ," Med. Phys. **16**, 313–329 (2006).

S. F. Petit, W. J. van Elmpt, S. M. Nijsten, P. Lambin, and A. L. Dekker "Calibration of megavoltage cone-beam CT for radiotherapy dose calculations: correction of cupping artifacts and conversion of CT numbers to electron density," Med. Phys. **35**, 849–865 (2008).

P. L. Petti, "Evaluation of a pencil-beam dose calculation technique for charged particle radiotherapy," Int. J. Radiat. Oncol. Biol. Phys. **35** 1049–57 (1996).

J.-P. Pignol, P.Cuendet, N. Brassart, G. Fares, F. Colomb, C. M. Diop, R. Sabattier, A. Hachem, and G. Prevot "Combined use of FLUKA and MCNP-4A for the Monte Carlo

simulation of the dosimetry of ^{10}B neutron capture enhancement of fast neutron irradiations," Med. Phys. **25**, 885–891 (1998).

E. B. Podgorsak, J. A. Rawlinson, M. Glavinovic, and H. E. Johns, "Design of x-ray targets for high energy linear accelerators in radiotherapy," Am. J. Roentgenol. Radium Ther. Nucl. Med. **121**, 873–882 (1974).

E. B. Podgorsak, *Radiation Physics for Medical Physicists* (Springer, 2005).

E. Poon and F. Verhaegen, "Accuracy of the photon and electron physics in GEANT4 for radiotherapy applications," Med. Phys. **32**, 1696–1711 (2005).

E. Poon, J. P. Seuntjens, and F. Verhaegen, "Consistency test of the electron transport algorithm in the GEANT4 Monte Carlo code," Phys. Med. Biol. **50**, 681–694 (2005).

R. A. Popple, R. Weinberg, J. A. Antolak, S. J. Ye, P. N. Pareek, J. Duan, S. Shen, and I. Brezovich, "A Comprehensive evaluation of a commercial macro Monte Carlo electron dose calculation implementation using a standard verification data set," Med. Phys. **33**, 1540–1551 (2006).

D. E. Raeside "Monte Carlo principles and applications," Phys. Med. Biol. **21**, 181–197 (1976).

L. E. Reinstein, L. Alquist, H. I. Amols, and B. Lagueux, "Quantitative evaluation of a portal film contrast enhancement technique," Med. Phys. **14**, 309 (1987).

L. E. Reinstein, M. Durham, M. Tefft, A. Yu, A. S. Glicksman, and W. Eaton, "Portal film quality: A multiple institutional study," Med. Phys. **11**, 555 (1984).

J. L. Robar, Riccio S. A., and M. A. Martin, "Tumour dose enhancement using modified megavoltage photon beams and contrast media," Phys. Med. Biol. **47**, 2433–2449 (2002).

D. W. O. Rogers and A. F. Bielajew, in Monte Carlo Transport of Electrons and Photons, edited by W. R. Nelson, T. M. Jenkins, A. Rindi, A. E. Nahum, and D. W. O. Rogers (Plenum, New York, 1988), pp. 407–419.

D. W. Rogers and A. F. Bielajew, "Monte Carlo techniques of electron and photon transport for radiation dosimetry," *The Dosimetry of Ionization Radiation*, Chapter 5, Vol III (1990).

D. W. O. Rogers, B. A. Faddegon, G. X. Ding, C. M. Ma, J. We, and T. R. Mackie, "BEAM: A Monte Carlo code to simulate radiotherapy treatment units," Med. Phys. **22**, 503–524 (1995).

D. W. O. Rogers and R. Mohan, "Questions for comparison of clinical Monte Carlo codes," *The Use of Computers in Radiotherapy, XIIIth Int'l Co*, e *nf., Heidelberg*dited by W. Schlegel and T. Bortfeld (Springer-Verlag, Heidelberg, 2000), pp. 120–122.

D. W. O. Rogers, B. Walters, and I. Kawrakow, "BEAMnrc Users Manual," NRC Report PIRS 509(a)revH, 2004.

D. W. Rogers, "Fifty years of Monte Carlo simulations for medical physics," Phys. Med. Biol. **51**, R287-301 (2006).

S. A. Rosenthal, J. M. Galvin, J. W. Goldwein, A. R. Smith, and P. H. Blitzer, "Improved methods for determination of variability in patient positioning for radiation therapy using simulation and serial portal film measurements," Int. J. Radiat. Oncol., Biol., Phys. **23**, 621–625 (1992).

M. Rosu, J. M. Balter, I. J. Chetty, M. L. Kessler, D. L. Mc Shan, P. Balter, and R. K. Ten Haken, "How extensive of a 4D dataset is needed to estimate cumulative dose distribution plan evaluation metrics in conformal lung therapy?," Med. Phys. **34**, 233–245 (2007).

M. Rosu, I. J. Chetty, D. S. Tatro, and R. K. Ten Haken, "The impact of breathing motion versus heterogeneity effects in lung cancer treatment planning," Med. Phys. **34**, 1462–1473 (2007).

K. J. Ruchala, G. H. Olivera, E. A. Schloesser, and T. R. Mackie, "Megavoltage CT on a tomotherapy system," Phys. Med. Biol. **44**, 2597–2621 (1999).

S. N. Rustgi and J. E. Rodgers, "Analysis of the bremsstrahlung component in 6-18 MeV electron beams," Med. Phys. **14**, 884–888 (1987).

K. Russell, U. Isacsson, M. Saxner, A. Ahnesjo, A. Montelius, E. Grusell, C. V. Dahlgren, S. Lorin, and B. Glimelius, "Implementation of pencil kernel and depth penetration algorithms for treatment planning of proton beams," Phys. Med. Biol. **45**, 9–27 (2000).

M. Sadeghi, G. Raisali, S. H. Hosseini, and A. Shavar "Monte Carlo calculations and experimental measurements of dosimetric parameters of the IRA-103Pd brachytherapy source," Med. Phys. **35,** 1288–1294 (2008).

A. Sarfehnia, K. Jabbari, J. P. Seuntjens, and E. B. Podgorsak, "Experimental verification of beam quality in high-contrast imaging with orthogonal bremsstrahlung photon beams," Med. Phys. **34**, 2896–2906 (2007).

C. Scherf, J. Scherer, and L. Bogner, "Verification and application of the Voxel-based Monte Carlo (VMC++) electron dose module of oncentratrade mark MasterPlan," Strahlenther. Onkol. **183**, 81–88 (2007).

J. Seco, G. C. Sharp, J. Turcotte, D. Gierga, T. Bortfeld, and H. Paganetti ,"Effects of organ motion on IMRT treatments with segments of few monitor units," Med. Phys. **34**, 923 (2007).

V. A. Semenenko and R. D. Stewart, "Fast Monte Carlo simulation of DNA damage formed by electrons and light ions," Phys. Med. Biol. **51**, 1693–1706 (2005).

J. Sempau, S. J. Wilderman, and A. F. Bielajew, "DPM, a fast, accurate Monte Carlo code optimized for photon and electron radiotherapy treatment planning dose calculations," Phys. Med. Biol. **45**, 2263–2291 (2000).

J. Sempau and A. F. Bielajew, "Towards the elimination of Monte Carlo statistical fluctuation from dose volume histograms for radiotherapy treatment planning," Phys. Med. Biol. **45**, 131–157 (2000).

D. Sheikh-Bagheri and D. W. O. Rogers, "Sensitivity of megavoltage photon beam Monte Carlo simulations to electron beam and other parameters," Med. Phys. **29**, 379–390 (2002).

R. Sheu, C. Chui, T. LoSasso, S. Lim, and A. Kirov, "Accurate and Efficient Monte Carlo Dose Calculation for Electron Beams," Med. Phys. **33**, 2067 (2006).

A. S. Shiu and K. R. Hogstrom, "Pencil-beam redefinition algorithm for electron dosedistributions," Med. Phys. **18**, 7–18 (1991).

K. R. Shortt, C. K. Ross, A. F. Bielajew, and D. W. O. Rogers, "Electron beam dose distribution near standard inhomogeneities," Med. Phys. **31**, 235–249 (1986).

R. L. Siddon, "Prism representation: a 3D ray-tracing algorithm for radiotherapy applications," Phys. Med. Biol. **30**, 817–24 (1985).

J. V. Siebers, I. Kawrakow, and V. Ramakrishnan, "Performance of a hybrid MC dose algorithm for IMRT optimization dose evaluation," Med. Phys. **34**, 2853 (2007).

J. Sillanpaa, J. Chang, G. Mageras, H. Riem, J. Ford, D. Todor, C. C. Ling, and H. Amols, "Developments in megavoltage cone beam CT with an amorphous silicon EPID: reduction of exposure and synchronization with respiratory gating," Med. Phys. **32**, 819–829 (2005).

R. Smith, "Proton therapy" Phys. Med. Biol. **45,** R491–R504 (2006).

T. D. Solberg *et al*., "A review of radiation dosimetry applications using the MCNP Monte Carlo code," Radiochim. Acta. **89**, 337–355 (2001).

M. Soukup, M. Fippel, and M. Alber, "A pencil beam algorithm for intensity modulated proton therapy derived from Monte Carlo simulations," Phys. Med. Biol. **50**, 5089–5104 (2005).

S. Stathakis, J. Li, and C. M. Ma, "Monte Carlo determination of radiation-induced cancer risks for prostate patients undergoing intensity- modulated radiation therapy," J. Appl. Clin. Med. Phys. **8**, 2685 (2007).

L. Strigari, E. Menghi, M. D'Andrea, and M. Benassi, "Monte Carlo dose voxel kernel calculations of beta-emitting and Auger-emitting radionuclides for internal dosimetry: A comparison between EGSnrcMP and EGS4," Med. Phys. **33**, 3383–3389 (2006).

W. Swindell, R. G. Simpson, and J. R. Oleson, "Computed tomography with a linear accelerator with radiotherapy applications," Med. Phys. **10**, 416–420 (1983).

J. R. Sykes, R. Lindsay, C. J. Dean, D. S. Brettle, D. R. Magee, and D. I. Thwaites, "Measurement of cone beam CT coincidence with megavoltage isocentre and image sharpness using the QUASARtrade mark Penta-Guide phantom," Phys. Med. Biol. **53**, 5275–5293 (2008).

H. Szymanowski, A. Mazal, C. Nauraye, S. Biensan, R. Ferrand, M. C. Murillo, S. Caneva, G. Gaboriaud, and J. C. Rosenwald, "Experimental determination and verification of the parameters used in a proton pencil beam algorithm," Med. Phys. **28**, 975–987 (2001).

H. Szymanowski and U. Oelfke, "Two-dimensional pencil beam scaling: an improved proton dose algorithm for heterogeneous media," Phys. Med. Biol. **47**, 3313–3330 (2002).

H. Szymanowski and U Oelfke, "CT calibration for two-dimensional scaling of proton pencil beams," Phys. Med. Biol. **48**, 861–874 (2003).

C. Theis, D. Forkel-Wirth, D. Perrin, S. Roesler, and H. Vincke, "Characterisation of ionisation chambers for a mixed radiation field and investigation of their suitability as radiation monitors for the LHC," Radiat. Prot. Dosimetry 116, 170–174 (2005).

M. Todorovic, M. Fischer, F. Cremers, E. Thom, and R. Schmidt, "Evaluation of GafChromic EBT prototype B for external beam dose verification," Med. Phys. **33**, 1321 (2006).

A. Tourovsky, A. J. Lomax, U. Schneider, E. Pedroni, "Monte Carlo dose calculations for spot scanned proton therapy," Phys. Med. Biol. **50,** 971–981 (2005).

W. C. Toye, K. R. Das, S. P. Todd, M. B. Kenny, R. D. Franich, and P. N. Johnston, "An experimental MOSFET approach to characterize (192)Ir HDR source anisotropy," Phys. Med. Biol. **52**, 5329–5339 (2007).

S. Trovati, F. Ballarini, G. Battistoni, F. Cerutti, A. Fassò, A. Ferrari, E. Gadioli, M. V. Garzelli, A. Mairani, A. Ottolenghi, H. G. Paretzke, V. Parini, M. Pelliccioni, L. Pinsky, P. R. Sala, D. Scannicchio, and M. Zankl, " Human exposure to space radiation: role of primary and secondary particles," Human exposure to space radiation: role of primary and secondary particles," Radiat. Prot. Dosimetry 122, 362–366 (2006).

N. Tyagi, J. M. Moran, D. W. Litzenberg, A. F. Bielajew, B. A. Fraass, and I. J. Chetty, "Experimental verification of a Monte Carlo-based MLC simulation model for IMRT dose calculation," Med. Phys. **34**, 651–663 (2007).

N. Tyagi, A. Bose, and I. J. Chetty, "Implementation of the DPM Monte Carlo Code on a parallel architecture for treatment planning applications," Med. Phys. **31**, 2721–2725 (2004).

A. Tzedakis, J. E. Damilakis, M. Mazonakis, J. Stratakis, H. Varveris, and N. Gourtsoyiannis, "Influence of initial electron beam parameters on Monte Carlo calculated absorbed dose distributions for radiotherapy photon beams," Med. Phys. **31**, 907–913 (2004).

F. Ubrich, J. Wulff, R. Kranzer, and K. Zink, "Thimble ionization chambers in medium-energy x-ray beams and the role of constructive details of the central electrode: Monte Carlo simulations and measurements," Phys. Med. Biol. **53**, 4893–4906 (2008).

M. Urie, M. Goitein, and M. Wagner, "Compensating for heterogeneities in proton radiation therapy," Phys. Med. Biol. **29**, 553–566 (1984).

J. Van Dyk, *The Modern Technology of Radiation Oncology* (Medical Physics Publishing, Madison, WI, 1999).

M. Van Herk and H. Meertens, "A matrix ionization chamber imaging device for on-line patient setup verification during radiotherapy," Radiother.Oncol. **11**(4), 369–378 (1988).

M. Van Herk, W. Fencl, and A. van Dalen, "Design and implementation of a high speed matrix ionization chamber system," Med. Phys. **22**, 991 (1995).

T. Vatanen, E. Traneus, and T. Lahtinen, "Dosimetric verification of a Monte Carlo electron beam model for an add-on eMLC," Phys. Med. Biol. **53**, 391–404 (2008).

P. V. Vavilov, "Ionization Losses of High-Energy Heavy Particles," *Soviet Physics JETP* **5,** 749–51 (1957).

D. Verellen, W. De Neve, F. Van den Heuvel, M. Coghe, O. Louis, and G. Storme, "On-line portal imaging: Image quality defining parameters for pelvic fields—a clinical evaluation," Int. J. Radiat. Oncol., Biol., Phys. **27** (4), 945–952 (1993).

F. Verhaegen, "Evaluation of the EGSnrc Monte Carlo code for interface dosimetry near high-Z media exposed to kilovolt and 60Co photons," Phys. Med. Biol. **47**, 1691–1705 (2002).

F. Verhaegen and H. Palmans "A systematic Monte Carlo study of secondary electron fluence perturbation in clinical proton beams (70–250 MeV) for cylindrical and spherical ion chambers," Med. Phys. **28,** 2088–95 (2001).

F. Verhaegen and J. Seuntjens, "Monte Carlo modelling of external radiotherapy photon beams," Phys. Med. Biol. **48**, R107–R164 (2003).

F. Verhaegen, B. Reniers, F. Deblois, S. Devic, J. Seuntjens and D. Hristov, "Dosimetric and microdosimetric study of contrast-enhanced radiotherapy with kilovolt x-rays," Phys. Med. Biol. **50**, 3555–3369 (2005).

B. R. B. Walters, I. Kawrakow, and D. W. O. Rogers, "History by history statistical estimators in the BEAM code system," Med. Phys. **29**, 2745–2752 (2002).

B. R. B. Walters, I. Kawrakow, and D. W. O. Rogers, DOSXYZnrc Users Manual, NRC Report PIRS 794 (rev B), 2005.

B. R. B. Walters and I. Kawrakow "A "HOWFARLESS" option to increase efficiency of homogeneous phantom calculations with DOSXYZnrc ," Med. Phys. **34**, 3794-3807 (2007).

L. L. Wang and D. W. Rogers, "Calculation of the replacement correction factors for ion chambers in megavoltage beams by Monte Carlo simulation," Med. Phys. **35**, 1747–1755 (2008).

L. Wang, C. S. Chui, and M. Lovelock, "A patient-specific Monte Carlo dose-calculation method for photon beams," Med. Phys. **25**, 867–878 (1998).

X. Weng, Y. Yan, H. Shu, J. Wang, S. B. Jiang, and L. Luo, "A vectorized Monte Carlo code for radiotherapy treatment planning dose calculation," Phys. Med. Biol. **48**, 111–120 (2003).

B. Wowk, T. Radcliffe, K. W. Leszczynski, S. Shalev, and R. Rajapakshe, "Optimization of metal/phosphor screens for on-line portal imaging," Med. Phys. **21**, 227–235 (1994).

J. Yang, J. S. Li, L. Qin, W. Xiong, and C. M. Ma "Modelling of electron contamination in clinical photon beams for Monte Carlo dose calculation," Phys. Med. Biol. **49**, 2657–2673 (2004).

C. Zakarian and J. O. Deasy, "Beamlet dose distribution compression and reconstruction using wavelets for intensity modulated treatment planning," Med. Phys. **31**, 368–375 (2004).

R. Zamenhof, E. Redmond, G. Solares, D. Katz, K. Riley, S. Kiger, and O. Harling, "Monte Carlo-based treatment planning for boron neutron capture therapy using custom designed models automatically generated from CT data," Int. J. Radiat. Oncol. Biol. Phys. **35**, 383–397 (1996).

W. Zhao and J. A. Rowlands, "X-ray imaging using amorphous selenium: Feasibility of a flat panel self-scanned detector for digital radiology," Med. Phys. **22**, 1595–1604 (1995).

Y. Zhu, X. Q. Jiang, and J. Van Dyk, "Portal dosimetry using a liquid ion chamber matrix: Dose response studies," Med. Phys. **22**, 1101–1106 (1995).